Sites NGHP-01-10, 12, and 13

By T. Collett, M. Riedel, J. Cochran, R. Boswell, J. Presley, P. Kumar, A. Sathe,
A. Sethi, M. Lall, and the National Gas Hydrate Program Expedition 01 Scientists

Scientific Investigations Report 2012–5054

U.S. Department of the Interior
U.S. Geological Survey

Contents

Background and Objectives....531
Operations....531
Site NGHP-01-10....531
Hole NGHP-01-10A....531
Hole NGHP-01-10B....532
Hole NGHP-01-10C....536
Hole NGHP-01-10D....536
Site NGHP-01-12....537
Hole NGHP-01-12A....537
Site NGHP-01-13....538
Hole NGHP-01-13A....538
Lithostratigraphy....538
Lithostratigraphic Units....539
Lithostratigraphic Unit I....539
Gas-Hydrate Occurrence....543
Inorganic Geochemistry....543
Interstitial Water Chloride—Gas-Hydrate Distribution....543
Sulfate Concentrations and the SMI....554
Alkalinity....554
Bromide....554
Organic Geochemistry....554
Microbiology....558
Hole NGHP-01-10B....558
Hole NGHP-01-10D....558
Physical Properties....567
Infrared Imaging....567
Environmental Conditions....567
Infrared Images....567
Core-End Temperature Readings....573
Index Properties....578
Strength....579
Electrical Resistivity....594
P-Wave Velocity....594
Magnetic Susceptibility....594
Thermal Conductivity....594
Downhole Temperature Measurements....594
Pressure Coring....594
Pressure Core Operations and Measurements....598
Gas Hydrate Concentration, Nature, and Distribution from Pressure Coring....625

Downhole Logging 626
Logging-While-Drilling 626
Operations 626
Gas Monitoring with Real Time LWD/MWD Data 630
LWD Log Quality 630
LWD Porosities 633
LWD Borehole Images 635
Wire-Line Logging in Hole NGHP-01-10D 635
Operations 635
Wire-Line Log Quality 642
Wire-Line Logging in Hole NGHP-01-13A 642
Operations 642
Logging Data Quality 645
Logging-While-Drilling and Wire-Line Logging Comparison 645
Logging Units 645
Gas Hydrate and Free Gas Occurrence 645
Gas Hydrate and Free Gas Occurrence in Hole NGHP-01-13A 648
References Cited 651

Figures

1. Location of Sites NGHP-01-10, NGHP-01-12 and NGHP-01-13 (GD-3-1) in the Krishna-Godavari (KG) Basin 532
2. Seismic line GDSW-16 (orientation is NW-SE) crossing drill Sites NGHP-01-10, NGHP-01-12, and NGHP-01-13 533
3. Seismic line GDSW-46 (orientation is NE-SW) crossing drill Site NGHP-01-10 534
4. Map showing all holes occupied at Sites NGHP-01-10, 12, and 13 (GD-3-1) 535
5. Lithostratigraphic summary of Hole NGHP-01-10B 540
6. Lithostratigraphic summary of Hole NGHP-01-10D 541
7. Lithostratigraphic summary of Hole NGHP-01-12A 542
8. Possible fossil chemosynthetic communities 547
9. Authigenic carbonate nodules 548
10. Moussey texture preserved in a split core (Section NGHP-01-10D-08X-1, 35–91 cm) due to the dissociation of gas hydrate 549
11. Interstitial water composition depth profiles of A, chloride; B, sulfate and methane; C, alkalinity; D, bromide; and E, bromide/chloride ratio at Holes NGHP-01-10B, NGHP-01-10D and NGHP-01-12A 553
12. Plot of headspace methane gas concentration with depth for Sites NGHP-01-10 and NGHP-01-12 557
13. Plot of headspace carbon dioxide gas concentration (mM) with depth for Sites NGHP-01-10 and NGHP-01-12 559
14. Plot of headspace (HS) (closed) and free/void (open) gas methane to carbon dioxide gas ratio with depth for Site NGHP-01-05, Holes C and D 560
15. Plot of free gas and PCS gas methane to ethane ratio with depth for Sites NGHP-01-10 and NGHP-01-12 562
16. Plot of free gas and PCS gas methane to ethane ratio with temperature at increasing depths for Sites NGHP-01-10 and NGHP-01-12 563

17. Catwalk temperature and humidity measurements as a function of time during drilling operations at Site NGHP-01-10 568
18. Infrared imaging and the derived downhole temperature profile for Hole NGHP-01-10B 572
19. Infrared imaging and the derived downhole temperature profile for Hole NGHP-01-10D 574
20. Infrared imaging and the derived downhole temperature profile for Hole NGHP-01-12A 575
21. Infrared track image collected from Core NGHP-01-10D-10X, with corresponding reference color temperature scale 576
22. Core-end infrared image of Core NGHP-01-10D-18X-6, with the corresponding reference temperature scale 577
23. Infrared image of extracted sediment collected from Section NGHP-01-10B-09X-5, with the corresponding temperature scale 577
24. Core-end temperature profiles for Holes NGHP-01-10B and NGHP-01-10D 578
25. Core-end temperature profiles for Hole NGHP-01-12A 579
26. Profiles of LWD Resistivity-At-Bit, core recovery, index, and strength properties for Hole NGHP-01-10B 580
27. Profiles of LWD resistivity-at-bit, infrared images, core recovery, electrical resistivity, acoustic *P*-wave velocity, magnetic susceptibility, and thermal conductivity for Hole NGHP-01-10B 581
28. Profiles of LWD resistivity-at-bit, core recovery, index, and strength properties for Hole NGHP-01-10D 582
29. Profiles of LWD resistivity-at-bit, infrared images, core recovery, electrical resistivity, acoustic *P*-wave velocity, magnetic susceptibility, and thermal conductivity for Hole NGHP-01-10D 583
30. Profiles of core recovery, index, and strength properties for Hole NGHP-01-12A 584
31. Profiles of LWD resistivity-at-bit, infrared images, core recovery, electrical resistivity, acoustic *P*-wave velocity, magnetic susceptibility, and thermal conductivity for Hole NGHP-01-12A 585
32. Peak and remolded vane shear strengths and sensitivity for Holes NGHP-01-10B, NGHP-01-10D, and NGHP-01-12A 592
33. PCS Core NGHP-01-10D-25P from 41–43 cm near the BSR contained wet, soft sediment with a Pocket Penetrometer strength <12 kPa 593
34. PCS Core NGHP-01-10D-25P from 83 cm had a Pocket Penetrometer strength of 24.5 kPa 593
35. Geothermal gradient and estimated depth to the BSR from *in situ* temperature measurements for Site NGHP-01-10 599
36. Temperature and pressure versus elapsed time for each pressure-corer deployment as recorded by the corer's internal data logger 601
37. Temperature versus pressure for successful pressure-corer deployments which contained DST loggers within the pistons, showing trajectories relative to gas-hydrate stability at 30 ppt and 45 ppt salinity 606
38. X-ray images, gamma density, and *P*-wave velocity collected at near *in situ* pressure and 7 °C for successful HYACINTH pressure cores 607
39. Summary of data taken from depressurized pressure cores before, during, and after depressurization, including gamma-density profiles collected before and after depressurization, X-ray images collected before and after depressurization, and line-scan images collected after depressurization 613

40. Pressure versus volume for depressurized pressure cores, also showing placement of intermediate X-ray or gamma density scans and gas samples 620
41. Pressure versus time for selected pressure cores....622
42. Flaky "cooked fish" texture seen in Core NGHP-01-10B-18Y....624
43. Methane phase diagram for Site NGHP-01-10, with total methane concentration measured from the nine depressurized pressure cores at Site NGHP-01-10....626
44. X-ray images of Cores NGHP-01-10B-08Y and NGHP-01-10B-18Y, with enlargements showing different gas-hydrate morphologies in fine-grained sediment....627
45. Gamma density versus P-wave velocity illustrating the relatively high velocities in the core from Site NGHP-01-10 compared with Site NGHP-01-12. 629
46. Monitoring and quality control LWD/MWD logs from Hole NGHP-01-10A....631
47. Summary of LWD log data from Hole NGHP-01-10A....632
48. Comparison of LWD resistivity curves from Hole NGHP-01-10A....634
49. LWD image data from Hole NGHP-01-10A....636
50. LWD resistivity image (GeoVISION deep button) from Hole NGHP-01-10A....637
51. Summary of the wire-line logs recorded in Hole NGHP-01-10D....643
52. Sonic waveform data, P-wave and S-wave velocities measured by the DSI wire-line log in Hole NGHP-01-10D....644
53. Summary of the wire-line logs recorded in Hole NGHP-01-13A....646
54. Comparison of LWD (Hole NGHP-01-10A) and wireline log data (Hole NGHP-01-10D)....647
55. Time-depth plot of first break times in the Hole NGHP-01-10D Vertical Seismic Profile 648
56. Water saturations from Archie's relationship and LWD porosity and resistivity logs in Hole NGHP- 01-10A 649
57. Water saturations from Archie's equation and wireline porosity and resistivity logs in Hole NGHP-01-13A 650

Tables

1. Smear-slide data for Hole NGHP-01-10B....544
2. Smear-slide data for Hole NGHP-01-10D....544
3. Smear-slide data for Hole NGHP-01-12A....546
4. Silt laminae and beds at Hole NGHP-01-10B 546
5. Silt laminae and beds at Hole NGHP-01-10D....546
6. Silt laminae and beds at Hole NGHP-01-12A....547
7. Interstitial-water data for Hole NGHP-01-10B 550
8. Interstitial-water data for Hole NGHP-01-10D 551
9. Interstitial-water data for Hole NGHP-01-12A 552
10. Headspace gas composition for Sites NGHP-01-10 and NGHP-01-12....555
11. Void (FG) gas composition for Sites NGHP-01-10 and NGHP-01-12....561
12. Pressure Core Sampler gas composition for Sites NGHP-01-10 and NGHP-01-12 561

13. List of microbiological samples taken for Hole NGHP-01-10B 564
14. List of microbiological samples taken for Hole NGHP-01-10D 565
15. List of infrared image files collected from Hole NGHP-01-10B 569
16. List of infrared image files collected from Hole NGHP-01-10C 569
17. List of infrared image files collected from Hole NGHP-01-10D 569
18. List of infrared image files collected from Hole NGHP-01-12A 570
19. List of infrared section-end image files from Hole NGHP-01-10B 570
20. List of infrared section-end image files from Hole NGHP-01-10D 571
21. List of infrared section-end image files from Hole NGHP-01-12A 571
22. Moisture and density (MAD) physical properties for Holes NGHP-01-10B, NGHP-01-10D and NGHP-01-12A 586
23. Vane shear strength results for Holes NGHP-01-10B, NGHP-01-10D, and NGHP-01-12A 589
24. Torvane strength results for Holes NGHP-01-10B, NGHP-01-10D, and NGHP-01-12A 590
25. Pocket Penetrometer strength results for Holes NGHP-01-10B, NGHP-01-10D, and NGHP-01-12A 591
26. Wenner array electrical resistivity results for Holes NGHP-01-10B, NGHP-01-10D, and NGHP-01-12A 595
27. Contact P-wave velocity results determined on split cores sections from Holes NGHP-01-10B, NGHP-01-10D, and NGHP-01-12A 598
28. Thermal conductivity results for Holes NGHP-01-10B, NGHP-01-10D, and NGHP-01-12A 598
29. *In situ* temperature estimates at Site NGHP-01-10 599
30. Summary of pressure-coring operations at Site NGHP-01-10 600
31. Methane-hydrate volume and concentration in pore space for successful pressure cores at Site NGHP-01-10 623

Sites NGHP-01-10, 12, and 13

By T. Collett, M. Riedel, J. Cochran, R. Boswell, J. Presley, P. Kumar, A. Sathe, A. Sethi, M. Lall, and the National Gas Hydrate Program Expedition 01 Scientists

Background and Objectives

Site NGHP-01-10 (near Prospectus Site KGGH03-A) is located at 15° 51.8609'N, 81° 50.0749' E in the Krishna-Godavari (KG) Basin (fig. 1). Water depth is around 1038 m. The objectives of the work carried out at this site follow the general objectives of NGHP Expedition 01:

- Study the occurrence of gas hydrate and establish the background geochemical, geological, geophysical and microbiological baselines for gas-hydrate proxy studies;
- Define the relationship between the sedimentology and structure of the sediments and the occurrence and concentration of gas hydrate;
- Calibrate remote sensing data such as seismic data by acquiring LWD/MWD and wire-line log data as well as VSP data for time-depth imaging.

Site NGHP-01-10 is located 50 m away from industry well GD-3-1, which had previously shown strong evidence for the occurrence of highly concentrated gas hydrate. Two high-resolution 2D seismic lines are available to describe the regional structural setting of the site (figs. 2 and 3). A nearby 2D seismic line (distance ~1.0 km to the SW) is also available, but contains much lower seismic frequencies and thus has lower resolution. The overall area is dominated by strong reflectivity about 0.25–0.30 s TWT below the seafloor. This high reflectivity likely results from free gas. The high-resolution 2D seismic lines GDSW-16 (fig. 2) and GDSW-46 (fig. 3) show a highly disrupted or faulted sedimentary sequence between the seafloor and the deeper gas occurrences. Individual reflectors can be traced for only a few hundred meters at most. A large-scale fault is identified on line GDSW-16 near shotpoint 600. Along the SW end of line GDSW-46 a possible shallow debris flow can be identified. This unit pinches out near Site NGHP-01-10 (GD-3-1). On line GDSW-16 this flow deposit (extruding from SP 260 to 370) is less clearly visible, but may correspond to a low-reflectivity unit in the immediate area surrounding of Site NGHP-01-10.

Along the line GDSW-46, a distinct seafloor high, about 350 m in length and ~30 m height is seen. This feature, located at the crest of the underlying free-gas anticline structure, may be associated with cold vent activity or mud-volcanism at the seafloor. Towards the NE, along this line, a potential BSR can be seen, which occurs at around 180 ms TWT below the seafloor. No such reflector is seen along the SW portion of the seismic line.

In order to delineate the gas-hydrate occurrence, two additional sites, Site NGHP-01-12 and Site NGHP-01-13, were occupied. Site NGHP-01-12 was chosen 500 m away from the industry well GD-3-1 towards the SE. Site NGHP-01-13, the third site, was located 150 m towards the NW away from Site NGHP-01-12 closer to Site GD-3-1. All of these sites are located within a seismically disrupted section best observed between SP 320 and 490 on line GDSW-16.

Operations

Site NGHP-01-10

This operations summary covers the Leg 2 transit from Site NGHP-01-09 (MNGH01-2) to Site NGHP-01-10 (GD-3-1), a tug boat rendezvous that took place during that transit, and LWD/MWD drilling in Hole NGHP-01-10A. It also covers the Leg 3A transit from Site NGHP-01-05 (KGGH02-A) to Site NGHP-01-10, and drilling/coring operations for Holes NGHP-01-10B through NGHP-01-10D (fig. 4). Schedule details and statistics for this site can be found as Appendixes:

- Appendix 1: NGHP Expedition 01 Operations Schedules
- Appendix 2: NGHP Expedition 01 Operations Statistics

Included in the "Methods" chapter and the glossary is a list of standard or commonly used operations terms and acronyms.

Hole NGHP-01-10A

The first hole of Site NGHP-01-10 (GD-3-1) was drilled on Leg 2 of NGHP Expedition 01 as the 10th hole in a 12-hole LWD/MWD transect. The 279 NMI transit from Site NGHP-01-09 (MNGH01-2) was accomplished in two segments. The first segment of 46.6 NMI to the supply boat rendezvous point was completed in 5.75 hr at an average speed of 8.1 kt. The *JOIDES Resolution* arrived at the rendezvous location while on an intercept course of 240° true at the approximate coordinates of 18° 25.1' N Latitude by 84° 59.4' E Longitude. After lowering thrusters the vessel was switched from cruise

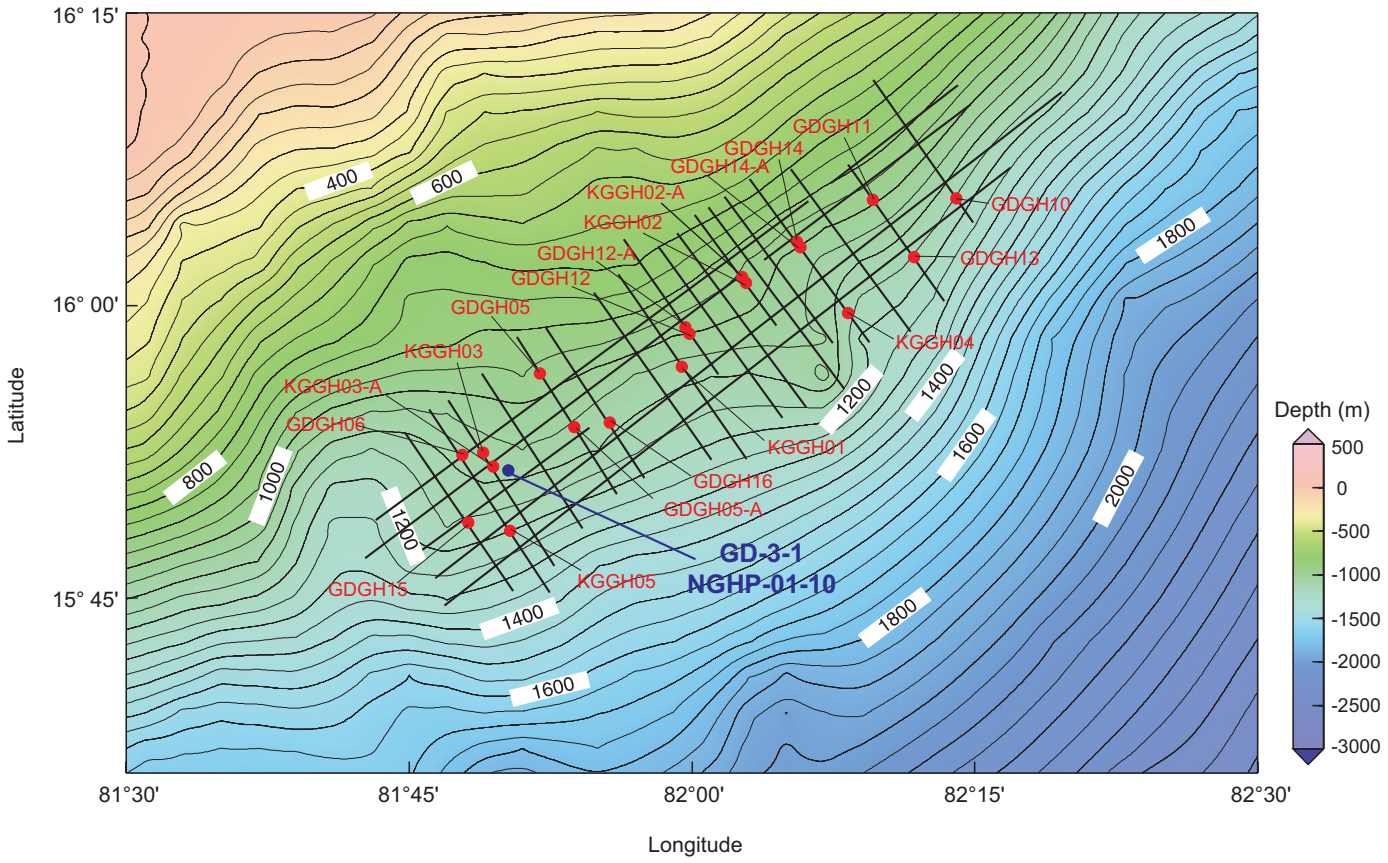


Figure 1. Location of Sites NGHP-01-10, NGHP-01-12 and NGHP-01-13 (GD-3-1) in the Krishna-Godavari (KG) Basin.

mode to DP control and at 1330 hr on June 1, 2006, the tug boat "Zeenne" was alongside. A replacement Schlumberger ProVISION (NMR) tool needed for the LWD/MWD program was loaded aboard and three members of the science party, who needed to return to India for various reasons, were transferred. The tug departed at 1410 hr with an ETA in the port city of Kakinada the following evening. Thrusters were raised and secured as the *JOIDES Resolution* got underway at 1418 hr for Site NGHP-01-10. The new NMR tool was successfully function tested during the remaining transit and the vessel arrived on location at 1830 hr on June 2, 2006. The 232.4 NMI transit was made at an average speed of 8.1 kt after battling headwinds and a strong current most of the way.

Prior to deploying the LWD/MWD tools, the radioactive source was loaded, and the stabilizers were changed out on the NMR tool. The remaining BHA was made up and the drill string was lowered to a depth of 143.0 mbrf. A second function test was performed at that depth before continuing the pipe trip to the seafloor. Since these position coordinates were for an ONGC well site, the vessel was offset 50 m to the NW. To further address concerns about possible seafloor obstructions (old abandoned well heads), the VIT/subsea TV camera was deployed, and a brief survey of the sea bottom beneath the pipe was conducted. No obstructions were identified, the vessel was offset an additional 2 meters N, and the drill string was spaced out for spudding. A seafloor tag indicated a mudline depth of 1,049.3 mbrf. Hole NGHP-01-10A was spudded at 0428 hr on June 3, 2006. LWD/MWD drilling continued for 11.5 hr at a controlled rate of 17.9 m/h (average net ROP including connection time) to a total depth of 205.5 mbsf (1,254.5 mbrf). The hole was displaced with 60 barrels of weighted 10.5 ppg Sepiolite mud and the drill string was pulled clear of the seafloor at 1740 hr. After recovering the drill string, the BHA was racked back in the derrick, data was downloaded from the NMR and this tool was laid out, the remaining LWD/MWD tools were rigged down, the source was removed, remaining data was downloaded, and the batteries were changed out on the GeoVISION tool. The vessel was switched from DP to cruise control and got underway for Site NGHP-01-11 (GDGH12-A) at 2135 hr on June 3, 2006.

Hole NGHP-01-10B

Site NGHP-01-10 was reoccupied during Leg 3A after completing drilling/coring operations at Site NGHP-01-05. The 15.5 NMI transit from Site NGHP-01-05 was completed in 2.5 hr at an average speed of 6.2 knots. The vessel was switched from cruise mode to DP control at 2230 hr on June 15, 2006, and a positioning beacon was deployed at the Hole NGHP-01-10A location coordinates. The ice bath was

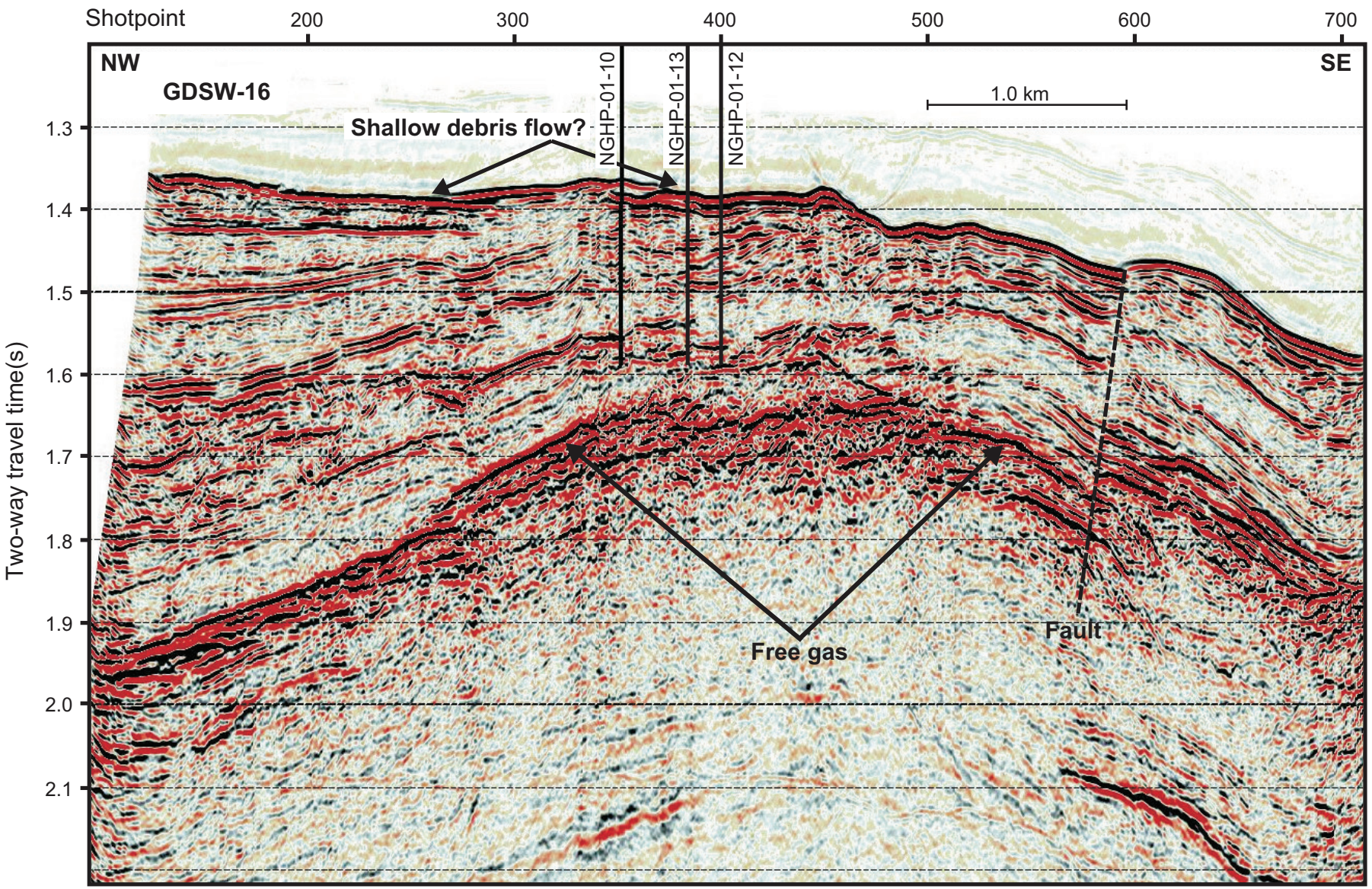


Figure 2. Seismic line GDSW-16 (orientation is NW-SE) crossing drill Sites NGHP-01-10, NGHP-01-12, and NGHP-01-13. Note the occurrence of deep-seated free gas brightening seismic reflectivity as well as a potential shallow debris flow at Site NGHP-01-10.

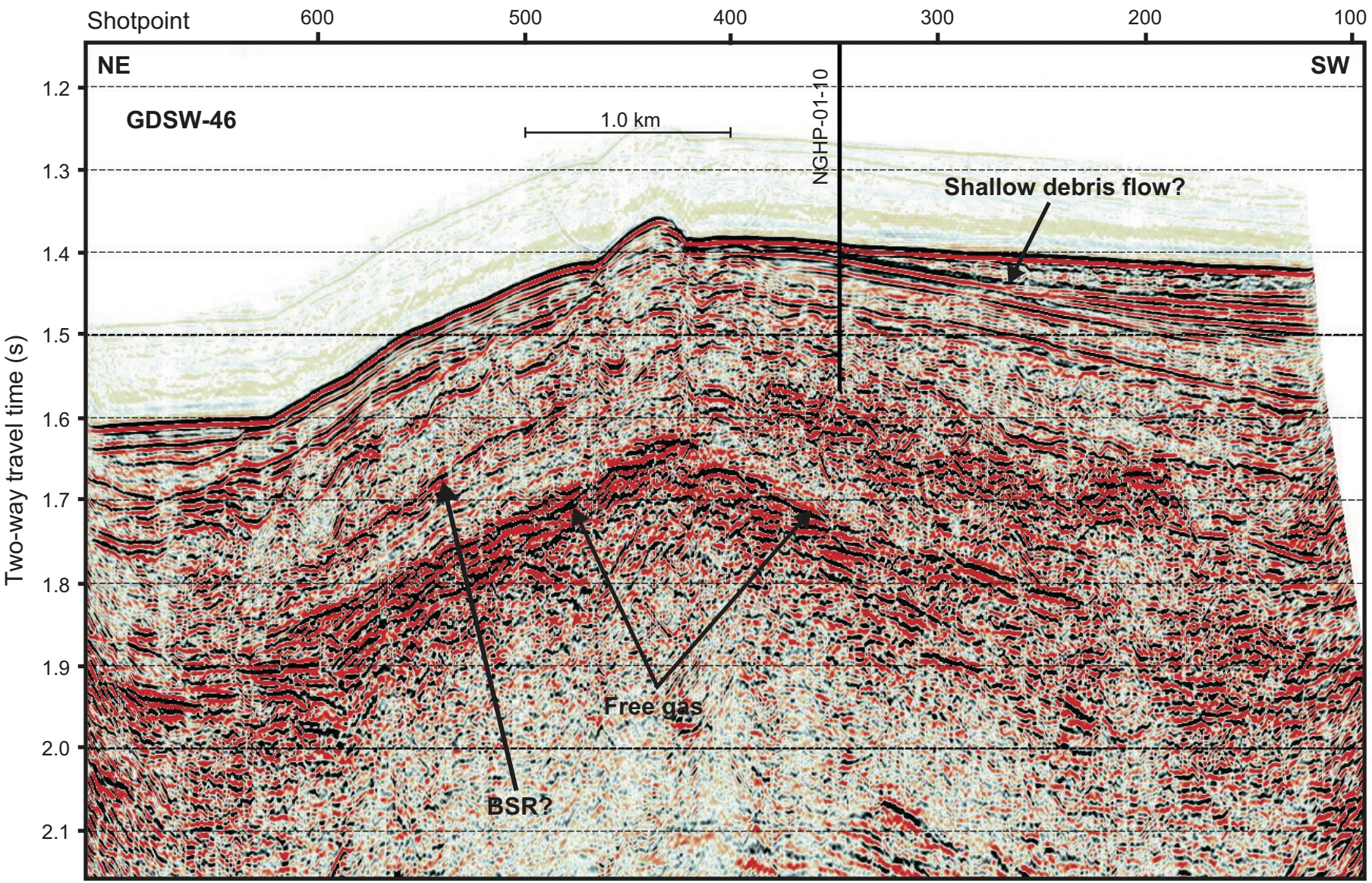


Figure 3. Seismic line GDSW-46 (orientation is NE-SW) crossing drill Site NGHP-01-10. Note the occurrence of deep-seated free gas brightening seismic reflectivity as well as a potential shallow debris flow pinching out near Site NGHP-01-10. A BSR can possibly be identified about 1.5 km towards the NE of the drill site. [BSR, bottom-simulating reflector]

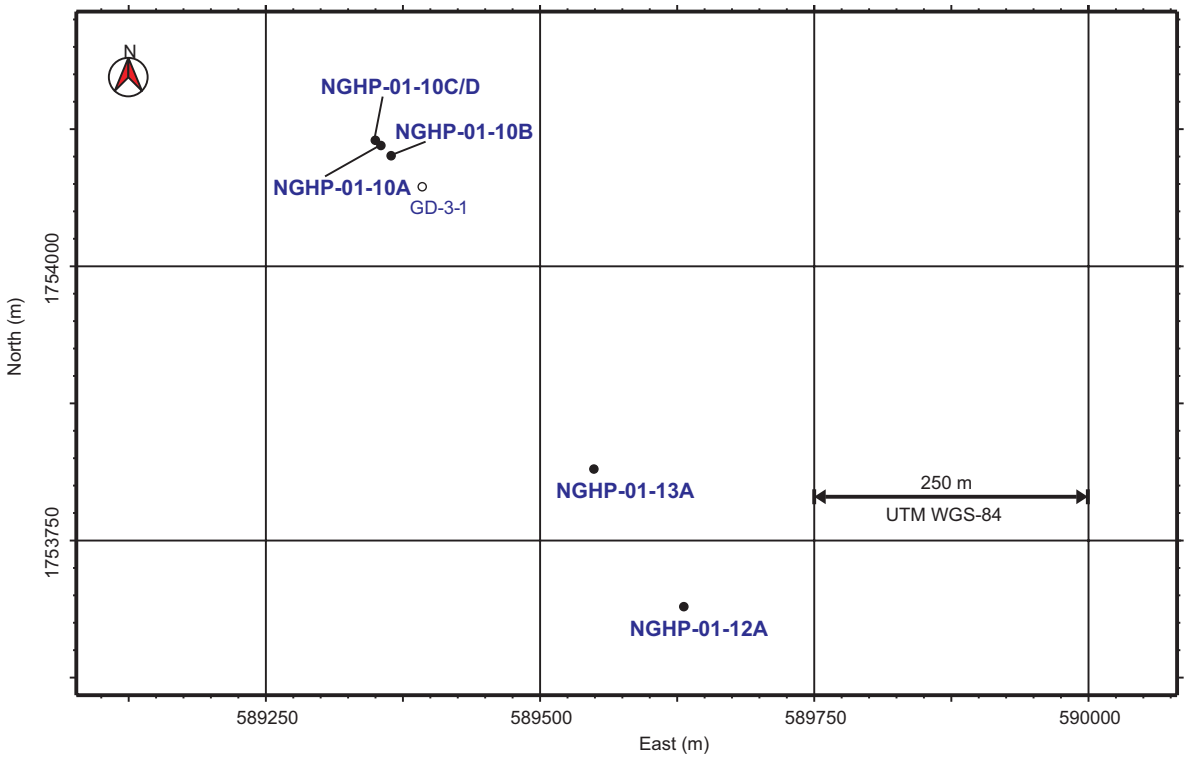


Figure 4. Map showing all holes occupied at Sites NGHP-01-10, 12, and 13 (GD-3-1).

installed in the moon pool and a standard 2-stand APC/XCB BHA was made up with a LFV and a typical 11-7/16" APC/XCB C-3 TCI roller cone bit.

Hole NGHP-01-10B was to focus on continuous APC/XCB coring complemented with additional pressure cores targeted for areas of high gas-hydrate concentration. Since gas hydrate was anticipated close to the seafloor, only two APC cores were scheduled (mudline through the SMI) and all temperature measurements were to be taken using only the DVTP system.

The vessel was offset 10 m to the SE of Hole NGHP-01-10A while the drill string was tripped to bottom. The bit was positioned at a depth of 1,043.0 mbrf and Hole NGHP-01-10B was spudded at 0215 hr on June 16, 2006, establishing a seafloor depth of 1,049.4 mbrf. The PDR depth for this site, corrected to the rig floor DES, was 1,055.4 mbrf. APC Core NGHP-01-10B-01H was on-deck at 0245 hr and APC coring continued through Core NGHP-01-10B-02H to a depth of 12.6 mbsf.

Two XCB cores (NGHP-01-10B-3X and NGHP-01-10B-4X) set up the first PCS Core NGHP-01-10B-05P recovered from 32.4 mbsf. The first DVTP temperature measurement was successfully taken at that depth. This was followed by XCB Cores NGHP-01-10B-06X through NGHP-01-10B-07X to 50.2 mbsf and the first FPC Core NGHP-01-10B-08Y, which was recovered from 51.2 mbsf. XCB Cores NGHP-01-10B-09X through NGHP-01-10B-10X to 70.0 mbsf set up the first HRC Core NGHP-01-10B-11E, which was recovered from 70.0 mbsf. XCB Cores NGHP-01-10B-12X through NGHP-01-10B-14X to 98.2 mbsf set up the second PCS Core NGHP-01-10B-15P, recovered from 99.2 mbsf. A second DVTP temperature measurement was successfully taken at that depth. XCB Cores NGHP-01-10B-16X through NGHP-01-10B-17X to 117.4 mbsf preceded the second FPC Core NGHP-01-10B-18Y, which was recovered from 118.4 mbsf. XCB Cores NGHP-01-10B-19X through NGHP-01-10B-20X to 136.6 mbsf were then cut, followed by the third FPC Core NGHP-01-10B-21Y, which was recovered from 136.6 mbsf. Five additional XCB cores (NGHP-01-10B-22X through NGHP-01-10B-26X) were cored to a depth of 174.1 mbsf before cutting the second HRC pressure Core NGHP-01-10B-27E to 175.1 mbsf. The final pressure core for this hole was PCS Core NGHP-01-10B-28P to 176.1 mbsf. A third and final DVTP temperature measurement was taken at the total depth of the hole at 204.9 mbsf.

The hole was displaced with 79 barrels of 10.5 ppg weighted mud and the drill string was POOH with the top drive. Hole NGHP-01-10B officially ended when the bit cleared the seafloor at 1145 hr on June 18, 2006.

In total, there were 21 XCB cores recovered from Hole NGHP-01-10B. Core-on-deck cycle times varied from 1.0 to 2.5 hours which included 20-minute wait periods on-bottom and again at the mudline during retrieval for Cores NGHP-01-10B-9X through NGHP-01-10B-23X. Core NGHP-01-10B-7X waited 20 minutes at the mudline only and Core NGHP-01-10B-22X waited 20 minutes on-bottom only. Penetration rates, with the exception of Core NGHP-01-10B-3X (37.6 m/h), ranged from 3.0 to 19.2 m/h and overall core recovery with the XCB system was 20.1 percent.

All PCS deployments included successful recovery of data with the PCSM "methane tool". Hole preparation prior to each pressure coring attempt included a Sepiolite mud sweep to provide as clean a hole on-bottom as possible.

Whirlpaks (microbeads) used to assess microbiological contamination were used for all APC/XCB cores with the exception of Cores NGHP-01-10B-23X, NGHP-01-10B-30X, and NGHP-01-10B-31X. Accelerated core barrel handling protocols were also used for all core barrels deployed in this hole. All APC/XCB core barrels were laid down immediately upon arrival at the rig floor before making another drill pipe connection or deploying the next core barrel.

For all pressure coring systems (PCS, FPC and HRC), a 20-min wait period was also employed at the mudline on the way in the hole and again during retrieval. This was to cool the core barrels down, thus aiding in keeping any entrained gas hydrate within the stability field. At the rig floor all pressure core barrels (PCS, FPC, and HRC) showing signs of proper actuation were placed in the moon pool ice bath prior to processing.

Hole NGHP-01-10C

Hole NGHP-01-10C was intended to be a duplicate of Hole NGHP-01-10B with continuous APC/XCB coring as well as use of specialty pressure-coring systems targeted to sample massive gas-hydrate accumulations. Limited APC coring was conducted through the SMI. Wire-line logging was also planned for this hole.

The vessel was offset 10 meters to the NW of Hole NGHP-01-10A and the bit was positioned at a depth of 1,045.0 mbrf. Hole NGHP-01-10C was spudded at 1305 hr on June 18, 2006; however, the core barrel was recovered full and an accurate mudline could not be established. Subsequent to the spud attempt it was determined that the driller had made a drill string space out error (one-stand too many) resulting in the bit being positioned significantly lower than planned. Because gas hydrate was recovered and sampled from this core it was important to identify at least the approximate depth that this core was recovered from. Using the ultimate seafloor depth from Hole NGHP-01-10D it was determined that the cored interval extended from 23.1 to 32.6 mbsf. Hole NGHP-01-10C ended with the recovery of Core NGHP-01-10C-01H on-deck at 1315 hr June 18, 2006.

Hole NGHP-01-10D

The bit was again positioned at a depth of 1,045.0 mbrf and Hole NGHP-01-10D was spudded at 1410 hr on June 18, 2006, establishing a seafloor depth of 1050.4 mbrf. The preceding hole demonstrated that the formation could be APC cored to a depth of ~36 m. Therefore APC coring continued through Core NGHP-01-10D-04H to a depth of 32.6 mbsf.

A short XCB Core NGHP-01-10D-05X, cut to a depth of 40.1 m, set up the first PCS Core NGHP-01-10D-06P taken from 41.1 mbsf. Two more XCB cores (NGHP-01-10D-07X and NGHP-01-10D-08X) to 58.8 mbsf set up the first FPC Core NGHP-01-10D-09Y, which was recovered from 59.8 mbsf. The first DVTP temperature measurement for this hole was successfully taken at that depth. XCB Cores NGHP-01-10D-10X and NGHP-01-10D-11X to 77.8 mbsf set up the first HRC Core NGHP-01-10D-12E, which was recovered from 78.8 mbsf. XCB Cores NGHP-01-10D-13X through NGHP-01-10D-14X to 97.0 mbsf set up the second PCS Core NGHP-01-10D-15P, which was recovered from 98.0 mbsf. XCB Cores NGHP-01-10D-16X through NGHP-01-10D-18X to 125.8 mbsf set up the second FPC Core NGHP-01-10D-19Y, which was recovered from 126.8 mbsf. The second DVTP temperature measurement was successfully taken at that depth. XCB Cores NGHP-01-10D-20X through NGHP-01-10D-21X to 145.1 mbsf preceded the second HRC Core NGHP-01-10D-22E, which was recovered from 145.1 mbsf. XCB Cores NGHP-01-10D-23X through NGHP-01-10D-24X to 164.4 mbsf were then cut, followed by the third PCS Core NGHP-01-10D-25P, which was recovered from 165.4 mbsf. Four additional XCB cores (NGHP-01-10D-26X through NGHP-01-10D-29X) were cored to a total depth for the hole of 203.8 mbsf. Coring was ended at 0800 hr on June 20, 2006, and preparations were made for conducting a wiper trip prior to taking the third and final DVTP temperature measurement at TD.

In total, 18 XCB cores were recovered from this hole. Core-on-deck cycle times varied from 1.25 to 2.0 hours including 20-minute wait periods on-bottom and again at the mudline during retrieval. Penetration rates ranged from 7.3 m/h to 15.1 m/h and overall core recovery with the XCB system was more than double that of Hole NGHP-01-07B at 54.0 percent. The improved recovery achieved in Hole NGHP-01-07D, relative to that of Hole NGHP-01-07B, was attributed to a change from the spring loaded, finger style core catcher combination to one using the four-petal "full closure" flapper style core catcher.

All PCS deployments included successful recovery of data with the PCS Methane tool (PCSM). Hole preparation prior to each pressure coring attempt included a Sepiolite mud sweep to provide as clean a hole on-bottom as possible.

Whirlpaks (microbeads) used to assess microbiological contamination were not used for any coring system deployed in this hole. Accelerated core barrel handling protocols were used for all core barrels deployed in this hole. All APC/XCB core barrels were laid down immediately upon arrival at the rig floor, before making another drill pipe connection or deploying the next core barrel.

For all pressure coring systems (PCS, FPC, and HRC), a 20-minute wait period was also employed at the mudline on the way in the hole and again during retrieval. This was to cool the core barrels down thus aiding in keeping any entrained gas hydrate within the stability field. At the rig floor all pressure-core barrels (PCS, FPC, and HRC) showing signs of proper actuation were placed in the moon pool ice bath prior to processing.

The drill string was tripped to 57.3 mbsf and back to TD. Sepiolite mud sweeps of fifty barrels each were circulated before and after the wiper trip to aid in preparing the hole for wire-line logging. Hole preparation was completed at 1200 hr and a third and final DVTP temperature measurement was taken. A go-devil was pumped to bottom to open the LFV, the hole was displaced with 81 barrels of 10.5 ppg weighted mud, and the pipe was pulled back and spaced out with the EOP placed at 73.3 mbsf.

Rig-up for wire-line logging began at 1500 hr on June 20, 2006. The first logging run was made with the Triple Combo tool suite. Tools went in at 1650 hr and reached only 152.6 mbsf. This limited amount of hole was logged and the tools were out at 2035 hr. After tying back the Schlumberger logging sheaves, the top drive was picked up and ~6 hours were spent reaming the hole and circulating multiple Sepiolite mud sweeps. The drill pipe was spaced out with the EOP placed at 63.9 mbsf and the Schlumberger logging sheaves were re-positioned. The next logging run, made up of the FMS-Sonic (DSI) tool, was deployed downhole at 0530 hr on June 21, 2006. Run No. 2 was successfully deployed to a depth of 160.0 mbsf and the tools were back out by 1005 hr. The third logging run was dedicated to zero offset VSP measurements. The IODP mammal watch (day light operations only) protocols were followed. VSP tools were deployed at 1130 hr and reached a depth of 144.6 mbsf. Shot points for the VSP were spaced 5 meters apart and the third suite of tools was recovered by 1645 hr. Logging operations were completed at 1800 hr after rigging down the logging sheaves. The drill string was pulled clear of the seafloor at 1835 hr ending operations for Hole NGHP-01-10D and Site NGHP-01-10.

Site NGHP-01-12

This operations summary covers a DP move from Site NGHP-01-10 to Site NGHP-01-12 and drilling/coring operations for Hole NGHP-01-12A (fig. 4). Schedule details and statistics for this site can be found in the "Appendix" as:

- NGHP Expedition 01 Operations Schedules
- NGHP Expedition 01 Operations Statistics

Included in the "Methods" chapter and the glossary is a list of standard or commonly used operations terms and acronyms.

Hole NGHP-01-12A

Site NGHP-01-12 was added to the drilling schedule as a delineation hole associated with Site NGHP-01-10.

The ~500 m move to the SE of Site NGHP-01-10 (GD-3-1) was made in DP mode with the drill string suspended below the ship, knobby joints installed through the guide horn, and the EOP located approximately three-stands off bottom. Prior to initiating the move, the Site NGHP-01-10 positioning beacon was recovered. The drill crew took advantage of this time to also slip and cut the drilling line. Once on location, the knobby joints were laid out, the positioning beacon was deployed, and the ice bath was re-installed in the moon pool.

Hole NGHP-01-12A was initially planned to consist of limited APC coring through the SMI, followed by a series of three pressure-coring packages targeting gas hydrate. Each pressure-coring package was to be set up with an XCB core and all three-pressure coring systems (PCS, FPC, and HRC) were to be deployed within each zone of interest. There were no temperature measurements scheduled; however, wire-line logging was planned.

The drill string was spaced out placing the bit at a depth of 1,039.0 mbrf. The first spud attempt received no sediment. The pipe was re-positioned 3.0 m lower at a depth of 1,042.0 mbrf and Hole NGHP-01-12A was spudded at 2255 hr on June 21, 2006, establishing a seafloor depth of 1,045.8 mbrf. The PDR depth for this site, corrected to the rig floor DES, was 1,049.4 mbrf.

APC Core NGHP-01-12A-01H was on-deck at 2305 hr and APC coring continued through Core NGHP-01-12A-03H to a depth of 24.7 mbsf. The first pressure-core target zone was 40.0 mbsf to 65.0 mbsf. Therefore an XCB center bit was used to wash/drill an additional 15.3 m to the target depth of 40.0 mbsf. This was followed with a single 5.7 m XCB Core NGHP-01-12A-04X to 45.7 mbsf setting up the first series of pressure cores. FPC Core NGHP-01-12A-05Y advanced from 45.7 mbsf to 46.7 mbsf followed by an HRC Core NGHP-01-12A-06E from 46.7 mbsf to 47.7 mbsf. The series ended with a PCS Core NGHP-01-12A-07P from 47.7 mbsf to 48.7 mbsf.

The second package began after washing/drilling an additional 35.1 m to a depth of 83.8 mbsf. This was followed with a single 9.5 m XCB Core NGHP-01-12A-08X to 93.3 mbsf setting up the second series of pressure cores targeted for an interval from 85.0 mbsf to 110.0 mbsf. FPC Core NGHP-01-12A-09Y advanced from 93.3 mbsf to 94.3 mbsf followed by an HRC Core NGHP-01-12A-10E from 94.3 mbsf to 95.3 mbsf. A PCS Core NGHP-01-12A-11P was then cut from 95.3 mbsf to 96.3 mbsf followed by another XCB Core NGHP-01-12A-12X to 102.9 mbsf.

The third pressure-coring package targeted the zone from 140.0 mbsf to 165.0 mbsf. An XCB center bit was used to wash/drill to a depth of 141.3 mbsf. A single 9.6 m XCB Core NGHP-01-12A-13X was then cut to 150.9 mbsf, setting up the third series of pressure cores. However, this series of pressure cores was not completed when hole problems and periodic episodes of stuck pipe ultimately forced the abandonment of all remaining pressure coring as well as wire-line logging. The drill string was repeatedly free and then stuck again over the next several hours with the typically associated loss of rotation, 400 to 600 amps of torque, and 40K to 50K pounds of overpull required. At 2230 hr on June 22, 2006, the sinker bars were pulled out and further coring attempts were suspended. The pipe was continually worked and after POOH to 110.1 mbsf the pipe eventually became free. The pipe trip continued with the top drive until clearing the seafloor at 0035 hr on June 23, 2006. This ended operations in Hole NGHP-01-12A and at Site NGHP-01-12.

As on previous sites, all HYACINTH pressure-coring systems (FPC and HRC) employed a 15–20 minute wait period at the mudline on the way in the hole and again during retrieval to cool the core barrels and aid in keeping any entrained gas hydrate within the stability field. At the rig floor all pressure-core barrels (PCS, FPC, and HRC) showing signs of proper actuation were placed in the moon pool ice bath prior to processing.

Both PCS deployments included successful recovery of data with the PCS Methane tool. Only four XCB cores were recovered from this hole; however, 20.60 m of XCB core was obtained, which was 66 percent of the interval penetrated. Rates of penetration with the XCB varied between 8.8 and 34.2 m/h. Whirlpaks (microbeads) used to assess microbiological contamination were not used in this hole. Accelerated core barrel handling protocols were used for all core barrels (APC, XCB, and PCS) deployed.

Site NGHP-01-13

This operations summary covers a DP move from Site NGHP-01-12 to Site NGHP-01-13 and drilling/coring operations for Hole NGHP-01-13A (fig. 4). Schedule details and statistics for this site can be found in the "Appendix" as:

- NGHP Expedition 01 Operations Schedules
- NGHP Expedition 01 Operations Statistics

Included in the "Methods" chapter and the glossary is a list of standard or commonly used operations terms and acronyms.

Hole NGHP-01-13A

Site NGHP-01-13 was added to the drilling schedule to provide a dedicated wire-line logging hole in support of both Sites NGHP-01-10 and NGHP-01-12. The original intent was to log the delineation Hole NGHP-01-12A; however, hole trouble and resultant stuck pipe issues precluded logging (see "Operations" for Hole NGHP-01-12A). The new Site NGHP-01-13 was selected based on borehole stability concerns. At Sites NGHP-01-10 and NGHP-01-12, it was felt that hole stability was directly related to gas-hydrate concentration in the formation. All holes drilled at Site NGHP-01-10 experienced severe hole instability once below or near the BSR. By moving back toward Site NGHP-01-10 and drilling an "intermediate" hole it was felt that gas-hydrate concentrations would likely be higher and therefore the potential of maintaining hole stability for wire-line logging would be greater.

The ~150 m move to the NW of Site NGHP-01-12 required only 30 minutes in DP mode with the drill string suspended below the ship.

Hole NGHP-01-13A was spudded at 0130 hr on June 23, 2006, establishing a seafloor depth of 1,044.0 mbrf. The hole was drilled using an XCB center bit to a depth 200.0 mbsf in 9.25 hr (net ROP including connections of ~21.6 m/h). A 50-barrel Sepiolite mud sweep was circulated at TD to thoroughly flush any remaining cuttings from the hole. The XCB center bit was recovered, and the hole was displaced to 78 bbls of 10.5 ppg Sepiolite mud for logging. The drill string was pulled out of the hole with the top drive and the EOP was placed at 60.7 mbsf by 1830 hr on June 23, 2006.

Rig-up of the Schlumberger logging sheaves began at 1330 hr on June, 23, 2006. The first logging run with the Triple Combo was deployed downhole at 1525 hr and was back on-deck by 1740 hr. The tools would not pass through the bit. A subsequent inspection of the logging go-devil attached to the bottom of the tool string showed deep axial striations consistent with the inability of the LFV actuation balls to retract as designed. The open flushing design of the LFV makes it extremely rare, if ever, that the tool becomes so packed with sediment or drill cuttings that proper actuation is prevented. The logging sheaves were tied back and the top drive was picked up. A center bit was deployed and an attempt was made to thoroughly flush any material that may have been impeding proper actuation of the LFV. The top drive was again set back and logging preparations resumed at 2030 hr. The Triple Combo was deployed at 2055 hr and this time no problems were encountered passing out of the bit. The tools reached a depth 149.0 mbsf or 51.0 m off bottom before encountering an impassable bridge. Logging commenced at that point and the tools were back on-deck by 2330 hr on June 23. Further wire-line logging was cancelled due to time constraints and the need to depart for Chennai. The logging sheaves were secured by 0130 hr, and the drill string was pulled clear of the seafloor at 0155 hr on June 24, 2006. The drill string was tripped back to the ship and all drill collar connections were visually inspected. The bit cleared the DES at 0530 hr. The positioning beacon was recovered by 0232 hr and all thrusters/hydrophones were raised. The vessel was switched to cruise mode and got underway for Chennai, India at 0536 hr on June 24th. This ended operations in Hole NGHP-01-13A and at Site NGHP-01-13.

Lithostratigraphy

Sites NGHP-01-10, -12, and -13 are located in the Krishna-Godavari (KG) Basin, along the eastern continental margin of India. At Sites NGHP-01-10, -12, and -13, a total of six holes (NGHP-01-10A, NGHP-01-10B, NGHP-01-10C, NGHP-01-10D, NGHP-01-12A and NGHP-01-13A) were drilled. Four wells were cored: Hole NGHP-01-10B to 204.9 mbsf, Hole NGHP-01-10C to 9.5 mbsf, Hole NGHP-01-10D to 203.8 mbsf, and Hole NGHP-01-12A to 150.9 mbsf. Hole NGHP-01-10A was drilled for LWD (logging-while-drilling) and Hole NGHP-01-13A was drilled for wire-line logging. Site NGHP-01-12 is close to Site NGHP-01-10 (~50 m) and therefore they are considered together in this section.

We classify the sedimentary sequence recovered at Sites NGHP-01-10B and NGHP-01-10D as well as NGHP-01-12A as a single lithostratigraphic unit (Lithostratigraphic Unit I) based on sedimentological criteria (for example variations in sedimentary structure and grain size or biogenic and lithologic

components) and additional parameters (for example, magnetic susceptibility, gamma ray, and density; figs. 5, 6, 7, and Sites 10, 12, and 13 Visual Core Descriptions in the supplemental data files). The lithostratigraphy at these sites is similar to the lithostratigraphy previously drilled at Sites NGHP-01-03 and NGHP-01-05 on the Krishna-Godavari slope. Finally, Site NGHP-01-03, which lies between Sites NGHP-01-10 and NGHP-01-05, also recovered similar stratigraphy, but deeper in the section. Therefore, in addition to describing the basic characteristics of Sites NGHP-01-10 and NGHP-01-12, we will also emphasize the significant differences and similarities of these sites from Sites NGHP-01-03 and NGHP-01-05.

Similar to other KG Basin sites, we observed cyclicity in the RGB color scans of the cores and a lack of *Discoaster* spp. in the record here. Both of these suggest that the age of the stratigraphy is Quaternary. Additional post cruise biostratigraphy, however, may help further constrain the history of deposition throughout the entire KG Basin.

Lithostratigraphic Units

Lithostratigraphic Unit I

Intervals: Hole NGHP-01-10B,
Sections NGHP-01-10B-01H-1 to TD;
Hole NGHP-01-10D-01H-1 to TD, and
Hole NGHP-01-12A-01H-1 to TD.

Depth: Hole NGHP-01-10B, 0–204.9 mbsf;
Hole NGHP-01-10D, 0–203.8 mbsf;
Hole NGHP-01-12A, 0–150.9 mbsf

Age: Quaternary

Core recovery was poor in Hole NGHP-01-10B throughout the cored interval (fig. 5). Core recovery was good at Hole NGHP-01-10D for the upper 47 mbsf and moderate in the 87–157 mbsf, 147–190 mbsf, and 175–190 mbsf intervals; outside these intervals in Hole NGHP-01-10D and throughout Hole NGHP-01-10B, cores recovered from apparent gas-hydrate-bearing sediments resulted in significantly less recovery (fig. 5; see "Downhole Logging" for LWD resistivity logs). Hole NGHP-01-12A was spot cored for high resolution geochemical sampling (fig. 7). Designation of Lithostratigraphic Unit I in all Holes was based on sediment characteristics and physical property data. Lithostratigraphic Unit I is composed of nannofossil-bearing-to-rich clay that ranges in color from very dark gray of various hues (yellowish – 2.5Y 3/1 to 2.5Y 3/2; neutral—N 3/1; or brown—10YR 3/1 to 10YR 3/2) to black (N 2.5/1). Minor lithological exceptions were encountered at Site NGHP-01-12A where the interval cored between 15 and 25 mbsf (that is, Core NGHP-01-12A-03) consisted of a foraminifera-bearing clay as well as in sediments near the top of the Hole (that is, Core NGHP-01-12A-01) that were very dark grayish brown to brown (2.5Y 3/1 to 2.5Y 4/1) in color. The darker clays in all holes consistently contain terrigenous organic matter that is visible in smear slides (tables 1, 2, and 3) and often contain a smaller percentage of nannofossils than the lighter colored clay zones. Thin (0.2–3.0 cm) silt laminae and beds are significantly less abundant at Sites NGHP-01-10 and NGHP-01-12 than at Site NGHP-01-05; however, limited recovery, sampling on the catwalk, and spot coring may have biased these results (figs. 5, 6, and 7; tables 4, 5, and 6). Similar to Site NGHP-01-05, the apparent lack of *Discoaster* spp., as well as the apparent meter- and decimeter-scale cyclicity in the RGB values of the DIS core images (suggesting either precession (21 ky) or obliquity (40 ky) cycles), implies a Quaternary to recent age for the stratigraphy.

Mollusk shells (primarily bivalves) and visible foraminifera tests occur sporadically throughout the sediment (figs. 5, 6, and 7). Possible fossil chemosynthetic communities (fig. 8) composed of a variety of mollusk shells with some encrusted by carbonatic worm tubes (*Serpula* sp.) were recovered at both Sites NGHP-01-10 and NGHP-01-12 (fig. 8). Concentrations of authigenic carbonate nodules (varying in size from a few mm's to over 5 cm) are also observed near these fossil assemblages (fig. 9). In addition to these concentrated zones, authigenic carbonates are observed in all holes (NGHP-01-10B, NGHP-01-10D, and NGHP-01-12A) below 15–20 mbsf to TD and occur as both small (1–3 cm) and large (7–8 cm) nodules (fig. 9) and thin (2–3 cm) fine-grained horizontal bands (for example Core NGHP-01-10D-14H; figs. 5 and 6). Bioturbated zones occur throughout the unit, but are usually best observed when highlighted by iron sulfide precipitates (figs. 5, 6, and 7; Sites 10, 12, and 13 Visual Core Descriptions in the supplemental data files). Down-core magnetic susceptibility measurements (figs. 5, 6, and 7) at all three holes show a consistent increase in susceptibility from 50 mbsf to 150 mbsf. Magnetic iron sulfides (likely gregite and(or) pyrrhotite) have been observed in gas-hydrate-bearing sediments offshore western North America (Musgrave and others, 2006) and may be responsible for some of the magnetic susceptibility highs observed here. Magnetic susceptibility is also high in stratigraphic packages containing abundant sand and silt beds, which often contain magnetite grains (opaque minerals in smear slide; for example, Trehu, and others, 2003). At Sites NGHP-01-10 and NGHP-01-12, some of the susceptibility highs in the upper 50 mbsf are associated with zones rich in silt laminae; however, the zones with the highest magnetic susceptibility appear to coincide with the abundance of iron sulfides, observed bioturbation, and authigenic carbonate (figs. 5, 6, and 7). This observation suggests the magnetic susceptibility may be responding mainly to magnetic minerals precipitated during diagenetic processes. The good correlation of magnetic susceptibility between Holes NGHP-01-10B, NGHP-01-10D, and NGHP-01-12A suggests diagenetic processes are similar at all three holes.

The major lithologies of Lithostratigraphic Unit I determined from smear slides are primarily clay sized (80–100 percent) grains with minor amounts of silt sized grains (up to 20 percent) and generally no sand (tables 1, 2, and 3). Minor lithologies described in smear slide include silt beds and the authigenic carbonate rich zones. The major nonbiogenic components of Lithostratigraphic Unit I are feldspar, quartz,

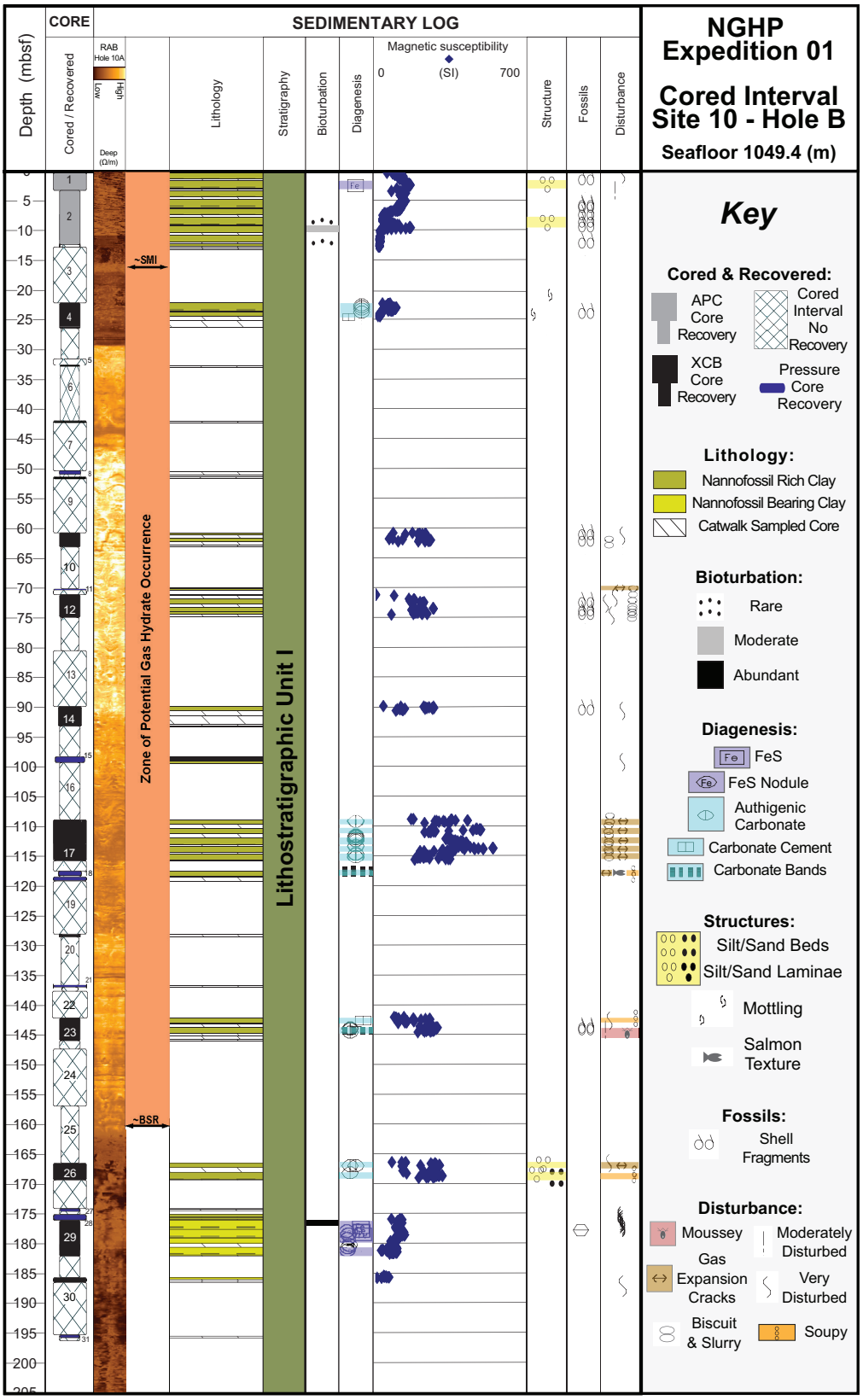


Figure 5. Lithostratigraphic summary of Hole NGHP-01-10B. Note: Colored intervals exceed symbol size when there is a range in the occurrence. Center point of each symbol represents true depth of occurrence, therefore colored bars may slightly exceed core recovery; see Sites 10, 12, and 13 Visual Core Descriptions for the expanded scale, detailed core descriptions; see Sites 10, 12, and 13 Oversized Figures for the enlarged version of this summary. [BSR, bottom simulating reflector; RAB, resistivity-at-bit; SMI, sulfate-methane interface]

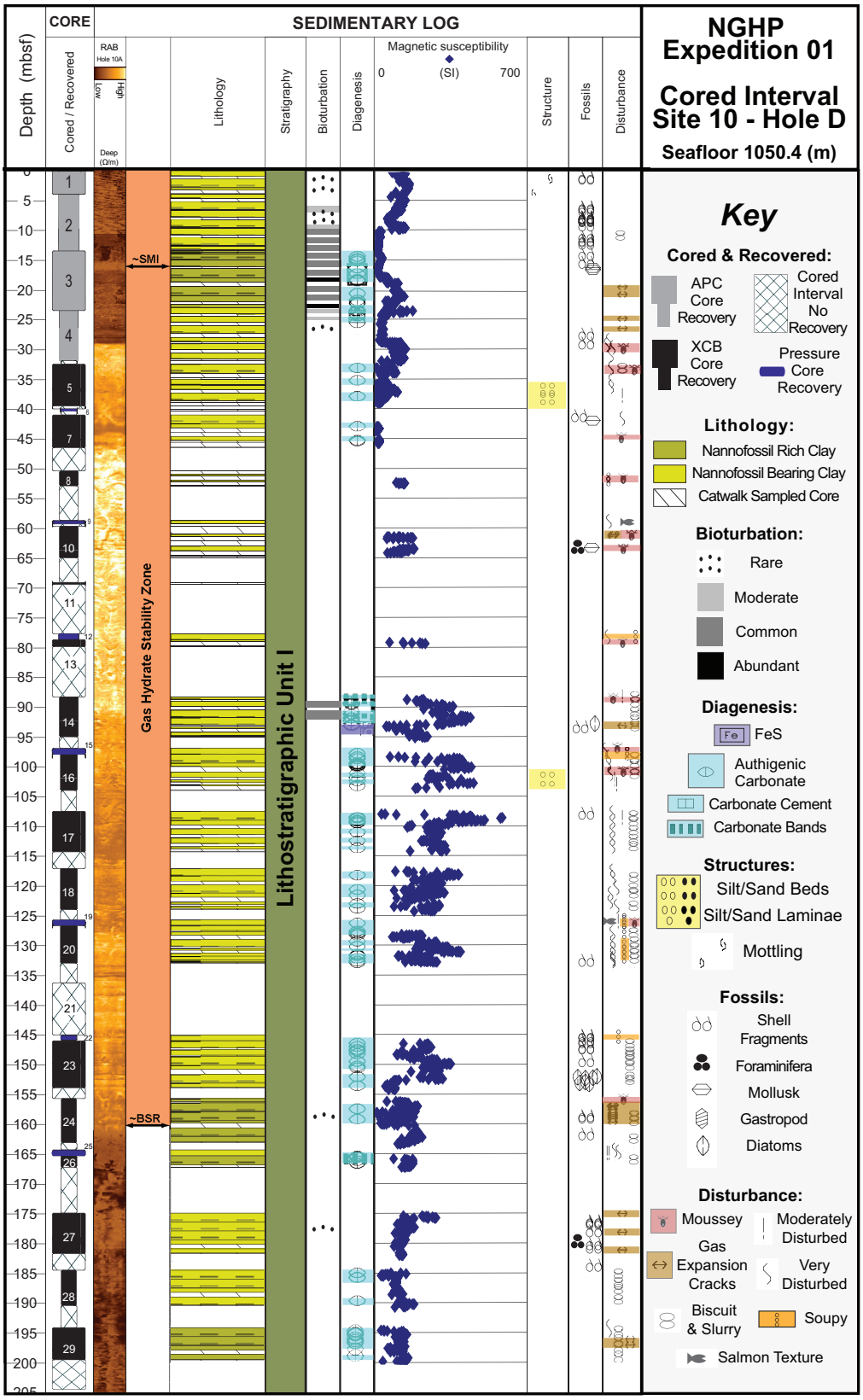


Figure 6. Lithostratigraphic summary of Hole NGHP-01-10D. Note: Colored intervals exceed symbol size when there is a range in the occurrence. Center point of each symbol represents true depth of occurrence, therefore colored bars may slightly exceed core recovery; see Sites 10, 12, and 13 Visual Core Descriptions for the expanded scale, detailed core descriptions; see Sites 10, 12, and 13 Oversized Figures for the enlarged version of this summary. [BSR, bottom simulating reflector; RAB, resistivity-at-bit; SMI, sulfate-methane interface]

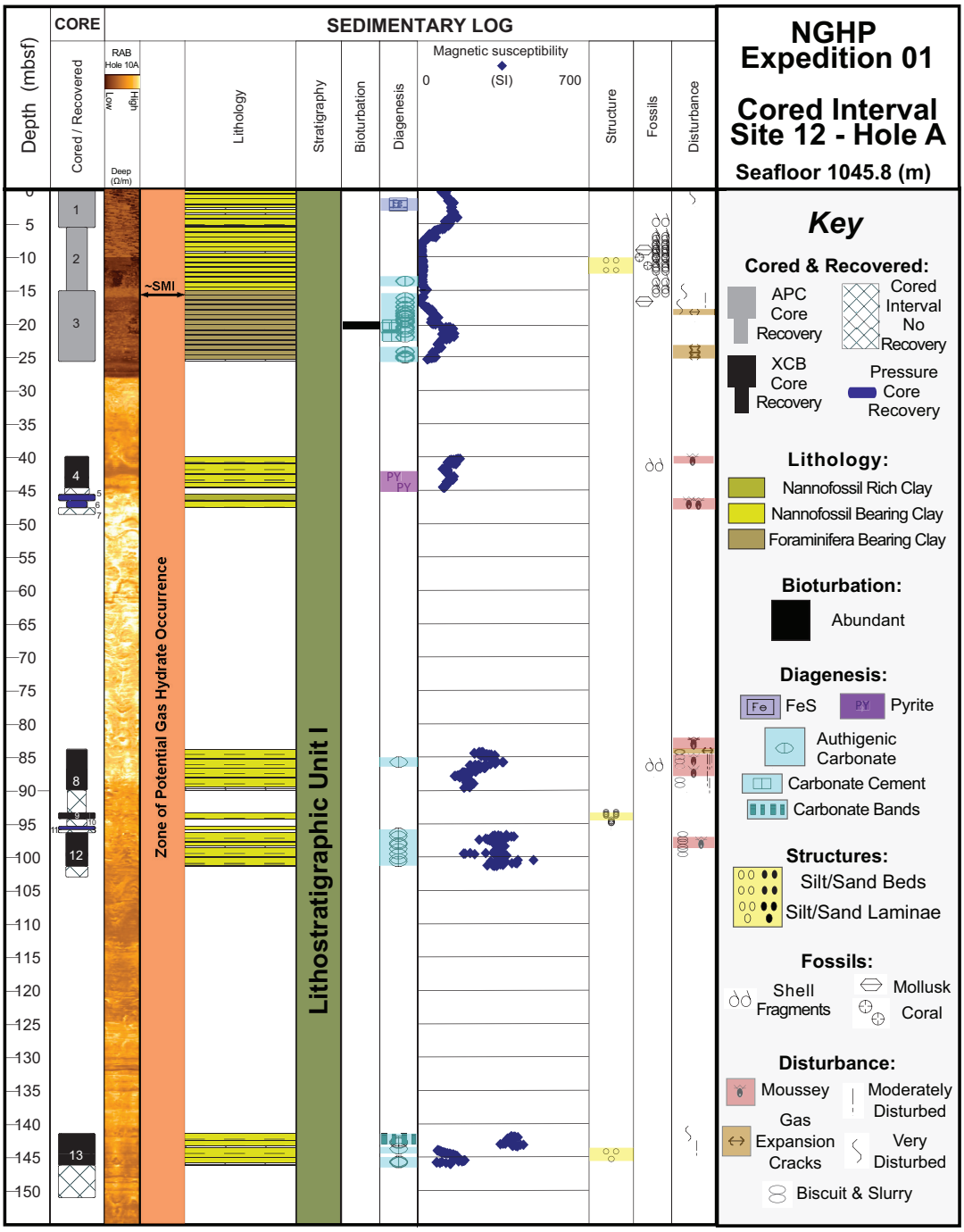


Figure 7. Lithostratigraphic summary of Hole NGHP-01-12A. Note the RAB image is from Hole NHGP-01-10A because there were no LWD data collected at Site NGHP-01-12. [LWD, logging-while-drilling; BSR, bottom simulating reflector; RAB, resistivity-at-bit; SMI, sulfate-methane interface] Note: Colored intervals exceed symbol size when there is a range in the occurrence. Center point of each symbol represents true depth of occurrence, therefore colored bars may slightly exceed core recovery; see Sites 10, 12, and 13 Visual Core Descriptions for the expanded scale, detailed core descriptions; see Sites 10, 12, and 13 Oversized Figures for the enlarged version of this summary.

clay, and opaque minerals. Opaque grains, mostly sulfides in irregular and framboidal forms, are common in all grain sizes, and typically comprise trace amounts of the total sediment. The total biogenic component of the sediment is dominated by calcareous nannofossils, which comprise 5–40 percent of the total (biogenic and nonbiogenic) sediment grains. Foraminifera are also common in the coarse fractions (>63 µm) of the sediments and in core 3H from Hole NGHP-01-12A, where they are the dominant biogenic component. Terrestrial organic matter was also observed in smear slide as trace up to 6 percent,throughout the sediments at both Sites NGHP-01-10 and NGHP-01-12.

Gas-Hydrate Occurrence

Gas hydrate was inferred from the LWD data at Site NGHP-01-10 and recovered in several cores on the catwalk (identified through IR images and photographed at the section and sample cuts in the cores). The observed gas hydrate existed as solid nodules, fracture fill in high angle and subhorizontal veins, and disseminated throughout the cores (the pressure-core degassing and X-ray results, as well as the semi-continuous cold spots in the IR data, confirm disseminated gas hydrate is common throughout the gas-hydrate occurrence zone; see "Physical Properties" and "Pressure Coring"). Upon examination of the pressure cores and other APC and XCB cores, no obvious lithologic control on gas-hydrate occurrence (in terms of grain size) was observed. The split cores from Sites NGHP-01-10 and NGHP-01-12 often exhibited moussey and soupy textures (figs. 5, 6, and 7; Sites 10, 12, and 13 Visual Core Descriptions in the supplemental data files) which commonly result from the dissociation of gas hydrate (fig. 10), and are consistent with the widespread observation of gas hydrate in the cores and well logs at these sites (figs. 5 and 6).

Inorganic Geochemistry

The main objectives of the inorganic geochemistry program at Sites NGHP-01-10 and NGHP-01-12, which are located ~500 meters apart, were to (1) identify and quantify the fluid and gas source(s), subsurface hydrology (transport mechanisms and migration pathways), and biogeochemical reactions associated with subsurface gas hydrate; and (2) determine the quantity and distribution of gas hydrate based on dissolved chloride concentrations. Interstitial water (IW) chemical composition data are tabulated in tables 7, 8, and 9, and illustrated in figure 11. The interstitial water data from these sites are similar and are considered as a combined group.

A total of 83 interstitial water samples were collected at Site NGHP-01-10 and 42 samples at Site NGHP-01-12. Whole-round lengths ranged from 10 to 20 cm, with longer sections subsampled from cores recovered deeper within the holes. In addition to the general whole-round sampling scheme, sediment intervals with IR anomalies identified on the catwalk were sampled. The IR anomaly whole-round samples were immediately transferred to the chemistry laboratory, taken out of the core liner, split in half, and imaged with a hand-held IR camera. The sediment anomaly was then separated from the whole-round sample and squeezed. If the sediment was heterogeneous, lithologies were separated (that is, silt and clay) and squeezed separately to determine the percent pore space gas-hydrate occupancy of each sediment type. Pressure cores (PCS) subsampled for IW sampling were in part based on X-ray images. Often, one gas-hydrate sample and one background sample were collected per PCS pressure core, and Cl^- concentration in each sub-sample will be used to determine the percent hydrate in gas-hydrate-bearing sections.

Interstitial Water Chloride—Gas-Hydrate Distribution

Similar to Site NGHP-01-05, the Cl^- concentration depth profile at these sites shows four distinct zones (fig. 11A). Between the seafloor and approximately 10 mbsf, chloride concentrations are relatively constant with an average of 556 mM. There is then a smooth increase of approximately 2.5 percent to 26 mbsf. This gradient is likely due to the diffusion of higher salinity interglacial water into the sediment column. If this is the case, this implies that vertical advection at this site is relatively small over the past approximately 18,000 years.

Between 26 and 175 mbsf, Cl^- varies widely between 398 and 634 mM at Site NGHP-01-10, whereas at Site NGHP-01-12, Cl^- concentrations are relatively consistent to 100 mbsf. The variation between 26 and ~160 mbsf is due to the decomposition of gas hydrate following recovery, which coincides with the zone of gas hydrates inferred from the Resistivity-At-Bit images (RAB; see "Downhole Logging"). Furthermore, downhole resistivity log analyses show the highest concentration of gas hydrates to be between 46 and 87 mbsf, which is manifested in the chloride concentration depth profile by a minimum within this depth range. The maximum values, which are nearly 14 percent elevated relative to chloride values in the upper part of these holes, represent a minimum estimate of the *in situ* Cl^- concentration in this interval as all of the samples may be diluted due at least some to gas hydrate decomposition. The increase in chlorinity is most likely due to the formation of gas hydrate while the large offset between this interval and that above and below it imply that diffusion has not effectively transported all of the excess chlorinity from this interval.

The elevated chlorinity requires a constant supply of CH_4 either *in situ* by methanogenesis or by transport through faults and fractures.

At depths greater than approximately 165 mbsf, Cl^- concentrations of the limited number of recovered samples are less variable. These Cl^- concentrations most likely reflect *in situ* values and are depleted relative to seawater and likely due to the decomposition of gas hydrate during progressive burial beneath the gas hydrate stability zone.

Table 1. Smear-slide data for Hole NGHP-01-10B.

Sample reference		Texture			Mineral								
Core, section, depth (cm, in section)	Lithology	Sand	Silt	Clay	Quartz	Feldspar	Mica	Heavy minerals	Clay minerals	Volcanic glass	Glauco-nite	Iron sulfides	Authigenic carbonates
NGHP-01-10B													
1H-2,70	D			100	1			2	57				
1H-1,60	D			100		2		1	62				
2H-2,122	D		10	90	3	trace		1	51				
2H-5,40	M		5	95	1				46				
4X-1,87	D		15	85	10	2			67				
12X-3,74	D		15	85	1	1			68			trace	2
14X-2,20	D		10	90	5			1	58				
15P-1,80	D		10	90	5	trace		trace	57				
17X-1,27	D			100	1				78				
18Y-1,40	D		5	95	1	trace	trace		70				3
23X-2,50	D		7	93	trace	trace			70				3
26X-2,55	M		55	45	47	2	trace	2	45				
26X-2,70	D		15	85	7	1	trace		81				
28P-2,35	D		10	90	5	2	trace		56				
29X-1,45	D		10	90	5	2	1		81				
29X-2,70	D		5	95	5	1			82				1
30X-1,19	D		5	95	1	1			90				

Table 2. Smear-slide data for Hole NGHP-01-10D.

Sample reference		Texture			Mineral								
Core, section, depth (cm, in section)	Lithology	Sand	Silt	Clay	Quartz	Feldspar	Mica	Heavy minerals	Clay minerals	Volcanic glass	Glauco-nite	Iron sulfides	Authigenic carbonates
NGHP-01-10D													
1H-2,71.5	D		5	95	5				82			1	
3H-5,90	D		15	85	10	2	trace		68			1	1
3H-2,80	M		20	80	1	1			67			1	5
4H-6,50	D		6	94	2		trace		84				
4H-3,70	D			100	trace	trace	trace		87				
5X-5,70	D		20	80	15	trace	trace	2	68				
5X-4,30	D		8	92	2			1	87				
7X-1,76	D		5	95	5				84				
8X-1,54	D		5	95	2				90				
9Y-1,25	D		5	95	2	trace	trace	1	84				
10X-2,30	D		15	85	8	2			82			1	
13X-1,15	D		10	90	3			2	50				
15P-1,80	D		5	95	2				92				
14X-2,16	D		10	90	5	2			76			5	
16X-2,30	D		10	90	5				87	trace			2
17X-2,70	D		7	93	1	1			88			1	2
18X-3,80	D		5	95	2	trace	trace		90				
19Y-1,40	D		4	96	2				91				
20X-2,26	D		6	94	2			1	74				
22E-1,20	D		6	94	2		trace	trace	84				
23X-6,22	D		5	95	3			trace	85				
23X-2,25	D		10	90	5	trace		1	85				
24X-2,30	D		5	95	2				67				
24X-3,39	D		5	95	2				56				1
26X-1,55	D		10	90	2	1			70				
26X-1,80	M		100		60	10							30
27X-1,64	D		25	75	7	3			82			2	
27X-2,66	D		5	95					70				
28X-1,70	D		10	90	5	5			84			1	
28X-3,40	D		10	90	5	5			81				
25P-1,116	D		15	85	7	3	1		78	1		1	
29X-1,83	D		5	95	1				71	trace		trace	trace

Table 1. Smear-slide data for Hole NGHP-01-10B. —Continued

Sample reference		Biogenic							Comments
Core, section, depth (cm, in section)	Lithology	Foraminifera	Nannofossils	Carbonate shell fragments	Diatoms	Radiolarians	Sponge spicules	Plant debris	
NGHP-01-10B—Continued									
1H-2,70	D		40						
1H-1,60	D		35						
2H-2,122	D		40					5	
2H-5,40	M	8	45						Foram shell fragments & silt sized grains
4X-1,87	D		20					1	
12X-3,74	D	3	35					trace	Trace aragonite & carb. shell fragments
14X-2,20	D	5	25				1	5	
15P-1,80	D	5	25				trace	8	
17X-1,27	D		20					1	
18Y-1,40	D		25					1	
23X-2,50	D	1	25					1	
26X-2,55	M		trace					4	Quartz grains subangular, subrounded and well sorted
26X-2,70	D	3	5					3	
28P-2,35	D		35					2	Trace aragonite
29X-1,45	D		10					1	
29X-2,70	D		10					1	
30X-1,19	D		8					trace	

Note: M = minor lithology, D = dominant lithology.

Table 2. Smear-slide data for Hole NGHP-01-10D. —Continued

Sample reference		Biogenic							Comments
Core, section, depth (cm, in section)	Lithology	Foraminifera	Nannofossils	Carbonate shell fragments	Diatoms	Radiolarians	Sponge spicules	Plant debris	
NGHP-01-10D—Continued									
1H-2,71.5	D	1	10					1	
3H-5,90	D	1	15					2	Trace aragonite, possible fish spine
3H-2,80	M	3	20					1	7% aragonite, trace barite
4H-6,50	D	2	10					2	
4H-3,70	D	2	10					1	
5X-5,70	D	2	10					3	
5X-4,30	D	3	5					2	
7X-1,76	D		10					1	
8X-1,54	D	1	6					1	Forams are small fragments
9Y-1,25	D	2	10					1	
10X-2,30	D	1	5					1	
13X-1,15	D	3	40					2	
15P-1,80	D		5					1	
14X-2,16	D		10					2	Plant seed
16X-2,30	D	trace	5					1	
17X-2,70	D	1	5					1	
18X-3,80	D	2	5					1	
19Y-1,40	D	1	5					1	
20X-2,26	D	2	20				trace	1	
22E-1,20	D	2	10					2	
23X-6,22	D	1	10					1	
23X-2,25	D	3	5					1	
24X-2,30	D		30					1	
24X-3,39	D		40					1	
26X-1,55	D		25					2	
26X-1,80	M								
27X-1,64	D		5					1	2% shell fragments, some pyrite
27X-2,66	D		30						
28X-1,70	D		5						
28X-3,40	D	2	5					2	
25P-1,116	D	1	7					1	
29X-1,83	D	1	25					2	Trace carb. shell fragments

Note: M = minor lithology, D = dominant lithology.

Table 3. Smear-slide data for Hole NGHP-01-12A.

Sample reference		Texture			Mineral								
Core, section, depth (cm, in section)	Lithology	Sand	Silt	Clay	Quartz	Feldspar	Mica	Heavy minerals	Clay minerals	Volcanic glass	Glauco-nite	Iron sulfides	Authigenic carbonates
Hole NGHP-01-12A													
1H-1,40	D		8	92	1				88				
1H-4,40	D		3	97	trace		trace		93				
2H-1,90	D		4	96	1				91				
2H-5,40	D		6	94	1				84				
3H-1,35	D		17	83	2				83				
3H-6,11	M		15	85	3	1		40	46				
4X-2,32	D		10	90	2	trace			80				
5Y-1,47	D		9	91	1				66				
6E-1,60	D		25	75	10				80				5
8X-1,50	D		7	93	2	trace			88				
9Y-1,50	D		5	95	4				90				1
12X-3,54	D		7	93	2	1			83	1		1	1
12X-1,48	D		5	95	2				85	trace		1	1
13X-3,87	D		10	90	2	2			81	trace		2	1

Sample reference		Biogenic							Comments
Core, section, depth (cm, in section)	Lithology	Fora-minifera	Nanno-fossils	Carbonate shell fragments	Diatoms	Radio-larians	Sponge spicules	Plant debris	
Hole NGHP-01-12A—Continued									
1H-1,40	D	4	5					2	
1H-4,40	D	2	4					1	
2H-1,90	D	2	5					1	
2H-5,40	D	3	10					2	
3H-1,35	D	10						5	
3H-6,11	M							10	Possible siderite, clay sized, abundant
4X-2,32	D	3	10					5	
5Y-1,47	D	2	25				trace	6	
6E-1,60	D		5					trace	
8X-1,50	D	2	5					3	
9Y-1,50	D		5						Trace organic carbon
12X-3,54	D		10					1	Trace carbonate shell fragments
12X-1,48	D		10					1	
13X-3,87	D	1	10					1	

Table 4. Silt laminae and beds at Hole NGHP-01-10B.

Core, section	Position start	Position end	Depth top (mbsf)	Depth base (mbsf)	Type
NGHP-01-10B					
1H-2	0	120	1.5	2.7	Multiple faint silt laminae
2H-5	36	47	9.46	9.57	Slightly silty zone
26X-1	0	75	166.5	167.25	Faint silt laminae
26X-2	0	120	168	169.2	Multiple silt laminae
26X-2	51.5	51.5	168.515	168.515	Silt bed
26X-2	53.5	53.5	168.535	168.535	Silt bed
26X-2	55	55	168.55	168.55	Silt bed
26X-2	58	58	168.58	168.58	Silt bed
26X-2	74	76	168.74	168.76	Silt bed
26X-2	107	107	169.07	169.07	Silt bed
26X-2	108.5	108.5	169.085	169.085	Silt bed

Table 5. Silt laminae and beds at Hole NGHP-01-10D.

Core, section	Position start	Position end	Depth top (mbsf)	Depth base (mbsf)	Type
NGHP-01-10D					
5X-5	69	72	36.77	36.8	Multiple silt beds
5X-6	0	130	37.33	38.63	Multiple silt laminae
16X-3	81	82	101.81	101.82	Silt bed

Table 6. Silt laminae and beds at Hole NGHP-01-12A.

Core, section	Position start	Position end	Depth top (mbsf)	Depth base (mbsf)	Type
			NGHP-01-12A		
9Y-1	28	36	93.58	93.66	Multiple silt laminae
9Y-1	49	50	93.79	93.8	Silt laminae
9Y-1	57	57	93.87	93.87	Silt laminae
9Y-1	66	68	93.96	93.98	Multiple silt laminae
9Y-1	78	79	94.08	94.09	Silt laminae

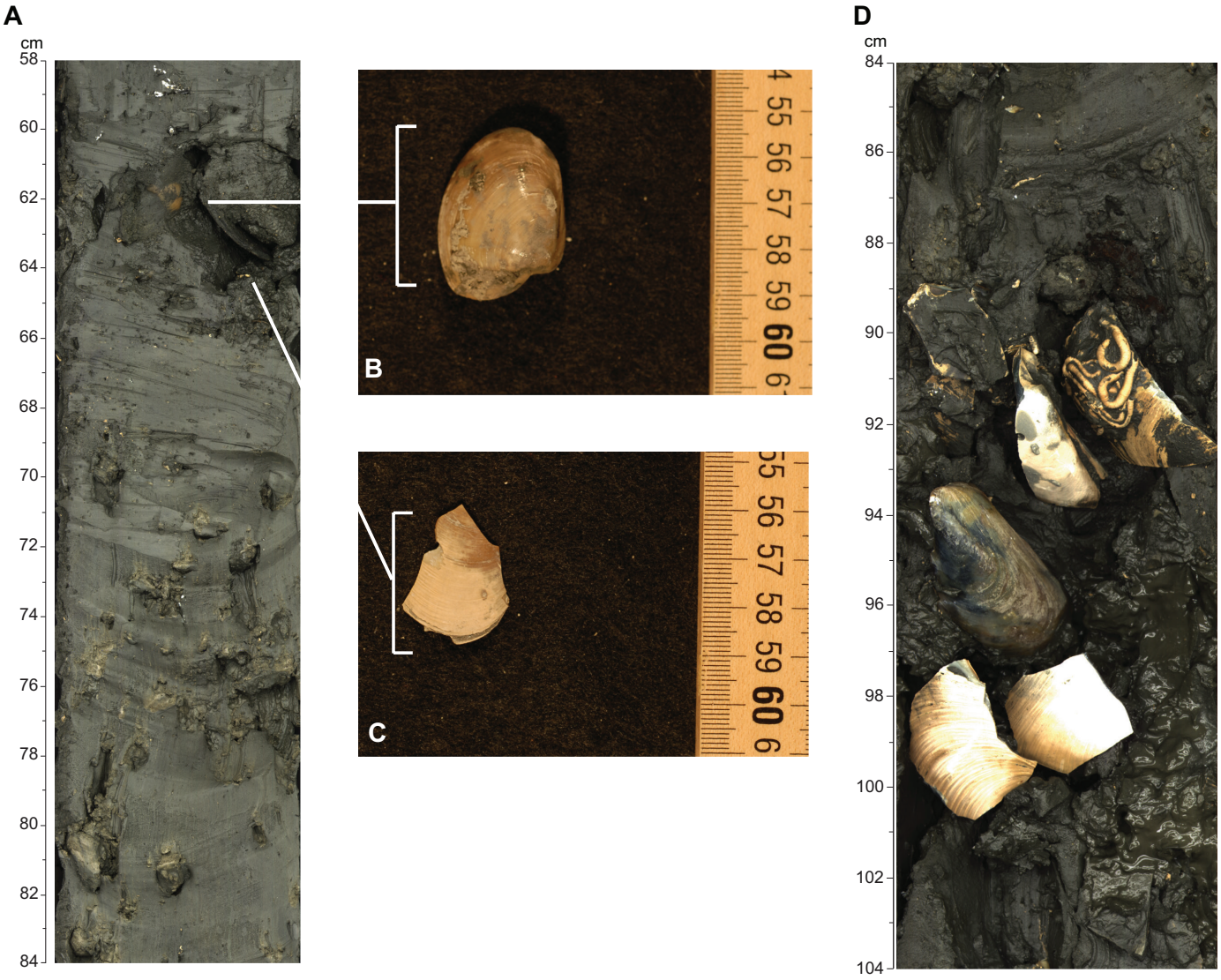


Figure 8. Possible fossil chemosynthetic communities (A–D). A, Section NGHP-01-10D-03H-2, 58–84 cm; also notice the large authigenic carbonates nodules, B, Section NGHP-01-10D-03H-2, 60–62 cm, C, Section NGHP-01-10D-03H-2, 60–62 cm, D, Section NGHP-01-12A-03H-2, 84–104 cm. Vertical scale is in centimeters.

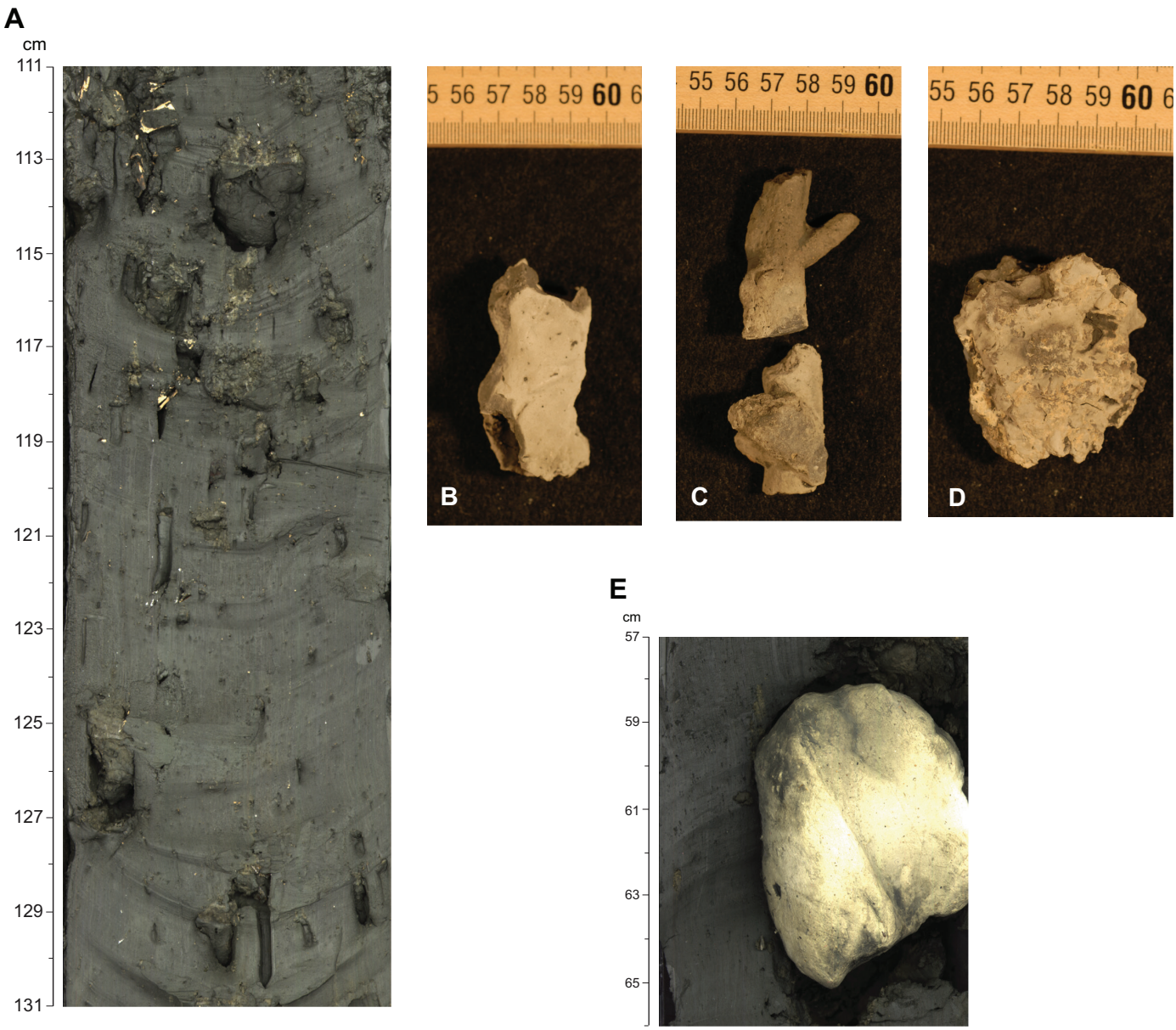


Figure 9. Authigenic carbonate nodules. A, concentration of gravel size nodules, Section NGHP-01-12A-03H-2, 111–131 cm, B, authigenic carbonate filled burrow, Section NGHP-01-10D-04H-2, 140–142 cm, C, authigenic carbonate filled burrows, Section NGHP-01-10D-03H-3, 22–24 cm, D, authigenic carbonate nodule, Section NGHP-01-10D-04H-1, 0–2 cm, E, authigenic carbonate nodule, Section NGHP-01-10D-03H-7, 58–65 cm. Vertical scale is in centimeters.

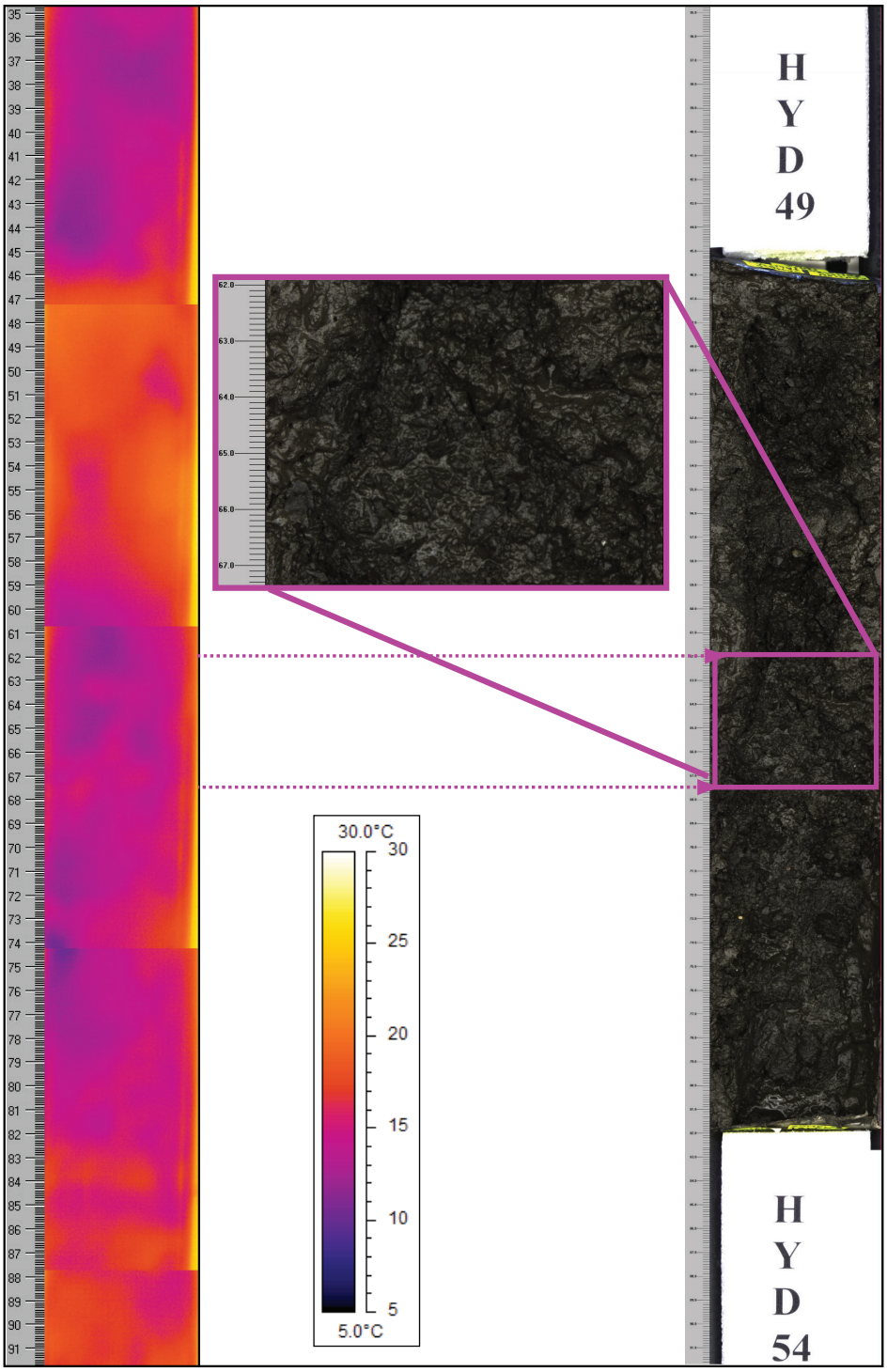


Figure 10. Moussey texture preserved in a split core (Section NGHP-01-10D-08X-1, 35–91 cm) due to the dissociation of gas hydrate; notice the corresponding infrared cold anomaly in the equivalent whole round core indicative of gas hydrate in the recovered core. HYD49 and HYD54 indicate locations where whole round gas-hydrate samples were removed. Inset shows a close up view of the moussey texture. Vertical scale is in centimeters.

Table 7. Interstitial-water data for Hole NGHP-01-10B.

Core, section	Top	Bottom	Depth (mbsf)	Volume (mL)	pH	Alkalinity (mM)	Salinity	Cl^- (mM)	Br^- (mM)	SO_4^{2-} (mM)	Comments
NGHP-01-10B											
1H-1	140	150	1.4	37	7.4	6.78	35.0	556	0.81	25.8	
2H-1	140	150	4.5	36	7.6	15.10	35.0	555	0.80	17.9	
2H-3	140	150	7.5	31	7.6	11.97	35.0	555	0.82	18.0	
2H-5	140	150	10.5	32	7.8	8.44	34.5	555	0.79	18.7	
2H-7	42	52	12.5	31	7.7	8.59	34.5	562	0.82	18.6	
4X-1	140	150	23.4	23	7.9	23.22	33.0	557	0.84	0.3	
4X-2	130	150	24.8	33	8.0	24.79	33.0			bdl	
4X-3	22	32	25.2	12	8.1	17.27	24.8	426	0.62	0.2	
7X-1	28	43	42.1	25	7.7	31.51	35.0	590	1.10	0.2	
9X-1	30	45	51.6	29	7.4	18.94	35.5	510	1.03	1.8	Hydrate
9X-1	30	45	51.6	17	7.7	20.32	35.0	599	1.14	3.7	Backround
10X-1	52	62	61.1	26			25.0	442	0.85	0.2	Hydrate
10X-1	52	62	61.1	35			35.0	593	1.19	1.7	Backround
12X-3	127	147	73.0	7			36.0	617	1.26	0.8	Hydrate
12X-3	127	147	73.0	18	8.3	10.80	36.0	624	1.29	0.3	Background
12X-5	43	58	74.3	13	7.9	11.05	34.5				Hydrate
12X-5	43	58	74.3	10	8.2	10.71	35.0	606	1.24	1.2	Background
14X-1	80	100	90.6	18	7.9		33.5	563	1.19	1.2	Hydrate
14X-1	80	100	90.6	2			35.0				Background
14X-1	120	140	91.0	20	8.1	14.73	35.5	537	1.11	1.8	Hydrate
14X-1	120	140	91.0	8			32.0	541	1.14	1.1	Background
15P-1	40	50	98.6	2			33.0				
17X-1	100	120	109.8	19	8.0	13.65	32.5	564	1.29	0.3	
17X-2	130	150	111.6	12			30.3	556	1.20	1.1	Hydrate
17X-2	130	150	111.6	14	7.9	12.21	30.5	532	1.17	0.9	Background
17X-4	119	134	114.5	14	8.0	12.94	33.5	608	1.36	1.4	Hydrate
17X-4	119	134	114.5	11			34.0	618	1.41	1.3	Background
18Y-1	47	60	117.9	16	7.7	16.77	35.0	606	1.35	0.7	
19X-1	25	40	118.7	26	7.8	16.85		587	1.27	6.4	
21Y-1	6	18	136.7	32	7.5	19.58	32.0	583	1.46	1.0	
23X-1	130	150	143.4	12			31.0				Hydrate
23X-3	0	28	145.1	8			33.0	462	1.14	0.2	
26X-1	130	150	167.8	19	8.0	23.79	32.0	562	1.46	0.1	
28P-1	17	38	175.3	12				530	0.98	13.6	
28P-2	105	117	176.5	10				527	1.36	0.3	
29X-3	130	150	180.4	21	7.6		32.0			bdl	
30X-1	33	63	186.0	10		17.77	31.5			bdl	

Table 8. Interstitial-water data for Hole NGHP-01-10D.

Core, section	Top	Bottom	Depth (mbsf)	Volume (mL)	pH	Alkalinity (mM)	Salinity	Cl^- (mM)	Br^- (mM)	SO_4^{2-} (mM)	Comments
						NGHP-01-10D					
1H-1	140	150	1.4	36	7.6	7.01		557	0.709	25.1	
1H-3	83	93	3.8	36	7.7	12.88		557	0.756	20.3	
2H-1	110	120	5.2	35	7.8	14.07	35.0	555	0.745	18.2	
2H-3	140	150	8.2	35	7.8	10.91		552	0.747	18.1	
2H-5	140	150	11.2	30	8.1	8.63	34.5	558	0.758	18.9	
2H-7	82	92	13.6	35	8.1	10.18	35.0	561	0.766	17.9	
3H-2	140	150	16.5	40	7.7	18.21	34.5	566	0.769	9.0	
3H-4	140	150	19.5	28.5	7.7	24.64		567	0.749	0.1	
3H-6	140	150	22.5	27.5	7.9	23.44		572		0.1	
4H-2	135	145	26.0	26	7.9	22.57		572	0.808	bdl	
4H-4	57	67	28.0	19	7.8	16.42		528		bdl	
4H-5	70	80	28.8	21	7.6	22.16	33.5	518	0.783	bdl	
4H-6	140	150	30.6	35	7.6		29.0	480	0.797	bdl	
5X-2	45	65	34.5	13			30.0	520	0.923	0.3	
5X-5	105	125	37.1	22	7.9	24.46	36.5	602	1.128	0.2	
6P-1	7	14	40.2	6			37.5	621	1.191	1.1	
7X-2	108	128	43.7	17	8.0	22.49	38.0	407	0.734	0.2	
7X-3	0	20	44.0	7			29.0	521	0.980	0.3	
7X-5	0	23	45.7	22	8.0	21.60	36.5	624	1.247	bdl	
8X-1	13	33	50.6	4			21.0				Hydrate
10X-1	90	110	60.7	15			36.5	618		bdl	
10X-2	95	115	62.0	19	7.8	11.81	26.0	418	0.782	0.1	
10X-4	80	100	63.8	16	7.8	12.33	29.8	466	0.895	1.7	
11X-1	7	27	69.3	23	8.0	15.04	30.0	515	0.973	2.2	
13X-1	70	90	79.5	22	7.9	14.32	35.0	555	1.168	0.7	
14X-2	130	150	90.4	10			33.5	555	1.197	bdl	Hydrate
14X-2	130	150	90.4	15		10.96	33.5	575	1.324	0.3	Background
14X-5	72	92	94.1	13			32.5	531	1.145	bdl	
16X-2	130	150	100.8	25	7.9			420	0.920	0.6	
16X-5	40	60	103.5	22	7.9			569	1.277	0.2	
17X-2	115	135	110.3	20	8.0		31.0	528	1.347	0.8	
17X-4	105	125	113.0	24	7.8	18.30		634	1.559	0.1	
18X-2	130	150	119.7	14	7.9	16.08		491	1.103	0.5	
18X-4	110	130	122.3	26	7.9	15.33		486	1.161	0.3	
20X-1	80	100	127.6	25	7.8			605	1.360	1.3	
20X-2	93	113	128.7	26	7.6	19.40		577	1.540	0.4	
20X-4	60	80	131.1	16		16.04		550	1.355	1.5	
23X-1	130	150	147.4	17	8.2	19.24	23.0	397.6	0.986	0.1	
23X-4	130	150	151.4	22	8.0	24.09	25.0	402.6	1.009	0.1	
24X-1	50	70	156.3	18	8.0	27.82	30.0	502.6	1.262	0.1	
24X-4	90	120	160.4	20	8.0	26.72	30.0	504.4	1.401	bdl	
25P-1	20	35	164.6	31	7.9	21.15					
25P-1	90	100	165.3	20	8.0	27.06	34.5	536			
27X-4	120	150	180.7	24	7.9	16.04	33.5	529.6	1.401	bdl	
28X-3	120	150	188.8	21	7.9	15.88	32.0	537.4	1.349	bdl	
29X-3	120	150	198.4	14	7.9	15.11	32.0	541.1		0.3	

Table 9. Interstitial-water data for Hole NGHP-01-12A.

Core, section	Top	Bottom	Depth (mbsf)	Volume (mL)	pH	Alkalinity (mM)	Salinity	Cl^- (mM)	Br^- (mM)	SO_4^{2-} (mM)	Comments
NGHP-01-12A											
1H-3	140	150	4.4	30	8.0	9.45	35.0				
1H-4	92	102	5.4	30	8.0	10.24	35.3	555	0.80	22.10	
2H-1	70	80	6.4	22	7.5	10.74		555	0.76	19.36	
2H-1	140	150	7.1	25	7.9	10.14		560	0.79	19.04	
2H-2	70	80	7.9	25	7.7	9.59	34.8	561	0.76	18.19	
2H-2	140	150	8.6	22	8.0	8.99	34.5	555	0.81	17.11	
2H-3	70	80	9.4	24	7.9	8.88		560	0.80	17.53	
2H-3	140	150	10.1	21	7.6	8.44	35.0	559		16.62	
2H-4	70	80	10.9	21	8.1	11.13	34.8	559	0.81	15.58	
2H-4	140	150	11.6	22		12.61	35.0	566	0.84	15.29	
2H-5	70	80	12.4	25	7.9		35.0	568	0.82	15.34	
2H-5	140	150	13.1	20	7.8	15.18	35.0	569	0.83	13.09	
2H-6	70	80	13.9	24	8.0	16.20	35.0	569	0.85	12.69	
2H-6	140	150	14.6	30	8.0	16.29	35.0	566	0.79	13.72	
2H-7	57	67	15.3	27	8.0	16.75	34.5	568	0.85	12.21	
3H-2	70	80	16.5	22	8.0	18.58		570	0.82	10.24	
3H-2	140	150	17.2	25	7.9	28.35	34.5	570	0.84	0.19	
3H-3	70	80	18.0	22	7.5	26.94		574	0.88	bdl	
3H-3	140	150	18.7	20	8.0			573	0.84	0.43	
3H-4	70	80	19.5	25	7.9	24.71		570	0.89	bdl	
3H-4	140	150	20.2	22		25.21	34.5	568	0.88	0.12	
3H-5	70	80	21.0	21	8.3	23.77	34.5	569	0.91	0.15	
3H-5	140	150	21.7	22	8.0	24.94		570	0.93	bdl	
3H-6	70	80	22.5	23	8.2	23.71	34.5	569		bdl	
3H-6	140	150	23.2	21	8.0	24.59		569	0.99	0.05	
3H-7	70	80	24.0	23	8.2	23.83		573		0.06	
3H-7	140	150	24.7	22	8.0	24.14		573	1.03	0.04	
3H-8	58	68	25.4	20	8.2	21.70	34.5	577		0.06	
4X-1	105	115	41.1		7.9	21.53		578.1	1.32	1.48	
4X-2	140	150	42.6	25	7.8	21.16	34.5	577	1.32	1.46	
4X-3	122	132	43.9	25	7.8	20.89	34.5	565	1.29	1.19	
8X-1	130	150	85.1	27	8.0	19.62		572	1.40	0.55	
8X-3	130	150	87.9	19	7.9	18.37		572	1.34	1.98	
12X-2	59	79	98.3	20	8.1	18.81		557	1.37	0.38	
12X-3	130	150	99.8	10				559.5	1.39	bdl	
13X-2	93	113	143.2	26	7.8	25.56		522	1.28	0.40	
13X-4	77	97	145.7	29	8.0	23.31		523	1.28	0.99	

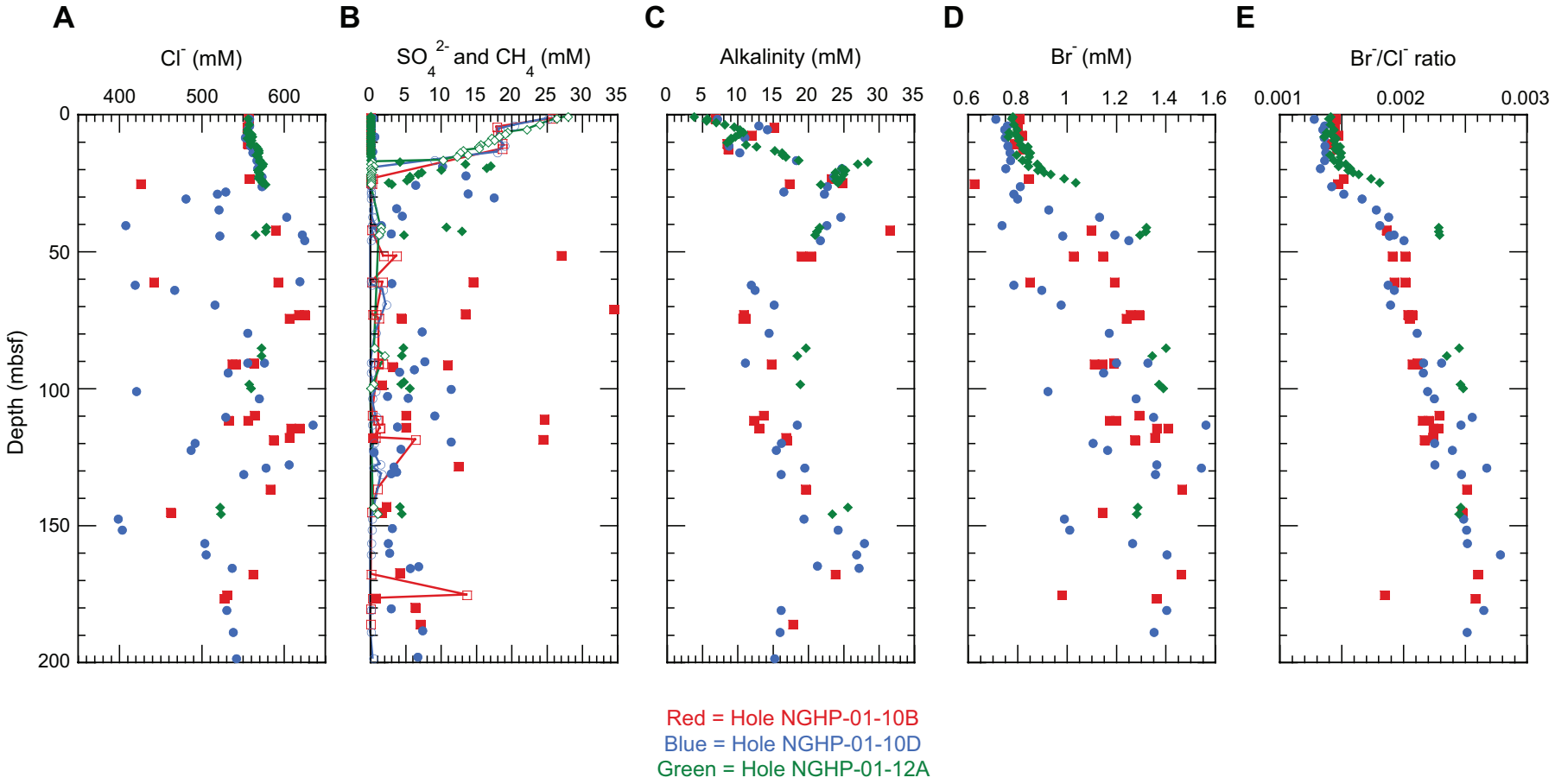


Figure 11. Interstitial water composition depth profiles of A, chloride (errors are smaller than the symbols); B, sulfate (connected by line) and methane; C, alkalinity; D, bromide; and E, bromide/chloride ratio at Holes NGHP-01-10B, NGHP-01-10D and NGHP-01-12A. [red squares, Hole NGHP-01-10B; blue dots, Hole NGHP-01-10D; and green diamonds Hole NGHP-01-12A]

Sulfate Concentrations and the SMI

Hole NGHP-01-12A defines the sulfate concentration trend in the upper part of the sediment column most clearly (fig. 11B). Sulfate values decrease smoothly from near seawater values in the shallowest sample to approximately 10 mM at 16.5 mbsf at ~1.2 mM/m. There is an abrupt large increase in the concentration gradient below this depth with the next deeper sample, collected from the same core section, at 17.2 mbsf with a concentration very near the estimated detection limit of 0.1 mM. The change in the concentration gradient to ~14 mM/m may be the result of high sedimentation rates or non-steady state conditions. Concomitant with the depletion in SO_4^{2-} is an abrupt increase in head-space methane concentrations from below the detection limit to ~4 mM (see "Organic Geochemistry"), thus constraining the depth of the sulfate methane interface (SMI) at 17.2 mbsf.

At greater depths, the majority of samples are below the detection limit while others scatter to higher values. The samples with higher values most likely reflect contamination with drilling fluid. The quality of the cores recovered at these sites was compromised by gas hydrate dissociation and subsequent degassing, which greatly increased the permeability of the sediments resulting in seawater infiltration. In these whole-rounds seawater penetrated the whole sample, thus making it near impossible to properly clean the whole-rounds and isolate uncontaminated sediment before squeezing. Minor sulfide oxidation to sulfate may also be responsible for some of the higher SO_4^{2-} values.

Alkalinity

Alkalinity increases by an order of magnitude from near seawater values to nearly 30 mM in the region of the SMI (fig. 11C). This reflects the production of alkalinity due to microbial sulfate reduction. However, the magnitude of the increase is only approximately one half of that expected if there is not also a sink for alkalinity. As the sediments are saturated with respect to carbonates, a likely sink is authigenic carbonate. At greater depths, there appears to be a broad concentration minimum centered in the middle of the gas hydrate interval. This must be interpreted with caution as the *in situ* values may be variously offset due to carbonate precipitation/dissolution due to pH and temperature changes as well as degassing during the core recovery process. Nonetheless, the interval of the minimum may be the result of the burial of low alkalinity fluids while the increase at the bottom of the hole may be driven by methanogenesis.

Bromide

Bromide concentrations are relatively constant to 20 mbsf (fig. 11D). Concentrations then scatter to higher values. However, much of this scatter appears to be related to hydrate decomposition as Br^-/Cl^- ratios vary more smoothly with depth (fig. 11E). The ratio is nearly constant to 20 mbsf indicating that the diffusive exchange with overlying water is greater than the production rate in this interval. The ratio then increases steeply to approximately 50 mbsf reflecting a source from the decomposition of marine organic matter. Below this depth, the ratio increases more gradually through the remainder of the sediment column sampled, increasing by approximately 25 percent. The increase with depth most likely reflects the continued breakdown of marine organic matter.

Organic Geochemistry

Organic geochemical studies at Site NGHP-01-10 (GDGH-03-1) and NGHP-01-12 (GDGH-03-1A) included analysis of the composition of volatile hydrocarbons including methane, ethane, and propane (C_1–C_3) and fixed natural gases (that is, O_2, CO_2, and N_2+Ar) from headspace, void gas, and pressure core sampler (PCS) degassing experiments. In general, these analyses indicate that the predominant hydrocarbon gas found in the cores at these sites was methane; however ethane was measurable in two headspace samples, all void gases, and all pressure core degassing experiment samples. The stratigraphic section overlying the sulfate-methane interface (SMI, about 0–18 mbsf) was depleted in methane. Conversely, methane and ethane were relatively enriched below the SMI and above the seismically-inferred bottom simulating reflector (BSR). Methane and ethane concentrations were consistently elevated below the SMI likely due to presence of gas hydrate in these cores. The C_1 and C_2 concentrations decline steadily below the BSR to the borehole completion depth of ~200 mbsf (see below). Specific details of the shipboard gas chemistry results for Site NGHP-01-10, Holes B and D, and Site NGHP-01-12, Hole A are provided in the following discussion.

Headspace gas analyses were performed on 27 samples from Hole NGHP-01-10B, 43 samples from Hole NGHP-01-10D, and 43 samples from Hole NGHP-01-12A ranging in depth from 0.7 to 197.8 meters below seafloor (mbsf). The concentrations given here represent minimum proxy measurements of the actual concentrations due to limitations of the gas headspace method (Kvenvolden and Lorenson, 2000). The sediment pore water contained methane at concentrations ranging from non-detectable near the surface to 8.6 mM at ~20 mbsf (table 10). Theoretical methane saturation in pore water under site-specific physical conditions, calculated using the Duan and others, (1992) and Xu (2002, 2004) methodologies, ranges from 60.7 mM at the seafloor to 124.6 mM at 160 mbsf, then gradually declines to 122.3 mM near the borehole completion depth of 200 mbsf (fig. 12). Two headspace samples in Hole NGHP-01-10D indicated the presence of C_2 gas at depths of ~35 and 52 mbsf (0.01 and 0.015 mM), however no C_3 or higher gases were detected. The presence of elevated levels of methane gas and only limited detection of ethane gas in headspace samples suggests hydrocarbon gases result from microbial methanogenesis.

Table 10. Headspace gas composition for Sites NGHP-01-10 and NGHP-01-12.

Core, section, interval (cm)	Sed wt. (g)	Sample depth (mbsf)	CO_2	C_1	C_2	C_3	O_2	N_2+Ar	H_2S	C_1 (mL/L WS)	C_1 (mM PW)	CO_2 (mL/L WS)	CO_2 (mM PW)	C_1/CO_2
			(ppmv)											
10B-1H1-105-110	6.8	1.1	12,300	nd	nd	nd	182,800	751,000	nd	nd	nd	44,700	2.3	-
10B-2H1-105-110	7.3	4.2	5,300	nd	nd	nd	191,200	749,700	nd	nd	nd	17,600	1.0	-
10B-2H3-105-110	8.0	7.2	3,400	nd	nd	nd	191,300	746,700	nd	nd	nd	9,900	0.6	-
10B-2H5-105-110	7.2	10.2	1,900	nd	nd	nd	189,300	737,100	nd	nd	nd	6,400	0.4	-
10B-2H7-37-42	7.3	12.5	1,800	nd	nd	nd	192,600	753,200	nd	nd	nd	5,900	0.4	-
10B-4X1-135-140	7.3	23.4	27,700	38,500	nd	nd	164,600	756,700	nd	127,700	8.6	91,700	6.2	1.4
10B-4X2-65-70	5.7	24.2	25,000	12,000	nd	nd	156,800	779,200	nd	54,400	3.7	113,200	7.6	0.5
10B-9X1-25-30	12.4	51.5	23,300	113,000	nd	nd	155,200	700,900	nd	174,000	13.0	36,000	2.7	4.8
10B-10X1-47-52	10.4	61.1	7,200	48,700	nd	nd	151,900	765,800	nd	98,800	7.4	14,600	1.1	6.8
10B-12X1-0-5	6.3	71.0	15,000	64,000	nd	nd	151,700	749,100	nd	256,000	19.0	60,000	4.5	4.3
10B-12X3-92-97	7.3	72.6	15,800	29,400	nd	nd	151,800	739,900	nd	97,500	7.3	52,400	3.9	1.9
10B-12X5-38-43	8.9	74.3	13,100	12,000	nd	nd	150,000	761,700	nd	30,500	2.3	33,300	2.5	0.9
10B-14X2-0-5	17.2	91.3	25,900	70,900	nd	nd	145,800	746,100	nd	59,000	4.9	21,500	1.8	2.7
10B-14X2-67-72	15.7	92.0	23,500	17,600	nd	nd	150,200	775,000	nd	17,700	1.4	23,700	1.9	0.7
10B-15P-50-55	11.7	98.7	7,000	6,100	nd	nd	160,900	786,000	nd	10,300	0.8	11,900	0.9	0.9
10B-17X1-95-100	7.3	109.8	20,900	11,000	nd	nd	136,800	802,400	nd	36,300	2.8	69,200	5.4	0.5
10B-17X2-85-90	6.4	111.2	10,000	38,800	nd	nd	180,800	754,800	nd	152,100	11.8	39,100	3.0	3.9
10B-17X4-94-99	8.3	114.2	16,100	10,600	nd	nd	102500	847,200	nd	29,600	2.3	44,900	3.5	0.7
10B-18Y-60-65	12.3	118.0	13,900	900	nd	nd	152500	786,700	nd	1,500	0.1	21,700	1.8	0.1
10B-19X1-10-15	9.1	118.5	59,000	57,800	nd	nd	142800	758,700	nd	142,400	11.2	145,300	11.5	1.0
10B-20X1-40-45	8.1	128.4	44,200	25,700	nd	nd	129700	782,500	nd	74,100	5.9	127,500	10.1	0.6
10B-23X1-95-100	13.5	143.1	19,100	8,600	nd	nd	125000	804,700	nd	11,400	1.0	25,500	2.1	0.5
10B-23X3-0-5	12.4	145.1	23,700	5,700	nd	nd	110800	821,300	nd	8,800	0.7	36,600	3.0	0.2
10B-26X1-70-75	11.4	167.2	13,800	12,900	nd	nd	158900	745,700	nd	22,700	1.9	24,400	2.0	0.9
10B-28P-100-105	10.6	176.5	4,800	1,900	nd	nd	184900	739,500	nd	3,700	0.3	9,400	0.8	0.4
10B-29X3-70-75	8.4	179.8	22,200	10,900	nd	nd	173600	777,500	nd	29,900	2.4	61,000	5.0	0.5
10B-30X1-28-33	9.2	186.0	27,200	13,400	nd	nd	122000	816,000	nd	32,600	2.7	65,900	5.4	0.5
10D-1H1-105-110	8.8	1.1	12,500	500	nd	nd	175600	775,400	nd	1,400	0.1	32,300	1.6	0.0
10D-1H3-33-38	8.3	3.3	26,000	nd	nd	nd	169600	772,400	nd	nd	nd	72,600	4.1	-
10D-2H1-75-80	6.2	4.9	23,600	nd	nd	nd	171200	771,600	nd	nd	nd	96,100	5.6	-
10D-2H3-105-110	5.6	7.9	12,500	600	nd	nd	194800	768,600	nd	2,600	0.2	57,700	3.5	0.0
10D-2H5-105-110	8.0	10.9	10,400	nd	nd	nd	179000	771,200	nd	nd	nd	30,500	1.9	-
10D-2H7-47-52	7.4	13.3	11,200	300	nd	nd	196400	779,000	nd	1,000	0.1	36,400	2.3	0.0
10D-3H2-95-100	12.2	16.1	20,100	300	nd	nd	140400	805,900	nd	500	0.0	31,900	2.1	0.0
10D-3H4-60-65	9.5	18.7	21,200	20,200	nd	nd	164400	762,900	nd	46,700	3.1	49,200	3.3	1.0
10D-3H6-95-100	7.9	22.1	20,200	21,600	nd	nd	151700	751,900	nd	64,500	4.3	60,500	4.1	1.1
10D-4H2-90-95	6.0	25.5	26,300	7,400	nd	nd	158200	746,100	nd	31,600	2.1	111,600	7.6	0.3
10D-4H5-65-70	11.0	28.7	26,800	32,700	nd	nd	137800	751,100	nd	60,900	4.3	49,900	3.5	1.2
10D-4H6-95-100	6.5	30.1	30,300	22,400	nd	nd	153400	762,200	nd	86,200	5.9	116,400	8.0	0.7
10D-5X2-0-5	15.9	34.1	33,600	13,900	nd	nd	131700	786,400	nd	13,600	1.0	32,900	2.4	0.4
10D-5X2-61-64	14.0	34.7	40,300	173,600	30	nd	88700	698,200	nd	217,000	15.7	50,400	3.6	4.3
10D-5X5-70-75	13.9	36.8	40,700	14,100	nd	nd	104700	819,800	nd	17,900	1.3	51,600	3.8	0.3
10D-6P-14-17	12.3	40.2	16,100	6,000	nd	nd	170800	751,500	nd	9,300	0.7	25,100	1.8	0.4
10D-7X2-63-68	17.9	43.2	48,500	19,200	nd	nd	136000	771,600	nd	14,600	1.1	36,800	2.8	0.4
10D-8X1-140-150	19.8	51.9	700	986,100	120	nd	33300	135,100	nd	582,700	47.1	400	0.0	1,408.7
10D-10X2-35-40	16.2	61.4	13,100	17,600	nd	nd	145200	775,700	nd	16,600	1.3	12,400	1.0	1.3
10D-10X4-75-80	12.7	63.8	6,600	221,300	nd	nd	150000	619,600	nd	327,500	25.0	9,800	0.7	33.5
10D-13X1-25-30	7.8	79.1	21,000	17,100	nd	nd	164500	776,500	nd	52,100	3.9	63,700	4.8	0.8
10D-14X2-85-90	9.1	90.0	4,000	21,600	nd	nd	165600	776,200	nd	53,100	4.1	9,900	0.8	5.4
10D-14X4-104-109	9.0	92.9	5,100	17,100	nd	nd	162200	792,600	nd	42,700	3.3	12,700	1.0	3.4
10D-14X5-37-42	9.5	93.7	4,300	12,100	nd	nd	179200	77,100	nd	28,000	2.2	9,900	0.8	2.8
10D-16X2-55-60	13.5	100.1	55,000	52,900	nd	nd	112000	776,400	nd	70,500	5.7	73,300	5.9	1.0
10D-16X4-32-39	11.2	102.6	28,300	8,500	nd	nd	78300	853,700	nd	15,400	1.2	51,300	4.1	0.3
10D-16X5-55-60	12.0	103.3	63,300	20,800	nd	nd	67200	819,900	nd	33,800	2.7	102,800	8.2	0.3
10D-17X2-70-75	16.1	109.8	37,000	53,600	nd	nd	77000	810,800	nd	51,300	4.3	35,400	3.0	1.4
10D-17X5-32-37	11.9	113.8	38,700	14,700	nd	nd	51800	855,100	nd	24,200	1.9	63,800	5.1	0.4
10D-18X2-85-90	13.8	119.3	3,300	54,600	nd	nd	135900	780,600	nd	70,000	5.7	4,300	0.3	16.5
10D-18X4-70-75	11.7	121.9	30,400	16200	nd	nd	118900	783,700	nd	27,400	2.2	51,400	4.1	0.5
10D-18X5-41-46	13.6	123.1	8,600	1500	nd	nd	190700	756,900	nd	1,900	0.2	11,300	0.9	0.2
10D-20X2-55-60	15.3	128.4	34,100	14900	nd	nd	67200	850,500	nd	15,800	1.3	36,100	3.0	0.4
10D-20X3-120-125	14.3	130.2	44,300	15300	nd	nd	74600	829,100	nd	18,400	1.5	53,200	4.4	0.3
10D-20X4-25-30	17.9	130.8	29,800	16300	nd	nd	137100	797,100	nd	12,400	1.1	22,600	2.0	0.5
10D-23X4-70-75	12.9	150.8	67,600	11000	nd	nd	35800	842,900	nd	15,800	1.3	97,400	8.1	0.2
10D-24X1-45-50	12.5	156.3	34,300	8400	nd	nd	104100	820,900	nd	12,700	1.1	52,200	4.3	0.2
10D-24X4-30-35	9.6	159.8	33,000	6500	nd	nd	105000	829,900	nd	14,800	1.2	75,200	6.1	0.2

Table 10. Headspace gas composition for Sites NGHP-01-10 and NGHP-01-12.—Continued

Core, section, interval (cm)	Sed wt. (g)	Sample depth (mbsf)	CO_2	C_1	C_2	C_3	O_2	N_2+Ar	H_2S	C_1 (mL/L WS)	C_1 (mM PW)	CO_2 (mL/L WS)	CO_2 (mM PW)	C_1/CO_2
			(ppmv)											
10D-25P-35-40	15.0	164.8	10,600	30,300	nd	nd	179,600	756,700	nd	33,300	2.9	11,700	1.0	2.9
10D-25P-100-110	9.5	165.4	13,100	13,800	nd	nd	171,500	768,900	nd	32,000	2.6	30,400	2.5	1.1
10D-27X4-60-65	12.3	180.1	11,000	9,700	nd	nd	179,200	737,000	nd	15,200	1.3	17,200	1.4	0.9
10D-28X3-60-65	12.1	188.2	24,200	24,600	nd	nd	15,300	768,600	nd	39,400	3.3	38,800	3.3	1.0
10D-29X3-60-65	9.1	197.8	34,700	15,600	nd	nd	141,100	779,000	nd	38,300	3.2	85,400	7.1	0.4
12A-1H1-65-70	13.7	0.7	900	nd	nd	nd	186,600	752,600	nd	nd	nd	1,100	0.1	-
12A-1H1-135-140	8.7	1.4	1,600	nd	nd	nd	186,700	755,400	nd	nd	nd	4,100	0.2	-
12A-1H2-65-70	8.2	2.2	6,700	nd	nd	nd	184,100	751,900	nd	nd	nd	19,200	1.0	-
12A-1H2-135-140	8.2	2.9	12,000	nd	nd	nd	181,200	750,100	nd	nd	nd	34,200	1.9	-
12A-1H3-65-70	9.4	3.7	11,800	nd	nd	nd	182,100	739,700	nd	nd	nd	27,800	1.6	-
12A-1H3-135-140	8.9	4.4	11,500	nd	nd	nd	181,600	755,500	nd	nd	nd	29,200	1.7	-
12A-1H4-87-92	8.4	5.4	13,200	nd	nd	nd	180,600	747,400	nd	nd	nd	36,300	2.1	-
12A-2H1-65-70	7.8	6.4	5,500	nd	nd	nd	187,000	742,600	nd	nd	nd	16,700	1.0	-
12A-2H1-135-140	7.8	7.1	11,400	nd	nd	nd	179,600	742,200	nd	nd	nd	34,600	2.1	-
12A-2H2-65-70	8.0	7.9	8,900	nd	nd	nd	181,300	749,400	nd	nd	nd	26,200	1.6	-
12A-2H2-135-140	6.2	8.6	9,600	nd	nd	nd	185,600	764,400	nd	nd	nd	39,100	2.4	-
12A-2H3-65-70	7.1	9.4	11,600	nd	nd	nd	174,100	756,500	nd	nd	nd	40,000	2.5	-
12A-2H3-135-140	7.7	10.1	10,600	nd	nd	nd	173,400	756,700	nd	nd	nd	32,800	2.1	-
12A-2H4-65-70	5.2	10.9	13,700	nd	nd	nd	176,300	745,800	nd	nd	nd	69,200	4.3	-
12A-2H4-135-140	6.9	11.6	14,000	nd	nd	nd	172,800	768,200	nd	nd	nd	49,900	3.2	-
12A-2H5-65-70	8.1	12.4	12,100	nd	nd	nd	171,600	759,900	nd	nd	nd	34,800	2.2	-
12A-2H5-135-140	6.7	13.1	13,000	nd	nd	nd	177,100	770,700	nd	nd	nd	48,000	3.1	-
12A-2H6-65-70	8.1	13.9	15,700	nd	nd	nd	173,200	770,500	nd	nd	nd	45,400	2.9	-
12A-2H6-135-140	7.7	14.6	18,100	nd	nd	nd	163,100	758,800	nd	nd	nd	56,000	3.6	-
12A-2H7-52-57	8.3	15.2	20,500	nd	nd	nd	162,300	775,400	nd	nd	nd	57,400	3.7	-
12A-3H2-65-70	6.5	16.5	15,400	nd	nd	nd	168,200	777,100	nd	nd	nd	59,400	3.9	-
12A-3H2-135-140	9.9	17.2	30,600	10,800	nd	nd	143,300	788,500	nd	23,700	1.6	66,700	4.4	0.4
12A-3H3-65-70	8.0	18.0	27,900	27,300	nd	nd	152,100	760,300	nd	80,200	5.3	81,900	5.4	1.0
12A-3H3-135-140	7.6	18.7	23,200	32,600	nd	nd	152,500	775,300	nd	102,600	6.8	72,800	4.8	1.4
12A-3H4-65-70	13.5	19.5	21,000	63,700	nd	nd	105,600	791,900	nd	84,900	5.8	28,000	1.9	3.0
12A-3H4-135-140	13.3	20.2	22,200	38,100	nd	nd	115,800	802,000	nd	52,100	3.6	30,300	2.1	1.7
12A-3H5-65-70	10.6	21.0	28,600	20,700	nd	nd	131,700	799,300	nd	40,800	2.8	56,400	3.8	0.7
12A-3H5-135-140	8.0	21.7	30,200	13,700	nd	nd	153,600	774,300	nd	40,400	2.7	88,700	6.0	0.5
12A-3H6-65-70	11.4	22.5	44,900	17,100	nd	nd	123,300	786,700	nd	30,100	2.1	79,200	5.4	0.4
12A-3H6-135-140	11.1	23.2	43,300	16,800	nd	nd	131,400	778,500	nd	30,800	2.1	79,600	5.4	0.4
12A-3H7-65-70	7.3	24.0	34,700	9,300	nd	nd	157,300	762,900	nd	30,800	2.1	115,000	7.8	0.3
12A-3H6-135-140	10.6	24.7	13,800	7,200	nd	nd	149,900	767,400	nd	14,200	1.0	27,100	1.9	0.5
12A-3H7-53-58	8.8	25.4	31,800	6,800	nd	nd	156,100	770,600	nd	17,400	1.2	82,100	5.6	0.2
12A-4X1-100-105	9.7	41.0	30,900	27,500	nd	nd	148,700	757,500	nd	61,800	4.4	69,500	5.0	0.9
12A-4X2-135-140	7.6	42.5	25,700	24,700	nd	nd	158,000	743,800	nd	77,700	5.5	80,800	5.8	1.0
12A-4X3-117-122	8.4	43.8	33,000	10,100	nd	nd	139,100	788,100	nd	27,700	2.0	90,900	6.5	0.3
12A-8X1-125-130	10.4	85.1	16,900	12,900	nd	nd	175,800	771,700	nd	26,100	2.0	34,200	2.6	0.8
12A-8X3-125-130	12.6	87.9	18,900	15,700	nd	nd	170,400	761,600	nd	23,600	1.9	28,400	2.2	0.8
12A-12X1-120-125	12.1	97.5	36,600	15,700	nd	nd	157,300	767,800	nd	25,200	2.0	58,700	4.7	0.4
12A-12X2-54-59	11.5	98.3	25,400	13,600	nd	nd	163,700	759,100	nd	23,700	1.9	44,200	3.5	0.5
12A-12X3-125-130	12.1	99.8	36,200	18,700	nd	nd	164,800	762,000	nd	30,000	2.4	58,000	4.6	0.5
12A-13X2-73-78	12.2	143.0	43,000	13,900	nd	nd	146,100	764,200	nd	22,000	1.8	68,000	5.6	0.3
12A-13X4-72-77	11.7	145.7	44,600	14,100	nd	nd	143,200	773,700	nd	23,800	2.0	75,400	6.2	0.3

Notes: nd = not detected. WS = Wet sediment. PW = porewater. Approximate detection limits are about 15 ppmv for methane, 30 ppmv for ethane, 50 ppmv for propane, and 20 ppmv for hydrogen sulfide.

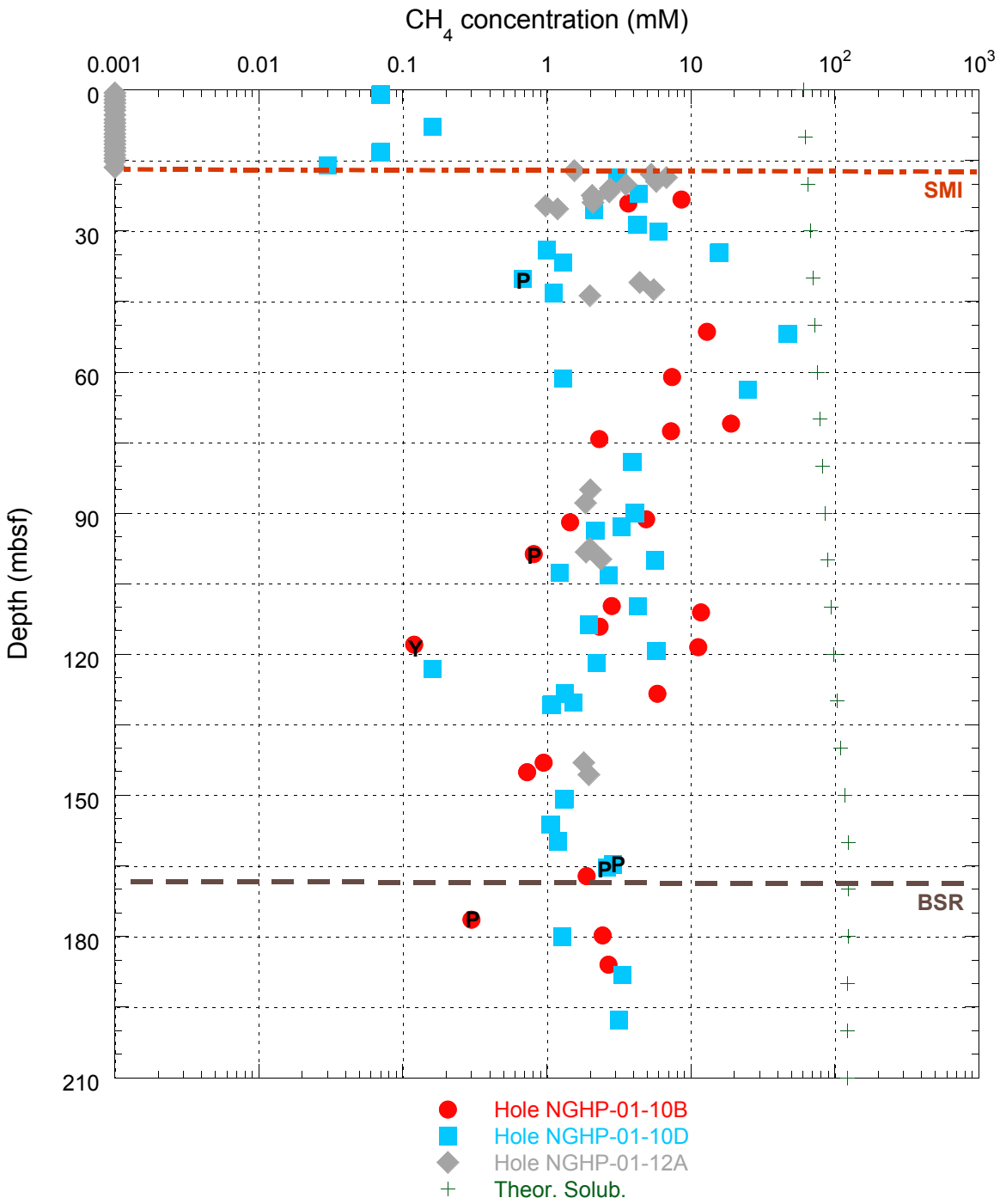


Figure 12. Plot of headspace methane gas concentration with depth for Sites NGHP-01-10 and NGHP-01-12. Note the apparent peak in methane between 35 and 75 mbsf corresponding to LWD results that show ~85 percent gas hydrate saturation from 27 to 90 mbsf. Text inside a symbol denotes special coring tool (E, HRC; P, PCS; Y, FPC). Theoretical solubility of methane calculated using the Duan and others (1992) and Xu (2002, 2004) methodologies. Hole NGHP-01-10D was not logged continuously, thus resulting in the spurious sampling intervals at depth. [LWD, logging-while-drilling]

Methane concentrations increase abruptly from non-detectable near the surface to nearly 10 mM at ~18 mbsf, concomitant with an abrupt increase in sulfate from 10 mM at 16.5 mbsf to 0.1 mM at 17.2 mbsf, thus likely denoting the sulfate-methane interface (SMI). Methane concentrations below the SMI range from 0.1 to 47 mM, with relative enrichment between ~35 and 65 mbsf, and from ~100 to 120 mbsf (fig. 12). These two peaks in methane concentration are confirmed in both boreholes at Site NGHP-01-10, however they are not apparent at nearby Site NGHP-01-12 (fig. 12). Pressure core samples from Site NGHP-01-12 indicate elevated methane gas in the same depth range (discussed below and in detail in "Pressure coring"). Both of these methane concentration peaks occur within the zone of potential gas hydrate as noted in the downhole logging from 27 to 157 mbsf. The presence of methane below the BSR at levels well above the theoretical saturation levels suggests that methane gas bubbles exist below the BSR (fig. 12). However the singular result from the PCS run below the BSR shows that methane concentrations are below saturation (see "Pressure Coring").

Carbon dioxide (CO_2) concentrations ranged from 0.03 to 11.5 mM in pore water contained within the sediment (fig. 13). An equivalent concentration expression of gas volume to sediment volume ranges from 420 to nearly 145,300 µL CO_2/L wet sediment (table 10). There is no consistent, fine-scale trend in the CO_2 concentration with depth, however concentrations are relatively uniform downcore with the exception of the apparent hydrate enrichment zones where the methane to carbon dioxide ratio is elevated (values above 10; fig. 14). The lowest concentrations are found in the upper 20 mbsf above the SMI. Air gases are present in all samples as the result of core plugs being degassed in an air headspace. The air gases (N_2+Ar), and O_2 were the sample balance gases, however the (N_2+Ar)/O_2 ratios were typically greater than air indicating that some oxygen reflects the ratios in pore fluids or has likely dissolved preferentially into the sediment porewater during sampling compared to N_2.

Void gas samples were collected from seven different intervals ranging in depth from 22 to 90.9 mbsf. The void gas samples contained methane and ethane in intervals except the uppermost (22 mbsf above the SMI), as noted in table 11. Methane concentrations within voids averaged nearly 87.7 percent (±26 percent due to one low value). No propane or higher molecular weight hydrocarbon gases were detected. Carbon dioxide concentrations ranged from non-detectable to 479 parts per million by volume (ppmv) and are tabulated with other gas data in table 11. The methane to carbon dioxide ratios are higher in the depths between the SMI and BSR indicating that gas hydrate has concentrated the methane relative to carbon dioxide (fig. 14). This is especially true for the highlighted datapoint, which was obtained adjacent to a hydrate (ratio ~1,500). This trend occurs in headspace gas samples although the magnitude of the ratios is typically 2 orders less due to the preferential loss of volatile methane by the headspace sample method (fig. 14). The presence of ethane in concentrations (70–485 ppmv in FG and 30–750 ppmv in PCS samples) infers that methane? is preferentially scavenged into gas hydrate during gas hydrate formation. This observation has been previously made at many gas hydrate accumulations around the world.

Gas was collected from nine pressure core sampler (PCS) cores, three in Hole NGHP-01-10B, three in Hole NGHP-01-10D, and two in Hole NGHP-01-12A. The gas concentration results are very similar to the void gas results (tables 11 and 12), however CO_2 concentrations were approximately 10 fold lower. The decrease in concentration can be attributed to the sampling method, whereby gas must first pass through the water-filled PCS chamber and into a water-filled inverted graduated cylinder. PCS core gases contained C_2 with concentrations ranging from 30 to 750 ppmv. Ratio values for C_1 to C_2 gases ranged from ~1,310 to ~20,000, and showed apparent ethane enrichment zones at ~30 mbsf and just above the BSR depth (figs. 15 and 16). The C_1/C_2 ratios suggest that microbial methanogenesis is the dominant source of methane. The increased concentration of ethane in the gas hydrate bearing zone is likely due to ethane enrichment by gas hydrate formation. Post cruise studies of the isotopic character of methane and ethane gases will assist in determination of microbial or thermogenic sources. Additional evidence that ethane may be concentrated due to hydrates at depth is provided in figure 16. The ratios trend toward "normal" with depth, thus become more methane enriched, which suggests that thermogenic sources of ethane are absent.

Microbiology

Hole NGHP-01-10B

Analysis of all microbiological samples will be shore-based. Fifteen samples were collected for cell enumeration (CEL), nine for hydrogenase activity analysis (SPH), and nine 30 cm sections identified as anomalous on the IR scan of the core (MAF, MAG, MAR) (table 13). The 30 cm sections were split into three subsections as described in the "Methods" chapter. Additional microbiological samples were taken (Lab code JUD, 33 samples; Lab code JAN, 21 samples).

Hole NGHP-01-10D

Nineteen samples were collected for cell enumeration (CEL), seventeen for hydrogenase activity analysis (SPH), four 30 cm sections identified as anomalous (MAF, MAG, MAR), and one 30 cm section identified as background (MBF, MBG, MBR) (table 14). The 30 cm sections were split into three sub-sections as described in the "Methods" chapter. Additional microbiological samples were taken (Lab code JUD, 13 samples; Lab code JAN, 17 samples).

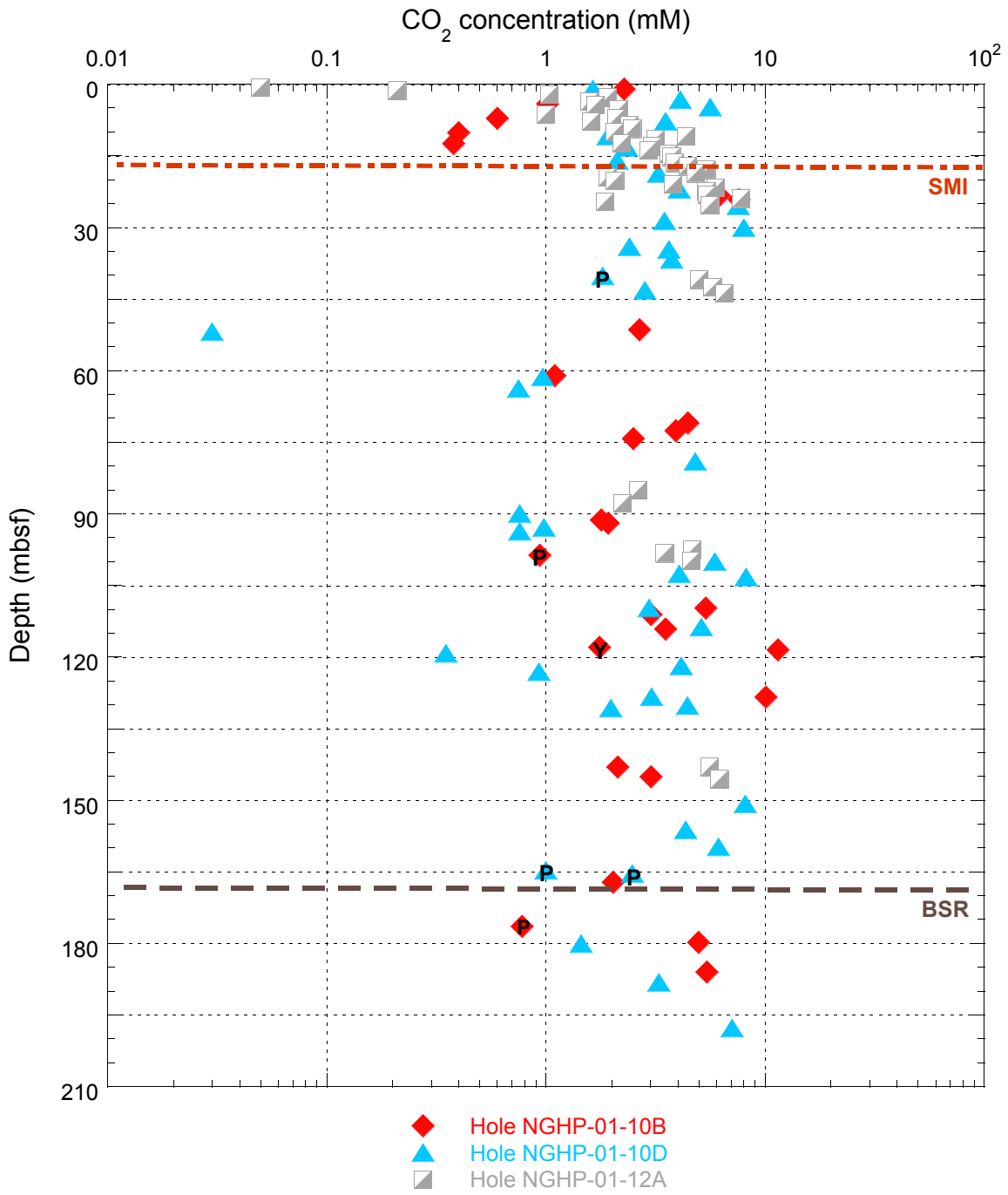


Figure 13. Plot of headspace carbon dioxide gas concentration (mM) with depth for Sites NGHP-01-10 and NGHP-01-12. Note the data tend to vary between 1 and 10 mM at these Sites. Text inside a symbol denotes special coring tool (E, HRC; P, PCS; Y, FPC). Hole NGHP-01-10D was not logged continuously, thus resulting in the spurious sampling intervals at depth, and could not confirm the peak in concentration at depth.

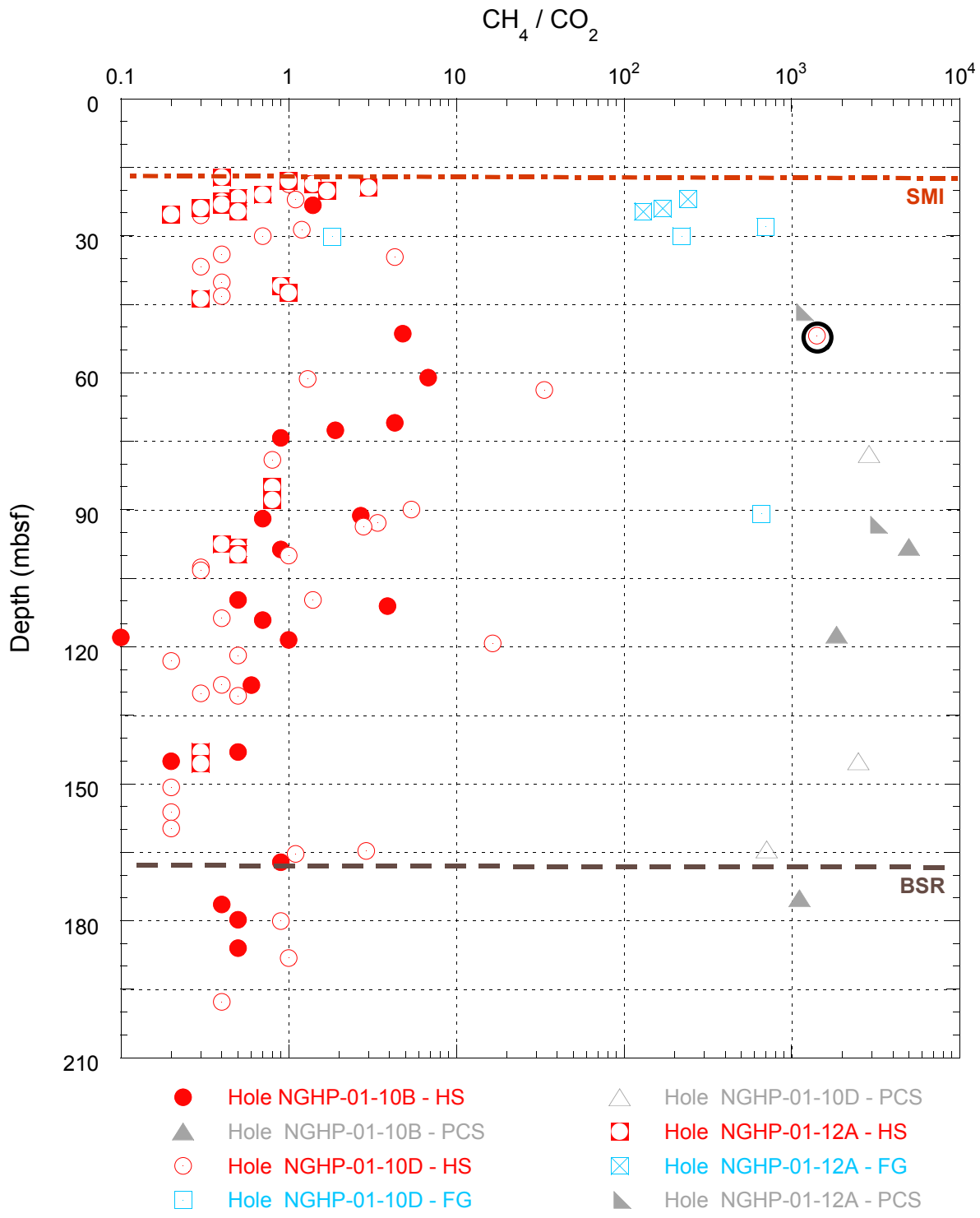


Figure 14. Plot of headspace (HS) (closed) and free/void (open) gas methane to carbon dioxide gas ratio with depth for Site NGHP-01-05, Holes C and D. Note that the spikes in concentration are a general indicator of concentrated 'pockets' of methane, perhaps indicating elevated levels of gas hydrate. Hole NGHP-01-10D was not sampled continuously and free gas samples are rarely obtained after XCB coring begins (~80 mbsf at this site), thus resulting in the random data collection intervals at depth. The circled HS datapoint (Hole NGHP-01-10D – HS, depth = 51.9 mbsf) was obtained next to gas hydrate.

Table 11. Void (FG) gas composition for Sites NGHP-01-10 and NGHP-01-12.

Core, section, interval (cm)	Sample depth (mbsf)	CO_2	C_1	C_2	C_3	O_2	N_2+Ar	H_2S	C_1/CO_2	C_1/C_2
		(ppmv) normalized to nitrogen+argon								
10C-1H5-105	30.19	5,500	980,300	170	nd	4,400	9,600	nd	180	5,800
10D-4H4-67	28.05	1,400	985,500	480	nd	3,900	8,700	nd	700	2,100
10D-4H6-110	30.15	4,500	980,300	370	nd	5,200	9,700	nd	220	2,600
10D-14X3-33	90.93	1,500	990,300	170	nd	2,800	5,300	nd	660	5,800
12A-3H6-20	22.03	1,100	266,200	nd	nd	155,200	577,500	nd	240	-
12A-3H7-75	24.08	5,700	983,100	70	nd	2,400	8,700	nd	170	14,000
12A-3H7-145	24.78	7,500	951,700	70	nd	10,200	30,500	nd	130	13,600

Notes: nd = not detected. nr = not recorded. Approximate detection limits are about 15 ppmv for methane, 30 ppmv for ethane, 50 ppmv for propane, and 20 ppmv for hydrogen sulfide.

Table 12. Pressure Core Sampler gas composition for Sites NGHP-01-10 and NGHP-01-12.

Core, section	Sample depth (mbsf)	Time	Gas vol. (ml)	CO_2	C_1	C_2	C_3	O_2	N_2+Ar	H_2S	C_1/CO_2	C_1/C_2
				(ppmv) normalized to nitrogen+argon								
10B-15P-t1	98.2	1	-	100	983,400	180	nd	4,800	11,400	nd	9,800	5,500
10B-15P-t2	98.2	2	-	480	404,500	190	nd	2,300	6,800	nd	800	2,100
10B-18Y-t1	117.4	1	-	240	963,100	180	nd	2,300	3,500	nd	4,000	5,400
10B-18Y-t2	117.4	2	-	340	962,700	190	nd	1,700	2,500	nd	2,800	5,100
10B-18Y-t3	117.4	3	-	400	813,900	180	nd	5,100	9,800	nd	2,000	4,500
10B-18Y-t4	117.4	4	-	230	991,500	190	nd	1,200	2,000	nd	4,300	5,200
10B-18Y-t5	117.4	5	-	230	995,600	210	nd	1,500	2,400	nd	4,300	4,700
10B-18Y-t6	117.4	6	-	220	995,400	190	nd	3,700	11,400	nd	4,500	5,200
10B-18Y-t7	117.4	7	-	250	994,400	160	nd	21,300	95,600	nd	4,000	6,200
10B-28P-t1	175.1	1	-	360	987,500	130	nd	10,000	120,700	nd	2,700	7,600
10B-28P-t2	175.1	2	-	1,080	987,200	140	nd	8,000	240,500	nd	900	7,100
10D-12E-t1	69.47	1	-	250	995,800	130	nd	12,500	35,300	nd	4,000	7,700
10D-12E-t2	69.47	2	-	310	997,100	150	nd	3,100	4,800	nd	3,200	6,600
10D-12E-t3	69.47	3	-	300	996,900	140	nd	3,300	7,900	nd	3,300	7,100
10D-12E-t4	69.47	4	-	290	997,200	130	nd	26,700	193,500	nd	3,400	7,700
10D-22E-t1	145.1	1	-	280	997,200	130	nd	7,800	17,800	nd	3,600	7,700
10D-22E-t2	145.1	2	-	1,030	976,100	160	nd	3,800	6,800	nd	900	6,100
10D-22E-t3	145.1	3	-	800	883,400	160	nd	5,800	12,900	nd	1,100	5,500
10D-22E-t4	145.1	4	-	340	897,500	180	nd	5,600	19,800	nd	2,600	5,000
10D-25P-t1	164.4	1	-	260	976,900	750	nd	2,800	12,400	nd	3,800	1,300
10D-25P-t2	164.4	2	-	490	976,000	490	nd	6,200	112,200	nd	2,000	2,000
12A-6E-t1	46.7	1	-	780	979,000	110	nd	5,600	23,100	nd	1,300	8,900
12A-6E-t2	46.7	2	-	290	956,500	40	nd	26,100	188,500	nd	3,300	23,900
12A-6E-t3	46.7	3	-	300	954,900	30	nd	65,900	356,900	nd	3,200	31,800
12A-9Y-t1	93.3	1	-	230	965,300	110	nd	1,400	2,200	nd	4,200	8,800
12A-9Y-t2	93.3	2	-	250	962,700	120	nd	600	1,100	nd	3,900	8,000
12A-9Y-t3	93.3	3	-	270	983,300	60	nd	1,300	2,100	nd	3,600	16,400
12A-9Y-t4	93.3	4	-	270	983,300	50	nd	40,300	189,800	nd	3,600	19,700

Notes: nd = not detected. Approximate detection limits are about 15 ppmv for methane, 30 ppmv for ethane, 50 ppmv for propane, and 20 ppmv for hydrogen sulfide.

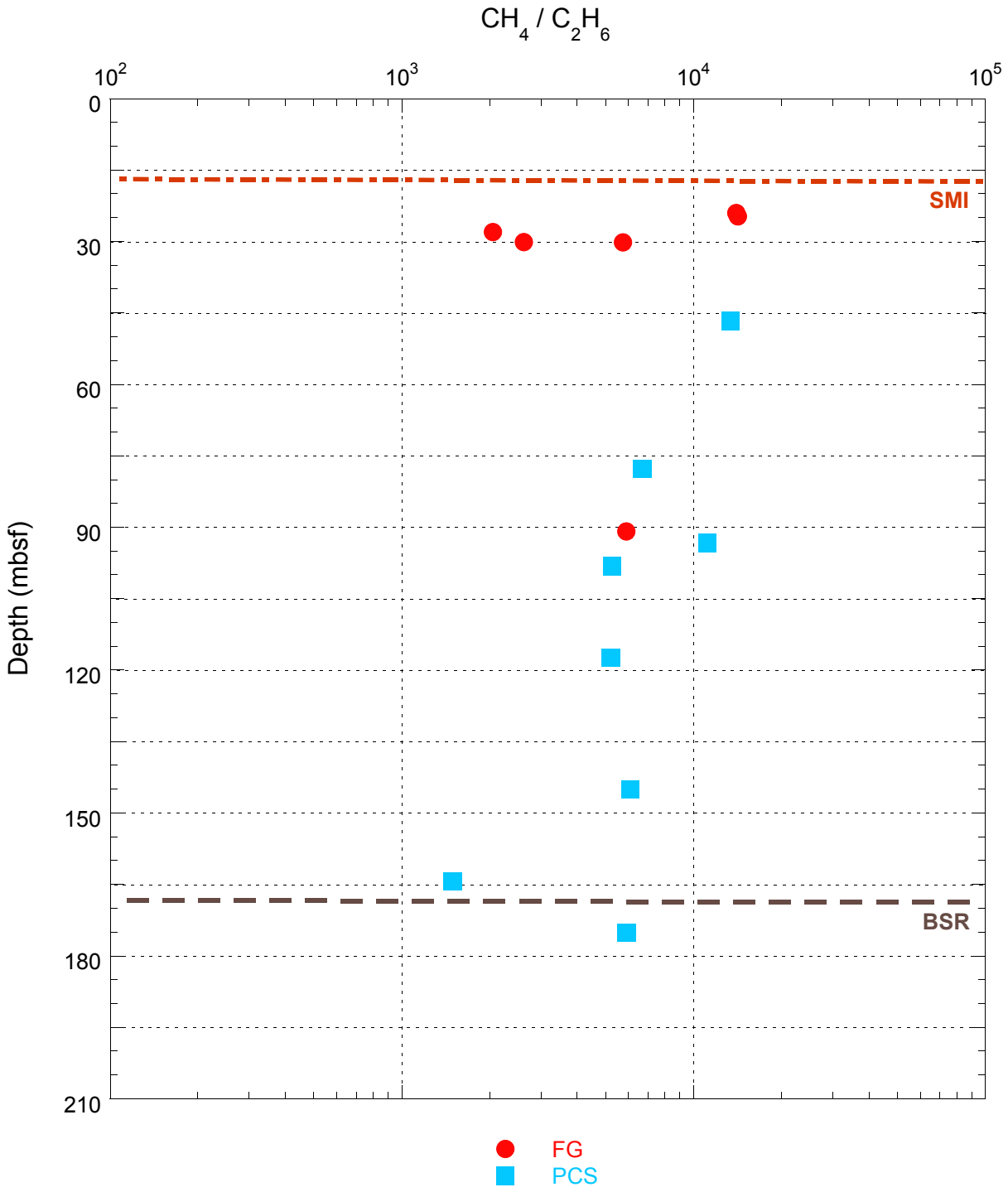


Figure 15. Plot of free gas and PCS gas methane to ethane ratio with depth for Sites NGHP-01-10 and NGHP-01-12. Note the apparent enrichment of ethane at ~30 mbsf and just above the BSR. [PCS, pressure core sampler; BSR, bottom-simulating reflector]

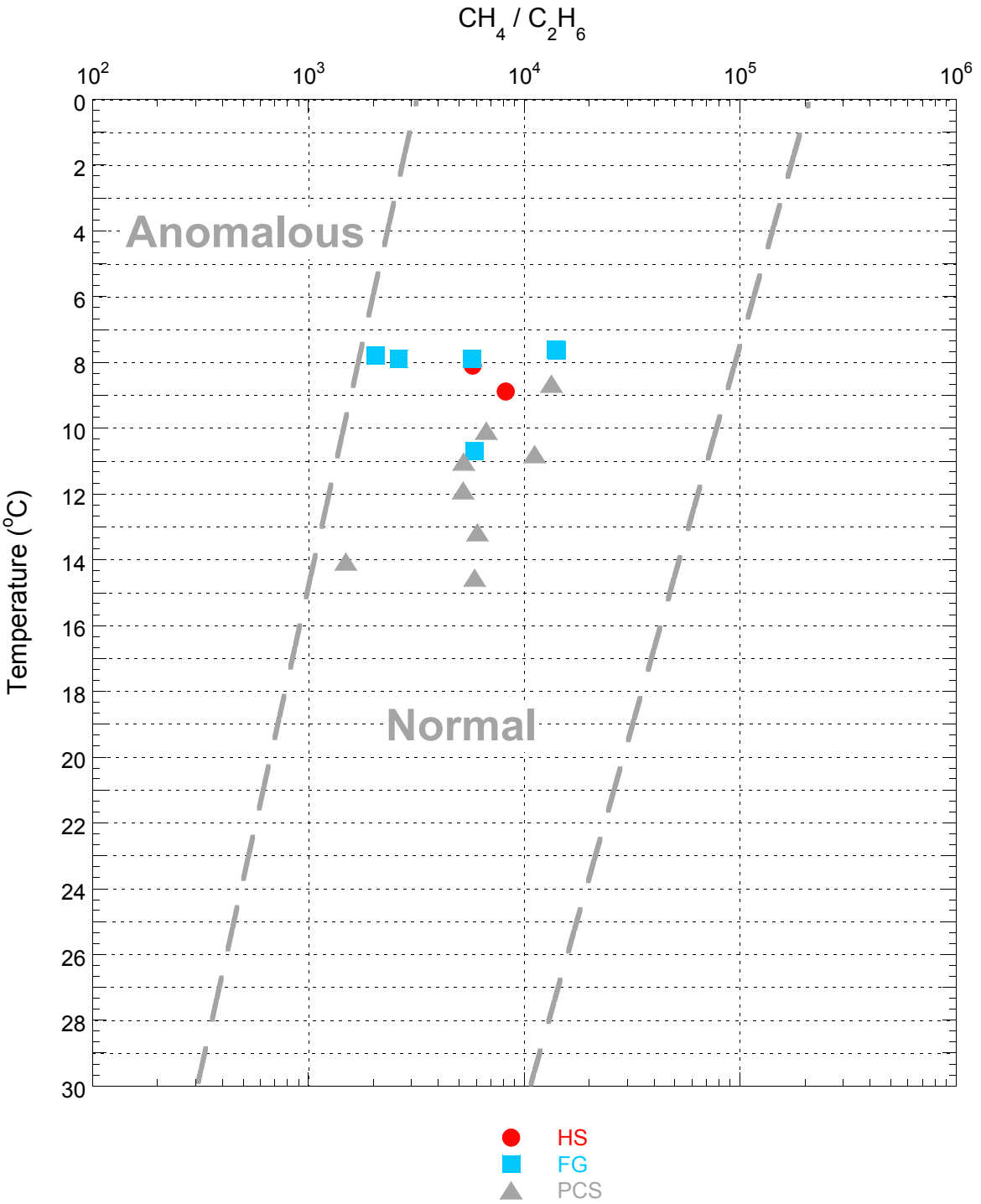


Figure 16. Plot of free gas and PCS gas methane to ethane ratio with temperature at increasing depths for Sites NGHP-01-10 and NGHP-01-12. Note the apparent enrichment of ethane leading to anomalous hydrocarbon occurrence, which may suggest that drilling hazards could be possible with depth near this site; however, levels trend toward "normal" with increasing depth/temperature. The elevated levels likely represent ethane enrichment due to gas hydrate. [PCS, Pressure Core Sampler]

Table 13. List of microbiological samples taken for Hole NGHP-01-10B.

Sample reference							Sample reference						
Core, section	Sample code	Top (cm)	Bottom (cm)	Depth (mbsf)	Volume (cc)	Comments	Core, section	Sample code	Top (cm)	Bottom (cm)	Depth (mbsf)	Volume (cc)	Comments
NGHP-01-10B													
2H-4	CEL	120	125	8.8	5		17X-2	JUD	110	120	111.4	374	
4X-1	CEL	145	150	23.45	5		23X-1	JUD	110	120	143.2	374	
10X-1	CEL	27	32	60.87	5		23X-2	JUD	130	140	144.9	374	
12X-3	CEL	92	97	72.64	5		26X-1	JUD	110	120	167.6	374	
14X-2	CEL	0	5	91.3	5		29X-3	JUD	110	120	180.2	374	
14X-2	CEL	68	72	91.98	5		4X-3	MAF	92	102	25.92	337	
17X-1	CEL	95	100	109.75	5		7X-1	MAF	9	18	41.89	337	
17X-4	CEL	89	94	114.19	5		9X-1	MAF	10	20	51.3	374	
18Y-1	CEL	60	65	118	5		10X-1	MAF	72	82	61.32	374	
19X-1	CEL	10	15	118.5	5		12X-2	MAF	10	20	71.27	374	
20X-1	CEL	40	45	128.4	5		14X-1	MAF	60	70	90.4	374	
23X-2	CEL	100	105	144.6	5		14X-2	MAF	87	104	92.17	636	
26X-1	CEL	70	75	167.2	5		17X-1	MAF	80	90	109.6	374	
29X-3	CEL	70	75	179.8	187		23X-3	MAF	38	48	145.48	374	
30X-1	CEL	28	33	185.98	5		4X-3	MAG	102	112	26.02	299	
2H-4	JAN	130	140	8.9	374		7X-1	MAG	18	27	41.98	299	
7X-1	JAN	27	28	42.07	10		9X-1	MAG	20	30	51.4	374	
9X-1	JAN	0	1	51.2	37		10X-1	MAG	82	91	61.42	374	
10X-1	JAN	91	92	61.51	37		12X-2	MAG	20	30	71.37	374	
12X-2	JAN	40	43	71.57	112		14X-1	MAG	70	79	90.5	337	
14X-1	JAN	79	80	90.59	37		14X-2	MAG	72	87	92.02	561	
14X-1	JAN	110	120	90.9	374		17X-1	MAG	90	100	109.7	374	
14X-2	JAN	104	105	92.34	37		23X-3	MAG	48	56	145.58	299	
15P-1	JAN	69	79	98.89	374		4X-3	MAR	82	92	25.82	337	
17X-4	JAN	99	109	114.29	374		7X-1	MAR	0	9	41.8	337	
18Y-1	JAN	45	47	117.85	75		9X-1	MAR	1	10	51.21	374	
21Y-1	JAN	23	28	136.83	187		10X-1	MAR	62	72	61.22	374	
23X-2	JAN	110	120	144.7	374		12X-2	MAR	0	10	71.17	374	
23X-3	JAN	56	58	145.66	75		14X-1	MAR	50	60	90.3	374	
26X-1	JAN	75	85	167.25	374		17X-1	MAR	70	80	109.5	374	
28P-2	JAN	48	60	175.96	449		23X-3	MAR	28	38	145.38	374	
29X-3	JAN	90	100	180	374		2H-4	SPH	125	130	8.85	187	
1H-1	JUD	120	130	1.2	374		10X-1	SPH	32	37	60.92	187	
2H-1	JUD	120	130	4.3	374		12X-3	SPH	87	97	72.59	374	
2H-3	JUD	120	130	7.3	374		14X-2	SPH	105	110	92.35	187	
2H-5	JUD	120	130	10.3	374		17X-4	SPH	94	99	114.24	187	
4X-2	JUD	110	120	24.6	374		19X-1	SPH	0	10	118.4	374	
10X-2	JUD	71	81	62.23	374		23X-2	SPH	105	110	144.65	187	
12X-3	JUD	107	117	72.79	374		26X-1	SPH	85	90	167.35	187	
14X-1	JUD	140	150	91.2	374		29X-3	SPH	75	80	179.85	187	

Table 14. List of microbiological samples taken for Hole NGHP-01-10D.

Sample reference							
Core, section	Sample code	Section	Top (cm)	Bottom (cm)	Depth (mbsf)	Volume (cc)	Comments
NGHP-01-10D							
1H-3	CEL	3	33	38	3.33	5	
2H-4	CEL	4	120	125	9.5	5	
3H-4	CEL	4	60	65	18.7	5	
4H-5	CEL	5	65	70	28.7	5	
5X-2	CEL	2	0	5	34.07	5	
7X-4	CEL	4	63	68	45.36	5	
10X-2	CEL	2	35	40	61.37	5	
10X-4	CEL	4	75	80	63.77	5	
13X-1	CEL	1	25	30	79.05	5	
14X-4	CEL	4	104	109	92.91	5	
16X-4	CEL	4	32	37	102.61	5	
17X-4	CEL	4	100	105	112.95	5	
18X-4	CEL	4	70	75	121.92	5	
20X-3	CEL	3	120	125	130.23	5	
23X-4	CEL	4	70	75	150.82	5	
24X-4	CEL	4	30	35	159.8	5	
27X-4	CEL	4	60	65	180.1	5	
28X-3	CEL	3	60	65	188.2	5	
29X-3	CEL	3	60	65	197.8	5	
1H-3	JAN	3	43	53	3.43	374	
2H-4	JAN	4	130	140	9.6	374	
3H-4	JAN	4	90	100	19	374	MBIO anomaly (freezer)
4H-4	JAN	4	7	17	27.45	374	
5X-4	JAN	4	90	100	35.98	374	
6P-1	JAN	1	0	7	40.1	262	MBIO anomaly (freezer)
7X-3	JAN	3	49	50	44.52	37	MBIO anomaly (grainsize)
7X-4	JAN	4	73	83	45.46	374	
10X-2	JAN	2	45	55	61.47	374	
10X-3	JAN	3	49	50	62.66	37	MBIO anomaly (grainsize)
14X-1	JAN	1	69	70	89.09	37	MBIO anomaly (reefer)
14X-4	JAN	4	114	124	93.01	374	
16X-4	JAN	4	42	52	102.71	374	
17X-4	JAN	4	130	140	113.25	374	MBIO anomaly (reefer)
18X-4	JAN	4	130	140	122.52	374	
20X-3	JAN	3	130	140	130.33	374	MBIO background (freezer)
23X-4	JAN	4	90	100	151.02	374	MBIO background (grainsize)
24X-4	JAN	4	50	60	160	374	MBIO background (reefer)
27X-4	JAN	4	80	90	180.3	374	
28X-3	JAN	3	80	90	188.4	374	
29X-3	JAN	3	80	90	198	374	
1H-1	JUD	1	120	130	1.2	374	
1H-3	JUD	3	63	73	3.63	374	
2H-1	JUD	1	90	100	5	374	
2H-3	JUD	3	120	130	8	374	
2H-5	JUD	5	120	130	11	374	
2H-7	JUD	7	62	72	13.42	374	
3H-2	JUD	2	120	130	16.3	374	
3H-4	JUD	4	120	130	19.3	374	
3H-6	JUD	6	120	130	22.3	374	
4H-2	JUD	2	115	125	25.75	374	
4H-4	JUD	4	37	47	27.75	374	
4H-6	JUD	6	120	130	30.35	374	
5X-2	JUD	2	25	35	34.32	374	

Table 14. List of microbiological samples taken for Hole NGHP-01-10D.—Continued

Sample reference							
Core, section	Sample code	Section	Top (cm)	Bottom (cm)	Depth (mbsf)	Volume (cc)	Comments
NGHP-01-10D—Continued							
5X-5	JUD	5	85	95	36.93	374	
7X-2	JUD	2	88	98	43.48	374	
8X-2	JUD	2	44	54	52.44	374	
10X-2	JUD	2	75	85	61.77	374	
13X-1	JUD	1	50	60	79.3	374	
14X-2	JUD	2	110	120	90.2	374	
14X-5	JUD	5	52	62	93.89	374	
16X-2	JUD	2	70	80	100.2	374	
16X-5	JUD	5	30	40	103.41	374	
17X-2	JUD	2	95	105	110.05	374	
17X-5	JUD	5	57	67	114.02	374	
18X-2	JUD	2	110	120	119.5	374	Taken only from working half
18X-4	JUD	4	90	100	122.12	374	
20X-2	JUD	2	73	83	128.53	374	
20X-4	JUD	4	40	50	130.93	374	
23X-4	JUD	4	110	120	151.22	374	
24X-4	JUD	4	70	80	160.2	374	
27X-4	JUD	4	100	110	180.5	374	
28X-3	JUD	3	100	110	188.6	374	
29X-3	JUD	3	100	110	198.2	374	
4H-5	MAF	5	90	100	28.95	374	MBIO HYD
7X-3	MAF	3	30	40	44.33	374	MBIO HYD
10X-3	MAF	3	30	40	62.47	374	MBIO
14X-1	MAF	1	50	60	88.9	374	MBIO HYD
4H-5	MAG	5	100	110	29.05	374	
7X-3	MAG	3	40	49	44.43	337	
10X-3	MAG	3	40	49	62.57	337	Liner length = 17 cm, sample length = 10 cm
14X-1	MAG	1	60	69	89	374	MBIO HYD
4H-5	MAR	5	80	90	28.85	374	
7X-3	MAR	3	20	30	44.23	374	MBIO HYD
10X-3	MAR	3	20	30	62.37	374	MBIO HYD
14X-1	MAR	1	40	50	88.8	374	MBIO
4H-1	MBF	1	123	136	24.33	486	
4H-1	MBG	1	136	150	24.46	523	
4H-1	MBR	1	110	123	24.2	486	Liner length = 15 cm, sample length = 10 cm
1H-3	SPH	3	38	43	3.38	187	MBIO HYD
2H-4	SPH	4	125	130	9.55	187	
3H-4	SPH	4	65	70	18.75	187	MBIO HYD
4H-4	SPH	4	0	7	27.38	262	MBIO HYD
5X-4	SPH	4	85	90	35.93	187	MBIO
7X-4	SPH	4	68	73	45.41	187	MBIO HYD
10X-2	SPH	2	40	45	61.42	187	
14X-4	SPH	4	109	114	92.96	187	
16X-4	SPH	4	37	42	102.66	187	MBIO HYD
17X-4	SPH	4	125	130	113.2	187	
18X-4	SPH	4	75	80	121.97	187	
20X-3	SPH	3	125	130	130.28	187	
23X-4	SPH	4	75	80	150.87	187	
24X-4	SPH	4	35	40	159.85	187	
27X-4	SPH	4	65	70	180.15	187	
28X-3	SPH	3	65	70	188.25	187	
29X-3	SPH	3	65	70	197.85	187	

Physical Properties

The physical properties program at Sites NGHP-01-10 and NGHP-01-12 used infrared (IR) imaging of whole-round cores on the catwalk to find temperature anomalies on the surface of core liners and facilitate the removal of sediment sections for gas hydrate preservation and study. Nondestructive measurements were conducted on temperature-equilibrated whole-round core sections with the MSCL. Thermal conductivity measurements were also conducted on whole-round cores. Various tests were performed on split cores including: electrical resistivity by use of a Wenner array, *P*-wave velocity by an inserted spade, and shear strength by mini-vane, Torvane, and Pocket Penetrometer. Core subsamples were placed in 10-mL beakers and dried at 105 °C to determine water content. Subsequently, the dried samples were analyzed for grain density using gas pycnometers and other index properties were then calculated. See "Physical Properties" in the "Methods" chapter for more details.

Holes NGHP-01-10B and NGHP-01-10D were drilled in the Krishna-Godavari Basin (~36 km off the eastern coast of India) in about 1040 m of water and were continuously cored to 204.9 and 203.8 mbsf respectively. However, because of gas hydrate dissociation, core recovery was only 27.1 and 62.5 percent at the two holes. Hole NGHP-01-10D is emphasized in the description of physical properties because of the greater core recovery. Site NGHP-01-12A, located only 0.5 km away, was spot cored to 150.9 mbsf.

The dissociation of gas hydrate adversely affects the physical properties of host sediment and the presence of gas hydrate was confirmed at NGHP-01-10 by (a) visual observations of gas hydrate in whole-round cores on the catwalk, (b) X-ray imaging of recovered cores at *in situ* pressure (see "Pressure Coring"), (c) numerous temperature anomalies in the IR record, and (d) soupy and moussey sediment sections observed in split cores. The gas hydrate was disseminated in the pore space, and also was present as nodules, lenses, and veins that apparently formed within the sediment matrix (see "Pressure Coring"). Since sand was not found in any appreciable amount, the gas hydrate is not related to the presence of coarse-grained sediment at this site.

Infrared Imaging

Environmental Conditions

Catwalk environment was monitored during the entire drilling operation at Sites NGHP-01-10 and NGHP-01-12. Temperature on the catwalk averaged about 30 °C, with interval temperature swings from 27 to 33 °C during the drilling operation (fig. 17). Average relative humidity of 80 percent was typical and ranged from 62 to 96 percent (fig. 17), consistent with a marine environment setting in the Indian Ocean. No adverse environmental conditions such as thunderstorms, rough seas, lightning, or high winds, persisted during drilling operations at this site.

Infrared Images

All APC and XCB cores from Sites NGHP-01-10 and NGHP-01-12 were systematically scanned upon arrival on the catwalk using the track-mounted IR camera described in the "Physical Properties" of the "Methods" chapter. IR anomalies, commonly referred to as "cold spots," may be indicative of gas hydrate dissociation during core recovery, which subsequently provides guidance to catwalk sampling. Summary digital maps of the scans of all cores are available on the data DVD that accompanies this report and listings of the image files are presented in tables 15, 16, 17, 18, 19, 20, and 21. Temperature arrays in text-formatted files (comma separated value or CSV) were exported from the IR camera software and then concatenated for each core. The arrays were then further concatenated for all cores available in a given borehole. Downcore temperatures were averaged for each pixel row in the array, excluding pixels ~1 cm from the edge of the image and 2 cm along the midline of the image. Exclusion of these particular pixels minimized the effects caused by major thermal artifacts in the images. This processing enabled us to measure the average amplitude of the cold anomalies and separate warm anomalies due to voids from the background temperature field.

IR track imaging at Site NGHP-01-10B consisted of 12 scans for a total scanned core length of 55.3 m. The complete set of IR images collected for Hole NGHP-01-10B is presented in figure 18 along with the corresponding downcore temperatures. The median core temperature extracted from the IR images for Hole NGHP-01-10B ranged from a high of 28.3 °C (Core NGHP-01-10B-09X, 51.2 mbsf), corresponding to a large amount of void spaces in the core liner, to a low of 14.8 °C (Core NGHP-01-10B-14X, 89.8 mbsf). The lowest core temperature (11.5 °C) measured on the IR imaging track for the 12 cores from Hole NGHP-01-10B examined was in Core NGHP-01-10B-14H (89.8 mbsf). As shown in figure 18, the shallowest gas-hydrate-bearing sediment appeared in Core NGHP-01-10B-07X, at an approximate depth of 41.8 mbsf. Gas-hydrate-bearing sediments appeared in all subsequent cores down through Core NGHP-01-10B-17X (108.9 mbsf). The higher temperature cored interval at 51.1 mbsf (Core NGHP-01-10B-9X), contained large void spaces, thus producing an IR response much warmer than the actual sediment.

A single infrared track image was collected from Hole NGHP-01-10C measuring 7.7 m in length at 23.1 mbsf. Gas hydrate was identified from Core NGHP-01-10C-01X starting in section six and continuing to the end of the core. The most abundant gas hydrate area positioned at the top of section six (30.19 mbsf), which also produced the coldest temperature response for Hole NGHP-01-10C (10.2 °C).

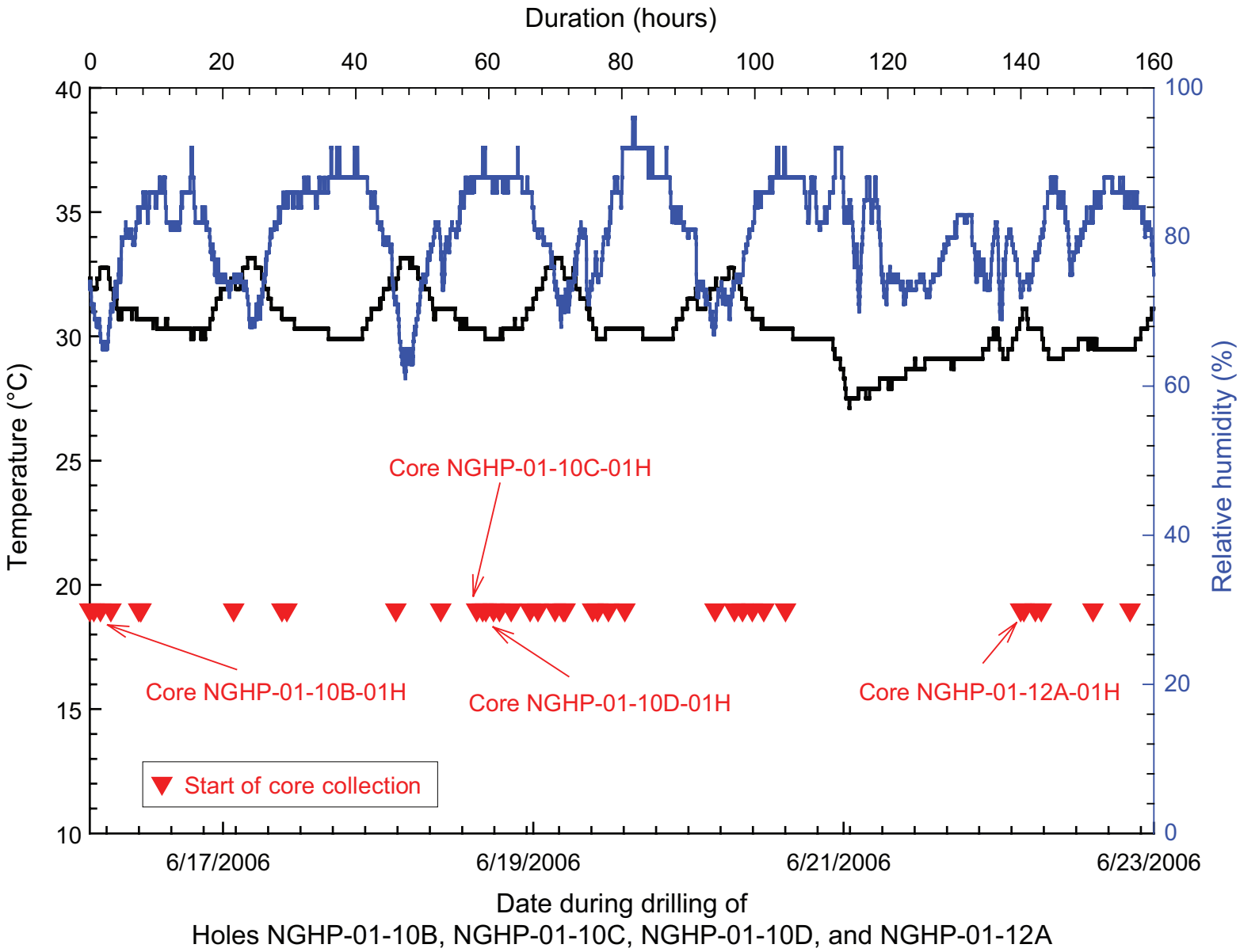


Figure 17. Catwalk temperature and humidity measurements as a function of time during drilling operations at Site NGHP-01-10.

Table 15. List of infrared image files collected from Hole NGHP-01-10B.

Core	Imaging length (cm)	First run	Date	Start time	Temperature (start/end) (°C)	File ID	Comments
1H	290	x	6/16	3:23	29.9/29.9	NGHP-10-B-1	15–25 °C
2H	970	x	6/16	4:00	29.9/29.9	NGHP-10-B-2	15–30 °C
4H	440	x	6/16	6:35	30.3/30.3	NGHP-10-B-4	15–30 °C
7X	150	x	6/16	11:05	32.4/32.4	NGHP-10-B-7	15–30 °C
9X	950	x	6/16	11:02	32.8/32.8	NGHP-10-B-9	15–30 °C
10X	230	x	6/16	17:00	32.9/32.9	NGHP-10-B-10	15–30 °C
12X	950	x	6/16	22:46	30.7/30.7	NGHP-10-B-12	15–30 °C
14X	325	x	6/17	1:02	30.3/30.3	NGHP-10-B-14	15–30 °C
17X	800	x	6/17	8:17	31.5/31.5	NGHP-10-B-17	15–30 °C
23X	360	x	6/17	21:02	30.3/30.3	NGHP-10-B-23	15–30 °C
26X	270	x	6/18	1:25	30.3/30.3	NGHP-10-B-26	15–30 °C
29X	590	x	6/18	8:10	31.9/31.9	NGHP-10-B-29	15–30 °C

*Temperature range for images displayed during core collection.

Table 16. List of infrared image files collected from Hole NGHP-01-10C.

Core	Imaging length (cm)	First run	Date	Start time	Temperature (start/end) (°C)	File ID	Comments*
1H	770	x	6/18	13:34	33.2/33.2	NGHP-10-C-1	15–30 °C

*Temperature range for images displayed during core collection.

Table 17. List of infrared image files collected from Hole NGHP-01-10D.

Core	Imaging length (cm)	First run	Date	Start time	Temperature (start/end) (°C)	File ID	Comments*
1H	390	x	6/18	14:28	32.8/32.8	NGHP_10_D_1	15–25 °C
2H	770	x	6/18	14:58	32.8/32.8	NGHP_10_D_2	15–30 °C
3H	950	x	6/18	16:07	32.0/32.0	NGHP_10_D_3	15–30 °C
4H	970	x	6/18	17:00	32.0/31.5	NGHP_10_D_4	15–30 °C
5X	950	x	6/18	18:45	31.1/31.1	NGHP_10_D_5	15–30 °C
7X	590	x	6/18	21:36	30.7/30.3	NGHP_10_D_7	15–30 °C
8X	230	x	6/18	22:48	30.7/30.3	NGHP_10_D_8	15–30 °C
10X	950	x	6/19	2:52	29.9/29.9	NGHP_10_D_10	15–30 °C
13X	100	x	6/19	7:45	30.7/30.2	NGHP_10_D_13	15–30 °C
14X	850	x	6/19	9:23	31.5/31.5	NGHP_10_D_14	15–30 °C
16X	610	x	6/19	11:51	32.8/32.8	NGHP_10_D_16	15–30 °C
17X	680	x	6/19	13:21	33.2/33.2	NGHP_10_D_17	15–30 °C
18X	750	x	6/19	14:36	32.2/32.4	NGHP_10_D_18	15–30 °C
20X	710	x	6/19	19:00	29.9/29.9	NGHP_10_D_20	15–30 °C
23X	770	x	6/20	12:00	30.3/30.3	NGHP_10_D_23	15–30 °C
24X	750	x	6/20	1:25	30.3/30.3	NGHP_10_D_24	15–30 °C
26X	180	x	6/20	4:20	29.9/29.9	NGHP_10_D_26	15–30 °C
27X	670	x	6/20	5:33	29.9/29.9	NGHP_10_D_27	15–30 °C
28X	570	x	6/20	7:00	30.3/30.3	NGHP_10_D_28	15–30 °C
29X	520	x	6/20	8:44	31.1/31.1	NGHP_10_D_29	15–30 °C

*Temperature range for images displayed during core collection.

Table 18. List of infrared image files collected from Hole NGHP-01-12A.

Core	Imaging length (cm)	First run	Date	Start time	Temperature (start/end) (˚C)	File ID	Comments
1	520	x	6/21	23:22	29.1/29.1	NGHP_12_A_1	15–30 °C
2	950	x	6/21	23:50	29.1/29.1	NGHP_12_A_2	15–30 °C
3	970	x	6/22	1:35	29.1/29.1	NGHP_12_A_3	15–30 °C
4	590	x	6/22	2:29	29.1/29.1	NGHP_12_A_4	15–30 °C
8	790	x	6/22	10:15	29.1/29.1	NGHP_12_A_8	15–30 °C
12	550	x	6/22	15:49	29.9/29.5	NGHP_12_A_12	15–30 °C
13	430	x	6/22	20:13	29.5/29.5	NGHP_12_A_13	15–30 °C

*Temperature range for images displayed during core collection.

Table 19. List of infrared section-end image files from Hole NGHP-01-10B.

Core	Section	Top	Date	Time	Image #	File ID	Comments
4			6/16	7:20	1	G06161	Extracted sediment
4			6/16	7:20	2	G06162	Extracted sediment
7	1		6/16	11:00	3	G06163	Extracted sediment
7	1		6/16	11:00	4	G06164	Extracted sediment
7	5		6/16	11:17	5	G06165	Extracted sediment
7	5		6/16	11:17	6	G06166	Extracted sediment
7	5		6/16	11:17	7	G06167	Extracted sediment
7	5		6/16	11:17	8	G06168	Extracted sediment
9	5		6/16	14:37	9	G06169	Extracted sediment
9	5		6/16	14:37	10	G061610	Extracted sediment
9	5		6/16	14:37	11	G061611	Extracted sediment
9	5		6/16	14:37	12	G061612	Extracted sediment
9	5		6/16	14:38	13	G061613	Extracted sediment
9	5		6/16	14:38	14	G061614	Extracted sediment
10	5		6/16	17:02	15	G061615	Extracted sediment
10	5		6/16	17:02	16	G061616	Extracted sediment
10	5		6/16	17:03	17	G061617	Extracted sediment
10	5		6/16	17:03	18	G061618	Extracted sediment
10	5		6/16	17:04	19	G061619	Extracted sediment
12	5		6/16	17:04	20	G061620	Extracted sediment
12	5	x	6/16	21:51	21	G061621	Core end
12	5	x	6/16	21:51	22	G061622	Core end
12	5		6/16	21:32	23	G061623	Extracted sediment
12	5		6/16	21:32	24	G061624	Extracted sediment
12	5		6/16	21:38	25	G061625	Extracted sediment
12	5		6/16	21:38	26	G061626	Extracted sediment
12	5		6/16	21:40	27	G061627	Extracted sediment
12	5		6/16	21:40	28	G061628	Extracted sediment
14	1		6/17	1:36	1	G06171	Extracted sediment
14	1		6/17	1:36	2	G06172	Extracted sediment
14	1		6/17	1:36	3	G06173	Extracted sediment
14	1		6/17	1:36	4	G06174	Extracted sediment
14	1		6/17	1:36	5	G06175	Extracted sediment
14	1		6/17	1:36	6	G06176	Extracted sediment
14	1		6/17	2:12	7	G06177	Extracted sediment
14	1		6/17	2:12	8	G06178	Extracted sediment
14	1		6/17	2:12	9	G06179	Extracted sediment
14	1		6/17	2:12	10	G061710	Extracted sediment
17	4	x	6/17	8:45	11	G061711	Core end
17	4	x	6/17	8:45	12	G061712	Core end
17	4		6/17	8:45	13	G061713	Extracted sediment
17	4		6/17	8:45	14	G061714	Extracted sediment
17	2		6/17	9:22	15	G061715	Extracted sediment
17	2		6/17	9:22	16	G061716	Extracted sediment
17	2		6/17	9:22	17	G061717	Extracted sediment
17	2		6/17	9:22	18	G061718	Extracted sediment

Table 20. List of infrared section-end image files from Hole NGHP-01-10D.

Core	Section	Top	Bottom	Date	Time	Image #	File ID	Comments
2	3		x	6/18	15:13	3	G06183	GO618; Core end image
2	3		x	6/18	15:13	4	G06184	Core end image
3	3		x	6/18	16:21	5	G06185	Core end image
3	3		x	6/18	16:21	6	G06186	Core end image
4	4		x	6/18	17:30	7	G06187	Core end image
4	4		x	6/18	17:30	8	G06188	Core end image
5	3		x	6/18	18:57	9	G06189	Core end image, 0–23 cm
5	3		x	6/18	18:57	10	G061810	Core end image, 0–23 cm
5	3	x		6/18	18:57	11	G061811	Core end image, 0–23 cm
5	3	x		6/18	18:57	12	G061812	Core end image, 0–23 cm
7	2			6/18	21:56	13	G061813	Extracted sediment
7	2			6/18	21:56	14	G061814	Extracted sediment
8				6/18	23:00	15	G061815	Extracted sediment
8				6/18	23:00	16	G061816	Extracted sediment
14				6/19	9:55	1	G06191	Extracted sediment
14				6/19	9:55	2	G06192	Extracted sediment
16	4			6/19	12:00	3	G06193	Core end image
16	4			6/19	12:00	4	G06194	Core end image
16	3			6/19	12:00	5	G06195	Core end image
16	3			6/19	12:00	6	G06196	Core end image
17	1			6/19	13:28	7	G06197	Core end image
17	1			6/19	13:28	8	G06198	Core end image
17	5			6/19	13:28	9	G06199	Core end image
17	5			6/19	13:28	10	G061910	Core end image
18	6		x	6/19	14:50	11	G061911	Core end image
18	6		x	6/19	14:50	12	G061912	Core end image
18	6		x	6/19	14:50	13	G061913	Core end image
18	6		x	6/19	14:50	14	G061914	Core end image
20	6	x		6/19	19:07	15	G061915	Core end image
20	6	x		6/19	19:07	16	G061916	Core end image
20	6		x	6/19	19:07	17	G061917	Core end image
20	6		x	6/19	19:07	18	G061918	Core end image
20	1		x	6/19	19:10	19	G061919	Core end image
20	1		x	6/19	19:10	20	G061920	Core end image

Table 21. List of infrared section-end image files from Hole NGHP-01-12A.

Core	Section	Top	Date	Time	Image #	File ID	Comments
1	2	x	6/21	11:26	1	GO621-01	Core end
1	2	x	6/21	11:26	2	GO621-02	Core end
2	2		6/21	11:59	3	GO621-03	Core end
2	2	x	6/21	11:59	4	GO621-04	Core end
12	2	x	6/22	15:59	1	GO622-01	Core end
12	5	x	6/22	15:59	2	GO622-02	Core end
12	5		6/22	15:59	3	GO622-03	Extracted sediment
12	5		6/22	15:59	4	GO622-04	Extracted sediment
12	5		6/22	15:59	5	GO622-05	Extracted sediment
12	5		6/22	15:59	6	GO622-06	Extracted sediment
13	2	x	6/22	20:35	7	GO622-07	Core end
13	2	x	6/22	20:35	8	GO622-08	Core end

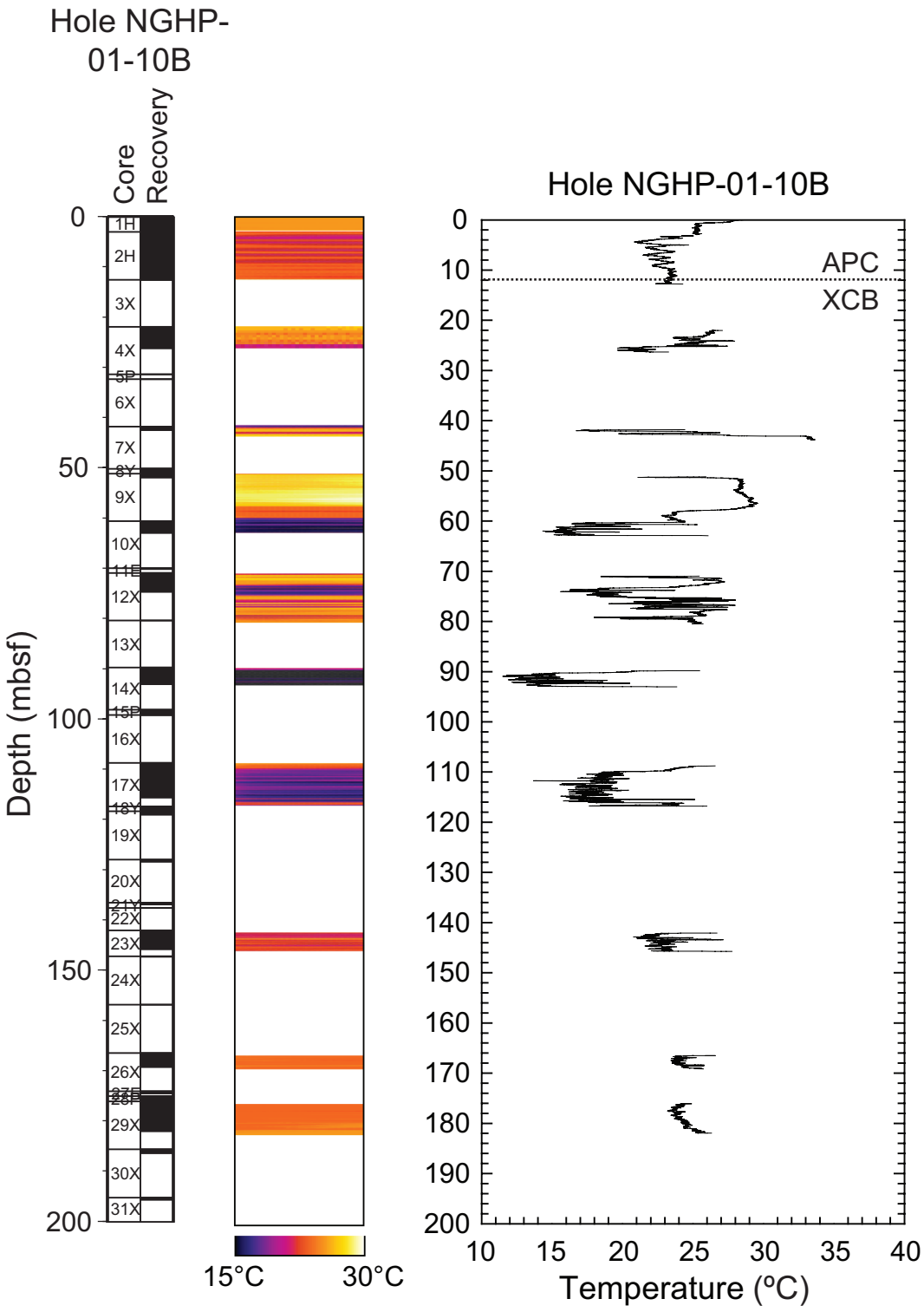


Figure 18. Infrared imaging and the derived downhole temperature profile for Hole NGHP-01-10B.

Infrared track imaging at Site NGHP-01-10D included twenty scans for a total combined scanned core length of 130 m. The complete set of IR images collected from Hole NGHP-01-10D is presented in figure 19 along with the corresponding downcore temperatures. Detailed examination of the IR imaging reveals close similarities to Hole NGHP-01-10B (fig. 18). Based on the IR track imaging for NGHP-01-10D (fig. 19), gas hydrate deposits were first detected in the lower section of Core NGHP-01-10D-07X (47 mbsf) and continuously detected through Core NGHP-01-10D-23X (146 mbsf). The minimum temperature recorded by the IR track for Hole NGHP-01-10C (11.5 °C) was in Core NGHP-01-10D-20X near the midpoint of Section 5 (132 mbsf).

Upon completion of activities at Site NGHP-01-10, the ship was moved to Site NGHP-01-12, where Hole NGHP01-12A was drilled. IR track images were collected on seven cores for a total imaging length of 42.5 m. Concatenated images for Hole NGHP-01-12A are shown in figure 20 with the digital temperature down-core readings. The minimum recorded IR temperature measured in Hole NGHP-01-12A was 17.2 °C, which was obtained from Core NGHP-01-12A-8. Only subtle IR anomalies were detected by the IR track imaging system in Hole NGHP-01-12A, for example at 98 mbsf. These anomalies may represent minor amounts of gas hydrate. Cold anomalies in the first 10 m below seafloor may represent intrusion of cold seawater into the cores.

Overall for Site NGHP-01-10, IR anomalies, typically used to identify gas hydrate dissociation or actual gas hydrate (in this case), were identified in seven of seven cores from NGHP-01-10B (-07X, -09X, -10X, -12X, -14X, -17X, and -23X) and numbered well over thirty. Cores NGHP-01-10B-10X and NGHP-01-10B-17X contained over half of the reported anomalies from this hole (Hole NGHP-01-10B). Although Hole NGHP-01-10C consisted of one cored interval (7.7 m), it contained five IR anomalies. Cores collected from Hole NGHP-01-10D represented the most cored interval at Site NGHP-01-10 and contained over forty identified IR anomalies. Cores from NGHP-01-10D containing gas hydrate anomalies included NGHP-01-10D-07X, -10X, -13X, -14X, -16X, -17X, -18X, -20X, and -23X. The bulk of the gas hydrate was observed in Core NGHP-01-10D-10X, and to a lesser extent Cores NGPH-01-10D-14X, -16X, and -20X.

Several cores from both boreholes (Cores NGHP-01-10B-10X and NGHP-01-10D-10X) contained meter-long sections of gas hydrate. For example, examination of the complete concatenated IR scanned images collected from Core NGHP-01-10D-10X reveals zones of continuous gas hydrate represented by dark colors in figure 21. Gas hydrate is almost continuous in the first 2.6 m of core as well as 5.4 m to 6.0 m and 7.6 m to the end. Once an IR anomaly is recorded, samples are immediately removed from that particular core section for interstitial pore water sampling. Often times after cutting the core into sections, large pieces of gas hydrate became visible. Select gas hydrate pieces were either processed in the chemical laboratory or immediately preserved in liquid nitrogen and one pressure vessel for shore-based characterization.

IR images of the ends of core sections were acquired with a hand-held IR camera on the catwalk during sampling activities when possible. Twenty-two core-end IR images were collected from Hole NGHP-01-10 and Hole NGHP-01-12, which are closely associated with coring activities at Hole NGHP-01-10D. Figure 22 shows a typical core-end IR image from Section NGHP-01-10D-18X-6 (bottom). The image has been processed and the calculated temperature profile with a scale ranging from 30° to –10 °C has been superimposed onto the IR image. The outside of the core end has a temperature of 22° to 23 °C and is evenly represented by the color red. The coldest portion of the core-end image is represented by the dark blue to black colors and can be seen as the dominant colors in the image. Notice that the inside temperature is approximately –1.3 °C for most of the interior section. The IR section end image represents alternating layers of sediment and gas hydrate.

In addition to the IR core-end images, a similar technique was used to identify cold anomalies in the sediment selected for interstitial water samples. Efforts were focused on Hole NGHP-01-10B where twenty-one such images were collected and analyzed. Sections were removed from the core and taken to the chemical laboratory for interstitial water sampling. After extracting the sediment from the liner, IR imaging with a hand held camera was used to identify gas hydrate or "cold spots" in the sediment and provide guidance for background sediment sampling. A typical IR image of extracted sediment from Core NGHP-01-10B-09X (fig. 23) shows extracted sediment with two distinct cold anomalies. Processing the image revealed the coldest temperature (dark blue) in the extracted sediment was –1 °C, clearly distinguishable from the nearby sediment, which measured as high as 20 °C. This technique was used extensively to determine which sediment contained gas hydrate or dissociated gas hydrate from background sediment.

Core-End Temperature Readings

Core-end temperature readings were taken on all cores immediately following the IR track imaging. Typically four temperature probes were inserted approximately 8 cm into the end of each core and allowed to remain there until the core was completely processed and removed from the catwalk. A summary of the core-end temperature results (center position only) for Holes NGHP-01-10B and NGPH01-10D are presented in figure 24. Core-end temperatures for Hole NGHP-01-10B ranged from 20.6° to –1.6 °C, with the lowest measurement occurring in Core NGHP-01-10B-14X. Due to the collection of more cored intervals at Hole NGHP-01-10D than at Hole NGHP-01-10B, more than twice as many core-end temperature measurements were collected (fig. 24). The temperature profile for Hole NGHP-01-10D is consistent with data collected from Hole NGHP-01-10B, with the coldest temperature recorded (–1.5 °C) at 60 mbsf (Core NGHP-01-10D-10X). Comparison of results from both boreholes to the IR imaging (figs. 18 and 19) show a strong correlation between the occurrence of gas hydrate and low core-end temperatures. Core-end temperatures for Site NGHP-01-12 (fig. 25) do not have low temperatures associated with the dissociation of large amounts of gas hydrate.

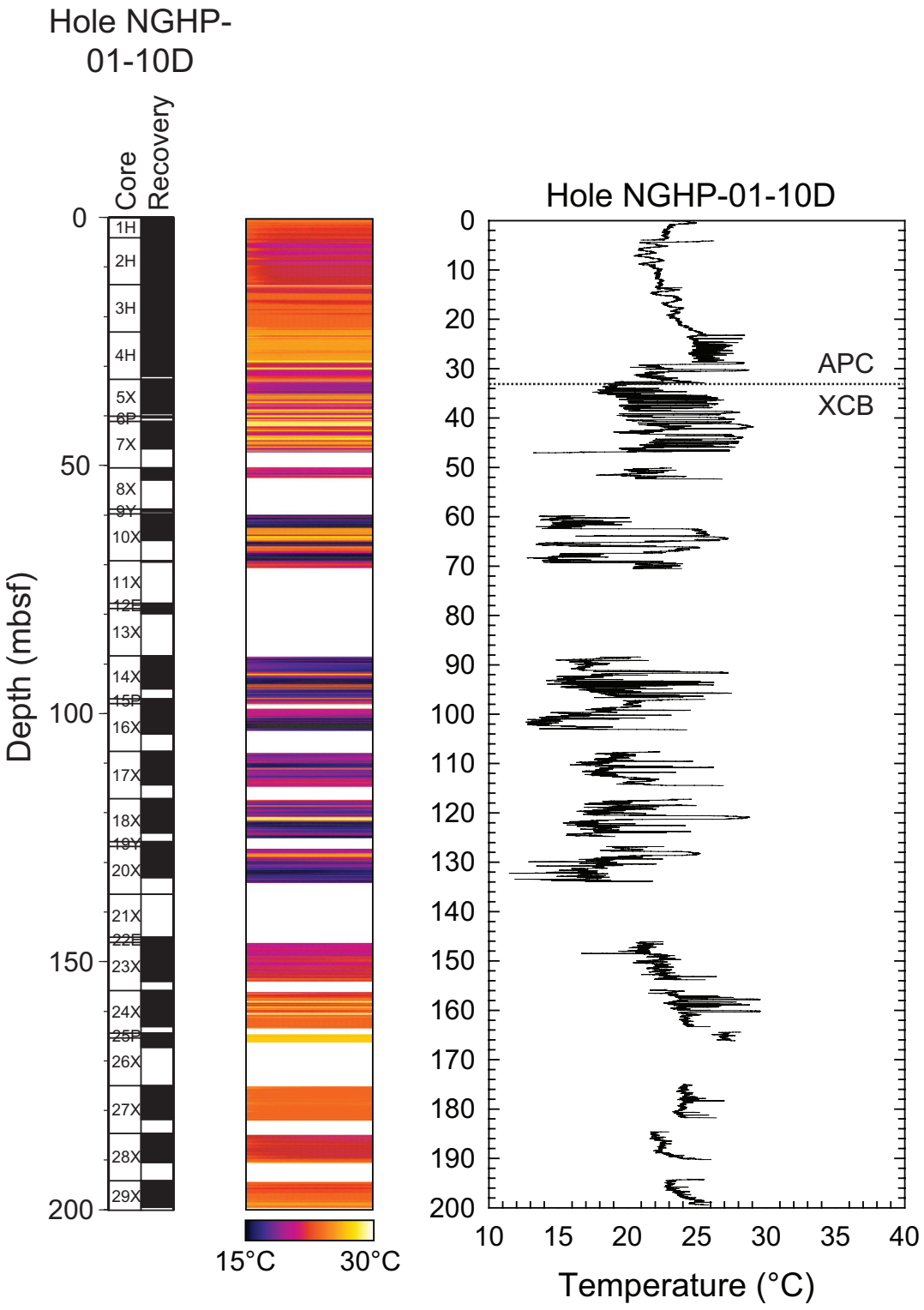


Figure 19. Infrared imaging and the derived downhole temperature profile for Hole NGHP-01-10D.

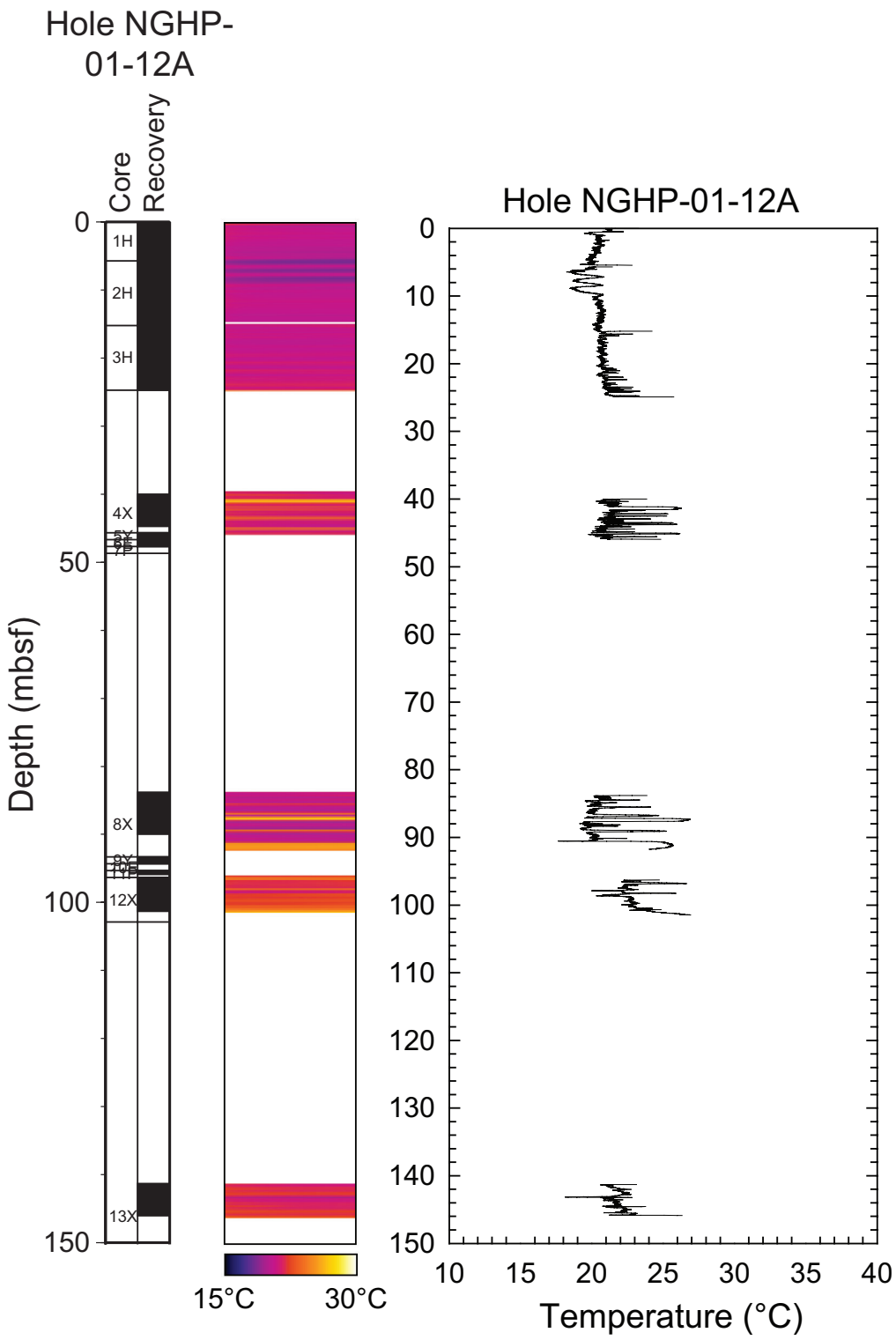


Figure 20. Infrared imaging and the derived downhole temperature profile for Hole NGHP-01-12A.

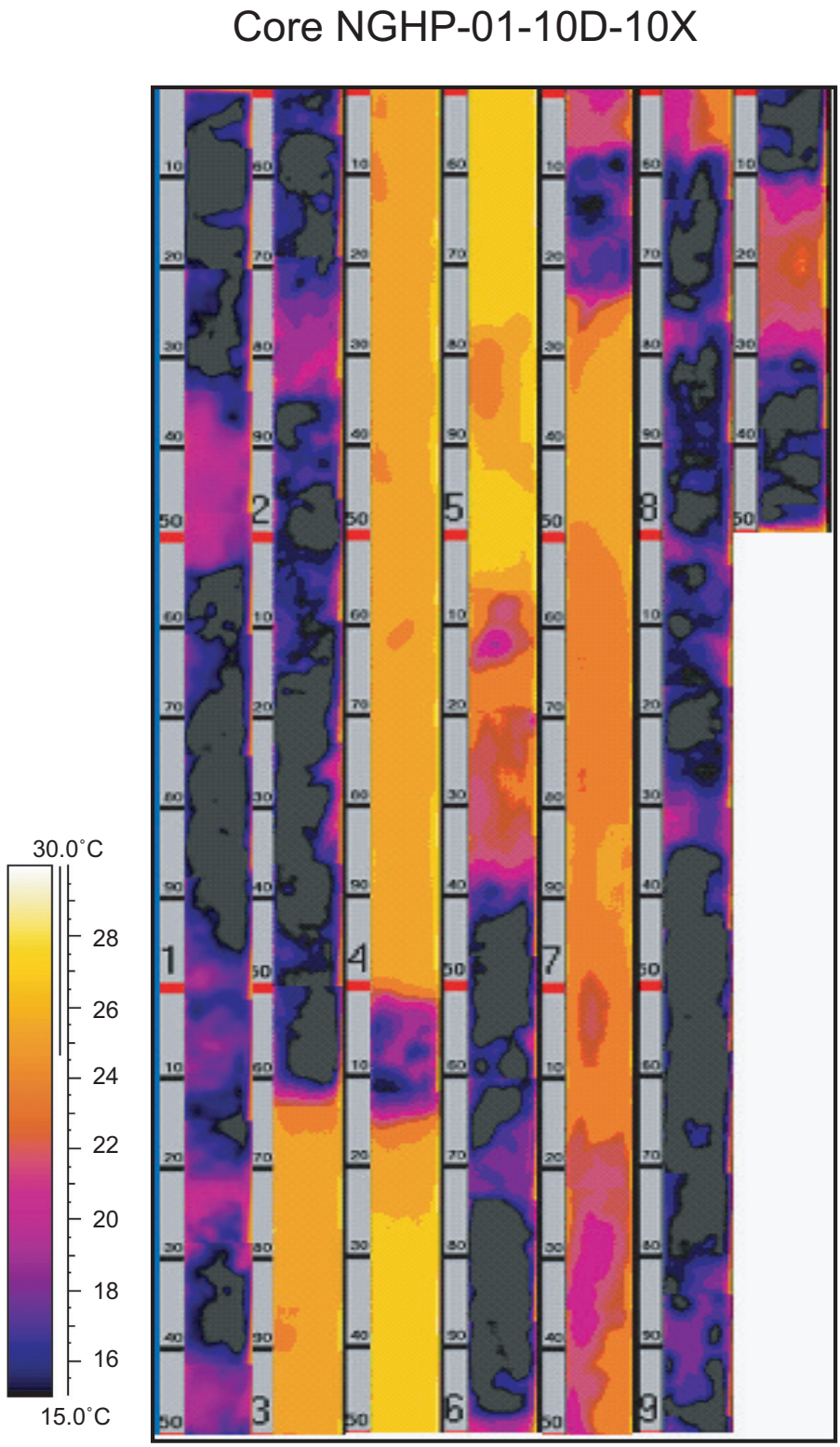


Figure 21. Infrared track image collected from Core NGHP-01-10D-10X with corresponding reference color temperature scale.

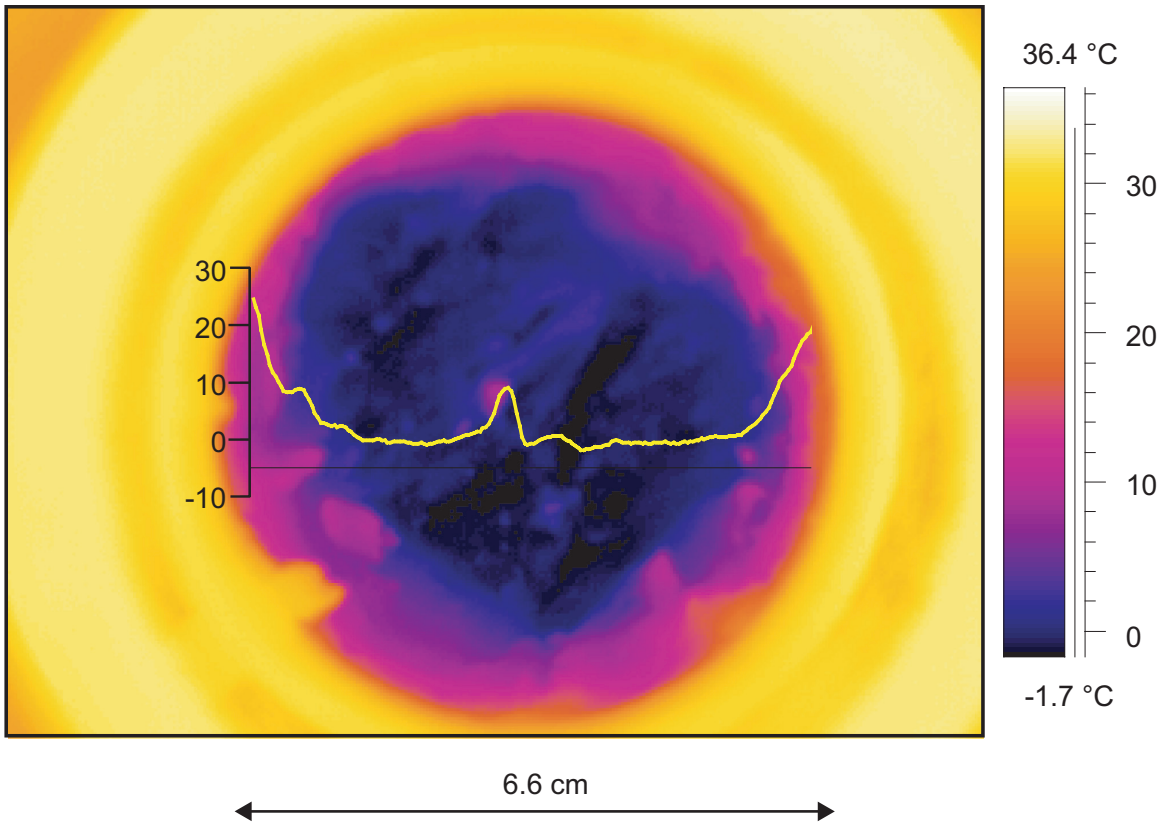


Figure 22. Core-end infrared image of Core NGHP-01-10D-18X-6, bottom, with the corresponding reference temperature scale.

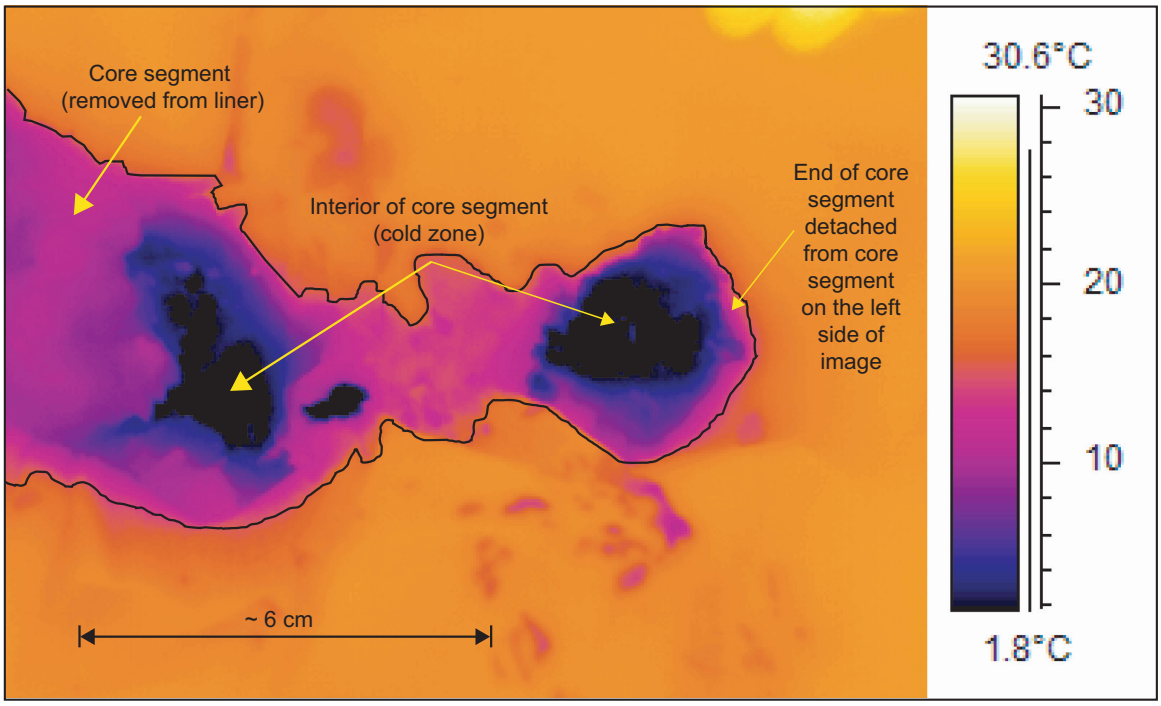


Figure 23. Infrared image of extracted sediment collected from Section NGHP-01-10B-09X-5, bottom, with the corresponding temperature scale.

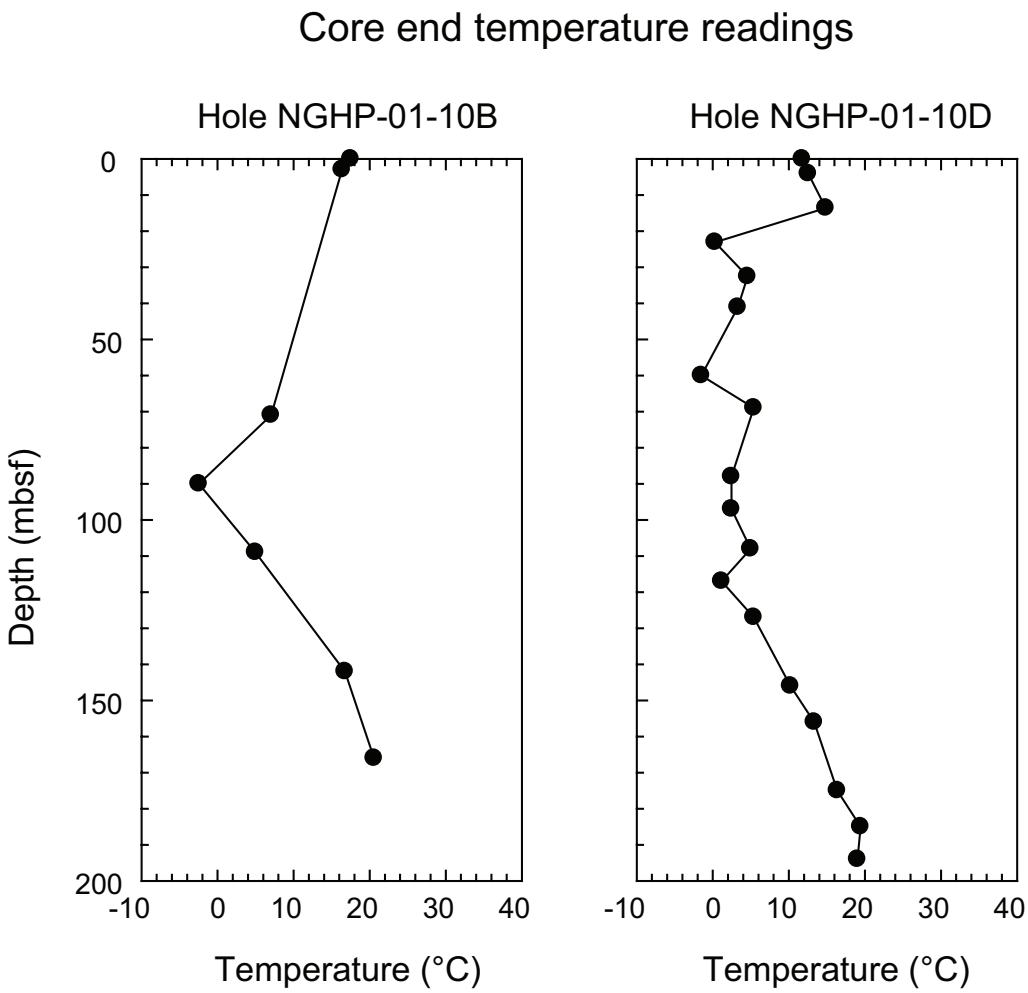


Figure 24. Core-end temperature profiles for Holes NGHP-01-10B and NGHP-01-10D.

Index Properties

Composite profiles of core recovery, measurements, and results from LWD, IR imaging, MSCL, MAD, and other programs are presented in figures 26, 27, 28, 29, 30, and 31. Water content (related to solids) varies from a high of 148 percent to a low of 39 percent, both in Hole NGHP-01-12A (table 22, figs. 26, 28, and 30). In each Hole (NGHP-01-10B, NGHP-01-10D, and NGHP-01-12A) water content rapidly decreases to subbottom depths of 8, 10, and 40 mbsf, respectively. Then water content decrease with depth becomes more gradual. One very high water content value is present in Hole NGHP-01-10D at a depth of 33 mbsf, but is probably a result of core disturbance at the APC – XCB boundary and hence may not reflect *in situ* conditions. Except for the upper 10 m of sediment, porosity determined from MAD samples decreases nearly linearly *downhole*. This trend is overall in close agreement with the porosity values determined from LWD data in Hole NGHP-01-10A except in the upper 20 m where borehole conditions prevented accurate *in situ* measurements. The LWD porosity values vary considerably immediately above and below the base of gas hydrate stability and limited physical property results support this trend. However, a comparison at that depth is hampered by poor core recovery. The dissociation of gas hydrate greatly influences the consistency of recovered cores. For example, water contents varied over a factor of two, from 102 to 49 percent, in PCS Core NGHP-01-10D-25P recovered from 165 mbsf in Hole NGHP-01-10D (table 22). Parts of the core that apparently contained gas hydrate exhibited classic soupy behavior, while nearby sediment was intact and less disturbed (see strength discussion below, this chapter). There is a change in slope of bulk density, LWD electrical resistivity, and thermal conductivity at the APC – XCB boundary located at about 32 mbsf in Hole NGHP-01-10D.

Bulk density from MAD, LWD, and MSCL measurements in Hole NGHP-01-10D all significantly decrease from above the APC–XCB boundary to the top of the gas hydrate zone about 50 mbsf where the trend reverses (fig. 28). Bulk density also varies considerably near the BSR at about 160 mbsf.

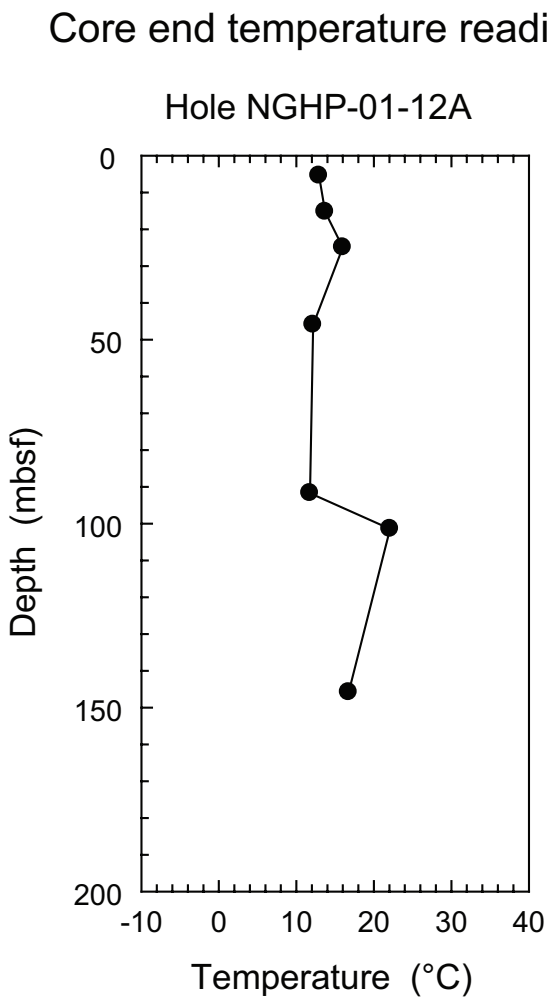


Figure 25. Core-end temperature profiles for Hole NGHP-01-12A.

Grain density varies from 2.44 to 2.86 g/cm^3 with an average value of 2.71. Some of this variation is a result of performing mass measurements at sea on small sediment samples after the water has been removed by drying. This result is most pronounced in the upper sections of the hole where water contents are highest. Grain densities are lower in the upper part of the hole, possibly the result of increased marine organic content (see "Lithostratigraphy"). The pycnometers often had difficulty measuring volume of samples from the top of the hole. Higher grain densities may be related to the presence of carbonate which has a slightly higher grain density (2.73 g/cm^3).

Strength

Shear strength increased nearly linearly with depth ~12 mbsf using three different methods (tables 23, 24, 25, and figs. 26, 28, and 30). Below that depth, great variation exists in a small data set, illustrating the effect of disturbance caused by rotary coring on sediment and in deeper cores, the pressure of huge amounts of gas hydrate. Although testing was to be restricted to intact biscuits, it was occasionally difficult to differentiate between intact biscuits and adjacent disturbed sediment.

The measured shear strengths were normalized to the effective vertical stress, σ'_v (fig. 28) to provide qualitative information on the stress history of the sediment. Similar plots for Holes NGHP-01-10B and NGHP-01-12A were not constructed because of the lack of adequate MAD data. The strength/effective vertical stress ranges from approximately 0.73 at the top of Hole NGHP-01-10D to 0.01 near the bottom of the hole. These values are in overall agreement with a number of other normally consolidated clays (Holtz and Kovacs, 1981), although the values below 0.1 probably represent the deeper subbottom depth from this hole compared to most engineering-type projects from which the comparison samples were taken. Hunt (1984) states that the strength/effective vertical stress ratio typically is between 0.4 and 0.16. The wide scatter in the results at the top of the hole reflect the dependency of this ratio on the stress path as well as the test method (Bjerrum, 1972; Ladd, and others, 1977). Because most of the values are below 0.4, the implication is that these sediments are depositional in nature and have not been overconsolidated by erosional or other geologic processes. The few higher strength/effective vertical stress values may be caused by pseudo-overconsolidation effects.

Although the peak (Sv) and remolded (Srem) vane shear strengths increase with subbottom depth, the sensitivity (St), which equals Sv/Srem, remained constant or decreased slightly with depth (fig. 32). Sensitivity values represent the amount of strength loss after remolding and in extreme examples can reach values of 500 (Lambe and Whitman,1969). Sensitivity values range from about 1 to 8, with values typically below 4. The classification typically used in the United States categorizes the clays as low to medium sensitive (Holtz and Kovacs, 1981). However, other classifications that are used in regions containing uplifted marine clays would only classify the sediment as low sensitivity (Holtz and Kovacs, 1981). High values of sensitivity are indicative of good quality core recovery because the sediment has not been highly disturbed.

Pressure cores provide a unique opportunity to study properties and structure of gas hydrate under *in situ*-like conditions. They also provide a mechanism for gradual degassing and dissociation of gas hydrate that may better preserve adjacent sediment than uncontrolled dissociation of APC and XCB cores. Fugro Pressure Core (FPC) NGHP-01-10B-18Y obtained in Hole NGHP-01-10B had a peak mini-vane shear strength of 31.5 kPa with a remolded strength of 5.4 kPa producing a sensitivity of 5.8 thereby indicating a core recovery of good quality. PCS Core NGHP-01-10D-25P from Hole NGHP-01-10D near the BSR contained gas hydrate and very wet, soft sediment at an interval of 41–43 cm with a Pocket Penetrometer (PP) strength of less than the detection limit of 12.3 kPa (fig. 33). Although an intact nearby sample at 83 cm had a PP strength of 24.5 kPa (fig. 34), this value is lower than most of the strengths determined from XCB cores.

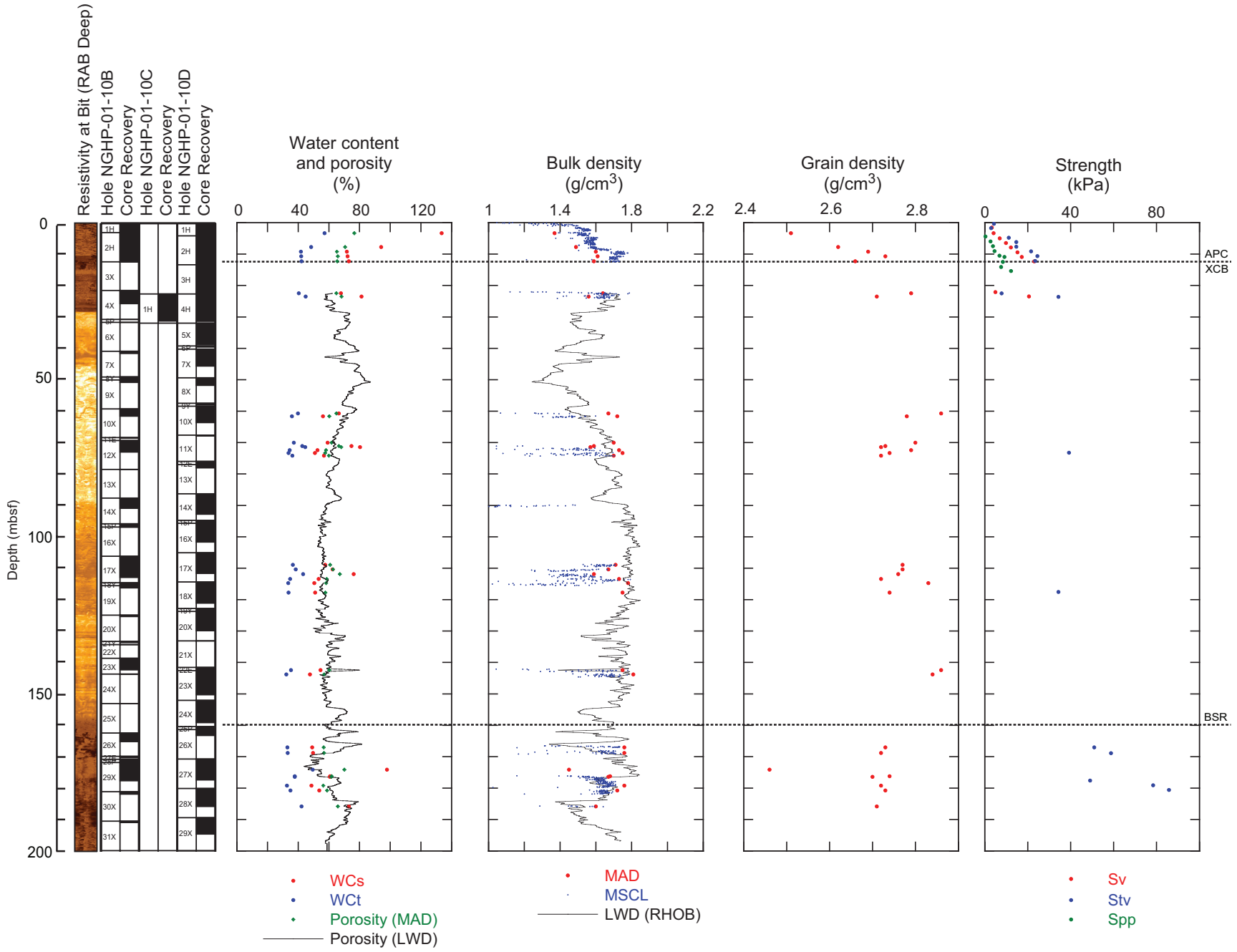


Figure 26. Profiles of LWD Resistivity-At-Bit, core recovery, index, and strength properties for Hole NGHP-01-10B. [LWD, logging-while-drilling]

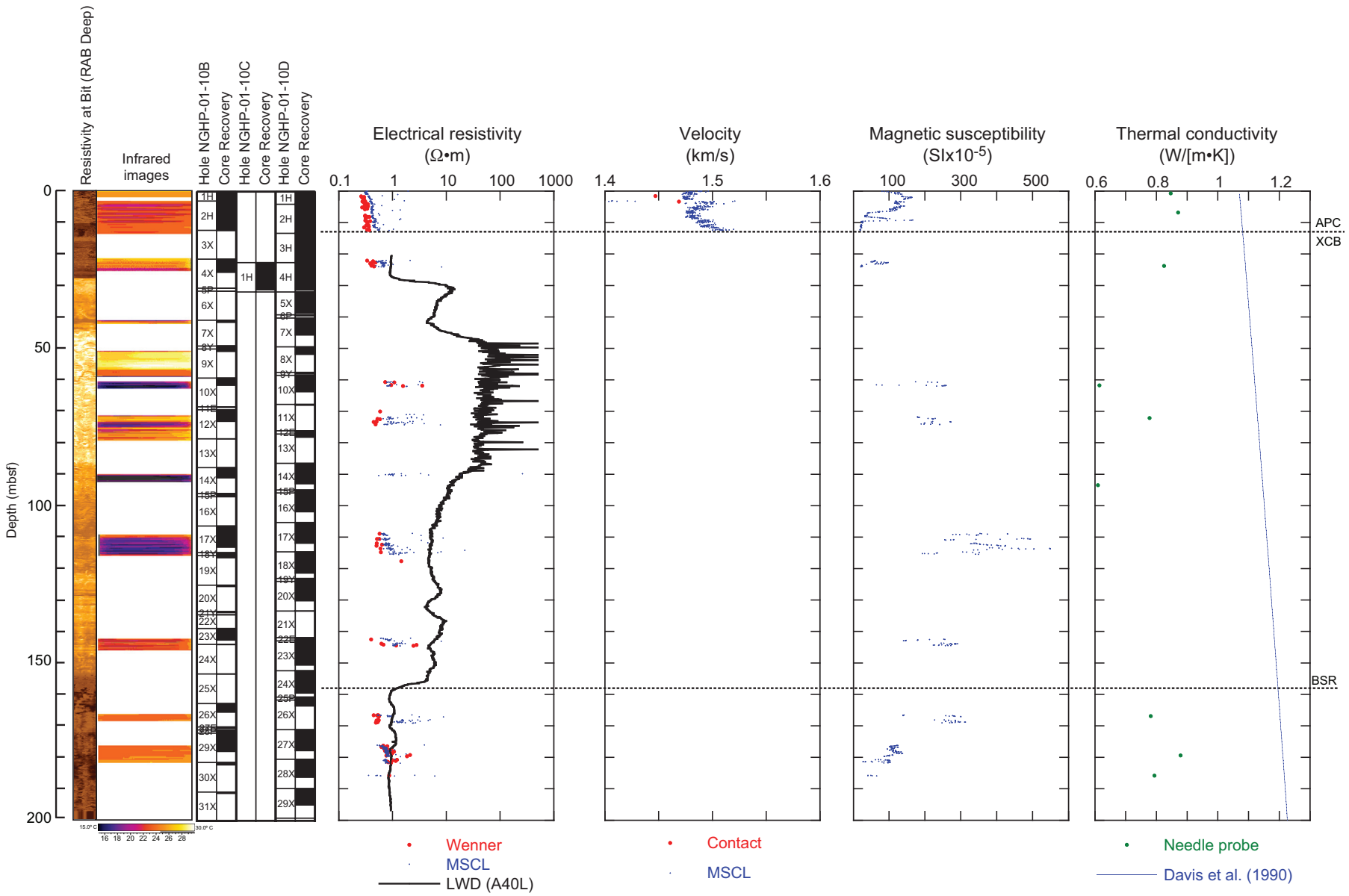


Figure 27. Profiles of LWD resistivity-at-bit, infrared images, core recovery, electrical resistivity, acoustic *P*-wave velocity, magnetic susceptibility, and thermal conductivity for Hole NGHP-01-10B. [LWD, logging-while-drilling]

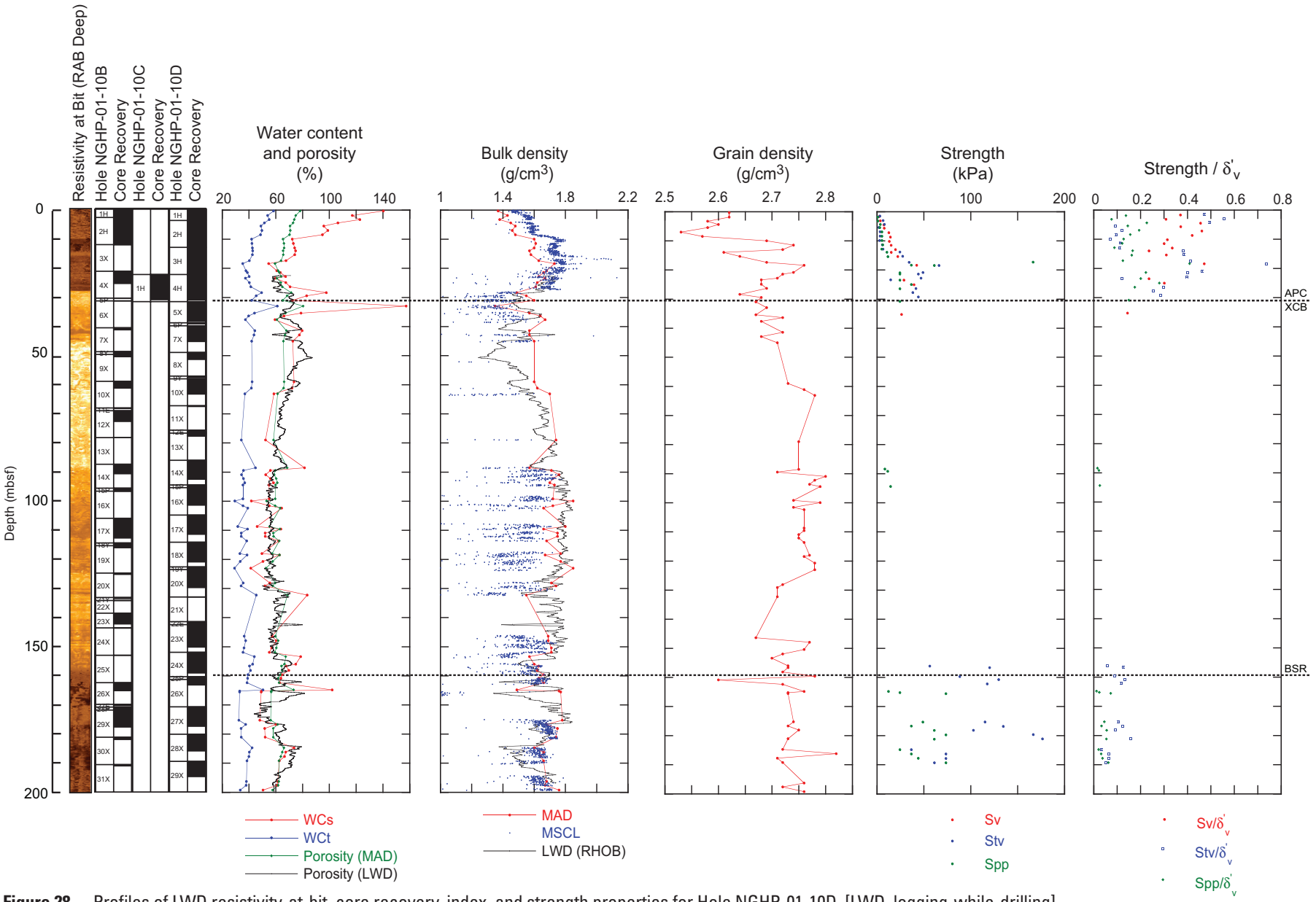


Figure 28. Profiles of LWD resistivity-at-bit, core recovery, index, and strength properties for Hole NGHP-01-10D. [LWD, logging-while-drilling]

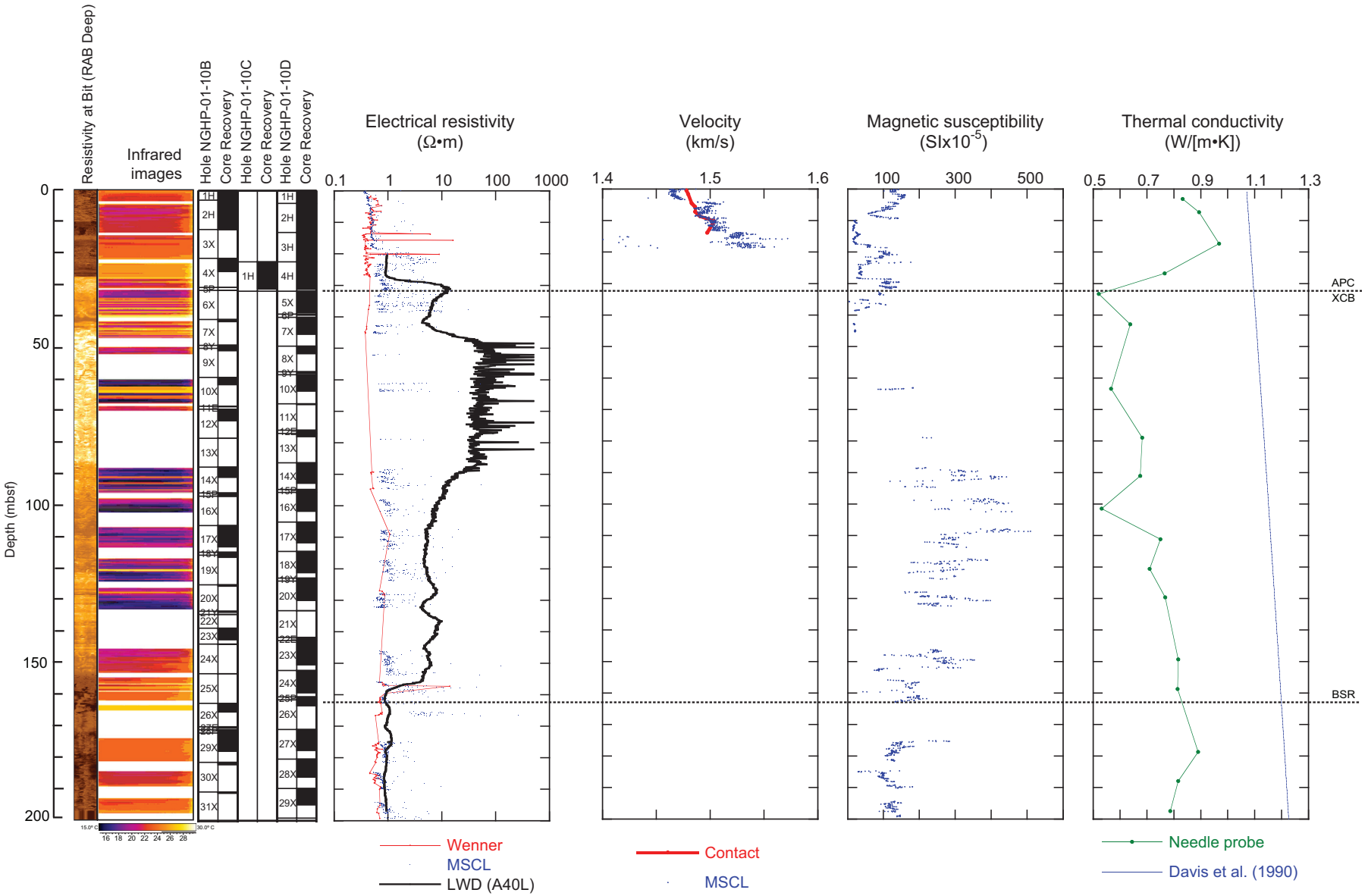


Figure 29. Profiles of LWD resistivity-at-bit, infrared images, core recovery, electrical resistivity, acoustic *P*-wave velocity, magnetic susceptibility, and thermal conductivity for Hole NGHP-01-10D. [LWD, logging-while-drilling]

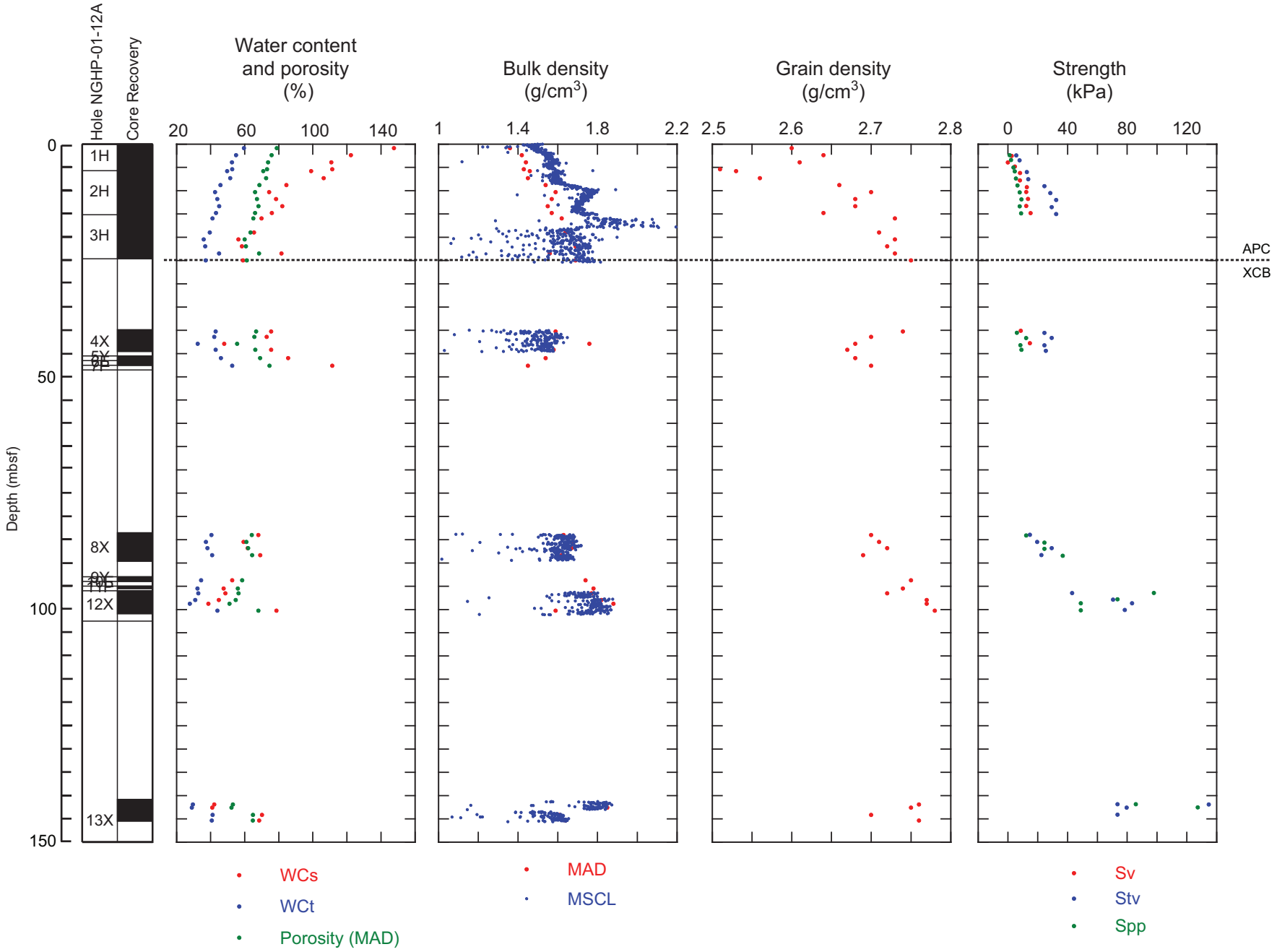


Figure 30. Profiles of core recovery, index, and strength properties for Hole NGHP-01-12A.

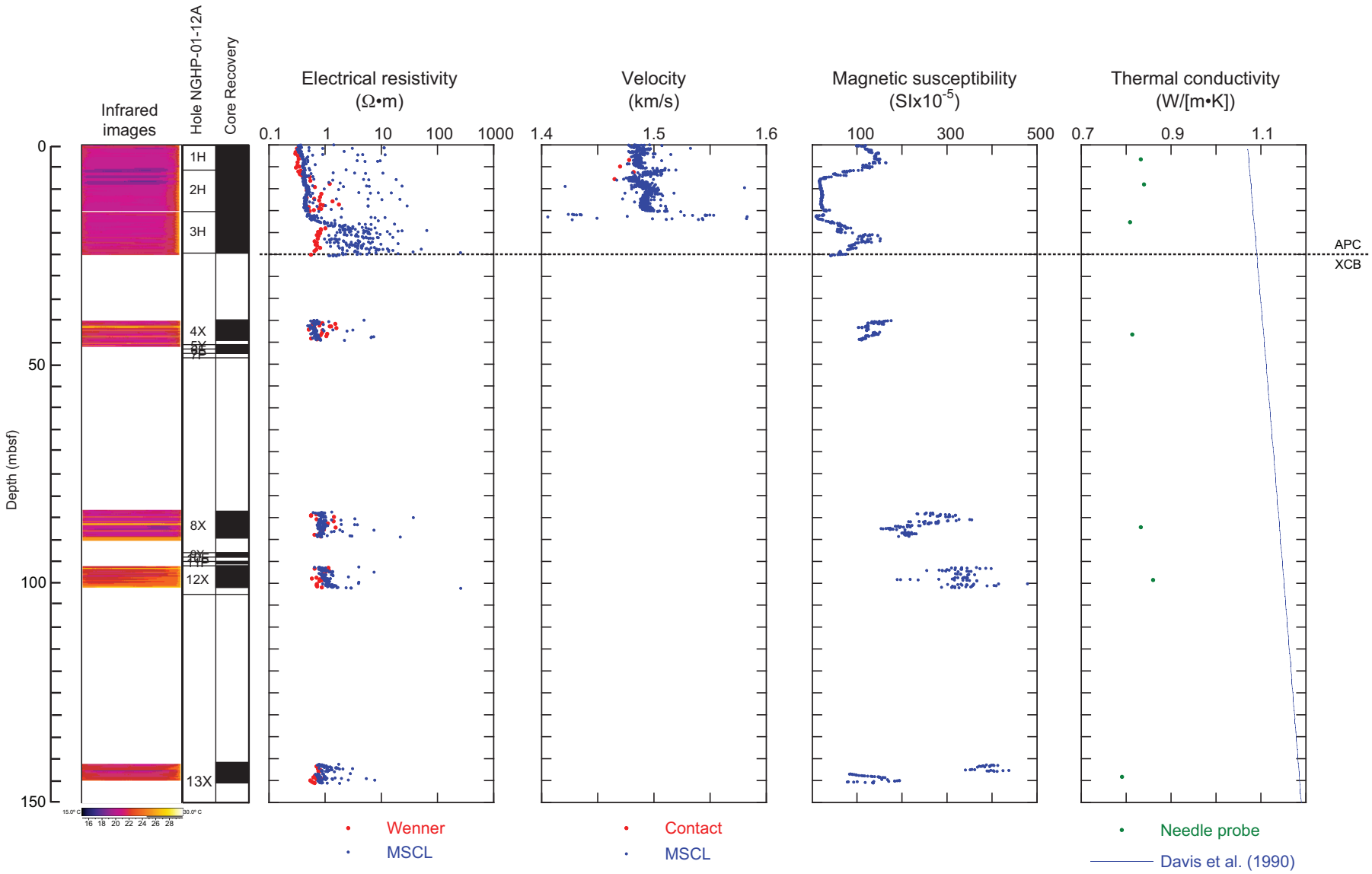


Figure 31. Profiles of LWD resistivity-at-bit, infrared images, core recovery, electrical resistivity, acoustic *P*-wave velocity, magnetic susceptibility, and thermal conductivity for Hole NGHP-01-12A. [LWD, logging-while-drilling]

Table 22. Moisture and density (MAD) physical properties for Holes NGHP-01-10B, NGHP-01-10D and NGHP-01-12A.

Core, section, interval (cm)	Sample code	Depth (mbsf)	WCt (%)	WCs (%)	Grain density (g/cm³)	Bulk density (g/cm³)	Dry bulk density (g/cm³)	Porosity (%)	Void ratio	Unit weight (kN/m³)
NGHP-01-10B										
2H-1,27-29	MAD	3.37	57.19	133.6	2.51	1.37	0.59	76.63	3.28	13.46
2H-4,16-18	MAD	7.76	48.5	94.18	2.62	1.49	0.77	70.65	2.41	14.63
2H-5,13-15	MAD	9.23	41.75	71.69	2.69	1.60	0.93	65.27	1.88	15.70
2H-6,11-13	MAD	10.71	41.96	72.29	2.73	1.61	0.93	65.86	1.93	15.77
2H-7,19-21	MAD	12.29	42.22	73.08	2.66	1.59	0.92	65.49	1.90	15.58
4X-1,47-49	MAD	22.47	40.45	67.91	2.79	1.64	0.98	64.90	1.85	16.12
4X-2,5-7	MAD	23.55	44.86	81.35	2.71	1.56	0.86	68.29	2.15	15.29
10X-1,12-14	MAD	60.72	39.93	66.47	2.86	1.67	1.00	64.96	1.85	16.34
10X-2,12-14	MAD	61.64	35.98	56.19	2.78	1.72	1.10	60.40	1.53	16.87
11E-1,5-7	MAD	70.05	37.2	59.23	2.80	1.70	1.07	61.81	1.62	16.69
12X-1,12-14	MAD	71.12	42.76	74.71	2.73	1.59	0.91	66.56	1.99	15.64
12X-2,32-34	MAD	71.49	44.55	80.33	2.72	1.57	0.87	68.11	2.14	15.36
12X-3,72-74	MAD	72.44	34.48	52.62	2.79	1.73	1.13	58.21	1.39	16.96
12X-4,18-20	MAD	73.37	33.77	50.99	2.74	1.75	1.16	57.68	1.36	17.16
12X-5,25-27	MAD	74.16	36.21	56.76	2.72	1.70	1.08	60.08	1.50	16.67
17X-1,15-17	MAD	108.95	36.57	57.65	2.77	1.71	1.08	60.88	1.56	16.73
17X-2,8-10	MAD	110.38	38.42	62.39	2.77	1.67	1.03	62.74	1.68	16.41
17X-3,13-15	MAD	111.93	43.26	76.25	2.76	1.59	0.90	67.25	2.05	15.62
17X-4,12-14	MAD	113.42	34.78	53.32	2.72	1.73	1.13	58.63	1.42	16.94
17X-5,11-13	MAD	114.75	33.59	50.58	2.83	1.78	1.18	58.26	1.40	17.43
18Y-1,36-38	MAD	117.76	33.79	51.03	2.74	1.75	1.16	57.71	1.36	17.16
23X-1,37-39	MAD	142.47	35.31	54.58	2.86	1.75	1.13	60.39	1.52	17.18
23X-2,27-29	MAD	143.87	32.32	47.75	2.84	1.81	1.22	56.99	1.32	17.72
26X-1,55-57	MAD	167.05	32.98	49.21	2.73	1.76	1.18	56.74	1.31	17.28
26X-2,88-90	MAD	168.88	33.21	49.72	2.72	1.76	1.17	56.94	1.32	17.23
27E-1,6-8	MAD	174.16	49.48	97.94	2.46	1.45	0.73	70.20	2.36	14.25
28P-2,99-101	MAD	176.47	37.8	60.77	2.70	1.67	1.04	61.59	1.60	16.37
29X-1,14-16	MAD	176.24	37.83	60.84	2.74	1.68	1.04	61.95	1.63	16.45
29X-3,15-17	MAD	179.25	32.73	48.66	2.72	1.76	1.19	56.39	1.29	17.31
29X-4,15-17	MAD	180.75	34.98	53.81	2.73	1.72	1.12	58.89	1.43	16.91
30X-1,15-17	MAD	185.85	42.22	73.08	2.71	1.60	0.92	65.91	1.93	15.68
NGHP-01-10D										
1H-1,35-37	MAD	0.35	58.38	140.3	2.62	1.37	0.57	78.17	3.58	13.48
1H-2,34-36	MAD	1.84	53.96	117.19	2.62	1.43	0.66	74.92	2.99	13.98
1H-3,29-31	MAD	3.29	55.11	122.79	2.58	1.38	0.62	73.91	2.83	13.50
2H-1,29-31	MAD	4.39	51.55	106.38	2.60	1.45	0.70	72.96	2.70	14.25
2H-2,20-22	MAD	5.50	48.96	95.92	2.58	1.48	0.76	70.65	2.41	14.53
2H-3,20-22	MAD	7.00	49.73	98.93	2.53	1.46	0.74	70.88	2.43	14.35
2H-4,20-22	MAD	8.50	48.66	94.8	2.57	1.48	0.76	70.34	2.37	14.55
2H-5,20-22	MAD	10.00	41.98	72.34	2.69	1.60	0.93	65.47	1.90	15.70
2H-6,20-22	MAD	11.50	42.25	73.17	2.74	1.61	0.93	66.14	1.95	15.76
2H-7,20-22	MAD	13.00	42.56	74.09	2.72	1.60	0.92	66.28	1.97	15.68
3H-1,40-42	MAD	14.00	42.81	74.86	2.61	1.57	0.90	65.55	1.90	15.42
3H-2,23-25	MAD	15.33	42.58	74.16	2.64	1.58	0.91	65.63	1.91	15.52
3H-3,77-79	MAD	17.37	40.34	67.63	2.69	1.63	0.97	63.93	1.77	15.96
3H-4,31-33	MAD	18.41	35.36	54.71	2.76	1.73	1.12	59.51	1.47	16.94
3H-5,126-128	MAD	20.86	37.77	60.7	2.74	1.68	1.05	61.80	1.62	16.47
3H-6,37-39	MAD	21.47	38.81	63.43	2.72	1.66	1.02	62.71	1.68	16.27
3H-7,25-27	MAD	22.85	40.23	67.32	2.71	1.63	0.98	63.99	1.78	16.01
4H-1,32-34	MAD	23.42	37.39	59.72	2.68	1.67	1.05	60.89	1.56	16.40
4H-2,32-34	MAD	24.92	40.31	67.53	2.68	1.62	0.97	63.80	1.76	15.94
4H-3,32-34	MAD	26.37	41.4	70.65	2.69	1.61	0.94	64.96	1.85	15.80
4H-5,32-34	MAD	28.37	49.43	97.75	2.64	1.49	0.75	71.57	2.52	14.58
4H-6,32-34	MAD	29.47	45.38	83.09	2.68	1.55	0.85	68.44	2.17	15.18
4H-7,32-34	MAD	30.97	42.05	72.57	2.67	1.60	0.92	65.36	1.89	15.65
5X-1,40-42	MAD	33.00	61.14	157.33	2.69	1.35	0.53	80.48	4.12	13.25
5X-4,32-34	MAD	35.40	44.1	78.88	2.67	1.57	0.88	67.25	2.05	15.35
5X-5,32-34	MAD	36.40	39.8	66.12	2.72	1.64	0.99	63.69	1.75	16.11

Table 22. Moisture and density (MAD) physical properties for Holes NGHP-01-10B, NGHP-01-10D and NGHP-01-12A.—Continued

Core, section, interval (cm)	Sample code	Depth (mbsf)	WCt (%)	WCs (%)	Grain density (g/cm³)	Bulk density (g/cm³)	Dry bulk density (g/cm³)	Porosity (%)	Void ratio	Unit weight (kN/m³)
NGHP-01-10D—Continued										
5X-6,32-34	MAD	37.65	37.32	59.53	2.68	1.67	1.05	60.87	1.56	16.42
7X-1,32-34	MAD	41.42	44.36	79.73	2.72	1.57	0.87	67.89	2.11	15.41
7X-2,32-34	MAD	42.92	43.7	77.63	2.68	1.57	0.89	66.96	2.03	15.43
7X-4,32-34	MAD	45.05	42.1	72.72	2.71	1.60	0.93	65.78	1.92	15.73
9Y-1,20-22	MAD	59.00	42.41	73.65	2.73	1.60	0.92	66.22	1.96	15.72
10X-2,10-12	MAD	61.12	41.9	72.13	2.76	1.62	0.94	66.00	1.94	15.86
10X-4,10-12	MAD	63.12	36.95	58.61	2.78	1.70	1.07	61.33	1.59	16.71
13X-1,20-22	MAD	79.00	34.37	52.36	2.75	1.74	1.14	58.35	1.40	17.10
14X-1,13-15	MAD	88.53	44.89	81.45	2.75	1.57	0.86	68.61	2.19	15.39
14X-2,35-37	MAD	89.45	35.91	56.02	2.71	1.71	1.09	59.69	1.48	16.74
14X-3,34-36	MAD	90.94	34.43	52.51	2.80	1.76	1.15	58.86	1.43	17.21
14X-4,39-41	MAD	92.26	35.94	56.09	2.78	1.72	1.10	60.29	1.52	16.89
14X-5,34-36	MAD	93.71	36.85	58.35	2.77	1.70	1.08	61.15	1.57	16.71
14X-6,14-16	MAD	94.43	35.47	54.96	2.79	1.73	1.12	59.87	1.49	17.00
16X-1,116-118	MAD	99.16	35.51	55.06	2.74	1.72	1.11	59.54	1.47	16.88
16X-2,43-45	MAD	99.93	29.44	41.72	2.79	1.85	1.31	53.11	1.13	18.16
16X-3,56-58	MAD	101.56	35.58	55.24	2.74	1.72	1.11	59.58	1.47	16.86
16X-4,8-10	MAD	102.37	39.16	64.36	2.76	1.66	1.01	63.34	1.73	16.29
17X-1,113-115	MAD	108.73	31.59	46.18	2.76	1.80	1.23	55.37	1.24	17.65
17X-2,50-52	MAD	109.60	38.98	63.88	2.76	1.66	1.02	63.17	1.72	16.32
17X-3,49-51	MAD	110.94	34.25	52.09	2.75	1.75	1.15	58.22	1.39	17.12
17X-4,18-20	MAD	112.13	34.28	52.17	2.75	1.75	1.15	58.29	1.40	17.12
17X-5,19-21	MAD	113.64	38.36	62.22	2.76	1.68	1.03	62.59	1.67	16.43
18X-1,84-86	MAD	118.04	33.22	49.73	2.77	1.77	1.18	57.26	1.34	17.36
18X-2,10-12	MAD	118.50	38.57	62.79	2.76	1.67	1.03	62.80	1.69	16.39
18X-3,84-86	MAD	120.74	33.49	50.36	2.78	1.77	1.18	57.72	1.37	17.35
18X-5,32-34	MAD	123.04	29.26	41.37	2.78	1.85	1.31	52.85	1.12	18.18
20X-1,68-70	MAD	127.48	43.26	76.25	2.59	1.58	0.90	66.66	2.00	15.52
20X-2,31-33	MAD	128.11	35.73	55.59	2.72	1.71	1.10	59.57	1.47	16.79
20X-3,8-10	MAD	129.11	34.14	51.83	2.71	1.74	1.14	57.75	1.37	17.03
20X-4,11-13	MAD	130.64	32.95	49.13	2.44	1.77	1.18	56.66	1.31	17.32
20X-6,38-40	MAD	132.27	45.51	83.5	2.71	1.55	0.85	68.81	2.21	15.23
23X-1,32-34	MAD	146.42	36.38	57.17	2.67	1.69	1.07	59.78	1.49	16.55
23X-2,32-34	MAD	147.92	37.63	60.33	2.77	1.69	1.05	61.92	1.63	16.57
23X-4,32-34	MAD	150.44	36.29	56.95	2.76	1.71	1.09	60.47	1.53	16.78
23X-5,32-34	MAD	151.94	35.57	55.2	2.72	1.71	1.10	59.36	1.46	16.80
23X-6,32-34	MAD	153.44	44.01	78.6	2.70	1.57	0.88	67.39	2.07	15.42
24X-1,21-23	MAD	156.01	42.83	74.92	2.73	1.60	0.91	66.58	1.99	15.65
24X-2,11-13	MAD	156.61	40.38	67.73	2.73	1.63	0.97	64.30	1.80	16.03
24X-3,16-18	MAD	158.16	41.1	69.78	2.72	1.62	0.96	64.93	1.85	15.91
24X-4,15-17	MAD	159.65	39.24	64.59	2.78	1.66	1.01	63.59	1.75	16.31
24X-5,17-19	MAD	160.87	38.99	63.9	2.60	1.63	0.99	61.79	1.62	15.96
24X-6,17-19	MAD	162.37	38.6	62.87	2.72	1.66	1.02	62.51	1.67	16.31
25P-1,41-43	MAD	164.81	50.52	102.11	2.76	1.49	0.74	73.32	2.75	14.61
25P-1,82-84	MAD	165.22	33.09	49.45	2.73	1.76	1.18	56.82	1.32	17.29
26X-1,15-17	MAD	165.55	32.96	49.17	2.73	1.77	1.18	56.68	1.31	17.31
27X-1,26-28	MAD	175.26	32.5	48.15	2.74	1.78	1.20	56.27	1.29	17.43
27X-2,18-20	MAD	176.68	37.57	60.19	2.73	1.68	1.05	61.52	1.60	16.48
27X-3,10-12	MAD	178.10	34.13	51.81	2.75	1.75	1.15	58.09	1.39	17.14
27X-5,10-12	MAD	181.10	34.25	52.09	2.73	1.74	1.15	58.10	1.39	17.08
28X-1,14-16	MAD	184.74	42.42	73.67	2.72	1.60	0.92	66.13	1.95	15.70
28X-2,12-14	MAD	186.22	40.25	67.37	2.82	1.66	0.99	64.95	1.85	16.25
28X-3,15-17	MAD	187.75	39.96	66.57	2.71	1.64	0.98	63.77	1.76	16.07
28X-4,13-15	MAD	189.23	38.53	62.67	2.72	1.66	1.02	62.41	1.66	16.31
29X-2,60-62	MAD	196.30	38.09	61.52	2.76	1.68	1.04	62.30	1.65	16.47
29X-3,43-45	MAD	197.63	37.9	61.04	2.72	1.67	1.04	61.79	1.62	16.42
29X-4,55-57	MAD	199.25	33.55	50.48	2.76	1.76	1.17	57.61	1.36	17.29

Table 22. Moisture and density (MAD) physical properties for Holes NGHP-01-10B, NGHP-01-10D and NGHP-01-12A.—Continued

Core, section, interval (cm)	Sample code	Depth (mbsf)	WCt (%)	WCs (%)	Grain density (g/cm³)	Bulk density (g/cm³)	Dry bulk density (g/cm³)	Porosity (%)	Void ratio	Unit weight (kN/m³)
NGHP-01-12A										
1H-1,85-87	MAD	0.85	59.62	147.65	2.60	1.36	0.55	78.91	3.74	13.33
1H-2,90-92	MAD	2.40	55.04	122.44	2.64	1.42	0.64	75.90	3.15	13.88
1H-3,90-92	MAD	3.90	52.6	110.95	2.61	1.44	0.68	73.82	2.82	14.13
1H-4,90-92	MAD	5.40	52.71	111.46	2.51	1.43	0.67	73.17	2.73	13.98
2H-1,12-14	MAD	5.82	49.76	99.04	2.53	1.46	0.74	70.95	2.44	14.36
2H-2,12-14	MAD	7.32	51.55	106.4	2.56	1.45	0.70	72.60	2.65	14.18
2H-3,12-14	MAD	8.82	45.8	84.5	2.66	1.54	0.83	68.68	2.19	15.10
2H-4,13-15	MAD	10.33	42.65	74.38	2.70	1.59	0.91	66.16	1.96	15.62
2H-5,14-16	MAD	11.84	43.97	78.49	2.68	1.57	0.88	67.21	2.05	15.39
2H-6,14-16	MAD	13.34	45.09	82.12	2.68	1.55	0.85	68.16	2.14	15.22
2H-7,12-14	MAD	14.82	43.18	76	2.64	1.57	0.89	66.15	1.95	15.42
3H-2,17-19	MAD	16.00	41.16	69.94	2.73	1.62	0.96	65.07	1.86	15.92
3H-4,17-19	MAD	19.00	39.6	65.57	2.71	1.64	0.99	63.40	1.73	16.12
3H-5,17-19	MAD	20.50	36.04	56.35	2.73	1.71	1.09	59.97	1.50	16.76
3H-6,17-19	MAD	22.00	36.89	58.46	2.72	1.69	1.07	60.77	1.55	16.58
3H-7,17-19	MAD	23.50	44.94	81.62	2.73	1.56	0.86	68.44	2.17	15.33
3H-8,17-19	MAD	24.99	37.13	59.05	2.75	1.69	1.07	61.25	1.58	16.61
4X-1,26-28	MAD	40.26	43.04	75.56	2.74	1.59	0.91	66.84	2.02	15.64
4X-2,26-28	MAD	41.41	42.19	72.99	2.70	1.60	0.93	65.77	1.92	15.70
4X-3,26-28	MAD	42.91	32.45	48.03	2.68	1.76	1.19	55.62	1.25	17.26
4X-4,26-28	MAD	44.23	43.05	75.6	2.67	1.58	0.90	66.29	1.97	15.50
5Y-1,30-32	MAD	46.00	46.12	85.61	2.68	1.54	0.83	69.05	2.23	15.07
6E-1,94-96	MAD	47.64	52.7	111.42	2.70	1.45	0.69	74.58	2.93	14.25
8X-1,22-24	MAD	84.02	40.48	68	2.70	1.63	0.97	64.20	1.79	15.97
8X-2,22-24	MAD	85.52	37.24	59.33	2.71	1.68	1.06	61.05	1.57	16.51
8X-3,22-24	MAD	86.86	38.18	61.75	2.72	1.67	1.03	62.07	1.64	16.37
8X-4,22-24	MAD	88.36	40.89	69.18	2.69	1.62	0.96	64.41	1.81	15.86
9Y-1,47-49	MAD	93.77	34.49	52.66	2.75	1.74	1.14	58.51	1.41	17.08
11P-1,22-24	MAD	95.52	32.31	47.73	2.74	1.78	1.20	56.01	1.27	17.46
12X-1,25-27	MAD	96.55	32.79	48.78	2.72	1.77	1.19	56.41	1.29	17.32
12X-2,25-27	MAD	98.00	31	44.92	2.77	1.82	1.25	54.81	1.21	17.80
12X-3,25-27	MAD	98.79	27.92	38.74	2.77	1.88	1.35	51.09	1.04	18.42
12X-4,25-27	MAD	100.29	44.05	78.73	2.78	1.59	0.89	68.04	2.13	15.55
13X-1,62-64	MAD	141.92	29.67	42.19	2.76	1.84	1.29	53.14	1.13	18.03
13X-2,29-31	MAD	142.59	29.07	40.98	2.75	1.85	1.31	52.32	1.10	18.12
13X-3,73-75	MAD	144.16	41.27	70.28	2.70	1.61	0.95	64.86	1.85	15.82
13X-4,47-49	MAD	145.40	40.67	68.54	2.76	1.64	0.97	64.81	1.84	16.05

Table 23. Vane shear strength results for Holes NGHP-01-10B, NGHP-01-10D, and NGHP-01-12A.

Core, section	Sample	Top (cm)	Depth (mbsf)	Sv (kPa)	Sres (kPa)	Srem (kPa)	St
NGHP-01-10B							
1H-2	VS	12	1.62	3.29	1.65	0.82	4.00
2H-1	VS	30	3.40	4.11	3.29	1.65	2.50
2H-2	VS	40	5.00	6.99	4.94	3.21	2.18
2H-3	VS	40	6.50	9.87	4.11	3.95	2.50
2H-4	VS	30	7.90	12.18	6.58	4.94	2.47
2H-5	VS	33	9.43	15.22	9.87	5.35	2.85
2H-6	VS	30	10.90	17.28	9.46	4.94	3.50
2H-7	VS	23	12.33	23.04	11.68	8.23	2.80
4X-1	VS	12	22.12	4.94	3.29	1.65	3.00
4X-2	VS	0	23.50	20.57	14.81	2.47	8.33
NGHP-01-10D							
1H-2	VS	18	1.68	2.47	1.48	0.82	3.00
1H-3	VS	15	3.15	3.70	0.82	0.66	5.63
2H-1	VS	40	4.50	7.41	4.11	1.81	4.09
2H-2	VS	40	5.70	7.82	4.11	2.30	3.39
2H-3	VS	40	7.20	12.75	6.58	4.11	3.10
2H-4	VS	41	8.71	14.40	7.41	4.94	2.92
2H-5	VS	40	10.20	13.17	7.41	3.29	4.00
2H-6	VS	22	11.52	15.14	8.23	4.44	3.41
2H-7	VS	21	13.01	19.75	12.34	6.17	3.20
3H-1	VS	40	14.00	15.22	5.76	4.77	3.19
3H-2	VS	29	15.39	22.22	11.52	7.90	2.81
3H-4	VS	30	18.40	42.38	20.57	20.90	2.03
4H-1	VS	42	23.52	28.80	20.57	9.87	2.92
4H-2	VS	46	25.06	39.50	27.15	27.15	1.45
5H-3	VS	45	35.30	26.33	18.93	9.87	2.67
NGHP-01-12A							
1H-2	VS	105	2.55	2.63	1.65	0.66	4.00
1H-4	VS	33	4.83	4.77	3.79	1.23	3.87
2H-1	VS	50	6.20	8.23	5.76	4.94	1.67
2H-2	VS	60	7.80	8.06	4.94	2.88	2.80
2H-3	VS	58	9.28	12.75	8.64	8.64	1.48
2H-4	VS	9	10.29	12.34	9.87	4.53	2.73
2H-5	VS	9	11.79	13.58	10.70	6.17	2.20
2H-6	VS	13	13.33	12.34	8.64	4.94	2.50
2H-7	VS	14	14.84	15.22	10.29	5.76	2.64
4H-1	VS	14	40.14	8.64	7.41	3.29	2.63
4H-3	VS	14	42.79	14.81	13.17	13.17	1.13

Table 24. Torvane strength results for Holes NGHP-01-10B, NGHP-01-10D, and NGHP-01-12A.

Core, section	Sample	Top (cm)	Bottom (cm)	Depth (mbsf)	Stv (kPa)
NGHP-01-10B					
1H-1	TV	36	40	0.36	4.3
1H-2	TV	26	30	1.76	2.9
2H-2	TV	19	23	4.79	11.2
2H-3	TV	9	11	6.19	14.7
2H-4	TV	6	8	7.66	14.7
2H-5	TV	5	7	9.15	21.6
2H-6	TV	5	7	10.65	24.5
2H-7	TV	10	12	12.20	23.5
4X-1	TV	52	54	22.52	7.8
4X-2	TV	14	16	23.64	34.3
12X-4	TV	8	10	73.27	39.2
18Y-1	TV	16	18	117.56	34.3
26X-1	TV	59	61	167.09	51.0
26X-2	TV	91	93	168.91	58.8
29X-2	TV	3	5	177.63	49.0
29X-3	TV	3	5	179.13	78.5
29X-4	TV	3	5	180.63	85.8
NGHP-01-10D					
1H-2	TV	2	4	1.52	3.1
1H-3	TV	2	4	3.02	6.7
2H-1	TV	24	26	4.34	8.0
2H-2	TV	12	14	5.42	2.0
2H-3	TV	10	12	6.90	3.3
2H-4	TV	9	11	8.39	3.3
2H-5	TV	9	11	9.89	2.9
2H-6	TV	6	8	11.36	5.7
2H-7	TV	5	7	12.85	6.5
3H-1	TV	29	31	13.89	24.5
3H-2	TV	19	21	15.29	27.5
3H-3	TV	77	79	17.37	34.3
3H-4	TV	35	37	18.45	66.2
3H-5	TV	130	132	20.90	49.0
3H-6	TV	34	36	21.44	44.1
3H-7	TV	22	24	22.82	47.1
4H-1	TV	31	33	23.41	14.7
4H-3	TV	38	40	26.43	41.7
4H-4	TV	41	43	27.79	38.2
4H-6	TV	14	16	29.29	44.1
NGHP-01-10D—Continued					
24X-1	TV	32	34	156.12	56.4
24X-2	TV	18	20	156.68	120.1
24X-4	TV	22	24	159.72	88.3
24X-5	TV	6	8	160.76	129.9
24X-6	TV	6	8	162.26	117.7
27X-1	TV	32	34	175.32	115.2
27X-2	TV	33	35	176.83	134.8
27X-3	TV	17	19	178.17	103.0
27X-4	TV	15	17	179.65	166.7
27X-5	TV	15	17	181.15	176.5
28X-1	TV	25	27	184.85	36.8
28X-2	TV	25	27	186.35	73.5
28X-3	TV	25	27	187.85	73.5
28X-4	TV	25	27	189.35	61.3
NGHP-01-12A					
1H-2	TV	94	96	2.44	5.7
1H-3	TV	50	52	3.50	7.8
2H-1	TV	33	35	6.03	12.7
2H-2	TV	33	35	7.53	13.7
2H-3	TV	33	35	9.03	24.5
2H-4	TV	33	35	10.53	28.4
2H-5	TV	33	35	12.03	32.4
2H-6	TV	33	35	13.53	29.4
2H-7	TV	33	35	15.03	32.4
4X-1	TV	60	62	40.60	24.5
4X-2	TV	52	54	41.67	29.4
4X-3	TV	59	61	43.24	24.5
4X-4	TV	48	50	44.45	25.5
8X-1	TV	19	21	83.99	14.7
8X-2	TV	19	21	85.49	19.6
8X-3	TV	19	21	86.83	29.4
8X-4	TV	19	21	88.33	22.6
12X-1	TV	19	21	96.49	43.1
12X-2	TV	16	18	97.91	70.6
12X-3	TV	16	18	98.70	83.4
12X-4	TV	11	13	100.15	78.5
13X-1	TV	64	66	141.94	134.8
13X-2	TV	30	32	142.60	79.7

Table 25. Pocket Penetrometer strength results for Holes NGHP-01-10B, NGHP-01-10D, and NGHP-01-12A.

Core, section	Sample code	Top	Depth (mbsf)	Spp (kPa)	Comment
NGHP-01-10B					
2H-2	PP	24	4.42	0.3	very soft
2H-2	PP	14	5.98	2.8	
2H-3	PP	14	7.51	3.8	
2H-4	PP	12	9.07	4.6	
2H-5	PP	9	10.50	6.9	
2H-6	PP	8	10.92	9.2	
2H-7	PP	16	12.49	8.4	
4X-1	PP	45	14.11	7.7	
4X-2	PP	21	15.39	12.3	
NGHP-01-10D					
1H-2	PP	38	1.88	0.9	
1H-3	PP	16	3.16	0.9	
2H-1	PP	31	4.41	3.7	
2H-2	PP	15	5.45	3.1	
2H-3	PP	15	6.95	5.4	
2H-4	PP	13	8.43	5.4	
2H-5	PP	13	9.93	5.4	
2H-6	PP	10	11.40	6.1	
2H-7	PP	8	12.88	5.2	
3H-1	PP	32	13.92	10.7	
3H-2	PP	35	15.45	11.6	
3H-3	PP	74	17.34	10.41	
3H-4	PP	28	18.38	36.8	
3H-4	PP	36	18.46	61.3	
3H-5	PP	141	21.01	24.5	
3H-6	PP	33	21.43	24.5	
4H-1	PP	39	23.49	24.5	
4H-2	PP	42	25.02	36.8	
4H-3	PP	39	26.44	24.5	
4H-7	PP	21	30.86	24.5	
14X-1	PP	5	88.45	8.4	
14X-2	PP	11	89.21	11.5	
14X-6	PP	10	94.39	14.5	
25P-1	PP	42	164.82	<12.3	soft, soupy
25P-1	PP	83	165.23	24.5	biscuit
NGHP-01-10D—Continued					
26X-1	PP	20	165.60	73.5	
27X-1	PP	36	175.36	49	
27X-2	PP	24	176.74	36.8	
27X-3	PP	24	178.24	61.3	
27X-4	PP	24	179.74	73.5	
27X-5	PP	24	181.24	61.3	
28X-1	PP	23	184.83	24.5	
28X-2	PP	22	186.32	36.8	
28X-3	PP	22	187.82	44.1	
28X-4	PP	22	189.32	73.5	
NGHP-01-12A					
1H-2	PP	90	2.40	1.2	
1H-3	PP	41	3.41	2.1	
1H-4	PP	52	5.02	3.8	
2H-1	PP	18	5.88	4.6	
2H-2	PP	18	7.38	5.4	
2H-3	PP	18	8.88	6.4	
2H-4	PP	18	10.38	8	
2H-5	PP	18	11.88	9.2	
2H-6	PP	18	13.38	8	
2H-7	PP	18	14.88	8.9	
4X-1	PP	56	40.56	6.1	
4X-2	PP	56	41.71	12.3	
4X-3	PP	56	43.21	8.4	
4X-4	PP	26	44.23	9.2	
8X-1	PP	34	84.14	12.3	
8X-2	PP	34	85.64	24.5	
8X-3	PP	34	86.98	24.5	
8X-4	PP	34	88.48	36.8	
12X-1	PP	15	96.45	98	
12X-2	PP	11	97.86	73.5	
12X-3	PP	15	98.69	49	
12X-4	PP	16	100.20	49	
13X-1	PP	57	141.87	85.8	
13X-2	PP	28	142.58	127.4	

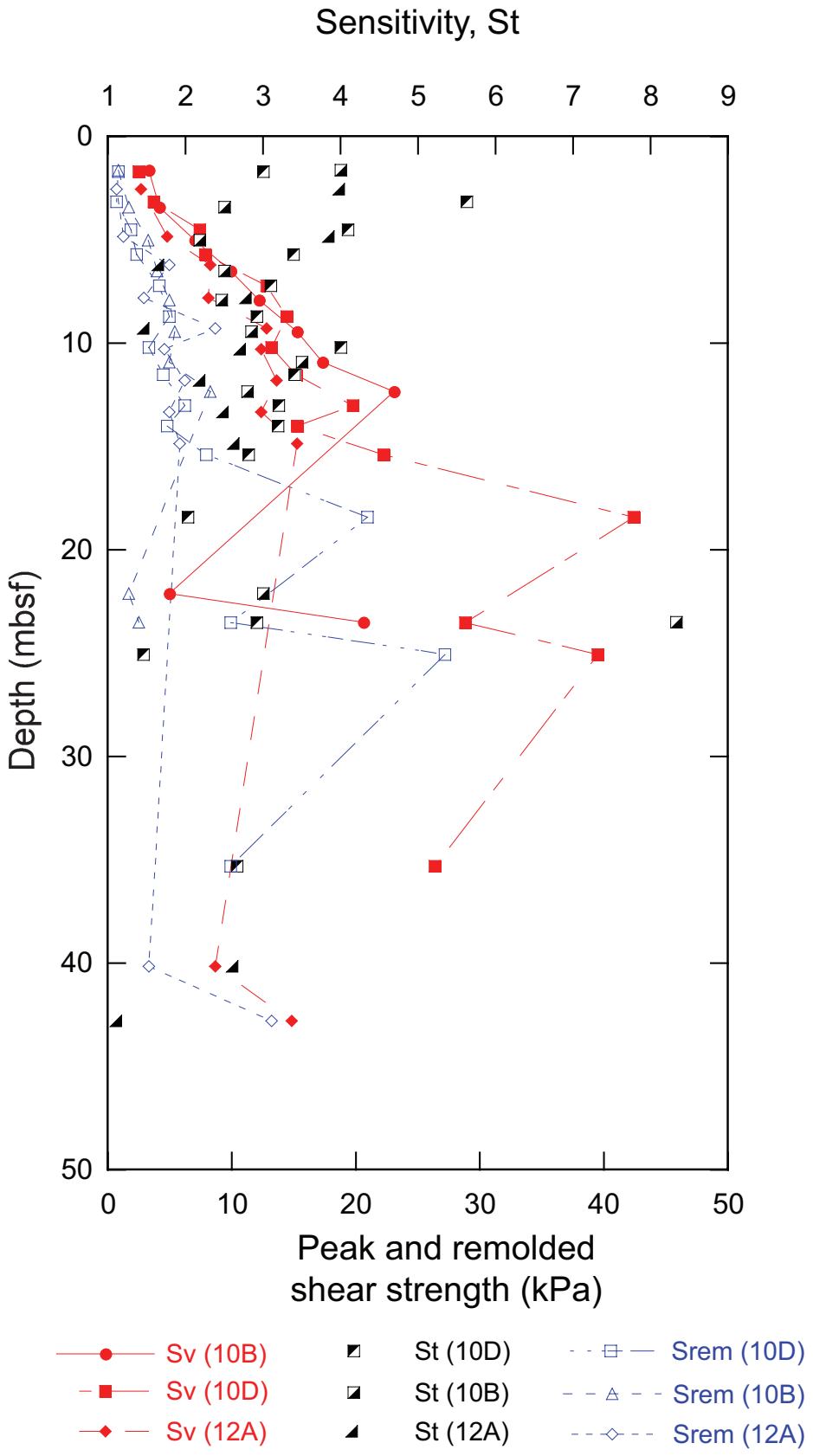


Figure 32. Peak and remolded vane shear strengths and sensitivity for Holes NGHP-01-10B, NGHP-01-10D, and NGHP-01-12A.



Figure 33. PCS Core NGHP-01-10D-25P from 41–43 cm near the BSR contained wet, soft sediment with a Pocket Penetrometer strength <12 kPa. [PCS, Pressure Core Sampler; BSR, bottom-simulating reflector; kPa, kilopascals per meter]



Figure 34. PCS Core NGHP-01-10D-25P from 83 cm had a Pocket Penetrometer strength of 24.5 kPa. [PCS, Pressure Core Sampler; kPa, kilopascals per meter]

Electrical Resistivity

LWD conducted previously in Hole NGHP-01-10A indicated that a high electrical resistivity zone was located between 30 and 160 mbsf underlain by a weak BSR at approximately 163 mbsf (see "Pressure Coring" and "Downhole Logging"). The Resistivity-At-Bit (RAB) images were strongest from 46 to 90 mbsf suggesting this zone has the greatest concentration of gas hydrate.

Overall, electrical resistivity values determined by LWD conducted in Hole NGHP-01-10D, MSCL, and the Wenner array performed on split cores compared favorably outside the gas-hydrate zone (above 30 mbsf and below the BSR) (table 26 and figs. 27 and 29). However, the presence of gas hydrate *in situ* can increase electrical resistivity up to two orders of magnitude and this causes large differences between the LWD and laboratory values. This is because the MSCL and Wenner-array data reflect background sediment values after gas hydrate has dissociated.

The Wenner values represent selected values on intact core material, hence the somewhat lower values than for the MSCL which senses a wider portion of core that may contain voids or small expansion cracks. Lower MSCL values are more representative of undisturbed sediment as they do not reflect the presence of such micro voids caused by gas expansion.

P-Wave Velocity

P-wave velocity measured with the MSCL increased slightly from 1.46 to 1.48 km/s in the top of the holes (figs. 27, 29, and 31) to 1.48 to 1.52 km/s at a subbottom depth between 12 and 20 mbsf, which represents the depth where gas and voids present in the sediment prevented further valid measurements from being logged. The contact V_p values (table 27 and figs. 27, 29, and 31) are in close agreement and increased from 1.44 km/s at the top of Hole NGHP-01-10B to 1.51 km/s in Hole NGHP-01-10D.

Magnetic Susceptibility

Background magnetic susceptibility trends are all similar in Holes NGHP-01-10B, NGHP-01-10D, and NGHP-01-12A. Initially they begin at the seafloor at just above $100x10^{-5}$ SI, increase slightly, then decrease to about $20–30\times10^{-5}$ SI. Within the gas hydrate stability zone magnetic susceptibility varies to as much as 300×10^{-5} SI, before decreasing towards the bottom of each hole (figs. 27, 29, and 31). Wide excursions exist in the data indicating that primary and secondary magnetic minerals are present in alternating non-uniform layers (see "Lithostratigraphy"). However, such excursions are not likely the result of lithologic controls and, although coincident to the location of gas hydrate, do not have a known direct influence on the formation of gas hydrate.

Thermal Conductivity

Thermal conductivities vary between 0.521 and 0.968 W/(m×k) and are typically independent of subbottom depth (table 28 and figs. 27, 29, and 31). Such values are well within the range of marine sediments (for example, Novosel and others, in press), although they are all lower than values determined by Davis and others (1990) for sediment from Cascadia and the Nankai Trough.

Downhole Temperature Measurements

A number of different tools are available for determining downhole sediment temperature (see "Physical Properties" in the "Methods" chapter). Although six attempts were made, only four provided usable *in situ* temperature data at Site NGHP-01-10. Seafloor temperature intercept was determined to be 6.5±0.3 °C and the geothermal gradient was determined at 45±3 °C per km (table 29 and fig. 35). The base of gas hydrate stability is predicted at 160 mbsf assuming pore methane and porewater salinity of 35 ppt (Sloan, 1998; shipboard calculated seafloor temperature 6.5 °C, geothermal gradient 45 °C per km).

Pressure Coring

The main objectives of pressure coring during NGHP Expedition 01 were to quantify natural gas composition and concentration in sediments and to determine the nature and distribution of gas hydrate and free gas within the sediment matrix. Secondary objectives were to obtain measurements of physical properties on gas-hydrate-bearing sediments under *in-situ* conditions, which can be used to help interpret regional seismic data, and obtain samples under full pressure for shorebased studies. To achieve these objectives, we conducted depressurization experiments and captured resultant gas to calculate gas hydrate quantity, made nondestructive measurements (X-ray imaging, *P*-wave velocity, gamma density) at *in situ* pressures and during depressurization to examine gas hydrate habit within sediments, and archived gas-hydrate-bearing sediments at *in situ* pressures for further investigations on shore.

Site NGHP-01-10 was drilled above a known conventional gas accumulation in the Krishna-Godavari Basin. Seismic data for Site NGHP-01-10 showed no BSR, but extremely high reflectivities below about 200 m. Site NGHP-01-12 was drilled 500 m away to the SE. LWD data from Hole NGHP-01-10A showed high electrical resistivities from 30 mbsf to 160 mbsf, with extremely high electrical resistivities (200 ohm-m) from 45–85 mbsf (see "Downhole Logging"). Specific objectives at Site NGHP-01-10 were to capture and quantify predicted massive gas hydrate in the layer of extremely high electrical

Table 26. Wenner array electrical resistivity results for Holes NGHP-01-10B, NGHP-01-10D, and NGHP-01-12A. (To view the complete table, please see the ASCII files.)

Core, section	Sample	Top	Depth (mbsf)	ER (W×m)
NGHP-01-10B				
1H-2	ER	20	1.70	0.262
1H-2	ER	40	1.90	0.297
1H-2	ER	60	2.10	0.276
1H-2	ER	80	2.30	0.287
1H-2	ER	100	2.50	0.295
2H-1	ER	20	3.30	0.312
2H-1	ER	23	3.33	0.277
2H-1	ER	43	3.53	0.29
2H-1	ER	63	3.73	0.317
2H-1	ER	83	3.93	0.302
2H-1	ER	103	4.13	0.347
2H-2	ER	20	4.80	0.352
2H-2	ER	20	4.80	0.327
2H-2	ER	40	5.00	0.296
2H-2	ER	40	5.00	0.295
2H-2	ER	60	5.20	0.296
2H-2	ER	60	5.20	0.274
2H-2	ER	80	5.40	0.309
2H-2	ER	80	5.40	0.334
2H-2	ER	100	5.60	0.329
2H-2	ER	100	5.60	0.34
2H-2	ER	120	5.80	0.307
2H-4	ER	20	7.80	0.311
2H-4	ER	30	7.90	0.312
2H-4	ER	40	8.00	0.312
2H-4	ER	60	8.20	0.371
2H-4	ER	60	8.20	0.347
2H-4	ER	80	8.40	0.332
2H-4	ER	100	8.60	0.318
2H-5	ER	30	9.40	0.314
2H-5	ER	50	9.60	0.384
2H-5	ER	70	9.80	0.345
2H-5	ER	90	10.00	0.337
2H-6	ER	20	10.80	0.358
2H-6	ER	40	11.00	0.325
2H-6	ER	72	11.32	0.365
2H-6	ER	100	11.60	0.296
2H-7	ER	20	12.30	0.339
2H-7	ER	30	12.40	0.369
4X-1	ER	12	22.12	0.339
4X-1	ER	32	22.32	0.435
4X-1	ER	52	22.52	0.434
4X-1	ER	72	22.72	0.484
4X-1	ER	92	22.92	0.39
4X-1	ER	112	23.12	0.389
4X-1	ER	132	23.32	0.41
4X-2	ER	5	23.55	0.423
4X-2	ER	25	23.75	0.407
4X-2	ER	45	23.95	0.453
10X-1	ER	11	60.71	0.733
10X-1	ER	23	60.83	1.084
10X-2	ER	17	61.69	0.949
10X-2	ER	36	61.88	3.572
10X-2	ER	50	62.02	1.569
11E-1	ER	8	70.08	0.59
12X-3	ER	72	72.44	0.528
12X-3	ER	82	72.54	0.586
12X-4	ER	10	73.29	0.5
12X-4	ER	18	73.37	0.507
12X-4	ER	24	73.43	0.448
12X-5	ER	25	74.16	0.488
17X-1	ER	17	108.97	0.579
17X-2	ER	27	110.57	0.568
17X-2	ER	36	110.66	0.519
17X-3	ER	24	112.04	0.509
17X-3	ER	61	112.41	0.64
17X-3	ER	99	112.79	0.506
17X-4	ER	35	113.65	0.599
17X-5	ER	16	114.80	0.609
18P-1	ER	27	117.67	1.463
23X-1	ER	50	142.60	0.401
23X-2	ER	29	143.89	0.624
23X-2	ER	60	144.20	0.683
23X-2	ER	70	144.30	2.8
23X-2	ER	87	144.47	1.174
23X-2	ER	94	144.54	2.459
26X-1	ER	12	166.62	0.542
26X-1	ER	17	166.67	0.447
26X-1	ER	24	166.74	0.518
26X-1	ER	35	166.85	0.566
26X-1	ER	44	166.94	0.555
26X-1	ER	54	167.04	0.559
26X-2	ER	12	168.12	0.541
26X-2	ER	23	168.23	0.557
26X-2	ER	33	168.33	0.506
26X-2	ER	51	168.51	0.532
26X-2	ER	62	168.62	0.52
26X-2	ER	69	168.69	0.51
26X-2	ER	79	168.79	0.536
26X-2	ER	89	168.89	0.513
26X-2	ER	99	168.99	0.493
29X-1	ER	20	176.30	0.677
29X-1	ER	40	176.50	0.802
29X-1	ER	63	176.73	0.624
29X-1	ER	80	176.90	0.708
29X-1	ER	100	177.10	0.73
29X-1	ER	120	177.30	0.698
29X-1	ER	140	177.50	0.81
29X-2	ER	20	177.80	0.971
29X-2	ER	40	178.00	0.727
29X-2	ER	62	178.22	1.074
29X-2	ER	80	178.40	1.015
29X-2	ER	100	178.60	0.836
29X-2	ER	120	178.80	0.989
29X-3	ER	18	179.28	2.126
29X-3	ER	40	179.50	0.768
29X-3	ER	60	179.70	1.864
29X-4	ER	20	180.80	1.209
29X-4	ER	40	181.00	1.015
29X-4	ER	60	181.20	1.146
29X-4	ER	80	181.40	0.802
29X-4	ER	100	181.60	0.838
29X-4	ER	120	181.80	0.939
30X-1	ER	13	185.83	0.872

Table 26. Wenner array electrical resistivity results for Holes NGHP-01-10B, NGHP-01-10D, and NGHP-01-12A. (To view the complete table, please see the ASCII files.)—Continued

Core, section	Sample	Top	Depth (mbsf)	ER (W×m)
NGHP-01-10D—Continued				
1H-2	ER	20	1.70	0.479
1H-2	ER	67	2.17	0.447
1H-2	ER	92	2.42	0.601
1H-2	ER	120	2.70	0.55
1H-3	ER	20	3.20	0.643
2H-1	ER	20	4.30	0.659
2H-1	ER	40	4.50	0.606
2H-1	ER	60	4.70	0.767
2H-2	ER	20	5.50	0.489
2H-2	ER	40	5.70	0.475
2H-2	ER	60	5.90	0.495
2H-2	ER	80	6.10	0.522
2H-2	ER	100	6.30	0.534
2H-2	ER	120	6.50	0.744
2H-3	ER	20	7.00	0.387
2H-3	ER	40	7.20	0.468
2H-3	ER	60	7.40	0.437
2H-3	ER	80	7.60	0.568
2H-4	ER	20	8.50	0.429
2H-4	ER	40	8.70	0.516
2H-4	ER	60	8.90	0.455
2H-4	ER	80	9.10	0.528
2H-4	ER	100	9.30	0.636
2H-4	ER	120	9.50	0.507
2H-5	ER	20	10.00	0.46
2H-5	ER	40	10.20	0.525
2H-5	ER	60	10.40	0.474
2H-5	ER	80	10.60	0.496
2H-5	ER	100	10.80	0.592
2H-6	ER	20	11.50	0.424
2H-6	ER	40	11.70	0.471
2H-6	ER	60	11.90	0.342
2H-6	ER	80	12.10	0.467
2H-6	ER	100	12.30	0.476
2H-6	ER	120	12.50	0.507
2H-7	ER	20	13.00	0.481
2H-7	ER	40	13.20	0.477
3H-1	ER	20	13.80	6.127
3H-1	ER	20	13.80	0.388
3H-1	ER	40	14.00	0.359
3H-1	ER	40	14.00	0.355
3H-1	ER	60	14.20	0.357
3H-1	ER	60	14.20	0.337
3H-1	ER	80	14.40	0.362
3H-1	ER	100	14.60	0.375
3H-1	ER	120	14.80	0.353
3H-2	ER	20	15.30	0.406
3H-2	ER	40	15.50	0.356
3H-2	ER	67	15.77	0.421
3H-2	ER	78	15.88	0.426
3H-2	ER	87	15.97	0.383
3H-3	ER	78	17.38	0.379
3H-3	ER	98	17.58	0.399
3H-3	ER	98	17.58	0.389
3H-3	ER	118	17.78	0.379
3H-3	ER	138	17.98	0.371
3H-4	ER	10	18.20	0.425
3H-4	ER	20	18.30	0.385
3H-4	ER	30	18.40	0.478
3H-4	ER	40	18.50	0.367
3H-4	ER	50	18.60	0.378
3H-5	ER	14	19.74	0.409
3H-5	ER	20	19.80	0.394
3H-5	ER	54	20.14	0.474
3H-5	ER	103	20.63	0.358
3H-5	ER	131	20.91	0.392
3H-6	ER	22	21.32	0.551
3H-6	ER	22	21.32	0.508
3H-6	ER	22	21.32	0.512
3H-6	ER	22	21.32	0.511
3H-6	ER	36	21.46	0.397
3H-6	ER	53	21.63	0.389
3H-6	ER	67	21.77	0.428
3H-6	ER	77	21.87	0.377
NGHP-01-12A				
1H-1	ER	85	0.85	0.315
1H-1	ER	120	1.20	0.351
1H-2	ER	17	1.67	0.298
1H-2	ER	55	2.05	0.296
1H-2	ER	105	2.55	0.332
1H-3	ER	22	3.22	0.341
1H-3	ER	98	3.98	0.324
1H-4	ER	20	4.70	0.322
1H-4	ER	30	4.80	0.325
1H-4	ER	50	5.00	0.347
1H-4	ER	70	5.20	0.302
2H-1	ER	20	5.90	0.372
2H-1	ER	40	6.10	0.335
2H-1	ER	60	6.30	0.37
2H-1	ER	100	6.70	0.356
2H-1	ER	120	6.90	0.383
2H-1	ER	140	7.10	0.4
2H-2	ER	14	7.34	0.536
2H-2	ER	98	8.18	0.548
2H-3	ER	20	8.90	1.208
2H-3	ER	95	9.65	0.659
2H-4	ER	17	10.37	0.469
2H-4	ER	97	11.17	0.859
2H-5	ER	20	11.90	0.816
2H-5	ER	40	12.10	0.471
2H-5	ER	60	12.30	0.638
2H-5	ER	100	12.70	0.784
2H-5	ER	120	12.90	1.36
2H-6	ER	20	13.40	0.448
2H-6	ER	40	13.60	0.838
2H-6	ER	60	13.80	0.931
2H-6	ER	100	14.20	0.515
2H-6	ER	120	14.40	0.791
2H-6	ER	140	14.60	0.781
2H-6	ER	140	14.60	0.852
2H-7	ER	20	14.90	0.63
2H-7	ER	40	15.10	0.535
3H-4	ER	20	19.03	1.011
3H-4	ER	40	19.23	0.844
3H-4	ER	61	19.44	0.848
3H-4	ER	105	19.88	0.754
3H-4	ER	132	20.15	0.821
3H-5	ER	26	20.59	0.712
3H-5	ER	40	20.73	0.771

Table 26. Wenner array electrical resistivity results for Holes NGHP-01-10B, NGHP-01-10D, and NGHP-01-12A. (To view the complete table, please see the ASCII files.)—Continued

Core, section	Sample	Top	Depth (mbsf)	ER (W×m)
NGHP-01-12A—Continued				
3H-5	ER	107	21.40	0.741
3H-6	ER	20	22.03	0.655
3H-6	ER	50	22.33	0.716
3H-6	ER	94	22.77	0.679
3H-6	ER	117	23.00	0.725
3H-7	ER	18	23.51	0.82
3H-7	ER	56	23.89	0.7
3H-7	ER	90	24.23	0.648
3H-8	ER	26	25.08	0.562
4X-1	ER	26	40.26	0.633
4X-1	ER	43	40.43	0.721
4X-1	ER	65	40.65	0.895
4X-1	ER	87	40.87	1.523
4X-1	ER	87	40.87	0.603
4X-2	ER	7	41.22	0.791
4X-2	ER	27	41.42	1.21
4X-2	ER	65	41.80	0.654
4X-2	ER	100	42.15	0.513
4X-2	ER	120	42.35	0.899
4X-3	ER	27	42.92	0.881
4X-3	ER	47	43.12	1.095
4X-3	ER	77	43.42	0.838
4X-3	ER	99	43.64	1.054
4X-4	ER	19	44.16	0.565
4X-4	ER	39	44.36	0.72
8X-1	ER	53	84.33	0.695
8X-1	ER	73	84.53	0.564
8X-1	ER	81	84.61	0.561
8X-1	ER	108	84.88	1.441
8X-2	ER	13	85.43	0.71
8X-2	ER	60	85.90	1.419
8X-2	ER	107	86.37	1.125
8X-3	ER	18	86.82	0.966
8X-3	ER	65	87.29	1.539
8X-3	ER	86	87.50	0.93
8X-3	ER	115	87.79	0.953
8X-4	ER	29	88.43	0.861
8X-4	ER	59	88.73	0.785
8X-4	ER	84	88.98	0.649
8X-4	ER	122	89.36	0.834
12X-1	ER	20	96.50	1.151
12X-1	ER	40	96.70	0.654
12X-1	ER	61	96.91	0.973
12X-1	ER	92	97.22	1.196
12X-1	ER	110	97.40	1.044
12X-2	ER	20	97.95	0.903
12X-2	ER	44	98.19	0.89
12X-3	ER	20	98.74	0.703
12X-3	ER	40	98.94	0.582
12X-3	ER	60	99.14	0.803
12X-3	ER	81	99.35	0.875
12X-3	ER	100	99.54	0.79
12X-4	ER	18	100.22	0.714
12X-4	ER	47	100.51	0.71
12X-4	ER	71	100.75	0.725
12X-4	ER	94	100.98	0.875
13X-1	ER	30	141.60	0.753
13X-1	ER	50	141.80	0.704
13X-1	ER	70	142.00	0.747
13X-1	ER	89	142.19	0.749
13X-2	ER	10	142.40	0.749
13X-2	ER	30	142.60	0.825
13X-2	ER	50	142.80	0.837
13X-2	ER	70	143.00	0.765
13X-3	ER	30	143.73	0.776
13X-3	ER	50	143.93	0.66
13X-3	ER	70	144.13	0.677
13X-3	ER	90	144.33	0.618
13X-3	ER	110	144.53	0.843
13X-3	ER	130	144.73	0.703
13X-4	ER	10	145.03	0.546
13X-4	ER	30	145.23	0.573
13X-4	ER	50	145.43	0.611
13X-4	ER	66	145.59	0.652

Table 27. Contact P-wave velocity results determined on split cores sections from Holes NGHP-01-10B, NGHP-01-10D, and NGHP-01-12A.

Core, section	Sample	Top	Depth (mbsf)	Temp (°C)	VP (km/s)
NGHP-01-10B					
1H-2	VP	12	1.62	22.27	1.447
2H-1	VP	30	3.40	22.82	1.469
NGHP-01-10D					
1H-1	VP	43	0.43	22.01	1.478
1H-2	VP	15	1.65	22.68	1.480
2H-1	VP	40	4.50	23.07	1.483
2H-2	VP	40	5.70	22.81	1.486
2H-3	VP	40	7.20	22.65	1.486
2H-4	VP	40	8.70	22.26	1.491
2H-5	VP	40	10.20	22.54	1.504
3H-1	VP	30	13.90	22.93	1.497
NGHP-01-12A					
1H-3	VP	47	3.47	19.79	1.478
1H-4	VP	43	4.93	20.5	1.470
2H-1	VP	50	6.20	21.4	1.482
2H-2	VP	60	7.80	21.69	1.465
2H-3	VP	58	9.28	21.85	1.494

resistivities, to compare the gas hydrate concentration between the extremely high electrical resistivities and the surrounding high electrical resistivity sediments, to determine if a free methane gas phase exists below the base of gas hydrate stability, and to examine the gas composition of dissociating gas hydrate to determine if Structure II gas hydrate exists. Specific objectives at Site NGHP-01-12 were to compare the quantity of gas hydrate in the sediment section with Site NGHP-01-10 to constrain the areal extent of the large gas hydrate deposit.

Pressure Core Operations and Measurements

Pressure coring tools were deployed fifteen times at Site NGHP-01-10 and six times at Site NGHP-01-12 (table 30); eight PCS cores (three in Hole NGHP-01-10B, three in Hole NGHP-01-10D, and two in Hole NGHP-01-12A), seven FPC cores (three in Hole NGHP-01-10B, two in Hole NGHP-01-10D, and two in Hole NGHP-01-12A) and six HRC cores (two in Hole NGHP-01-10B, two in Hole NGHP-01-10D, and two in Hole NGHP-01-12A). Figures 36 and 37 show the pressure and temperature history of the cores during deployment, coring, recovery, and chilling (in the ice shuck) of the pressure coring tools. Figures 38 and 39 show the measurements made on the nine successful cores at full recovered pressure and during depressurization. Figures 40 and 41 show the gas and fluid released from the successful cores and the character of the pressure decrease during depressurization.

Site NGHP-01-10 was the first site where pressure cores contained internal DST Micro pressure-temperature recorders (see "Pressure Coring" in the "Methods" chapter). These small data loggers, fixed in the piston of the coring tool, showed that

Table 28. Thermal conductivity results for Holes NGHP-01-10B, NGHP-01-10D, and NGHP-01-12A.

Core, section	Sample	Top	Depth (mbsf)	Thermal conductivity (W/[m×K])
NGHP-01-10B				
1H-1	TC	75	0.75	0.847
2H-3	TC	75	6.85	0.871
4X-2	TC	30	23.80	0.825
10X-2	TC	30	61.82	0.615
12X-3	TC	45	72.17	0.778
14X-3	TC	75	93.55	0.61
26X-1	TC	42	166.92	0.782
29X-3	TC	37	179.47	0.879
30X-1	TC	15	185.85	0.794
NGHP-01-10D				
1H-3	TC	19	3.19	0.833
2H-3	TC	54	7.34	0.894
3H-3	TC	76	17.36	0.968
4H-3	TC	76	26.81	0.766
5X-1	TC	75	33.35	0.521
7X-2	TC	34	42.94	0.638
10X-4	TC	40	63.42	0.567
13X-1	TC	15	78.95	0.683
14X-3	TC	47	91.07	0.675
16X-3	TC	46	101.46	0.532
17X-3	TC	75	111.20	0.75
18X-3	TC	75	120.65	0.71
20X-3	TC	60	129.63	0.768
23X-3	TC	75	149.37	0.816
24X-3	TC	75	158.75	0.814
27X-3	TC	75	178.75	0.89
28X-3	TC	35	187.95	0.816
29X-3	TC	35	197.55	0.787
NGHP-01-12A				
1H-3	TC	30	3.30	0.833
2H-3	TC	35	9.05	0.840
3H-3	TC	35	17.68	0.809
4X-3	TC	61	43.26	0.814
8X-3	TC	59	87.23	0.833
12X-3	TC	76	99.30	0.860
13X-3	TC	75	144.18	0.791

the cores do not warm as fast as the internal corer temperature records imply (figs. 36 and 37; for further discussion, see "Pressure Coring" in the "Methods" chapter).

Core NGHP-01-10B-08Y (50.1 mbsf), collected in the zone of extremely high electrical resistivity, retrieved a full core (0.86 m) close to *in situ* pressure (table 30). No data were collected during the coring operation for Core NGHP-01-10B-08Y. The core was transferred to the MSCL-P and X-ray images and gamma density were collected (fig. 38A). Unusually, *P*-wave velocities were unreliable due to very low amplitudes, indicating that small amounts of gas may have been present in the core. This gas may have been generated by partial dissociation of gas hydrate as the core warmed during recovery. The X-ray image and gamma density profile, which correlate closely, showed five or six horizontal layers of presumed gas hydrate and wispy subvertical veins within a relatively homogenous matrix, as

Table 29. *In situ* temperature estimates at Site NGHP-01-10.

Core	Assumed thermal conductivity (W/m•K)	Tool	Temperature (°C)	Ad-hoc calibration correction	Corrected temperature (°C)	Estimated uncertainty	Data quality
B06X	0.95	DVTP	7.5	0.50	8	0.05	good
B16X	0.95	DVTP	10.8	0.50	11.19	0.6	
B29X	0.95	DVTP	NA	0.50	NA	0.6	poor
D10X	0.86	DVTP	NA	0.50	NA		poor
D20X	0.95	DVTP	11.87	0.50	12.37	0.1	good
D29X	0.95	DVTP	15.35	0.50	15.85		good

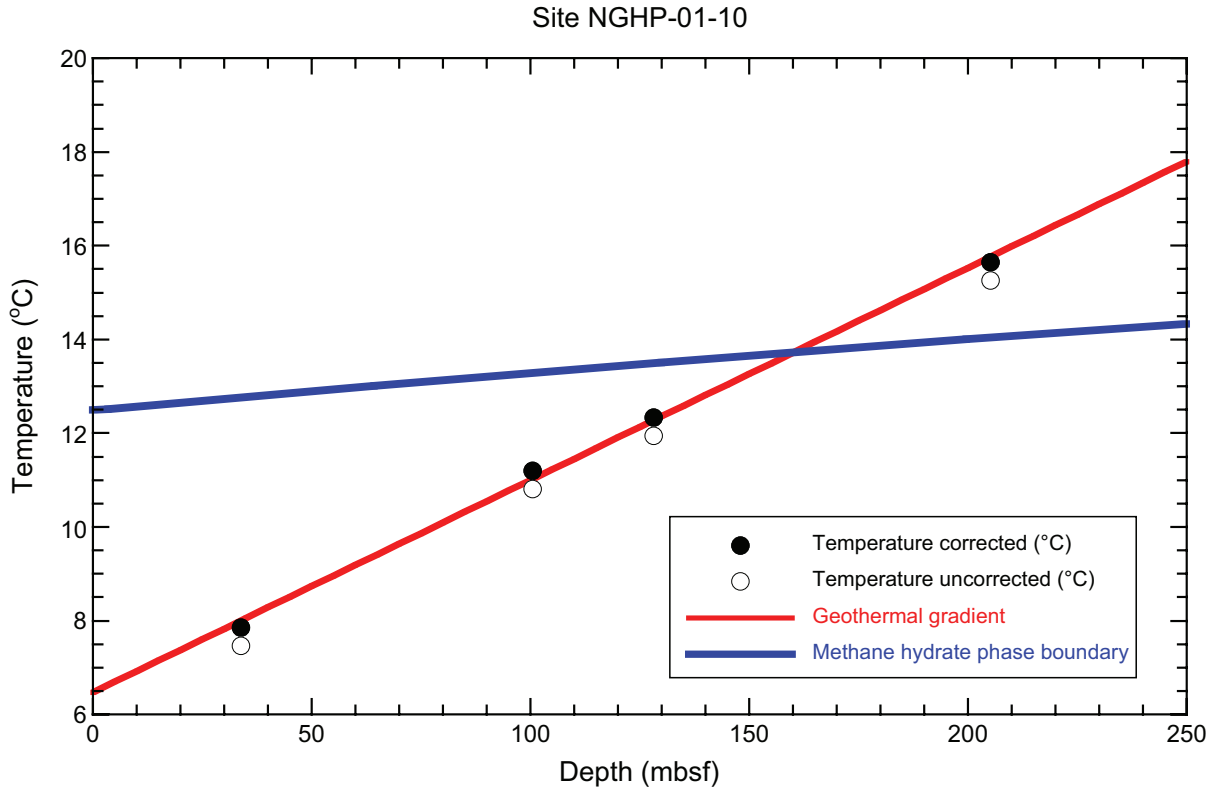


Figure 35. Geothermal gradient and estimated depth to the BSR from *in situ* temperature measurements for Site NGHP-01-10. [BSR, bottom-simulating reflector]

well as broad patches of lower density which were previously interpreted as finely-distributed, grain-displacing gas hydrate. Core NGHP-01-10B-08Y was transferred to a storage chamber for further work after the cruise (see "Singapore Pressure Core Studies" in the "Appendix").

Core NGHP-01-10B-15P, collected below the zone of extremely high electrical resistivity (98.2 mbsf), retrieved a full core (1.00 m) under low pressure (table 30). The pressure corer did not seal until the core was less than 200 mbsl (fig. 36A). No X-rays or gamma density measurements were made on this core. Core NGHP-01-10B-15P released over 31 L of methane, corresponding to 21 percent methane hydrate as a percent of pore volume or 174 mL of gas hydrate (table 31), but this is likely to be a large underestimate of the volume of gas hydrate contained in the core due to the loss of pressure and mass during recovery. The depressurization profile (fig. 40A) shows a steady release of gas, indicating that the methane being released from the core was already in the gas phase. Expelled liquid volumes were not measured for this core. Core NGHP-01-10B-15P had no nondestructive measurements made on it after depressurization. No chlorinity measurements were made on this core.

Core NGHP-01-10B-18Y (117.4 mbsf), collected below the zone of extremely high electrical resistivity, retrieved a full core (0.86 m) at full *in situ* pressure (table 30). This core showed an increase in pressure as it warmed during handling on

Table 30. Summary of pressure-coring operations at Site NGHP-01-10.

Core ID	Top of core (mbsf)	Length recovered (cm)*	Length curated (cm)*	Pressure at core depth (bar)	Pressure recovered (bar)				Comments
					logged**		gauge***		
NGHP-01-10B									
05P	31.4	--	0	108	0		--		Ball valve did not close
08Y	50.1	86	90	110	100		100		Data logger did not record; stored in storage chamber
11E	70.0	--	17	112	0		--		No retraction
15P	98.2	100	113	115	23	@12 °C	17		Low pressure, no x-ray
18Y	117.4	86	90	117	118		118		Normal operation
21Y	136.6	--	33	119	0		--		Core did not retract
27E	174.1	--	42	123	0		--		No retraction; tool modified after run
28P	175.1	100	167	123	60		60		Normal operation
NGHP-01-10D									
06P	40.1	--	29	109	0		--		Ball valve did not close
09Y	58.8	--	51	111	0		--		Overretracted
12E	77.8	68	115	113	95	@12 °C	95		Normal operation
15P	97.0	--	92	115	0		--		No pressure
19Y	125.8	--	88	118	0		--		Top seals leaked
22E	145.1	44	105	120	110		110		Data logger did not record
25P	164.4	100	122	122	90		87		Normal operation
NGHP-01-12A									
05Y	45.7	--	86	107	0		--		Overretracted
06E	46.7	102	108	107	90		95		Normal operation
07P	47.7	12	0	107	51		53		Normal operation
09Y	93.3	86	88	112	131	@12 °C	131	@12 °C	Normal operation
10E	94.3	--	0	112	0		--		Liner collapsed
11P	95.3	--	58	112	0		--		No pressure

Notes:
Water depth at Site NGHP-01-10 is 1049 mbsl. Water depth at Site NGHP-01-12 is 1018 mbsl. P=PCS, Y=FPC, E=HRC.
*Length measured from X-ray and gamma density analysis, which may not match curated core length.
**Last pressure recorded before data logger disconnected from corer autoclave. Temperature 2–4 °C unless otherwise noted.
***Pressure measured when autoclave pressure transducer connected to external gauge. Pressure measured at 7 ˚C unless otherwise noted.

deck before being placed in the ice shuck, indicating that minor gas hydrate dissociation may have occurred (fig. 36A). Core NGHP-01-10B-18Y was transferred to the MSCL-P and X-ray images, gamma density and *P*-wave velocity measurements were collected (fig. 38B). The X-ray image and gamma density profile showed thin low-density layers within a layered sediment structure. The *P*-wave velocity showed unusual variability on a scale of 5–10 cm that was not reflected in the gamma density but loosely correlated to 5–10-cm-thick light and dark patches on the X-ray image. Core NGHP-01-10B-18Y was depressurized in the MSCL-P, releasing 52.94 L of methane, corresponding to 25.4 percent methane hydrate as a percent of pore volume, or 299 mL of methane hydrate (table 31). Pressure rebounds during depressurization and a pressure-volume plateau near 60 bar pressure (figs. 40A and 41A) indicated gas hydrate dissociation at 7 °C (laboratory temperature). One intermediate MSCL-P scan was made at 44 bar, showing crack evolution but limited disturbance, and a final MSCL-P scan was collected at atmospheric pressure which showed an intact core but with much lower density (fig. 40A). The texture of the split core was light and flaky, like a properly-cooked salmon fillet (fig. 42). One chlorinity measurement was made on this core (47–60 cm, 606 mM), which only showed a small amount of freshening compared with the estimated baseline chlorinity at this depth (see "Inorganic Geochemistry"). However, there is considerable uncertainty in the baseline chlorinity in this region of high gas hydrate concentrations.

Core NGHP-01-10B-28P (175.1 mbsf), collected below the estimated base of gas hydrate stability, retrieved a full core (1.00 m) under pressure (table 30). The autoclave was placed in the MSCL-P for X-ray and gamma density measurements, which showed that the top half of the core was relatively uniform and that sediment existed in the lower half (fig. 39B). The core was depressurized, releasing 1.34 L of methane, which is less than methane saturation at *in situ* temperature and pressure (table 31). After depressurization, the autoclave was again measured in the MSCL-P, and a final X-ray image was collected when the outer barrel was removed, showing the overall expansion of the core due to gas (fig. 39B). The core was pinched as it was extruded, which deformed the core and caused it to lengthen from 1.00 m to 1.67 m. One chlorinity measurement was made on this core (105–117 cm, 527 mM), which was very similar to other chlorinity measurements made below the estimated depth of the BSR at this site (see "Inorganic Geochemistry").

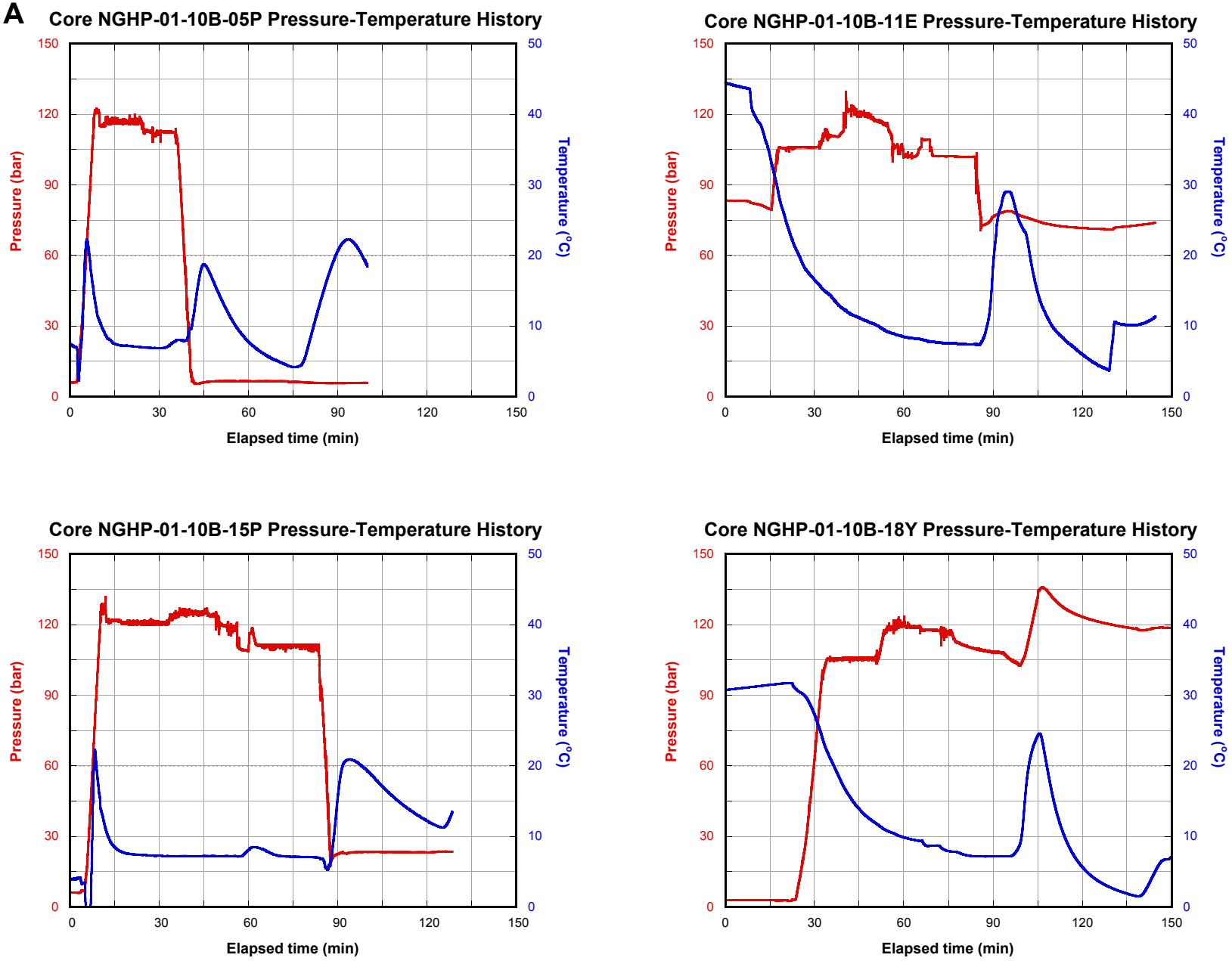


Figure 36. Temperature and pressure versus elapsed time for each pressure-corer deployment as recorded by the corer's internal data logger. There are no data for Core NGHP-01-10D-10E. Core NGHP-01-10C-12P is missing data at the beginning of the deployment.

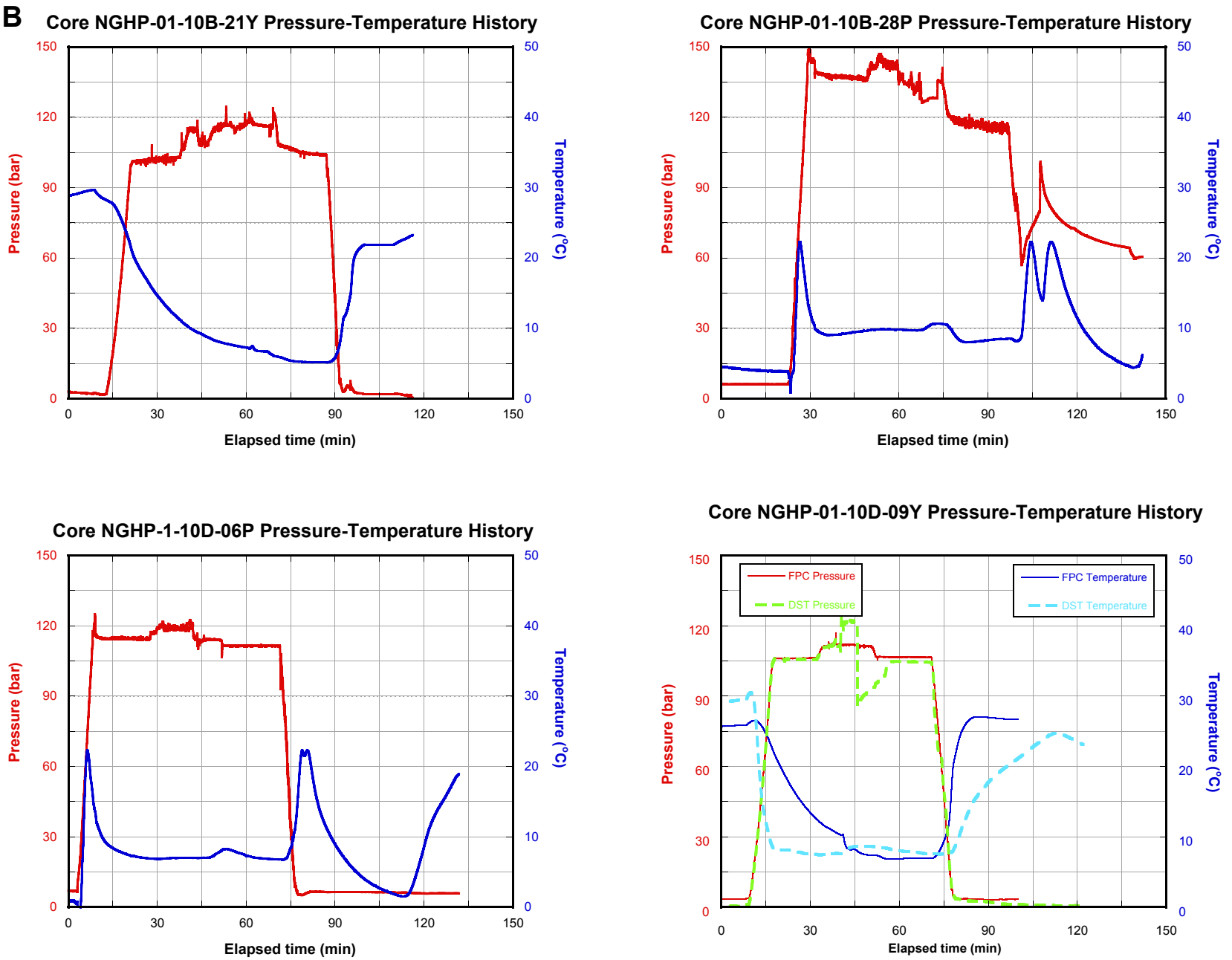


Figure 36. Temperature and pressure versus elapsed time for each pressure-corer deployment as recorded by the corer's internal data logger. There are no data for Core NGHP-01-10D-10E. Core NGHP-01-10C-12P is missing data at the beginning of the deployment.—Continued

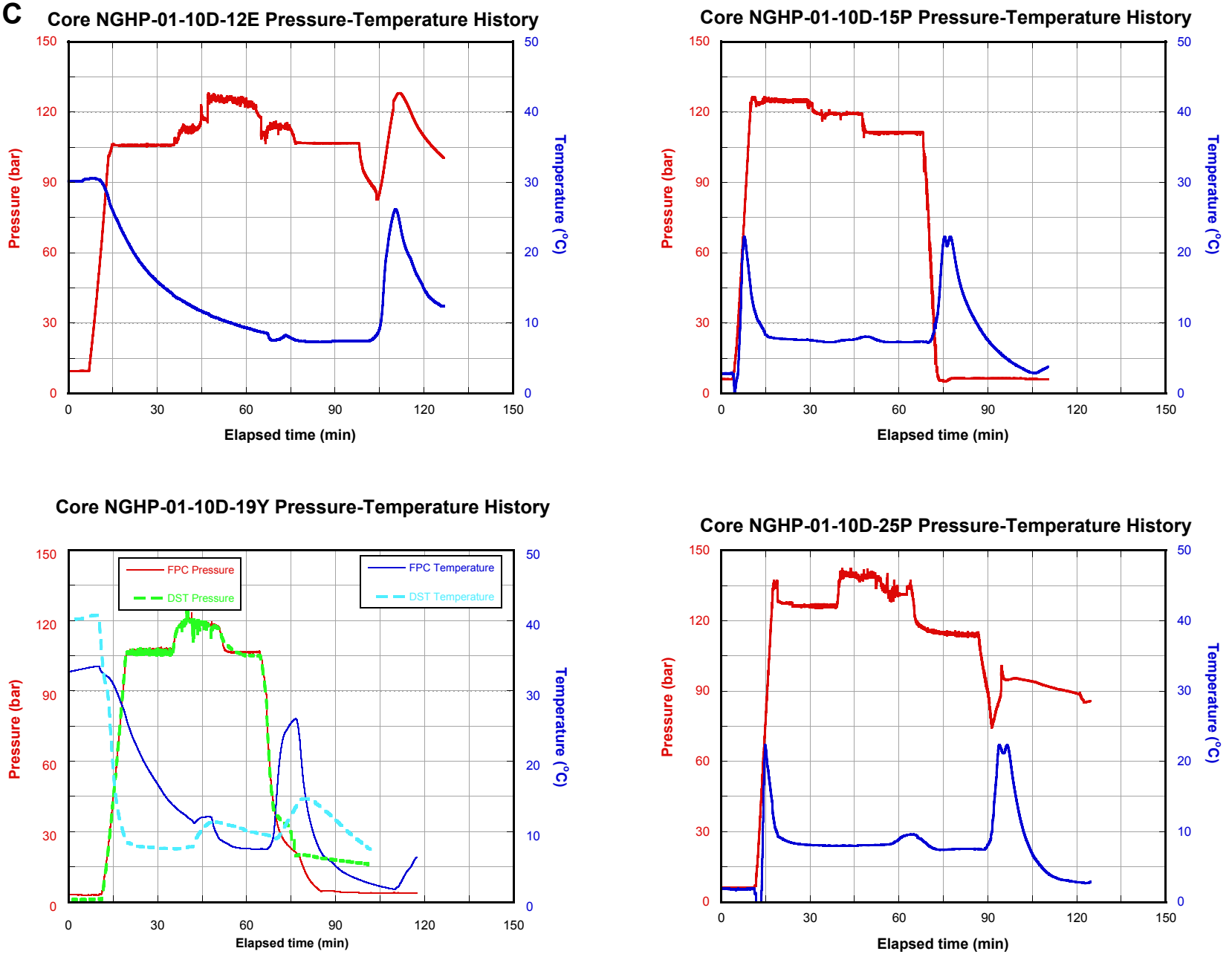


Figure 36. Temperature and pressure versus elapsed time for each pressure-corer deployment as recorded by the corer's internal data logger. There are no data for Core NGHP-01-10D-10E. Core NGHP-01-10C-12P is missing data at the beginning of the deployment.—Continued

D

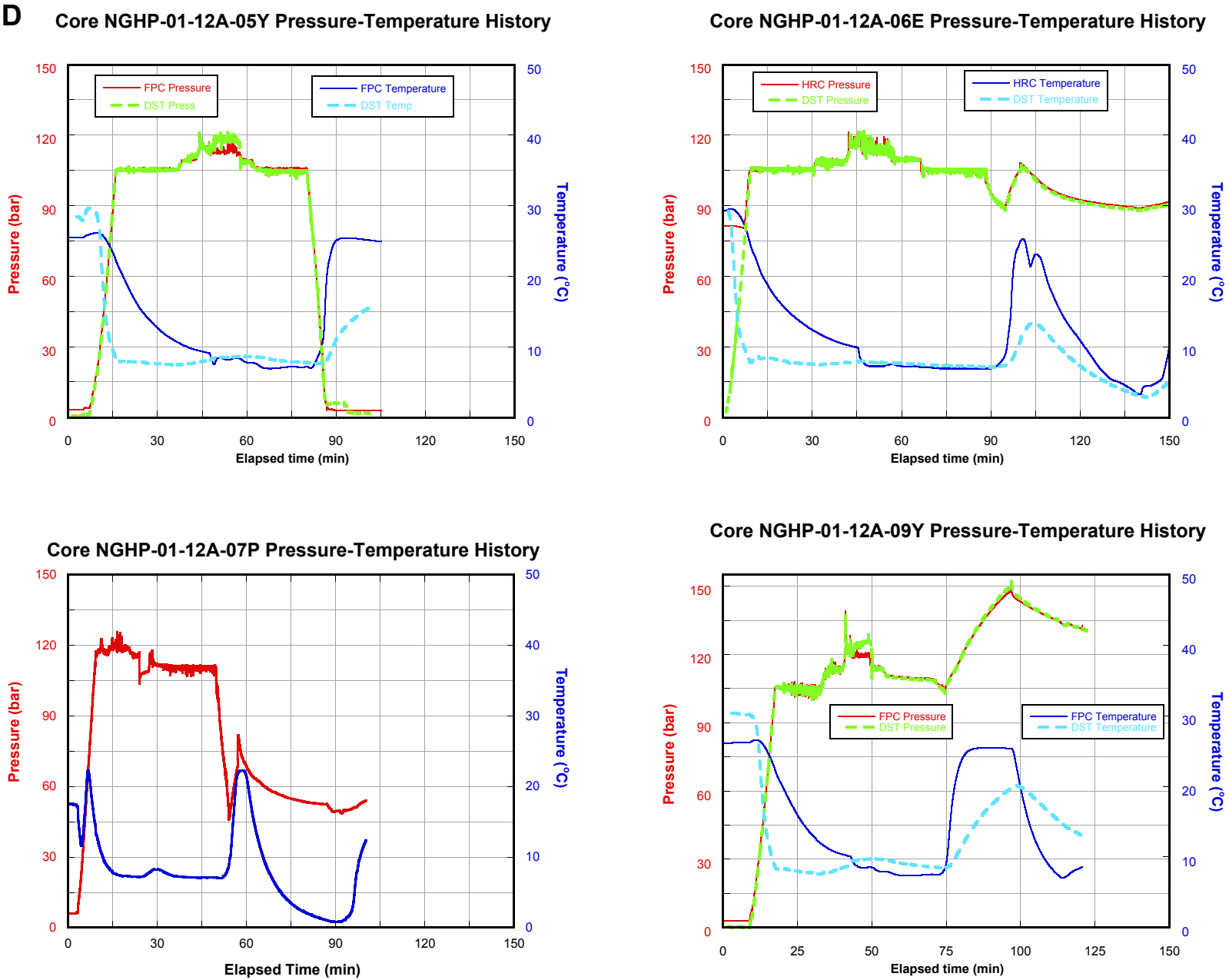


Figure 36. Temperature and pressure versus elapsed time for each pressure-corer deployment as recorded by the corer's internal data logger. There are no data for Core NGHP-01-10D-10E. Core NGHP-01-10C-12P is missing data at the beginning of the deployment.—Continued

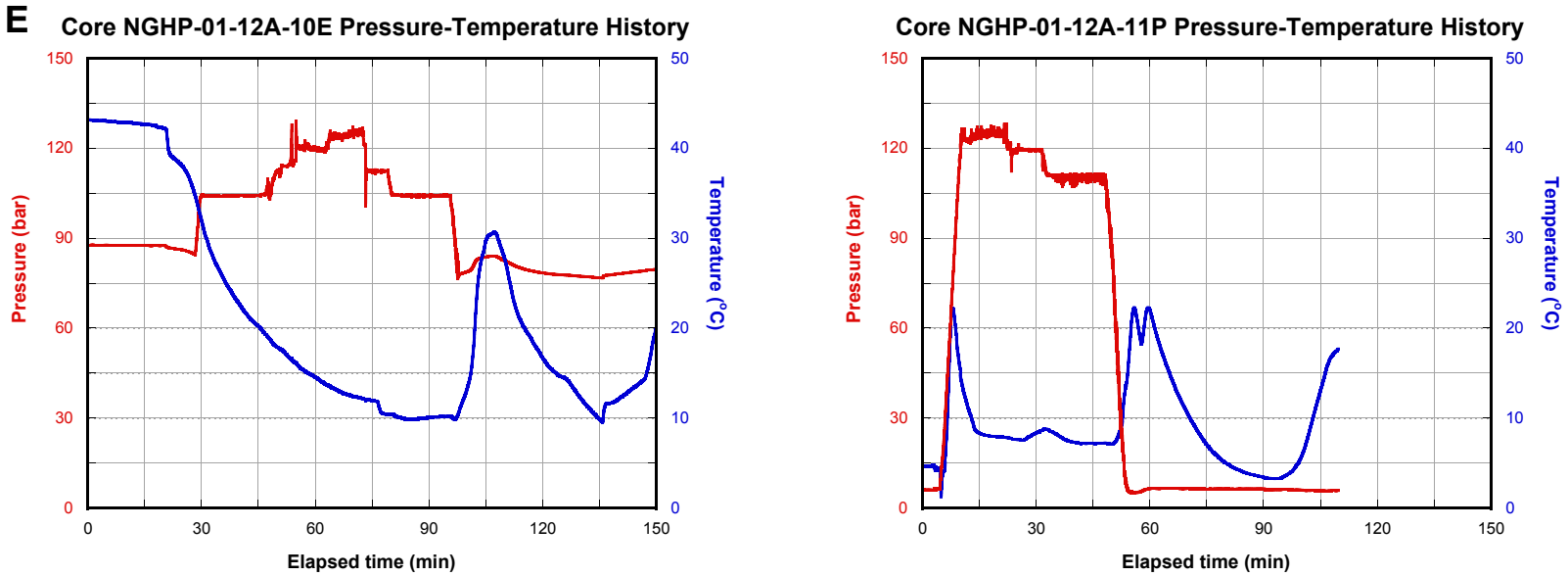


Figure 36. Temperature and pressure versus elapsed time for each pressure-corer deployment as recorded by the corer's internal data logger. There are no data for Core NGHP-01-10D-10E. Core NGHP-01-10C-12P is missing data at the beginning of the deployment.—Continued

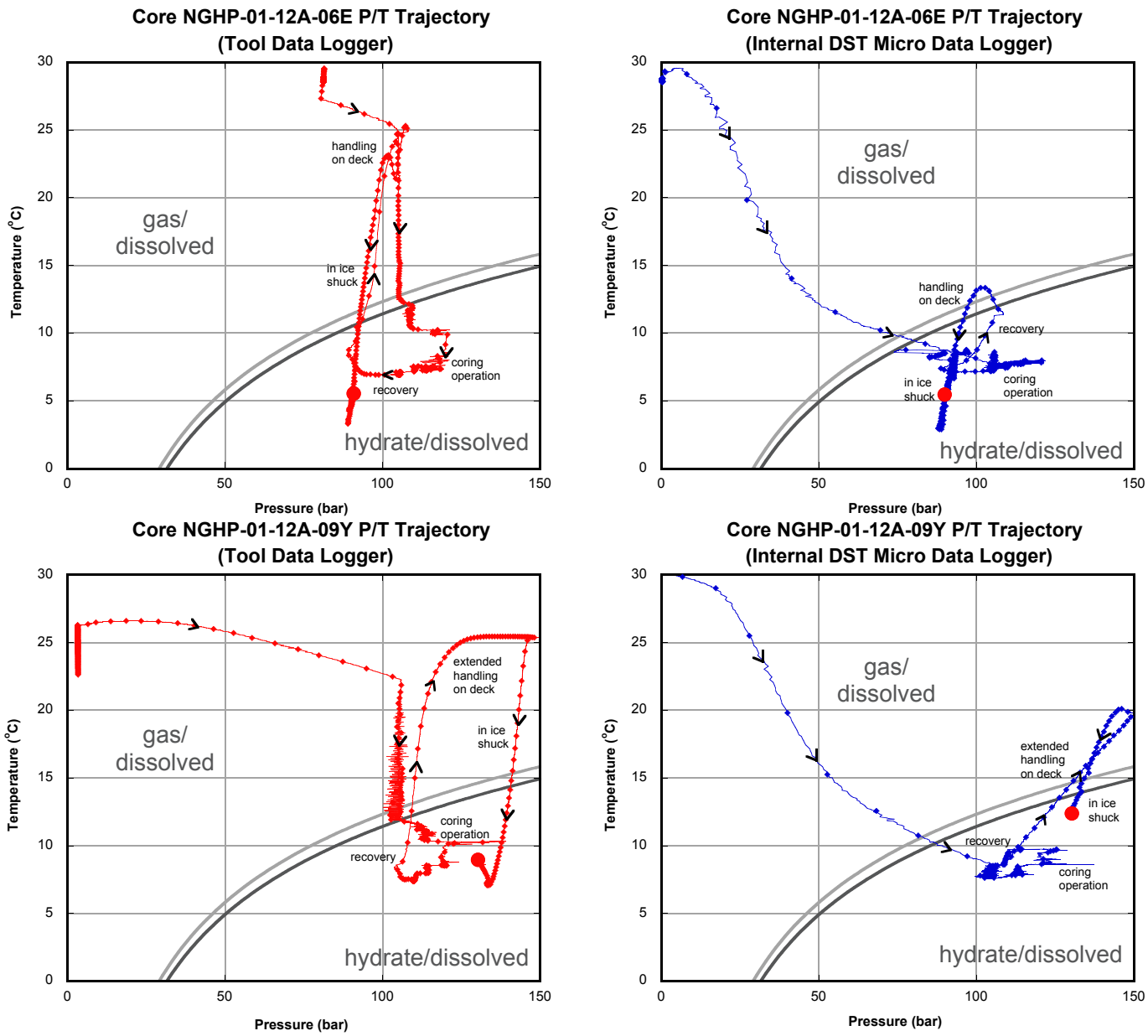


Figure 37. Temperature versus pressure for successful pressure-corer deployments which contained DST loggers within the pistons, showing trajectories relative to gas-hydrate stability at 30 ppt and 45 ppt salinity, calculated from Xu (2002, 2004). Small dots are every half-minute. Large dot is final temperature and pressure of autoclave prior to data logger removal.

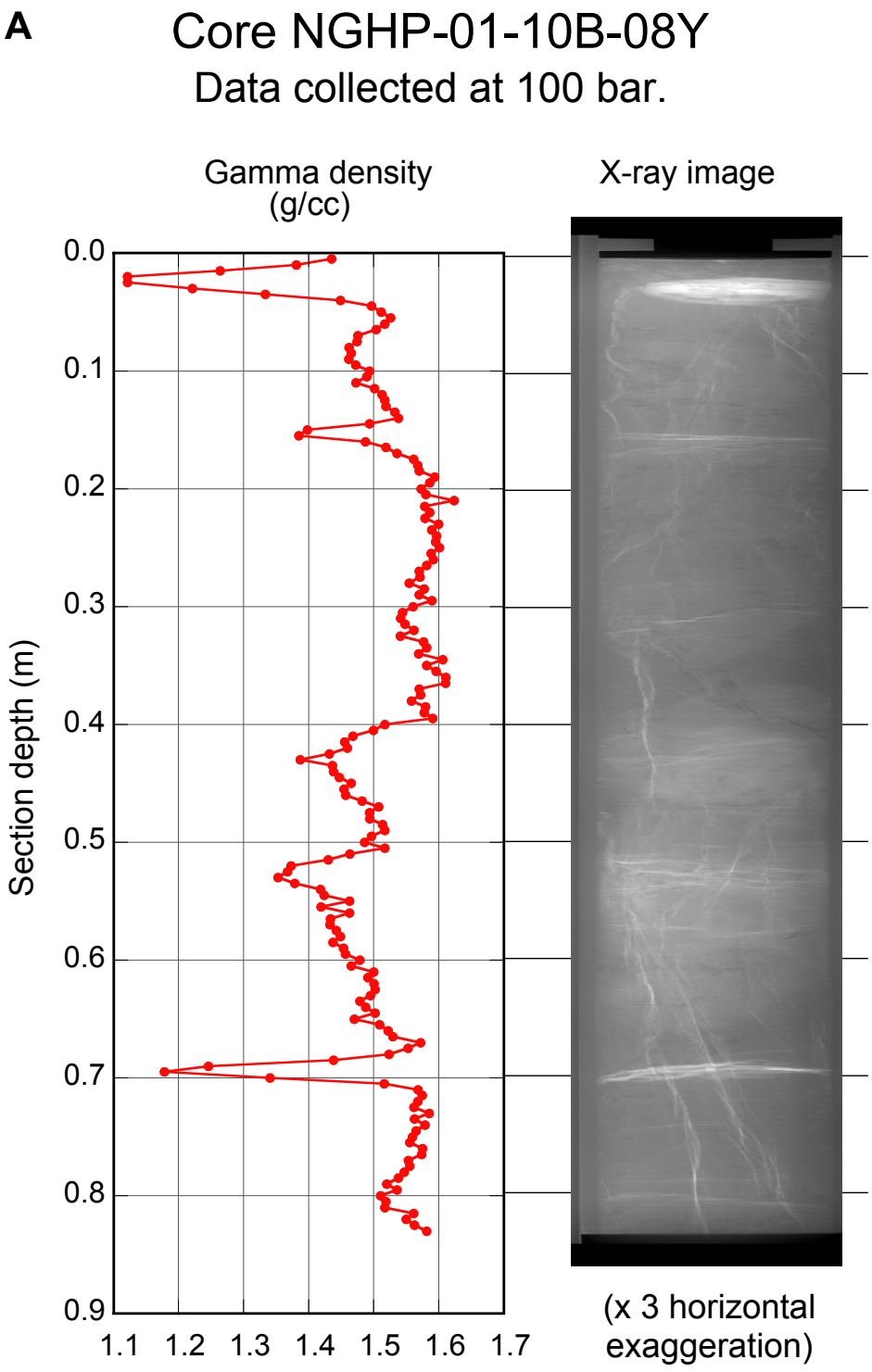


Figure 38. X-ray images, gamma density, and *P*-wave velocity collected at near *in situ* pressure and 7 °C for successful HYACINTH pressure cores. X-ray images have been stretched 300 percent in the cross-core direction to show detail.

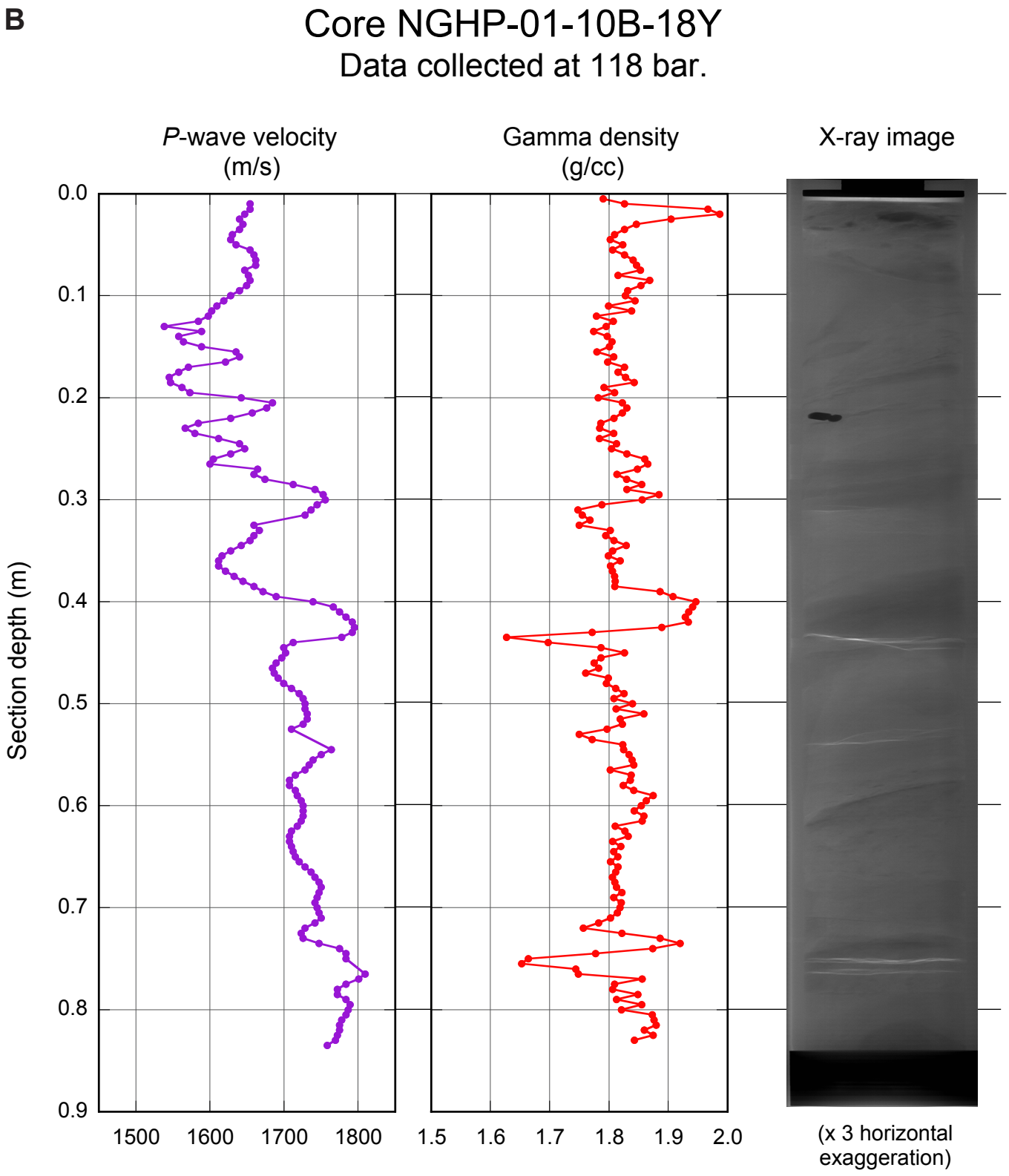


Figure 38. X-ray images, gamma density, and *P*-wave velocity collected at near *in situ* pressure and 7 °C for successful HYACINTH pressure cores. X-ray images have been stretched 300 percent in the cross-core direction to show detail.—Continued

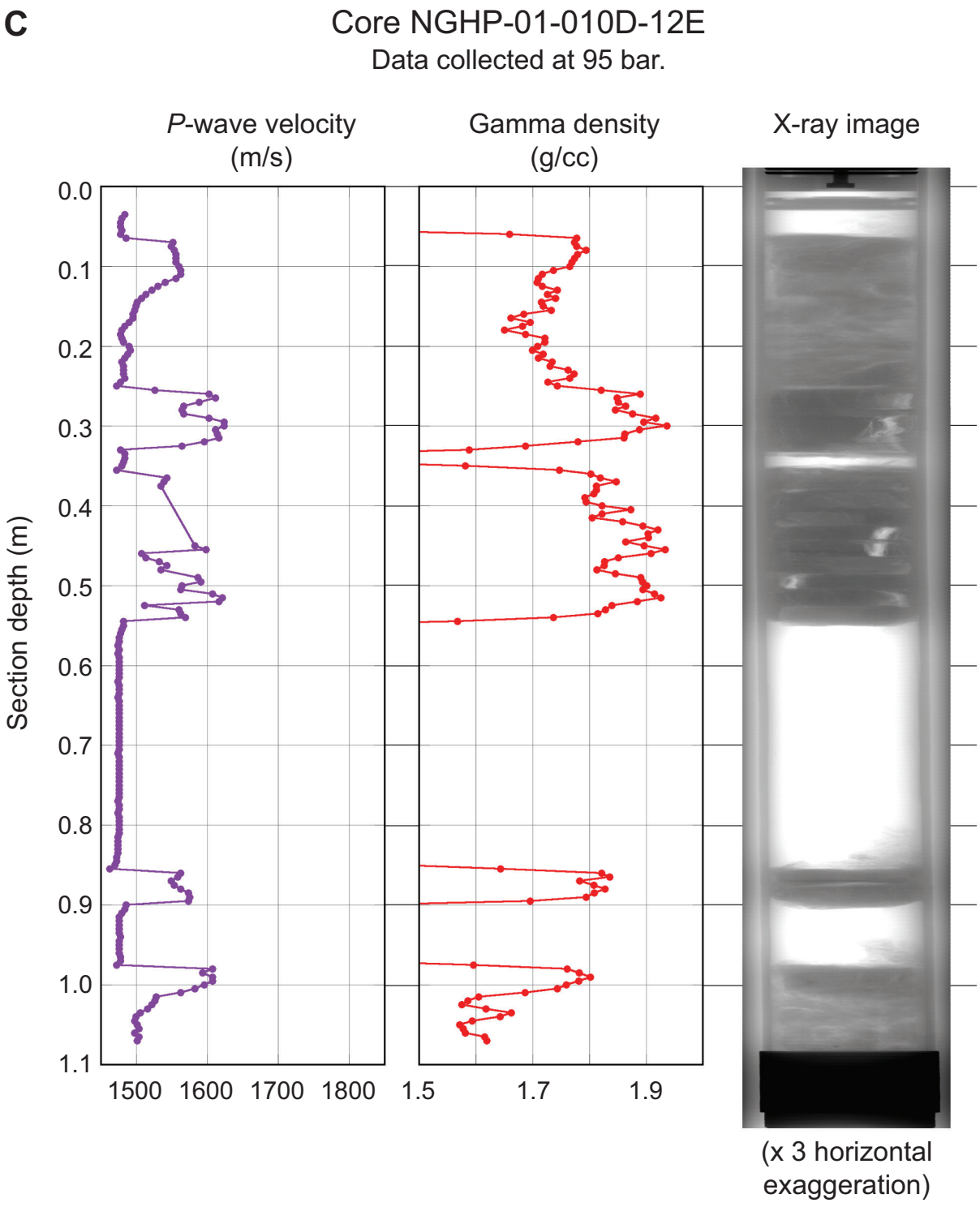


Figure 38. X-ray images, gamma density, and *P*-wave velocity collected at near *in situ* pressure and 7 °C for successful HYACINTH pressure cores. X-ray images have been stretched 300 percent in the cross-core direction to show detail.—Continued

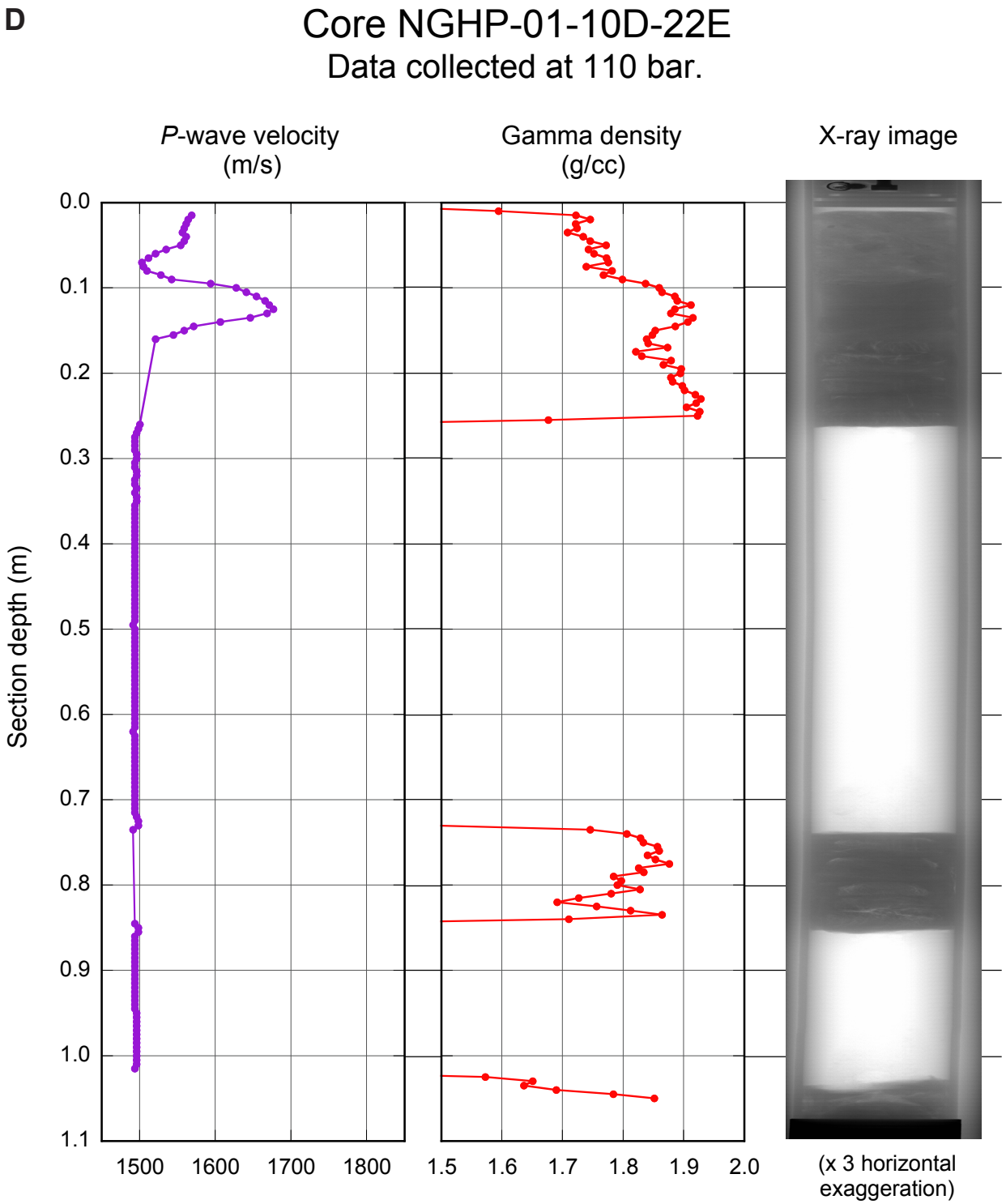


Figure 38. X-ray images, gamma density, and *P*-wave velocity collected at near *in situ* pressure and 7 °C for successful HYACINTH pressure cores. X-ray images have been stretched 300 percent in the cross-core direction to show detail.—Continued

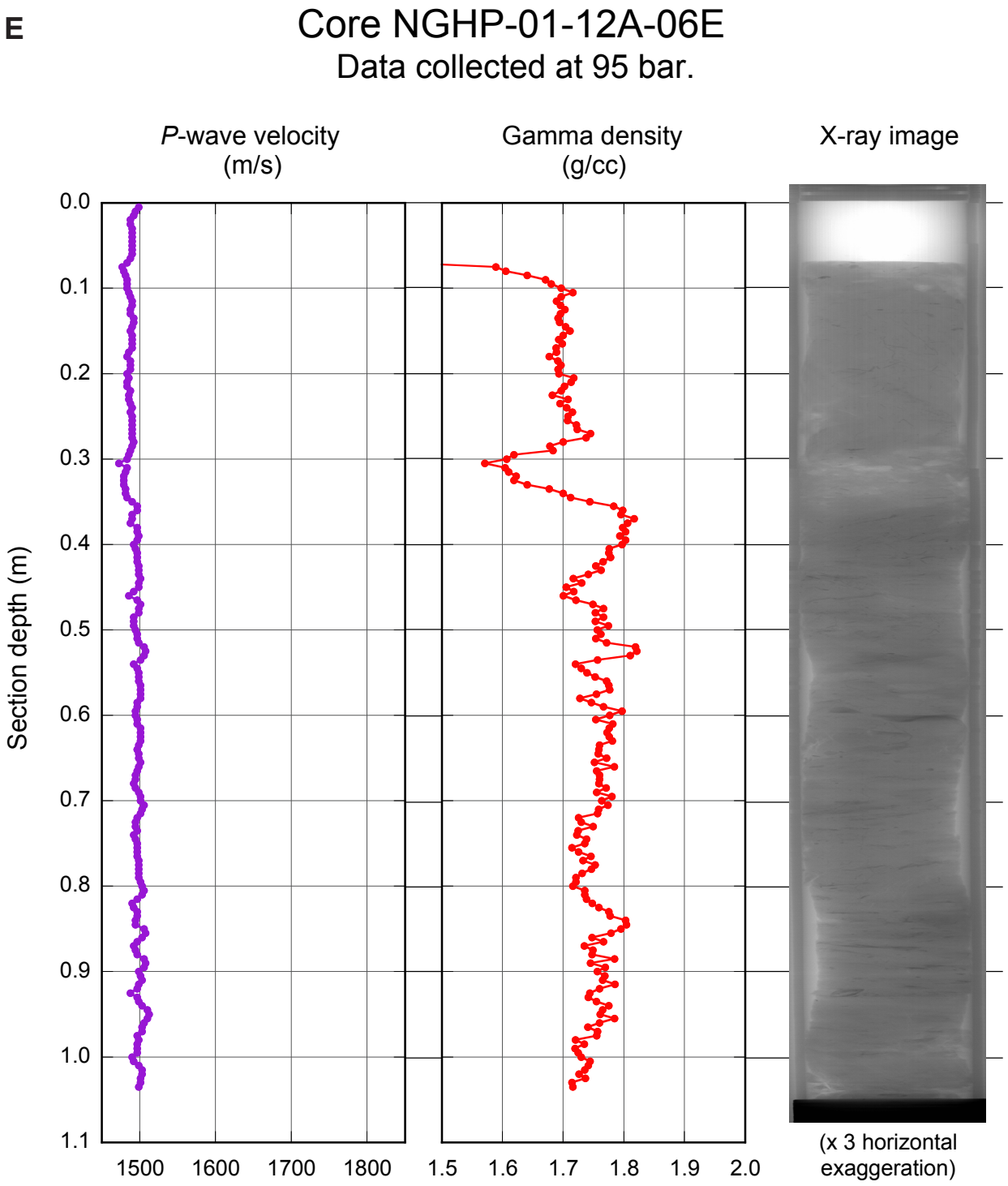


Figure 38. X-ray images, gamma density, and *P*-wave velocity collected at near *in situ* pressure and 7 °C for successful HYACINTH pressure cores. X-ray images have been stretched 300 percent in the cross-core direction to show detail.—Continued

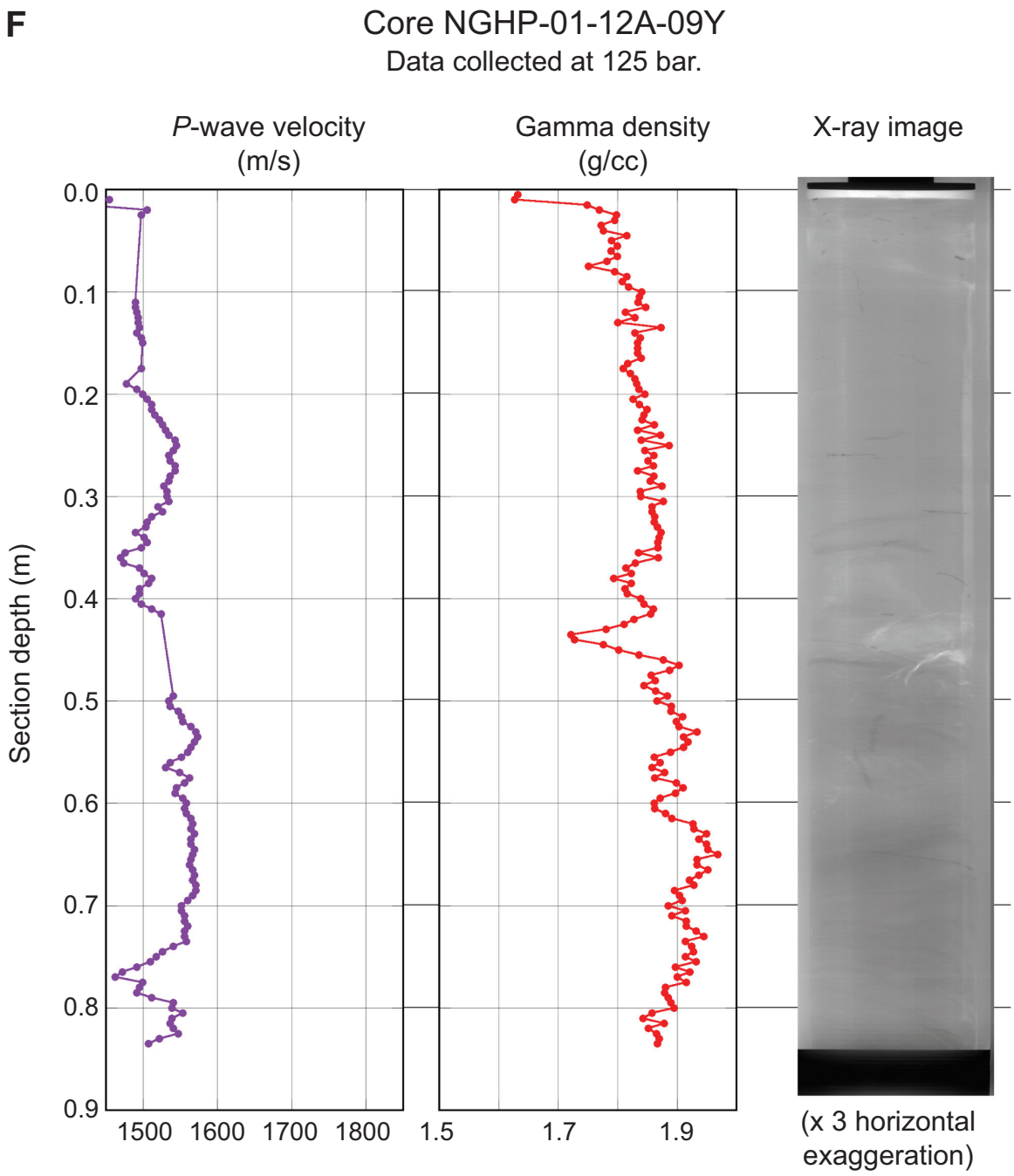


Figure 38. X-ray images, gamma density, and *P*-wave velocity collected at near *in situ* pressure and 7 °C for successful HYACINTH pressure cores. X-ray images have been stretched 300 percent in the cross-core direction to show detail.—Continued

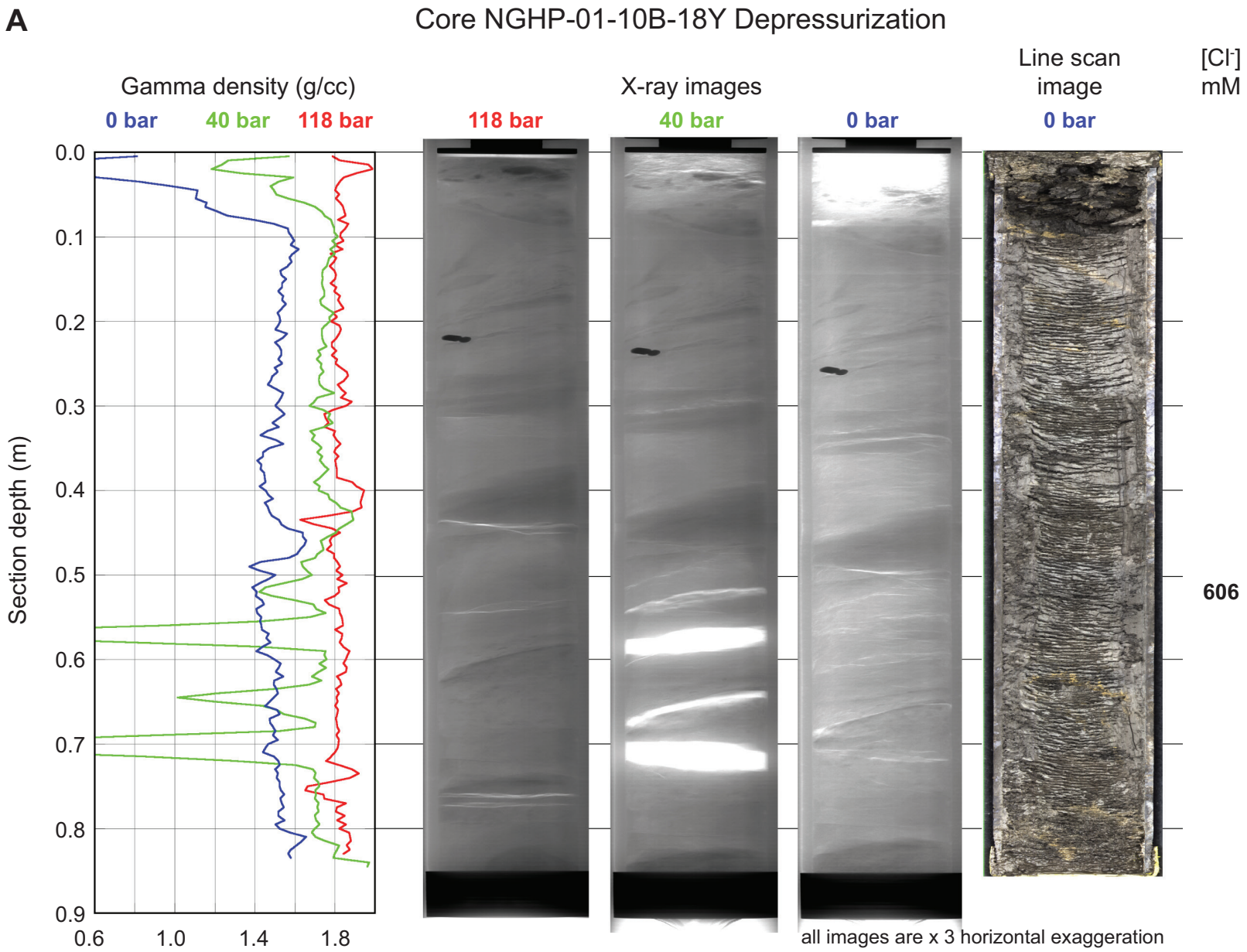


Figure 39. Summary of data taken from depressurized pressure cores before, during, and after depressurization, including gamma-density profiles collected before and after depressurization, X-ray images collected before and after depressurization, and line-scan images collected after depressurization. Curated "voids" in PCS cores have been removed from split-core images. Only Section NGHP-01-10B-18Y-2 is shown in the line-scan image for Core NGHP-01-10B-28P. There are no data for Cores NGHP-01-10B-15B and NGHP-01-12A-07P. [PCS, Pressure Core Sampler]

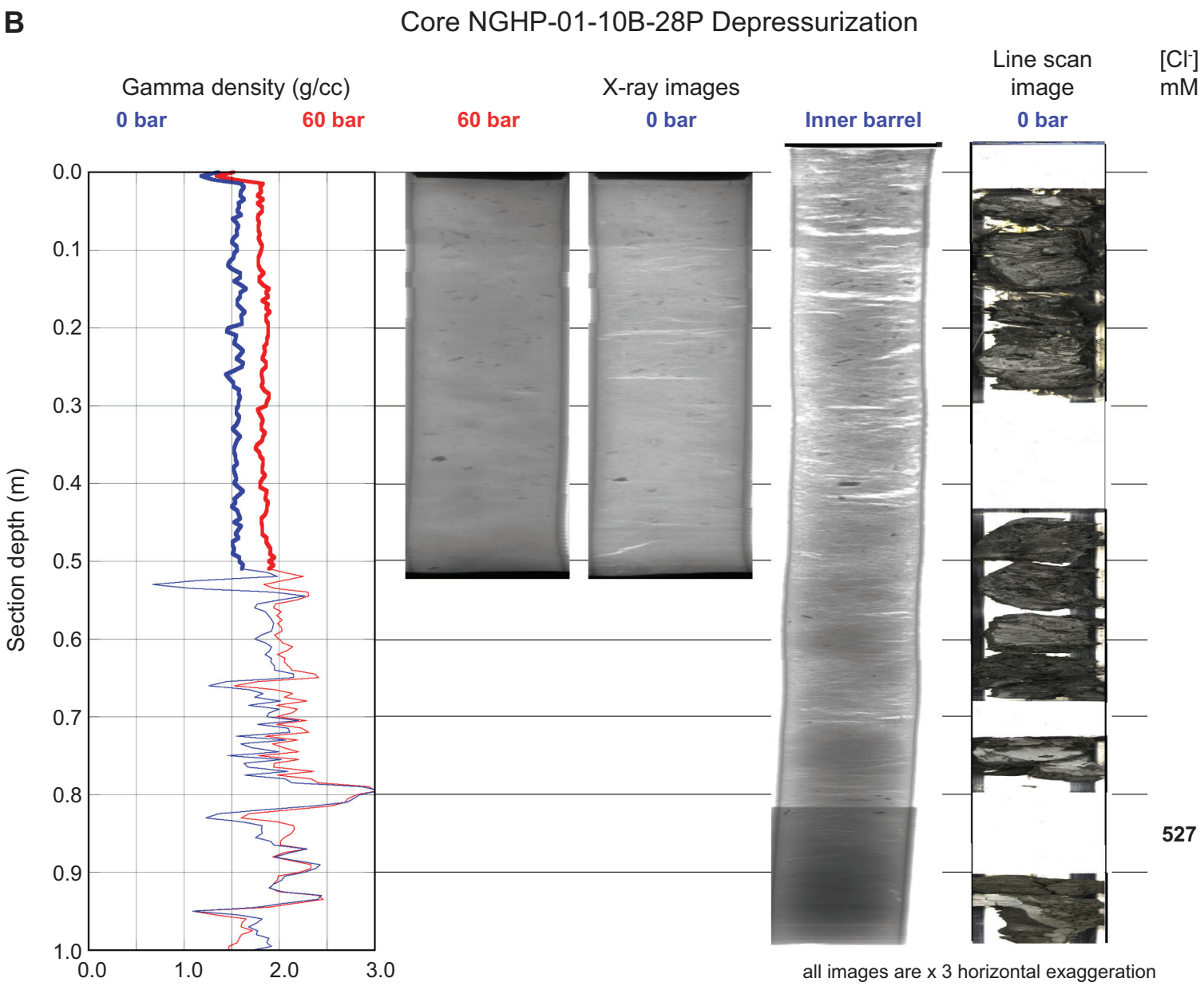


Figure 39. Summary of data taken from depressurized pressure cores before, during, and after depressurization, including gamma-density profiles collected before and after depressurization, X-ray images collected before and after depressurization, and line-scan images collected after depressurization. Curated "voids" in PCS cores have been removed from split-core images. Only Section NGHP-01-10B-18Y-2 is shown in the line-scan image for Core NGHP-01-10B-28P. There are no data for Cores NGHP-01-10B-15B and NGHP-01-12A-07P. [PCS, Pressure Core Sampler]—Continued

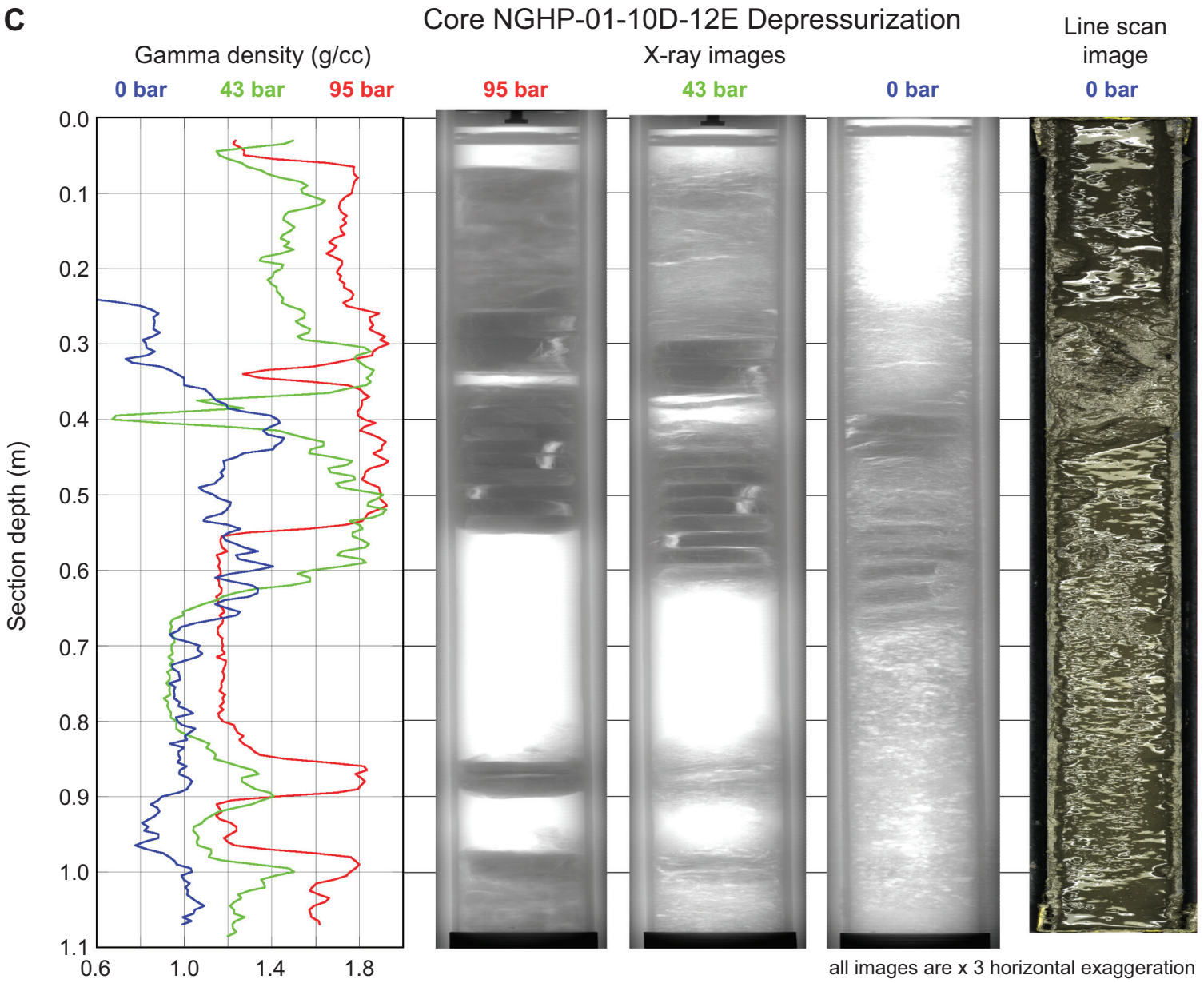


Figure 39. Summary of data taken from depressurized pressure cores before, during, and after depressurization, including gamma-density profiles collected before and after depressurization, X-ray images collected before and after depressurization, and line-scan images collected after depressurization. Curated "voids" in PCS cores have been removed from split-core images. Only Section NGHP-01-10B-18Y-2 is shown in the line-scan image for Core NGHP-01-10B-28P. There are no data for Cores NGHP-01-10B-15B and NGHP-01-12A-07P. [PCS, Pressure Core Sampler]—Continued

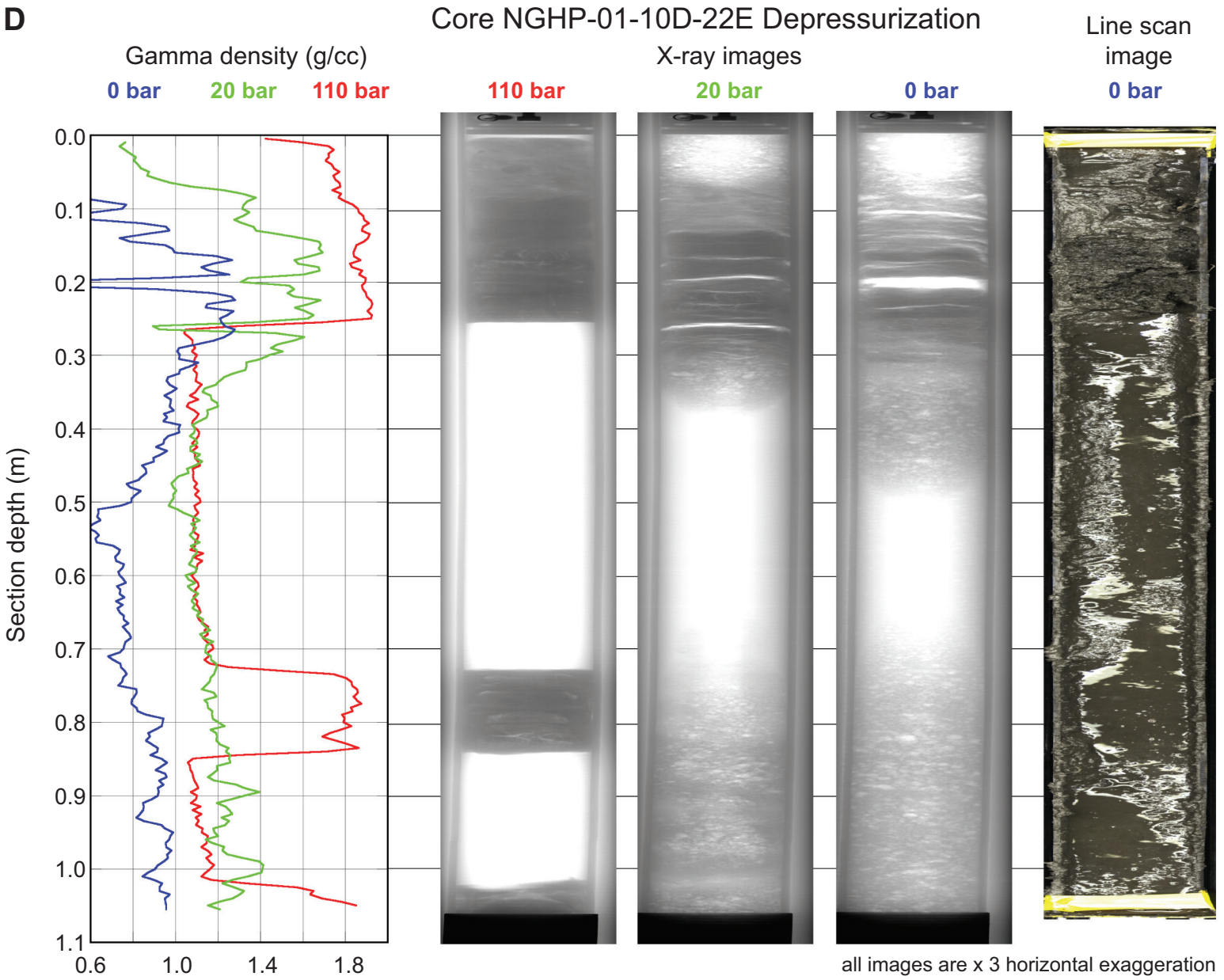


Figure 39. Summary of data taken from depressurized pressure cores before, during, and after depressurization, including gamma-density profiles collected before and after depressurization, X-ray images collected before and after depressurization, and line-scan images collected after depressurization. Curated "voids" in PCS cores have been removed from split-core images. Only Section NGHP-01-10B-18Y-2 is shown in the line-scan image for Core NGHP-01-10B-28P. There are no data for Cores NGHP-01-10B-15B and NGHP-01-12A-07P. [PCS, Pressure Core Sampler]—Continued

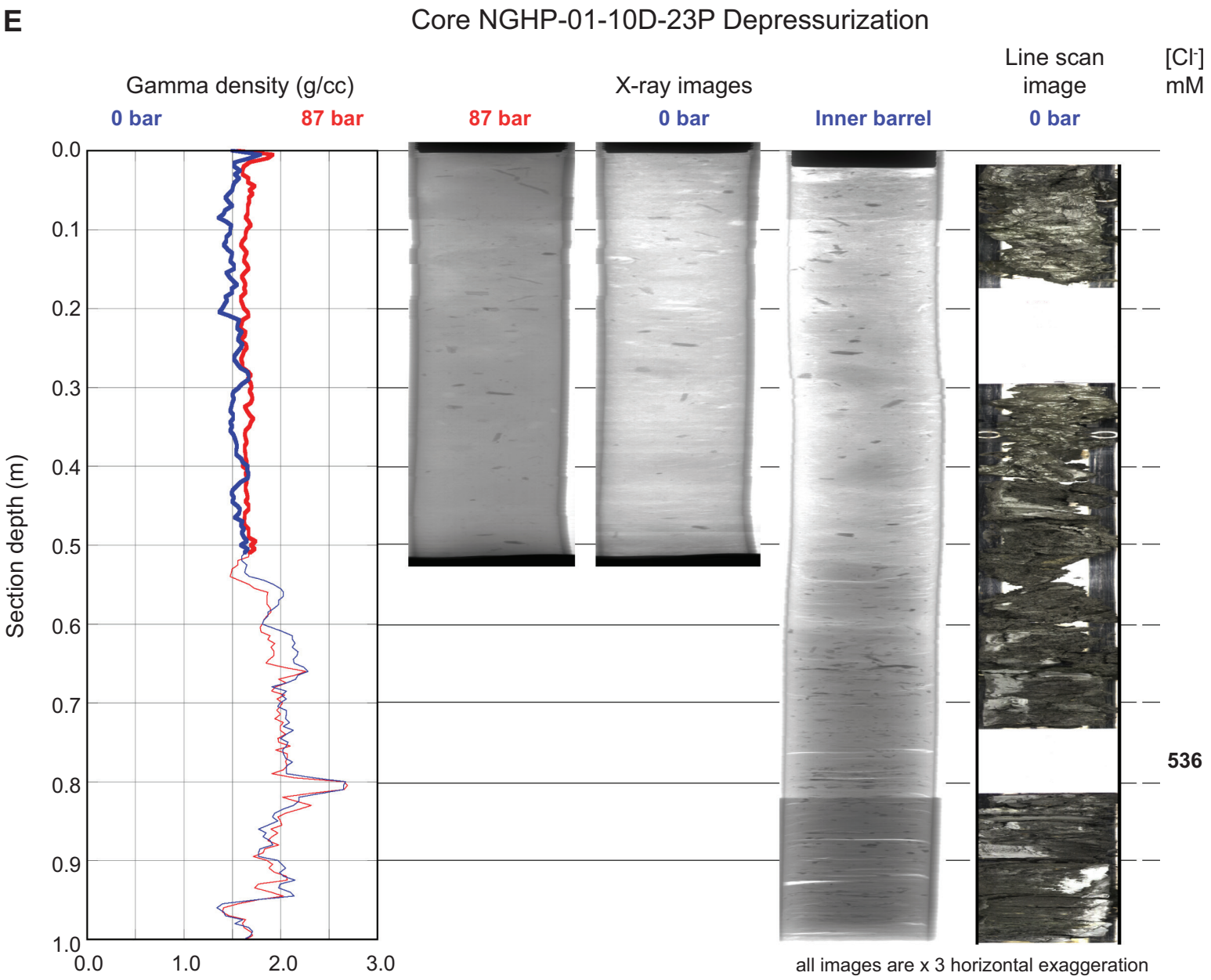


Figure 39. Summary of data taken from depressurized pressure cores before, during, and after depressurization, including gamma-density profiles collected before and after depressurization, X-ray images collected before and after depressurization, and line-scan images collected after depressurization. Curated "voids" in PCS cores have been removed from split-core images. Only Section NGHP-01-10B-18Y-2 is shown in the line-scan image for Core NGHP-01-10B-28P. There are no data for Cores NGHP-01-10B-15B and NGHP-01-12A-07P. [PCS, Pressure Core Sampler]—Continued

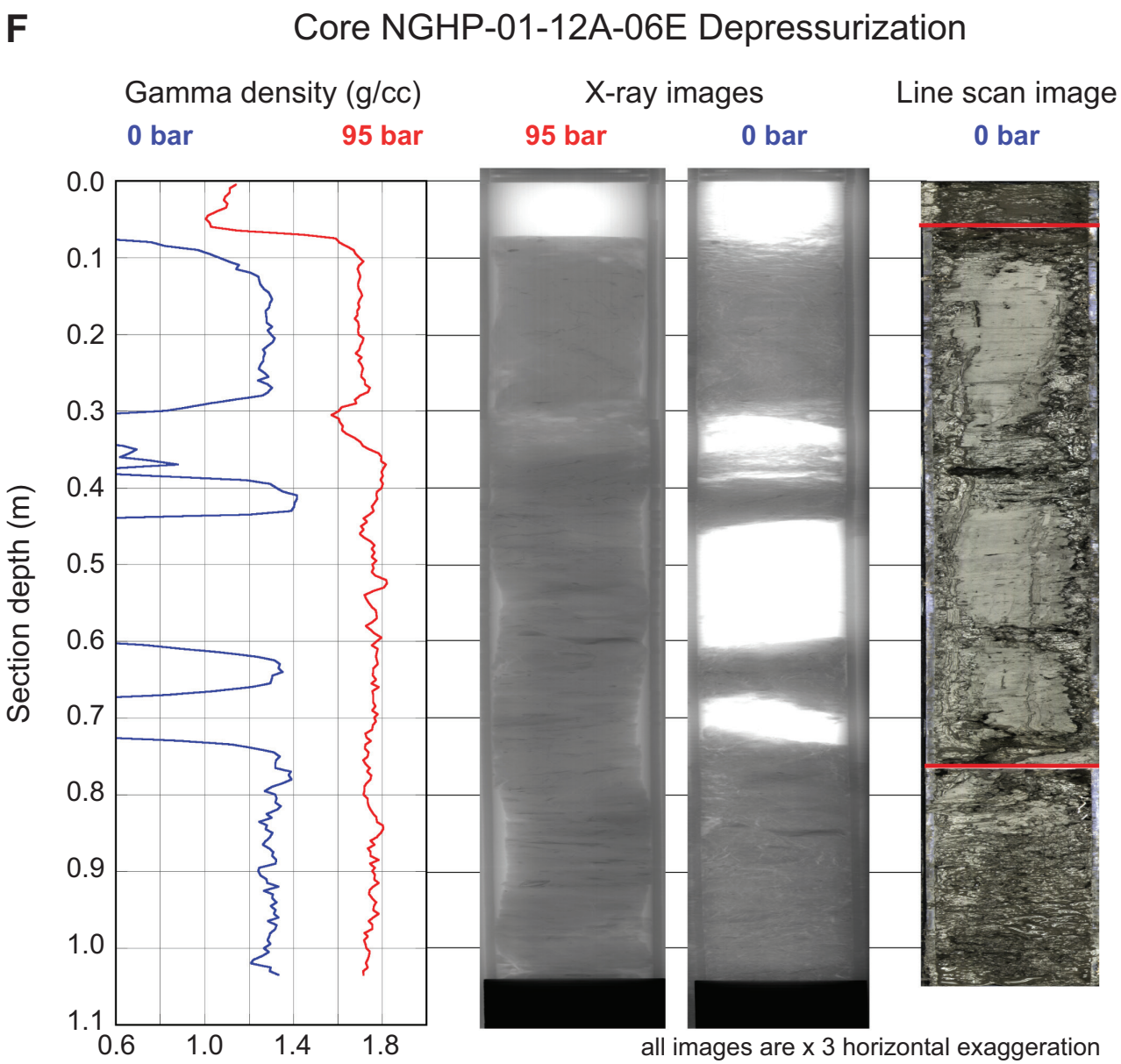


Figure 39. Summary of data taken from depressurized pressure cores before, during, and after depressurization, including gamma-density profiles collected before and after depressurization, X-ray images collected before and after depressurization, and line-scan images collected after depressurization. Curated "voids" in PCS cores have been removed from split-core images. Only Section NGHP-01-10B-18Y-2 is shown in the line-scan image for Core NGHP-01-10B-28P. There are no data for Cores NGHP-01-10B-15B and NGHP-01-12A-07P. [PCS, Pressure Core Sampler]—Continued

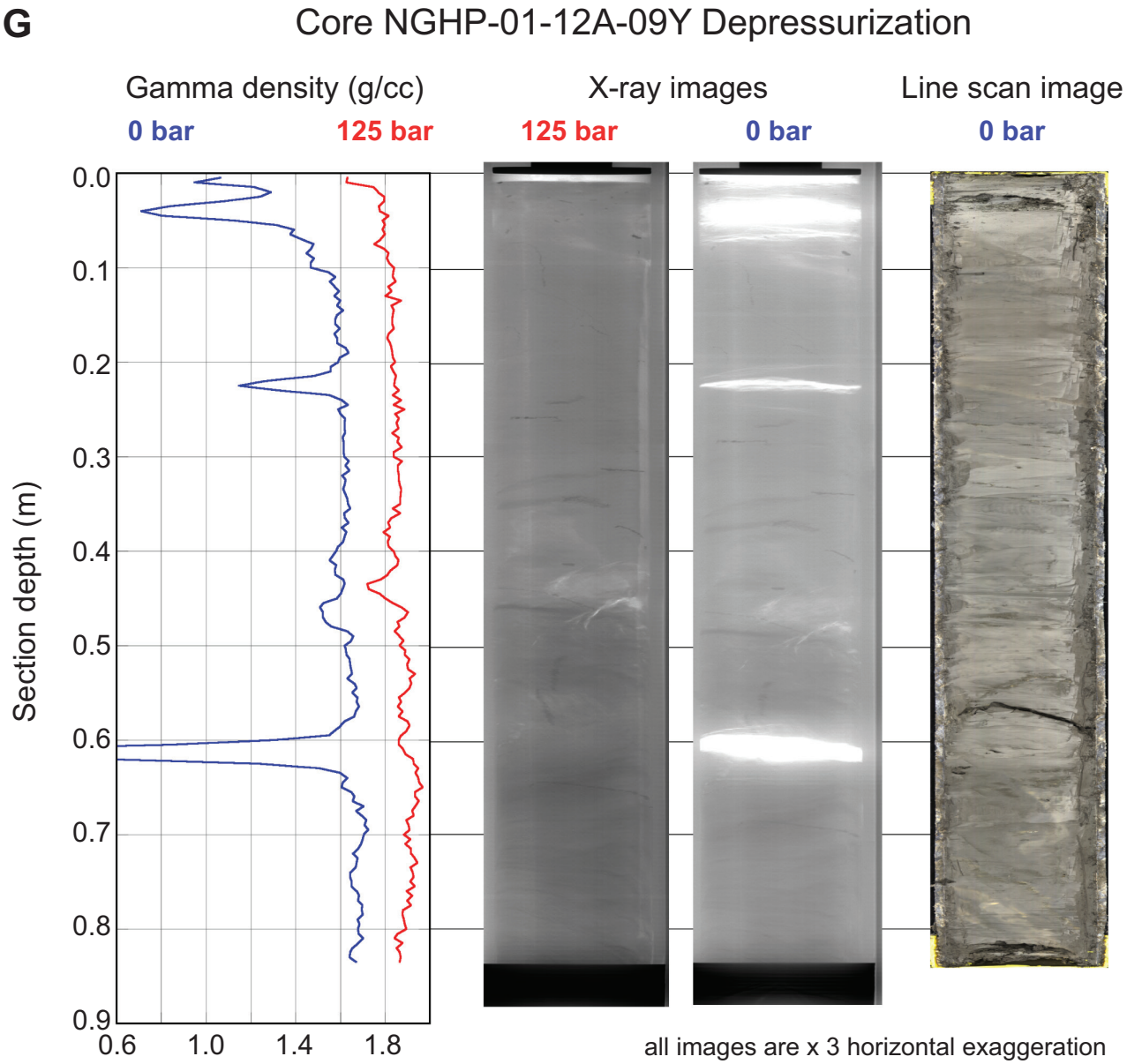


Figure 39. Summary of data taken from depressurized pressure cores before, during, and after depressurization, including gamma-density profiles collected before and after depressurization, X-ray images collected before and after depressurization, and line-scan images collected after depressurization. Curated "voids" in PCS cores have been removed from split-core images. Only Section NGHP-01-10B-18Y-2 is shown in the line-scan image for Core NGHP-01-10B-28P. There are no data for Cores NGHP-01-10B-15B and NGHP-01-12A-07P. [PCS, Pressure Core Sampler]—Continued

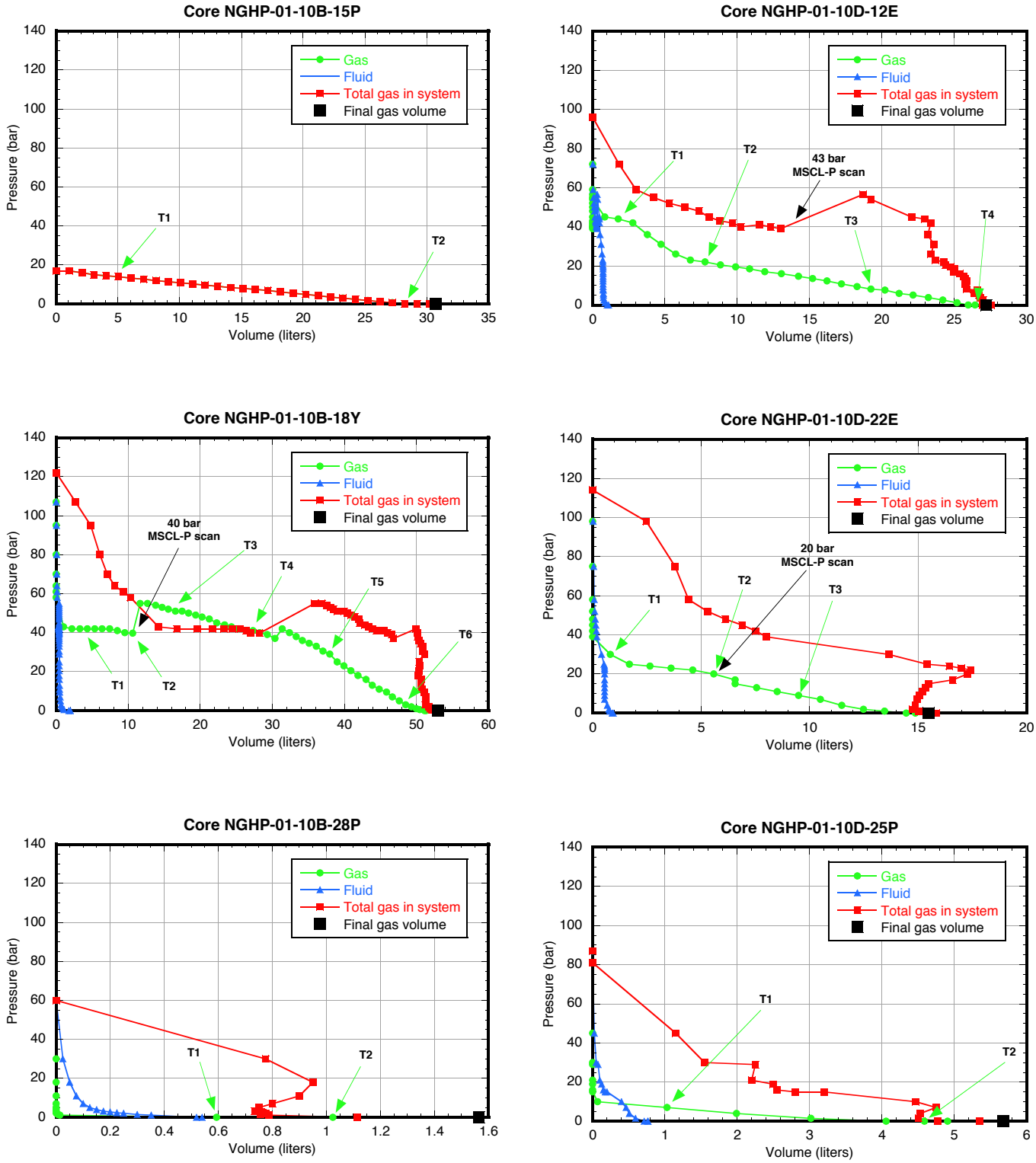


Figure 40. Pressure versus volume for depressurized pressure cores, also showing placement of intermediate X-ray or gamma density scans and gas samples (see "Organic Geochemistry"). [Green circles, gas volume; blue triangles, fluid volume; red squares, total gas volume in system (calculated as described in the "Methods" chapter); large black square, final calculated gas volume from cores; and T(number), gas samples]

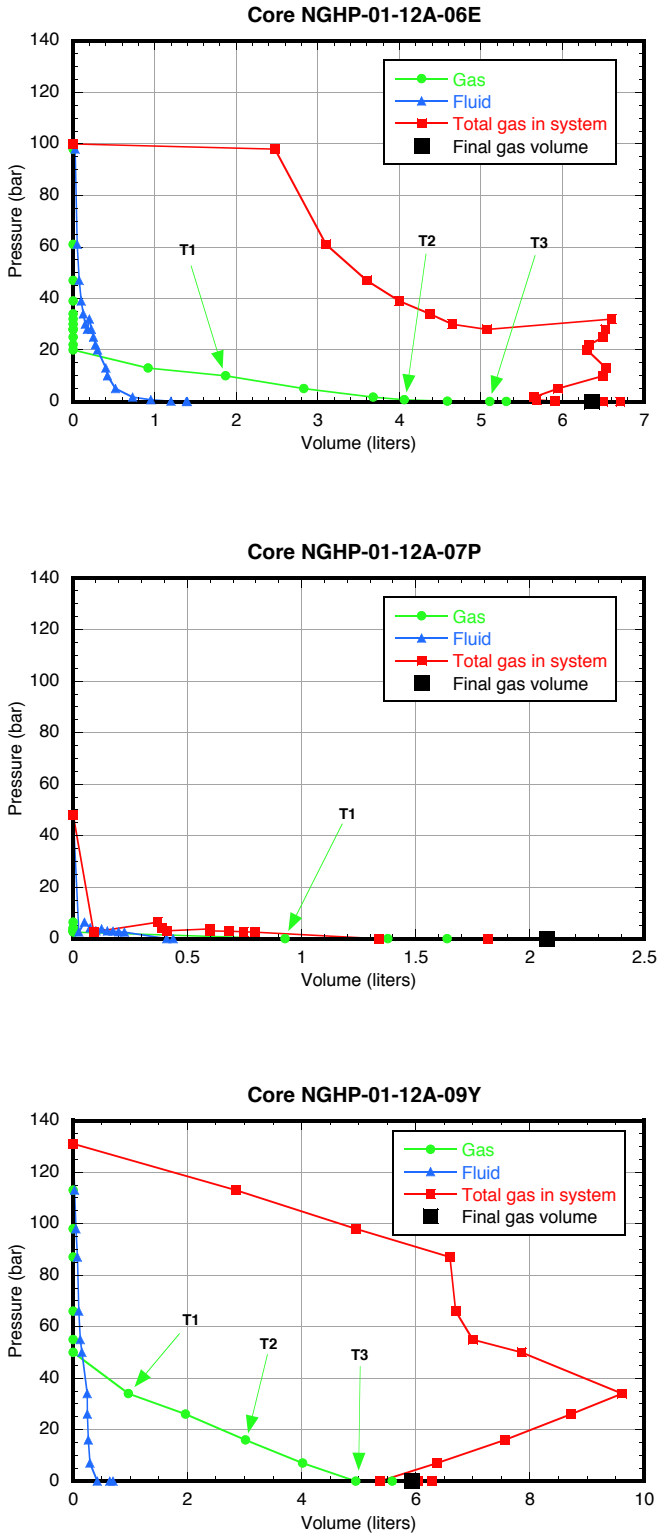


Figure 40. Pressure versus volume for depressurized pressure cores, also showing placement of intermediate X-ray or gamma density scans and gas samples (see "Organic Geochemistry"). [Green circles, gas volume; blue triangles, fluid volume; red squares, total gas volume in system (calculated as described in the "Methods" chapter); large black square, final calculated gas volume from cores; and T(number), gas samples]—Continued

Core NGHP-01-10D-12E (77.8 mbsf), collected within the zone of extremely high electrical resistivity, retrieved a partial core (0.68 m) under pressure (table 30). As the accumulator was not fully pressurized on this coring run and the ice shuck was not cold, the core was stabilized outside of the gas hydrate stability zone (fig. 36C). Core NGHP-01-10D-12E was transferred to the MSCL-P and X-ray images, gamma density and *P*-wave velocity measurements were collected and showed veins and layers of gas hydrate that were somewhat disturbed by coring (fig. 38C). Core NGHP-01-10D-12E was depressurized in the MSCL-P, releasing 27.0 L of methane, corresponding to 19.3 percent methane hydrate as a percent of pore volume, or 152 mL of methane hydrate (table 31). The steady decrease in pressure with respect to both volume and time is an indication that much of the gas hydrate in this core was either massive or had already dissociated during recovery (see "Pressure Coring" in the "Methods" chapter). One intermediate MSCL-P scan was made at 43 bar and a final MSCL-P scan was collected at atmospheric pressure which showed that the lumps of massive gas hydrate had dissociated and that the core was almost completely homogenized (fig. 39C). No chlorinity measurements were made on this core.

Core NGHP-01-10D-22E (145.1 mbsf), collected well below the zone of extremely high electrical resistivity but above the base of gas hydrate stability, retrieved a partial core (0.44 m) under full *in situ* pressure (table 30). No data were collected during the coring operation for Core NGHP-01-10D-22E. Core NGHP-01-10D-22E was transferred to the MSCL-P and X-ray images, gamma density and *P*-wave velocity measurements were collected (fig. 38D). This core contained wispy veins and layers of gas hydrate, though the gas hydrate had partially dissociated, causing loss of *P*-wave signal in the gas-hydrate-bearing sections. Core NGHP-01-10D-22E was depressurized in the MSCL-P, releasing 15.48 L of methane, corresponding to 17.6 percent methane hydrate as a percent of pore volume, or 85 mL of methane hydrate (table 30). The steady decrease in pressure with respect to both volume and time is an indication that much of the gas hydrate in this core had already dissociated during recovery. One intermediate MSCL-P scan was made at 20 bar and a final MSCL-P scan was collected at atmospheric pressure which showed that the core was almost completely homogenized (fig. 39D). No chlorinity measurements were made on this core.

Core NGHP-01-10D-25P (164.1 mbsf), collected near the calculated base of gas hydrate stability, retrieved a full core (1.00 m) under full pressure (table 30). The autoclave was placed in the MSCL-P for X-ray and gamma density measurements, which showed that the top half of the core was relatively uniform, studded with dense particles of metal sulfide or carbonate, and that sediment existed in the lower half (fig. 39E). There was no evidence of grain-displacing gas hydrate structures. The core was depressurized, releasing 5.55 L of methane, corresponding to 2.6 percent methane hydrate as a percent of pore volume or, if the core is actually below the base of the gas hydrate stability zone, 29.6 mL of

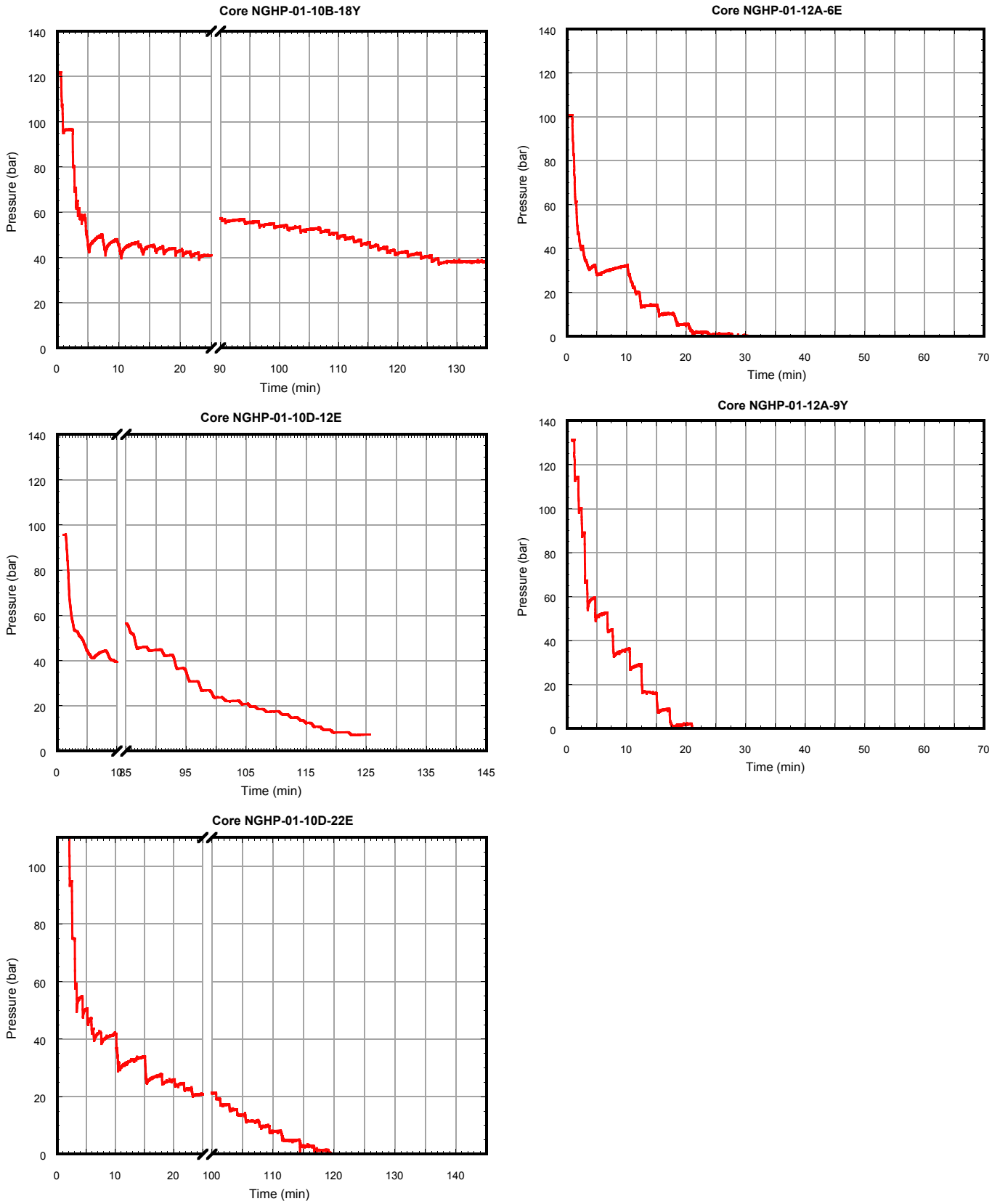


Figure 41. Pressure versus time for selected pressure cores. Note the pressure rebounds during depressurization of Core NGHP-01-10B-18Y.

Table 31. Methane-hydrate volume and concentration in pore space for successful pressure cores at Site NGHP-01-10. Values required for calculation of methane hydrate concentration are also included.

Core ID	Top of core (mbsf)	Length recovered (cm)*	Length curated (cm)*	Pressure at core depth (bar)	Pressure recovered (bar)				Comments
					logged**		gauge***		
NGHP-01-10B									
05P	31.4	--	0	108	0		--		Ball valve did not close
08Y	50.1	86	90	110	100		100		Data logger did not record; stored in storage chamber
11E	70.0	--	17	112	0		--		No retraction
15P	98.2	100	113	115	23	@12 °C	17		Low pressure, no x-ray
18Y	117.4	86	90	117	118		118		Normal operation
21Y	136.6	--	33	119	0		--		Core did not retract
27E	174.1	--	42	123	0		--		No retraction; tool modified after run
28P	175.1	100	167	123	60		60		Normal operation
NGHP-01-10D									
06P	40.1	--	29	109	0		--		Ball valve did not close
09Y	58.8	--	51	111	0		--		Overretracted
12E	77.8	68	115	113	95	@12 °C	95		Normal operation
15P	97.0	--	92	115	0		--		No pressure
19Y	125.8	--	88	118	0		--		Top seals leaked
22E	145.1	44	105	120	110		110		Data logger did not record
25P	164.4	100	122	122	90		87		Normal operation
NGHP-01-12A									
05Y	45.7	--	86	107	0		--		Overretracted
06E	46.7	102	108	107	90		95		Normal operation
07P	47.7	12	0	107	51		53		Normal operation
09Y	93.3	86	88	112	131	@12 °C	131	@12 °C	Normal operation
10E	94.3	--	0	112	0		--		Liner collapsed
11P	95.3	--	58	112	0		--		No pressure

Notes:

Water depth at Site NGHP-01-10 is 1049 mbsl. Water depth at Site NGHP-01-12 is 1018 mbsl. P=PCS, Y=FPC, E=HRC.

*Length measured from X-ray and gamma density analysis, which may not match curated core length.

**Last pressure recorded before data logger disconnected from corer autoclave. Temperature 2–4 °C unless otherwise noted.

***Pressure measured when autoclave pressure transducer connected to external gauge. Pressure measured at 7 °C unless otherwise noted.

methane gas (table 31). The gas from this core had a methane to ethane ratio between 1000 and 2000, which is lower than other pressure cores from Site NGHP-01-10, where the methane to ethane ratios ranged between 5000–7000 (see "Organic geochemistry"). When the core was fully depressurized, the autoclave was again measured in the MSCL-P, and when the outer barrel was removed, a final X-ray image was collected (fig. 39E). One chlorinity measurement was made on this core (90–100 cm, 536 mM), which was very similar to other chlorinity measurements made below the estimated depth of the BSR at this site (see "Inorganic Geochemistry").

Core NGHP-01-12A-06E (46.7 mbsf), collected at Site NGHP-01-12 at a depth equivalent to the extremely high resistivity layer at Site NGHP-01-10, retrieved a full core (1.02 m) under pressure (table 30). This was the first successful coring run with a DST Micro logger in the piston, showing that the core made a much briefer excursion out of the gas hydrate stability field (about five minutes) than would have been estimated from the standard data logger inside the coring tool (figs. 36D and 37). Core NGHP-01-12A-06E was transferred to the MSCL-P and X-ray images, gamma density and *P*-wave velocity measurements were collected (fig. 38E), which showed a stratified core with dense particles of sulfide or carbonate and tiny, wispy low-density veins. Core NGHP-01-12A-06E was depressurized in the MSCL-P, releasing 6.0 L of methane, corresponding to 2.1 percent methane hydrate as a percent of pore volume, or 24 mL of methane hydrate (table 31). A final MSCL-P scan was collected at atmospheric pressure which showed the core had developed voids and the bottom 30 cm had been extruded out of the core catcher (fig. 39F). No chlorinity measurements were made on this core.

Core NGHP-01-12A-07P (47.7 mbsf), collected at Site NGHP-01-12 at a depth equivalent to the extremely high resistivity layer at Site NGHP-01-10, retrieved a small amount of sediment under pressure (table 30). The autoclave was placed in the MSCL-P for X-ray and gamma density measurements, which showed that the top half of the core was empty. Depressurization of Core NGHP-01-12A-07P yielded 2.08 L of methane, equivalent to 11 mL of methane hydrate. The sediment

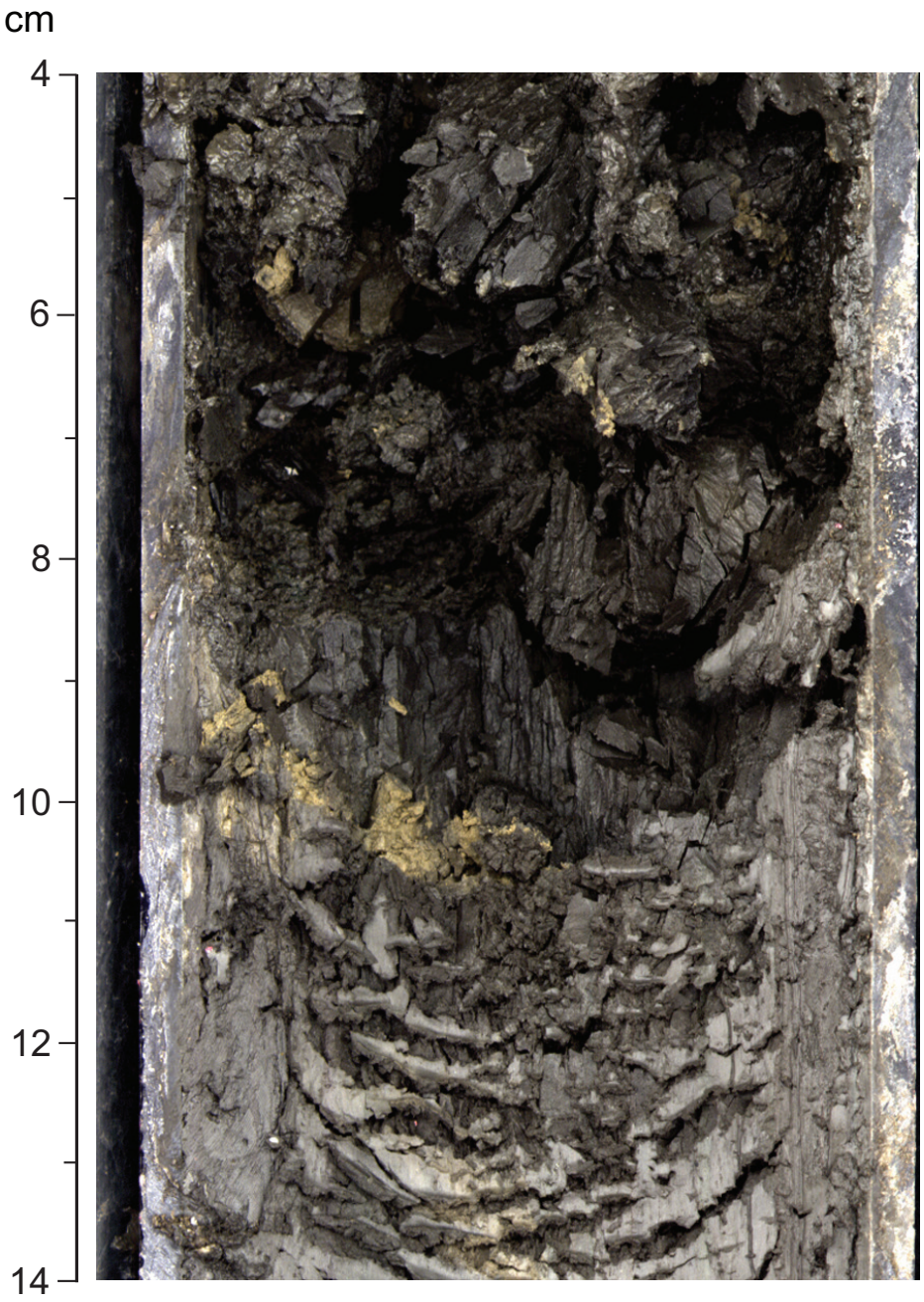


Figure 42. Flaky "cooked fish" texture seen in Core NGHP-01-10B-18Y.

contained in the core was washed out during removal of the outer barrel and left to settle; the original sediment length was estimated at approximately 12 cm, which corresponds to 11.4 percent methane hydrate by pore volume.

Core NGHP-01-12A-09Y (93.3 mbsf), collected at Site NGHP-01-12 at a depth below the extremely high resistivity layer at Site NGHP-01-10, retrieved a full core (0.86 m) at full *in situ* pressure (table 30). This core showed an increase in pressure as it warmed during an extended handling period on deck before being placed in the ice shuck, indicating that minor gas hydrate dissociation may have occurred (fig. 36D). Core NGHP-01-12A-09Y was transferred to the MSCL-P and X-ray images, gamma density and *P*-wave velocity measurements were collected (fig. 38F). The X-ray image showed a core with some horizontal structure and a 10-cm low-density zone that contained free gas, based on low *P*-wave signal, and possibly remnant gas hydrate. Core NGHP-01-12A-09Y was depressurized in the MSCL-P, releasing 5.94 L of methane, corresponding to 2.0 percent methane hydrate as a percent of pore volume, or 22 mL of methane hydrate (table 31). A final MSCL-P scan was collected at atmospheric pressure which showed an intact core with much lower density and a few small voids (fig. 39G). No chlorinity measurements were made on this core.

Gas Hydrate Concentration, Nature, and Distribution from Pressure Coring

Nine of the 15 pressure cores at Site NGHP-01-10 were recovered at sufficient pressure (and depressurized) to accurately assess the total concentration of methane and hence the predicted amount of gas hydrate. The calculated methane concentration for these cores is shown in figure 43 in relation to the phase boundaries for Structure I methane hydrate and the LWD resistivity borehole image. Calculated concentrations of gas hydrate of 17.6 percent to 25.4 percent of pore volume were found in cores from Site NGHP-01-10 collected in the zone of high electrical resistivity seen in the LWD logs (see "Downhole Logging"). There was only one core collected in the zone of extremely high electrical resistivity at Site NGHP-01-10 (Core NGHP-01-10D-12E), which had a gas hydrate concentration of 19.3 percent of pore volume, no different from the cores taken outside of this zone. The single core collected below the base of gas hydrate stability (Core NGHP-01-10B-28P) was undersaturated in methane, so there is no evidence for a free gas phase from pressure coring at Site NGHP-01-10. The two pressure cores collected at Site NGHP-01-12 contained much less gas hydrate than the pressure cores at Site NGHP-01-10 (about 2 percent of pore volume vs. 20 percent at Site NGHP-01-10), so pressure core analysis supports the conclusions from IR imaging (see "Physical Properties") and chlorinity analysis (see "Inorganic Geochemistry") that the gas hydrate deposit at Site NGHP-01-10 did not extend to Site NGHP-01-12.

The composition of the gas released from pressure cores at Site NGHP-01-10 was relatively uniform throughout depressurization experiments and between cores, showing no fractionation due to sequestration of heavier hydrocarbons in gas hydrate (table 12). Only Core NGHP-01-10D-25P, near the base of gas hydrate stability, had a substantially lower methane to ethane ratio. The gas samples from this core showed the highest concentrations of ethane at Site NGHP-01-10 (see "Organic Geochemistry"). However, the concentration of ethane was still low enough to assume Structure I methane hydrate for purposes of stability calculations. The Site NGHP-01-12 pressure cores contained lower concentrations of ethane, suggesting that the gas hydrate system at Sites NGHP-01-10 and NGHP-01-12 are not intimately linked.

The many gas-hydrate-bearing sediment samples observed at Site NGHP-01-10, both visually on the catwalk and from the X-ray images of pressure cores, provide insight into gas hydrate morphology and distribution in fine-grained sediments. The catwalk visual observations from APC and XCB cores are limited to the more massive forms of gas hydrate, as the finer structures will have dissociated. However, the preserved morphologies in the pressure cores provide a unique opportunity to examine the *in situ* nature of gas hydrate from the nondestructive measurements (*P*-wave velocity and gamma density) as well as from the more revealing X-ray images.

Figure 44 shows the complete X-ray images of the well-preserved FPC Cores NGHP-01-10B-08Y and NGHP-01-10B-18Y, taken at full recovered pressure, along with enlarged sections to illustrate the different gas hydrate morphologies observed. Core NGHP-01-10B-18Y shows more lithological changes, characterized by regions of dark and light intensity with sharp boundaries, than Core NGHP-01-10B-08Y, which shows only gradual changes in overall intensity. In the more homogenous core, Core NGHP-01-10B-08Y, the gas hydrate takes the form of nodules (figs. 44A), distinct horizontal veins (fig. 44A), and many thin wispy vertical/subvertical hydrate structures (fig. 44A). In Core NGHP-01-10B-18Y, where there are more distinct lithological changes, the only visible gas hydrate occurrence is in horizontal layers (fig. 44B). No vertical veins of gas hydrate are visible in this core.

Simple calculations show that only a small amount of the gas hydrate in Core NGHP-01-10B-18Y (299 mL) can be accounted for by the thin wispy layers of gas hydrate that are visible on the X-ray. A single layer 0.5 cm thick would only contain 13 mL of gas hydrate (FPC core). The bulk of the gas hydrate in this core must be in a more distributed form that is below the resolution of the X-ray images, or indeed the naked eye. This distributed gas hydrate could take two quite different forms:

Disseminated gas hydrate that replaces pore water but does not significantly displace the sediment grain matrix. In this case, no significant reduction in overall bulk density would occur, and no change would be visible in the X-ray image. However, some increase in matrix rigidity could occur, resulting in increased *P*-wave velocities.

Finely distributed grain-displacing gas hydrate where fine grains of gas hydrate replace the sediment matrix and lower the overall density of the sediment, which should be visible in the gamma density data and X-ray image. Finely distributed grain-displacing gas hydrate may also have a "cementing" effect which could cause an increase in *P*-wave velocity.

The low-density zones with diffuse boundaries in Core NGHP-01-10B-08Y, seen in both the gamma density profile and the X-ray images (figs. 28A and 44A), may contain distributed grain-displacing gas hydrate. Core NGHP-01-10B-18Y had anomalously high *P*-wave velocities throughout the core (fig. 45) but showed no decrease in density, so it is possible that the core contained gas hydrate in disseminated form. The darker layers in the X-ray images correlated with local maxima in *P*-wave velocities (fig. 38A) and these (lithologically distinct?) intervals may have contained grain-cementing concentrations of disseminated gas hydrate. The flaky "cooked fish" texture (fig. 42) seen in Core NGHP-01-10B-18Y may be a result of the dissociation of disseminated gas hydrate in fine-grained sediments.

However, the X-ray computed tomography scans of pressure cores performed post-cruise (see "Singapore Pressure Core Studies" in the "Appendix") showed that all cores examined from Site NGHP-01-10 and nearby Site NGHP-01-21 contained pervasive, mm-scale veins of gas hydrate that were not visible on the original X-rays. These thin veins sometimes showed preferred orientations, which could affect the density and velocity profiles of the cores.

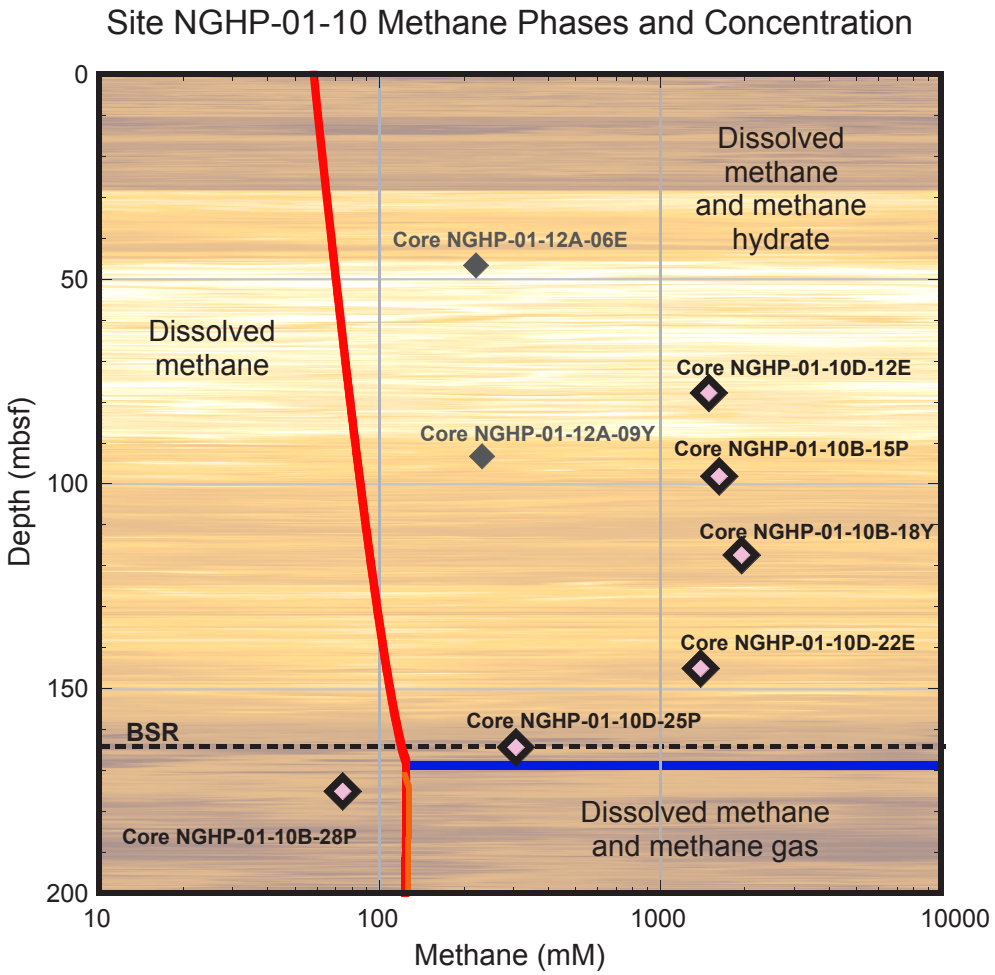


Figure 43. Methane phase diagram for Site NGHP-01-10, with total methane concentration measured from the nine depressurized pressure cores at Site NGHP-01-10. The shipboard-calculated seafloor temperature (6.0 °C) and thermal gradient (45 °C/km) were taken from "Downhole Temperature Measurements" in "Physical Properties," the salinities were the average background salinities around the depths of the pressure cores (35 ppt; table 7), and methane saturation was calculated according to Xu (2002, 2004). The background is the LWD deep borehole resistivity (RAB) image. [LWD, logging-while-drilling]

Downhole Logging

Logging-While-Drilling

Operations

Hole NGHP-01-10A was drilled 50 m NW from the position of a pre-existing well (GD-3-1) and before spudding we ran a camera down the drill pipe to check for existing equipment and debris on the seafloor. None was detected. After tagging the seafloor at 1049 mbrf (as seen from the camera), Hole NGHP-01-10A was spudded at 0428 hr on 3 June. LWD tools in the BHA included the GeoVISION, the EcoScope, the SonicVISION, the TeleScope MWD tool and the ProVISION NMR. For details on each LWD tool and measurements, see "Downhole Logging" in the "Methods" chapter.

To avoid washing out the hole near the seafloor, Hole NGHP-01-10A was spudded at a relatively low flow rate. The first 10 m were drilled at 100 gpm with a rotation rate of 20 rpm and a rate of penetration (ROP) of 25 m/h. Below 10 mbsf, the rotation rate was increased to 30 rpm; at 30 mbsf, the rotation rate was increased to 60 rpm and the flow rate was increased until all LWD tools turned on (~370 gpm). As we needed to drill this hole quickly to keep our schedule, we started drilling at a relatively high ROP of 50 m/h, planning to slow down when we saw evidence of gas hydrate on the GeoVISION resistivity logs (which are measured close to the bit). We found high resistivities near the seafloor, and decreased the target penetration rate to 30 m/h at 1089 mbrf (40 mbsf).

Drilling was uneventful until 1302 hr, when after a connection with the bit at 1219 mbrf (170 mbsf) the annular pressure increased suddenly by about 130 psi (from about 1800 to 1930 psi). Following the agreed safety protocol (see "Downhole Logging" in the "Methods" chapter), we stopped drilling and circulated sea water and a mud sweep. Once the pressure decreased to about 1850 psi, drilling was resumed. Two more pressure increases were observed, but they were not as large as

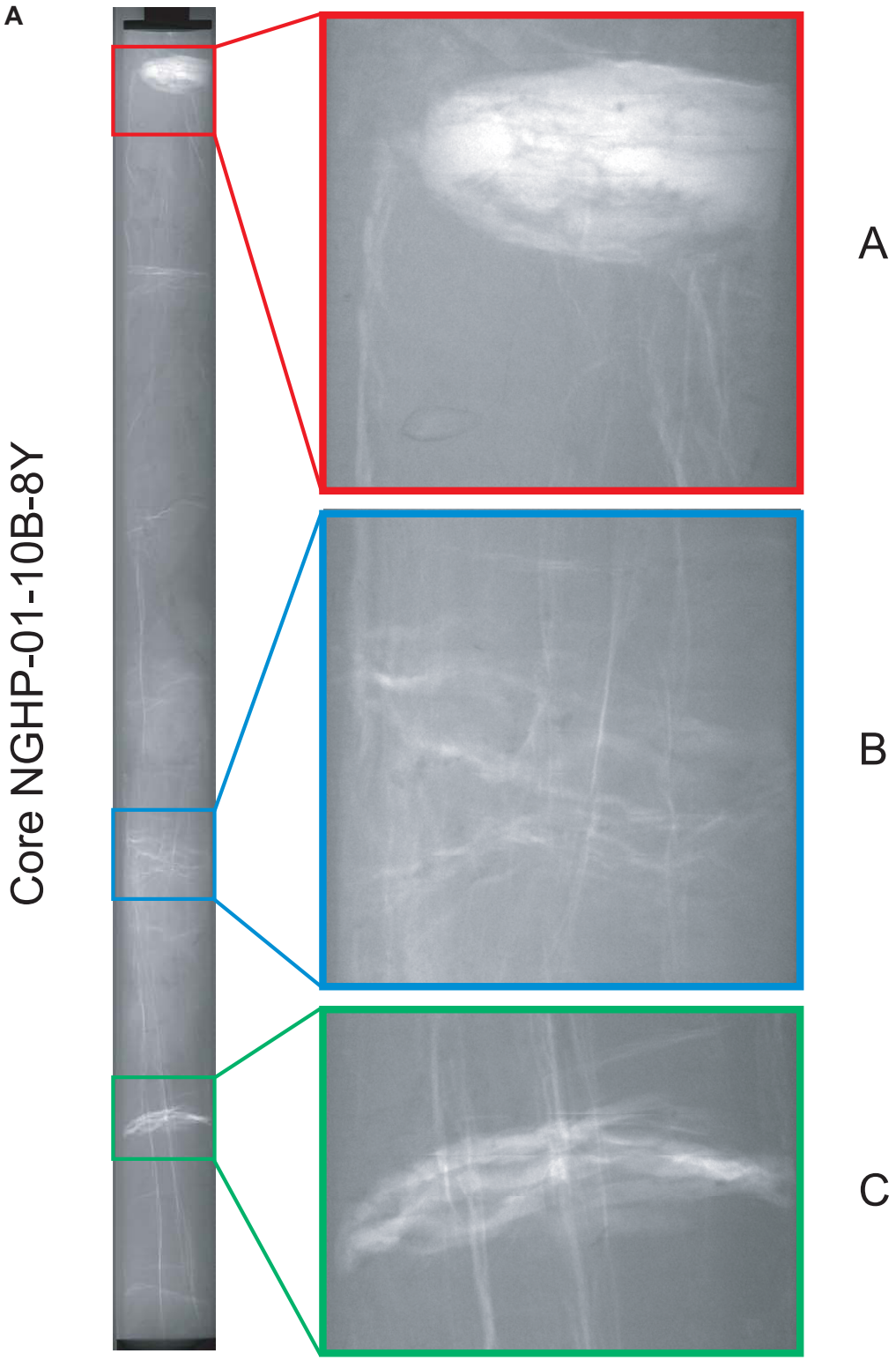


Figure 44. X-ray images of Cores NGHP-01-10B-08Y and NGHP-01-10B-18Y, with enlargements showing different gas-hydrate morphologies in fine-grained sediment.

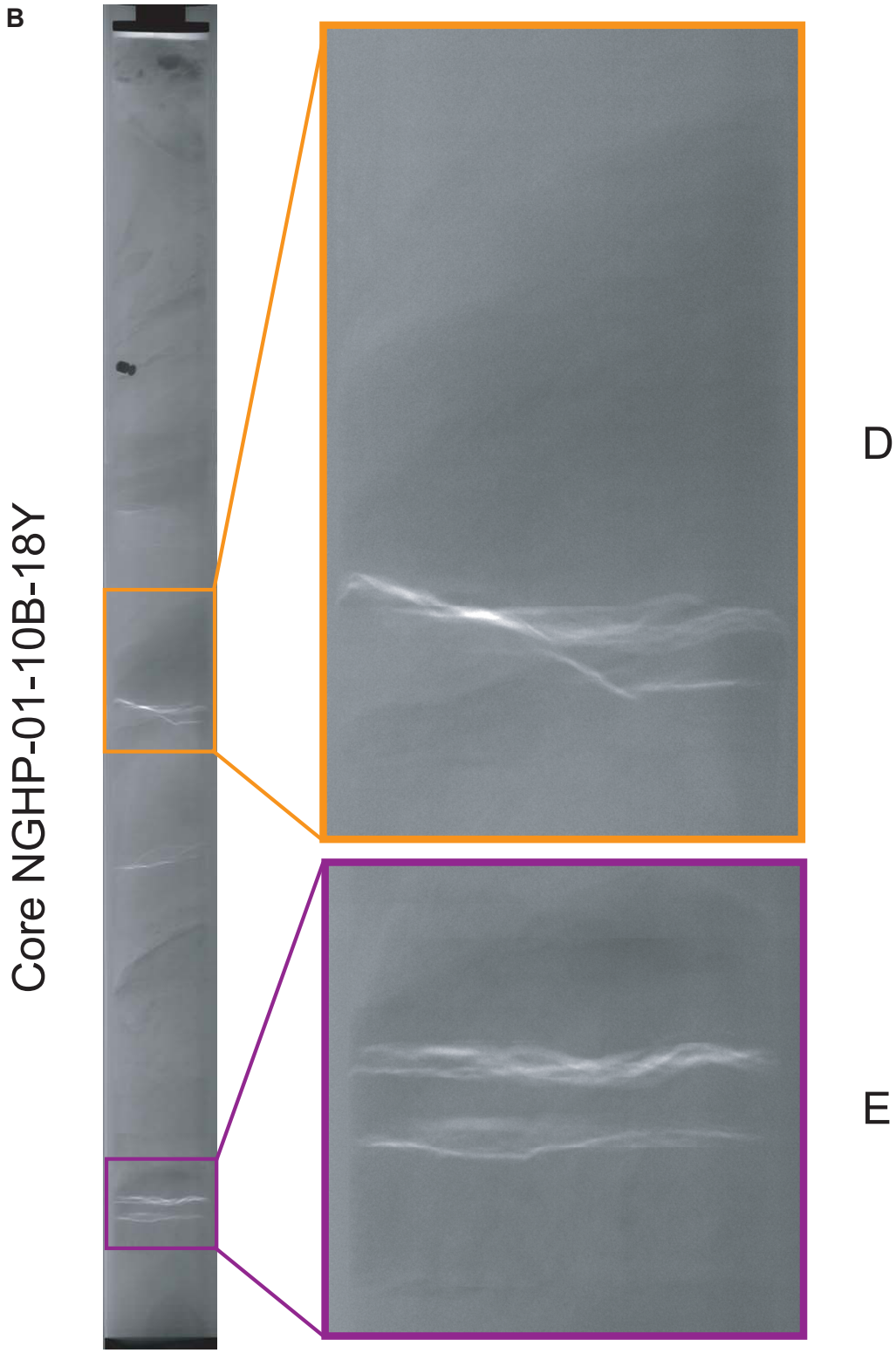


Figure 44. X-ray images of Cores NGHP-01-10B-08Y and NGHP-01-10B-18Y, with enlargements showing different gas-hydrate morphologies in fine-grained sediment.—Continued

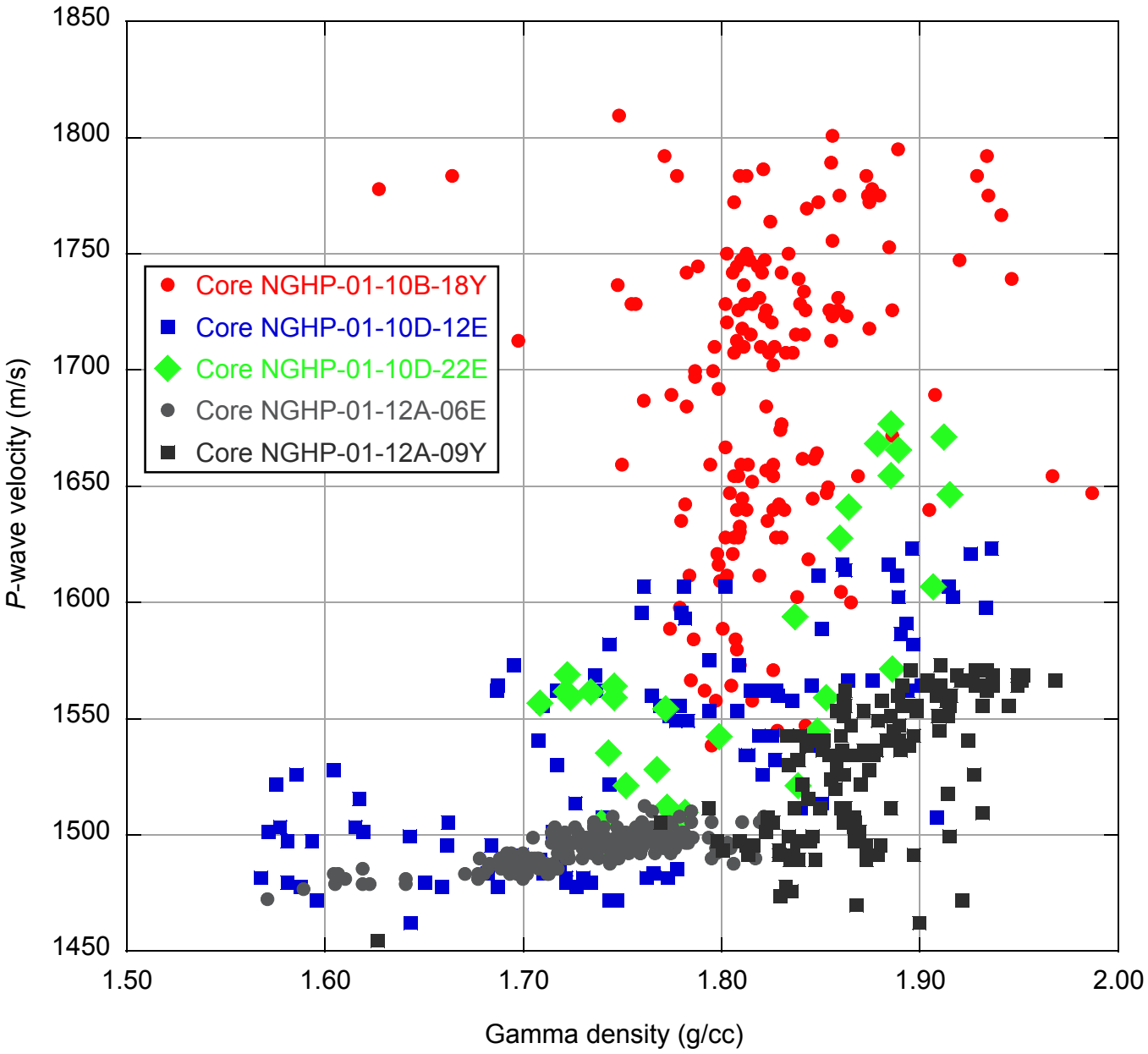


Figure 45. Gamma density versus P-wave velocity illustrating the relatively high velocities in the core from Site NGHP-01-10 compared with Site NGHP-01-12.

the first and in both cases pressure returned to its overall trend. The most likely cause of these pressure increases was a borehole restriction that made it difficult for the drilling fluid to flow through the annulus, and/or the formation washing out with cuttings loading up and packing off. (For details on the measured borehole pressures and hole size, see the next section).

We finally reached the planned target depth of 205 mbsf (1254 mbrf) at 1609 hr. The hole was displaced with 10.5 ppg mud, and the tools were brought back to the surface by 1920 hr. Data download and rig down were completed at 2114 hr on 3 June. (The depths in mbsf mentioned above are referenced to the seafloor depth tagged by the driller.)

Gas Monitoring with Real Time LWD/MWD Data

The LWD logs were acquired in the first holes drilled at Site NGHP-01-10 to plan coring and pressure coring operations in subsequent holes. As Hole NGHP-01-10A was drilled without coring, the LWD data had to be monitored for safety to detect gas entering the wellbore. As explained in "Downhole Logging" of the "Methods" chapter, the primary measurement used in the gas monitoring was the "annular pressure while drilling" (APWD) measured by the EcoScope tool in the borehole annulus. We looked for sudden decreases of more than 100 psi in the annular pressure, which could be due to low-density gas entering the wellbore. We also monitored pressure increases of the same magnitude, which could be due to fluid acceleration caused by a gas kick (Aldred and others, 1998).

Figure 46 shows the measured borehole fluid pressure profile in Hole NGHP-01-10A after subtraction of the hydrostatic pressure trend. As noted earlier, this residual pressure curve displayed only minor fluctuations until pressure suddenly increased by about 130 psi after a connection, with the bit at about 167 mbsf. (The pressure increase is at 160 mbsf in figure 46 because the pressure gauge is located about 6.5 m above the bit). This first pressure increase was followed by two smaller ones (~60 psi) with the pressure gauge at 170 and 177 mbsf. As noted earlier, the most likely cause of these pressure increases was not free gas but a restriction of the borehole that interfered with the upward flow of drilling fluid in the annulus. The ultrasonic caliper (UCAV in fig. 46) shows a borehole smaller than the bit size at 157–165 mbsf. Another possible explanation for the pressure increases is that the formation was washing out with cuttings loading up and packing off. The ultrasonic and density calipers show a washout in the interval 165–190 mbsf (fig. 46).

We also monitored the coherence of the sonic waveforms acquired by the SonicVISION tool, focusing on the sound velocity in the borehole fluid. Gas indicators are loss of coherence in the waveforms and a slower sound velocity for the drilling fluid. The sonic waveform coherence was generally high except for the interval with the bit below 160 mbsf, where the drilling fluid pressure increased and the hole was washed out. As noted earlier, this borehole pressure increase was not related to free gas.

LWD Log Quality

Figure 46 also shows the quality control logs for Hole NGHP-01-10A. The two curves for rate of penetration are an instantaneous rate of penetration (ROP_RM) and a rate of penetration averaged over the last 5 feet (ROP5_RM). The occasional large peaks in the instantaneous rate of penetration are artifacts due to depth fluctuations during pipe connections. We started drilling the hole with a ROP around 50 m/h, but decreased to a target ROP of 30 m/h below 40 mbsf, where we saw the first signs of high resistivities probably due to gas hydrate. Below 40 mbsf, the ROP is generally less than 30 m/h, which is sufficient to record high resolution GeoVISION resistivity images and ProVISION NMR data (for details, see "Downhole Logging" in the "Methods" chapter).

The density (DCAV) and ultrasonic caliper logs (UCAV) show an enlarged hole near the seafloor (30–60 mbsf), with a hole diameter up to 14 in. The bit size (dashed line in fig. 46) is 9 7/8 in, and the ultrasonic caliper shows that most of the borehole below 60 mbsf is about 10.5 in. The ultrasonic caliper also shows a borehole shrunk to less than the bit size in the interval 157–165 mbsf (see above). Both the density and the ultrasonic caliper also show a hole washout in the interval 165–190 mbsf.

The density correction, calculated from the difference between the short- and long-spaced density measurements, is everywhere less than 0.2 g/cm^3 (fig. 46), suggesting that the density measurements should be of good quality (see below, however).

Figure 47 is a summary of the LWD gamma ray, density, neutron porosity, and resistivity logs measured in Hole NGHP-01-10A. (SonicVISION and ProVISION results are not shown because they need processing on shore.) The gamma ray and resistivity logs measured by the GeoVISION (red and orange curves) and EcoScope LWD tools (green and blue curves) generally agree. The GeoVISION and EcoScope gamma ray curves have the same shape, but are offset by about 20–30 gAPI; this difference is most likely due to tool calibration.

Figure 47 also shows two bulk density curves: RHOB is the average density obtained by the EcoScope tool while rotating, while IDRO (image-derived density) is the value of density measured when the sensors were in closest contact with the formation. The two density curves are generally close, except for the interval 165–190 mbsf, where the hole is enlarged (see caliper curves in fig. 46). In this interval, the image-derived density is greater and is likely to be more accurate. Both curves agree well with the density measurements made on core samples onboard.

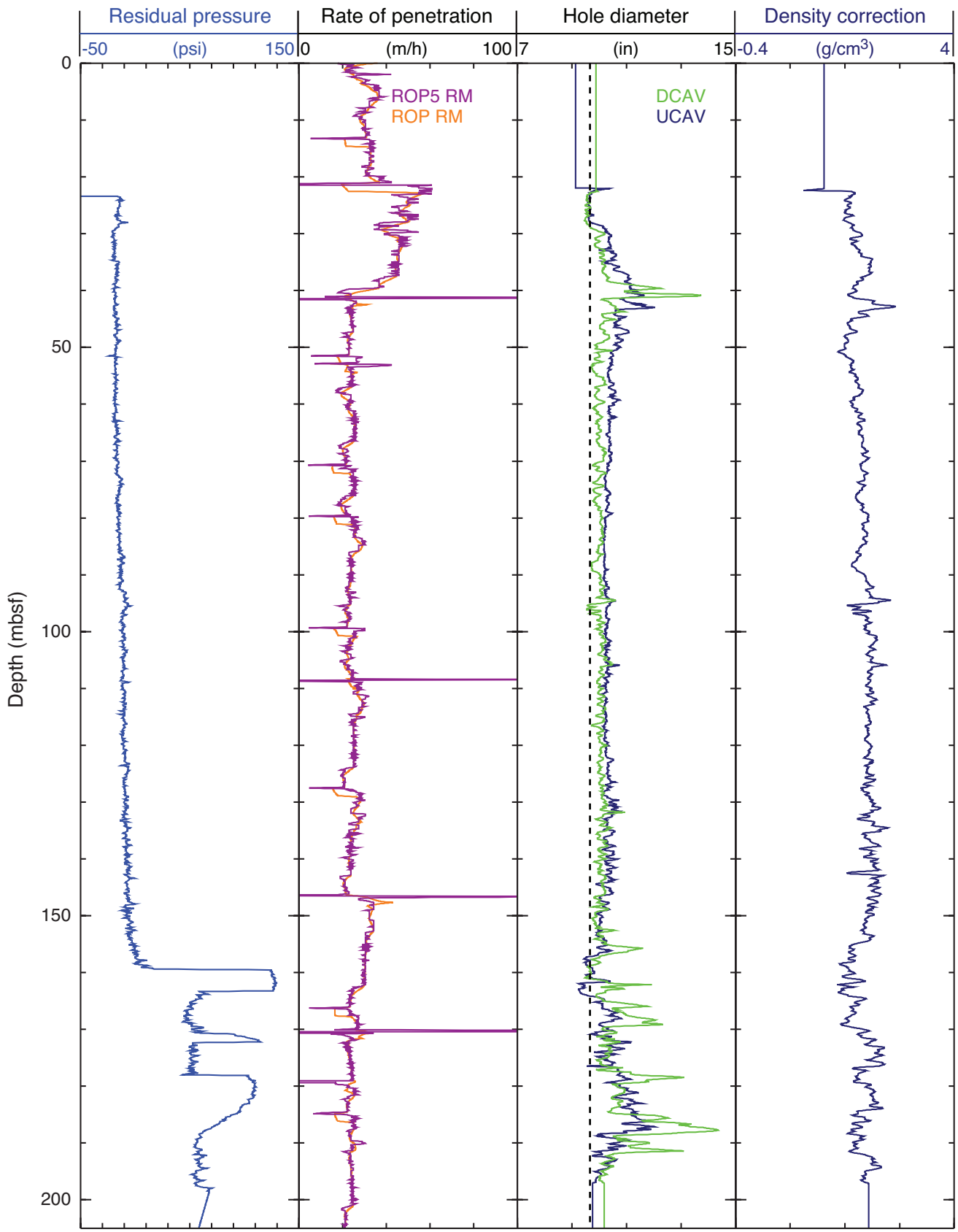


Figure 46. Monitoring and quality control LWD/MWD logs from Hole NGHP-01-10A. [LWD/MWD, logging-while-drilling/measuring-while-drilling; ROP_RM, Instantaneous rate of penetration; ROP5_RM, Rate of penetration averaged over a 5-ft interval; UCAV, ultrasonic caliper; DCAV, density caliper]

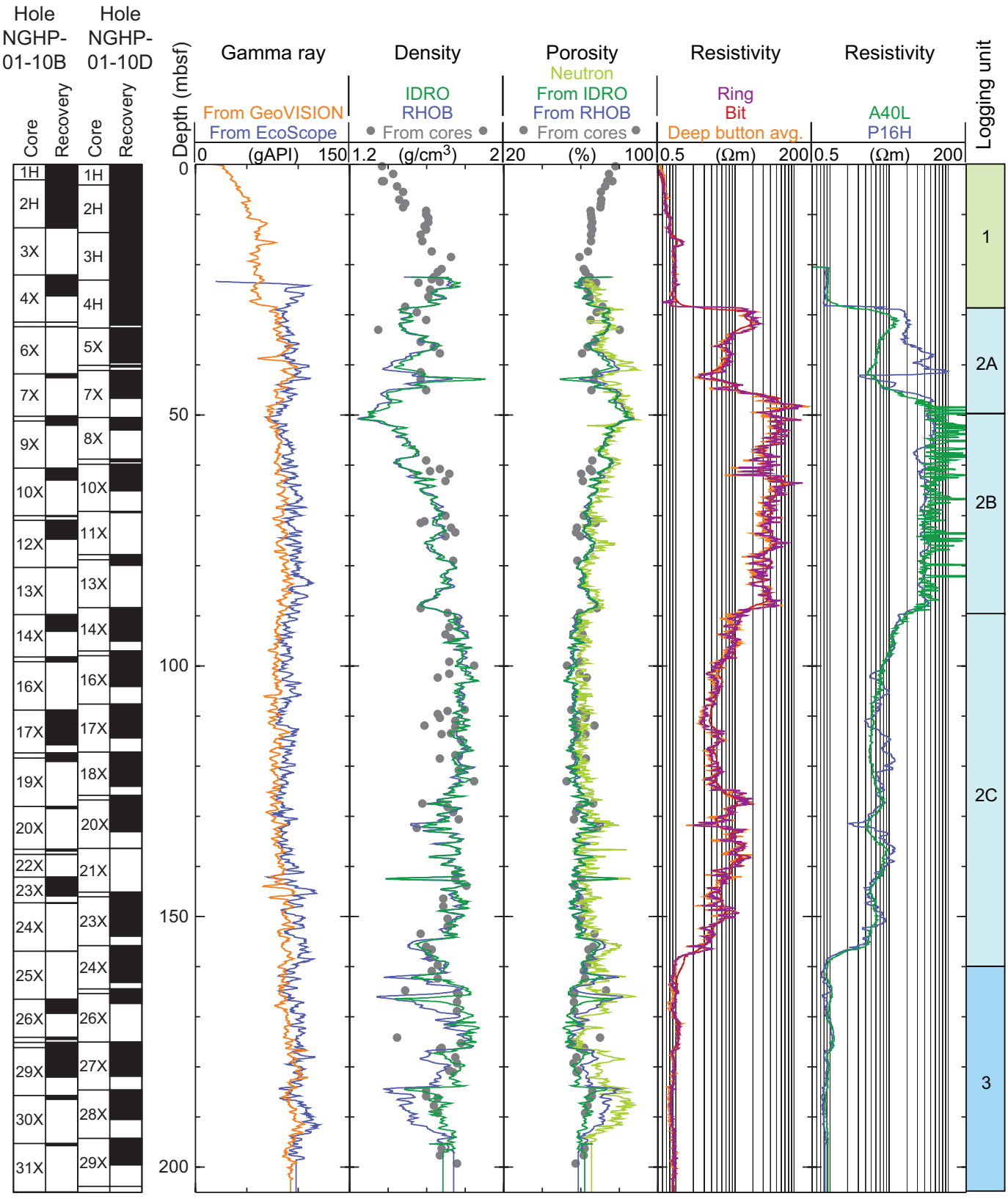


Figure 47. Summary of LWD log data from Hole NGHP-01-10A. [LWD, logging-while-drilling; gAPI, American Petroleum Institute gamma ray units; IDRO, Image-derived density (EcoScope); RHOB, bulk density (EcoScope); neutron, thermal neutron porosity (EcoScope); RING, ring resistivity (GeoVISION); BIT, Bit resistivity (GeoVISION); Deep Button avg., button deep resistivity (GeoVISION); A40L, Attenuation resistivity measured at 400 kHz and a transmitter-receiver spacing of 40 in (EcoScope); and P16H, phase-shift resistivity at 2 MHZ and a transmitter-receiver spacing of 16 in (EcoScope)]

Figure 48 shows a comparison of the ring resistivity measured by GeoVISION with the attenuation and phase-shift resistivity curves obtained by the EcoScope tool at different frequencies and transmitter-receiver spacings. These resistivity measurements are based on different physical principles. The GeoVISION tool obtains resistivity by measuring current for a given voltage as in Ohm's law, and uses a low-frequency 1.5 kHz alternating current. The EcoScope tool instead measures resistivity from the attenuation and phase shift of 400 kHz and 2 MHz electromagnetic waves propagating through the formation (for more details, see "Downhole Logging" in the "Methods" chapter). For a given transmitter-receiver spacing, the phase-shift resistivities have higher vertical resolution than the attenuation resistivities and thus show more detail.

While in general the resistivities measured by GeoVISION and EcoScope in the NGHP Expedition 01 holes agree in water-saturated zones where resistivities are around 1 Wm, they differ in the high resistivity, gas hydrate-rich intervals of Hole NGHP-01-10A. The differences observed for the attenuation resistivities (two left tracks in fig. 48) in the interval 45–90 mbsf are easy to explain: the attenuation of electromagnetic waves is small for resistivities greater than a few tens of ohm-meters and tends to a constant value related to spreading losses; attenuation resistivity measurements are unreliable in these high-resistivity regions (see the resistivity-attenuation plots shown by Clark and others, 1990 and Bonner and others, 1995 for different transmitter-receiver spacings). In practice, attenuation resistivity measurements are reliable up to formation resistivities of 20–50 mW (depending on transmitter-receiver spacing) while phase-shift resistivity measurements are reliable up to 200 Wm.

The differences between the GeoVISION and the EcoScope phase-shift resistivities in the intervals 30–43 mbsf and 100–157 mbsf are harder to explain, even after discounting phase-shift resistivities above 200 Wm. The general pattern shown by the phase-shift resistivities in these intervals resembles conductive invasion, where the measurements for longer coil spacings, which read deeper, measure higher resistivities. In this interpretation, conducting seawater would invade a gas hydrate-rich, resistive formation. Conductive invasion, however, should be observed in all cases, but the invasion pattern is absent in the 400 kHz attenuation resistivities.

An alternative explanation involves resistivity anisotropy. The resistivity images show nearly vertical fractures throughout most of the gas hydrate-rich intervals in Hole NGHP-01-10A (see below). This will result in resistivity anisotropy if the electrical resistivity of the material that fills the fractures is different from the resistivity of the unfractured formation. In such a composite medium, the effective resistance to electrical currents flowing perpendicular to the fracture planes will be greater than the resistance to currents flowing parallel to the fractures. This is because current flowing parallel to the fractures will concentrate in the low-resistivity portion of the medium (the fracture-filling material or the formation), while current flowing perpendicular to the fractures will be influenced by the resistivity of both formation and fracture fill.

When the well trajectory is nearly parallel to the fracture planes, phase-shift propagation resistivity measurements are more sensitive than attenuation resistivities to the resistance perpendicular to the fractures (Anderson and others, 1994). In the presence of fracture-induced anisotropy, the phase-shift resistivities should be greater than the attenuation resistivities measured at the same frequency and coil spacing, and this is the pattern observed in figure 48. Note that if anisotropy is the cause for the high phase-shift resistivities, it requires the presence of highly resistive heterogeneities (for example, fractures filled by gas hydrate). This explanation can be tested by detailed modeling, which is beyond the scope of this initial report.

The bottom-simulating reflector (BSR) that is observed on seismic reflection data and that should mark the bottom of the gas hydrate stability zone was estimated to be at a depth of 160 mbsf in this hole. At this depth, the logged resistivities in figure 48 decrease abruptly to a background value of 1 Wm that is characteristic of water-saturated sediments in the area. Below 160 mbsf, the hole shows first a restriction and then a washout in the interval 165–190 mbsf (fig. 46), and the interval below 160 mbsf was also difficult to drill (see above).

The depths relative to seafloor were fixed for all of the LWD logs by identifying the step change in the GeoVISION gamma ray log at the seafloor. For Hole NGHP-01-10A, the gamma ray logging pick for the seafloor was at a depth of 1049.3 mbrf, just 0.3 m deeper than the initial depth seen on the camera (1049 mbrf). The rig floor logging datum was located 10.5 m above sea level.

LWD Porosities

Sediment porosities can be determined from analyses of recovered cores and from downhole measurements (see "Physical Properties" and "Downhole Logging" in the "Methods" chapter). Sediment porosities were calculated from the LWD density and neutron logs in Hole NGHP-01-10A. Core-derived physical property data, including porosity (see "Physical Properties"), can be used to calibrate and evaluate the log-derived sediment porosities.

The LWD log-derived density measurements from Hole NGHP-01-10A were used to calculate sediment porosities (φ) with the standard density-porosity relation $\varphi = (r_g - r_b) / (r_g - r_w)$.

We used a constant water density (r_w) equal to 1.03 g/cm^3 and a grain/matrix density (r_g) equal to 2.75 g/ cm^3. The density log-derived porosities from Hole NGHP-01-10A range from a maximum of about 85 percent at 51 mbsf to a minimum around 55 percent in the interval 90–155 mbsf (fig. 47). The density porosities in figure 47 have been calculated from both the bulk density and from the image-derived density curve.

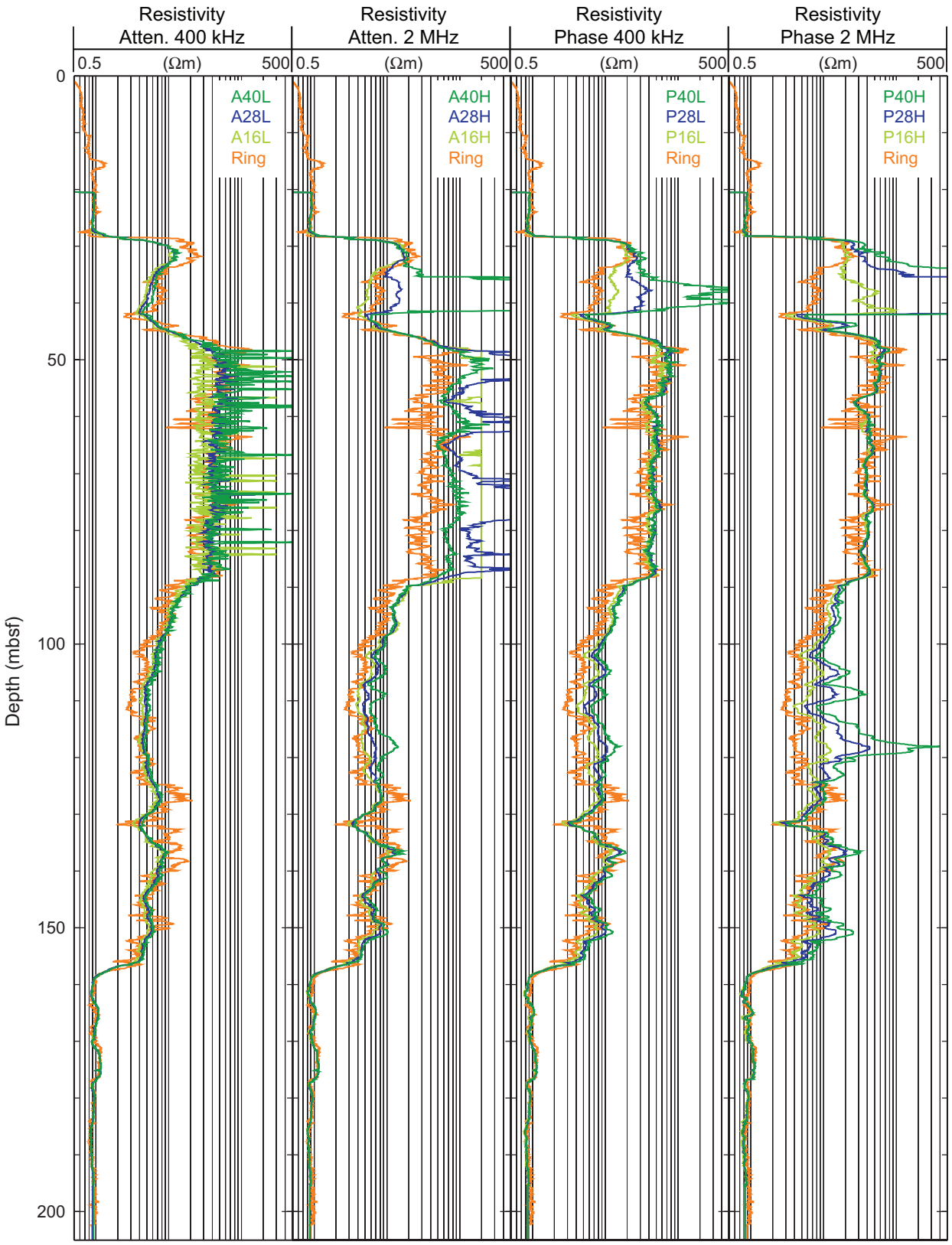


Figure 48. Comparison of LWD resistivity curves from Hole NGHP-01-10A. [LWD, logging-while-drilling; RING, ring resistivity (GeoVISION); AXXL, Attenuation resistivity measured at a frequency of 400 kHz, where XX is the transmitter-receiver spacing in inches (EcoScope); AXXH, Attenuation resistivity measured at a frequency of 2 MHz, where XX is the transmitter-receiver spacing in inches (EcoScope); PXXL, Phase-shift resistivity measured at a frequency of 400 kHz, where XX is the transmitter-receiver spacing in inches (EcoScope); PXXH, Phase- shift resistivity measured at a frequency of 2 MHz, where XX is the transmitter-receiver spacing in inches (EcoScope)]

The LWD neutron porosity log from Hole NGHP-01-10A (fig. 47) yielded sediment porosities ranging from a maximum of about 85 percent at 51 mbsf to a minimum around 60 percent in the interval 90–155 mbsf. Porosities measured by the neutron log are expected to be higher than those computed from the density log in clay-rich sediments, because the neutron log essentially quantifies hydrogen abundance, and counts hydrogen in clay minerals as porosity. The neutron porosity measured by the EcoScope tool shown in figure 47 is the "best thermal neutron porosity" (BPHI); it has been corrected so that the effect of clay is reduced (Adolph and others, 2005), and it is only marginally higher than the density porosity. Both curves agree reasonably well with the porosity measurements made on core samples onboard shown in the same figure.

LWD Borehole Images

The GeoVISION and EcoScope LWD tools generate high-resolution images of borehole log data. The EcoScope tool produces images of density and hole radius (computed on the basis of the density correction, which depends on the borehole standoff). The GeoVISION produces a gamma ray image and resistivity images with shallow, medium and deep depths of investigation.

Figure 49 shows some of the LWD images collected by the EcoScope and GeoVISION tools. It should be noted that the display in figure 49 is highly compressed in the vertical direction. The unwrapped images are about 80 cm wide (for a 10 in diameter borehole) and the vertical scale is compressed relative to the horizontal by a factor of about 55:1. These high-resolution images can be used for detailed sedimentological and structural interpretations and to image gas hydrate distribution in sediments (for example, in layers, nodules, fractures). Gas hydrate-bearing sediments exhibit high resistivities within intervals of uniform or low bulk density. Layers with high resistivities and high densities are likely to be low porosity, compacted, or carbonate-rich sediments. The two resistivity images in figure 49 correspond to two depths of investigation (for details, see "Downhole Logging" in the "Methods" chapter).

The resistivity images clearly show a prominent high-resistivity interval between 28 and 158 mbsf. These resistivities are extremely high compared to the background values (around 1 Wm) typically observed in water-saturated marine sediments and thus indicate possibly significant gas hydrate accumulations. Figures 50A through 50E display in detail the 28–158 mbsf high-resistivity interval. In each figure, the image on the right ("Dynamic Deep Image") has been equalized in a moving 2 m-thick window to emphasize small-scale features. Figures 50A through 50E show a number of fractures intersecting the borehole. In the unwrapped resistivity images, these fractures appear as sinusoidal curves (for example, Bonner and others, 1996). Clear examples are at 41 mbsf (a resistive fracture, likely to be filled by gas hydrate), 52 mbsf (a conductive fracture), and the interval 90–124 mbsf. The vertical distance between the top and the bottom of these sinusoidal fractures is generally 2 m or more; as the borehole diameter is around 11 in (28 cm), this means that these fractures are nearly vertical. The intervals that show clear evidence of quasi-vertical fractures coincide with the interval where the phase-shift resistivities are greater than the corresponding attenuation resistivities (fig. 48), which supports the hypothesis of resistivity anisotropy due to fractures (see above).

Wire-Line Logging in Hole NGHP-01-10D

Operations

Hole NGHP-01-10D was primarily dedicated to pressure coring and logging and was completed to 1254.2 mbrf (203.8 mbsf) at 0830 hr on 20 June. It was then conditioned for logging with a wiper trip, several mud sweeps and displaced with 105 bbl of barite in order to improve stability. The bit was then set at 1123.7 mbrf, with the possibility to be raised to 1108 mbrf, the top drive was removed and rig floor preparation for logging started at 1430 hr.

Rig-up of the triple combo tool string for the first logging run started at 1555 hr and the tool was rigged into the hole (RIH) at 1650 hr. The tool string reached the bit at 1740 hr, had some trouble exiting the pipe, and once in open hole could no go deeper than 1204 mbrf (153.6 mbsf). The up-log started at 1910 hr at a speed of 900 ft/hr, and was complete at 1950 hr, after recording the seafloor with the gamma ray log at 1047.5 mbrf. The tool was back on the rigfloor at 2025 hr and rigged down at 2135 hr.

In order to try to reach a deeper depth with the following logging runs, the logging sheaves and equipments were laid down and a wiper trip was made to clear the bottom of the hole. Following the wiper trip, the hole was again displaced with barite and the pipe was set at 1114.3 m, to be raised to 1098.6 m.

The FMS/Sonic rig up started at 0435 hr on June 21, 2006, and the tool was RIH at 0530 hr. There was again some problem going down through the bit, and once in open hole, the tools string could not be lowered below 1210 mbrf, indicating that the efforts to clean the hole had only gained a few meters. Three passes were made, starting at 0730 hr, with the DSI configured first to record Low Frequency Monopole/Low Frequency Upper Dipole/Standard frequency Lower Dipole/Stoneley modes, then Low frequency Monopole/X-dipole/Stoneley modes and an unsuccessful attempt at recording Low frequency cross dipole on the last pass. FMS images were recorded during the three passes. The tool was brought back to the surface at 1005 hr and rigged down at 1045 hr.

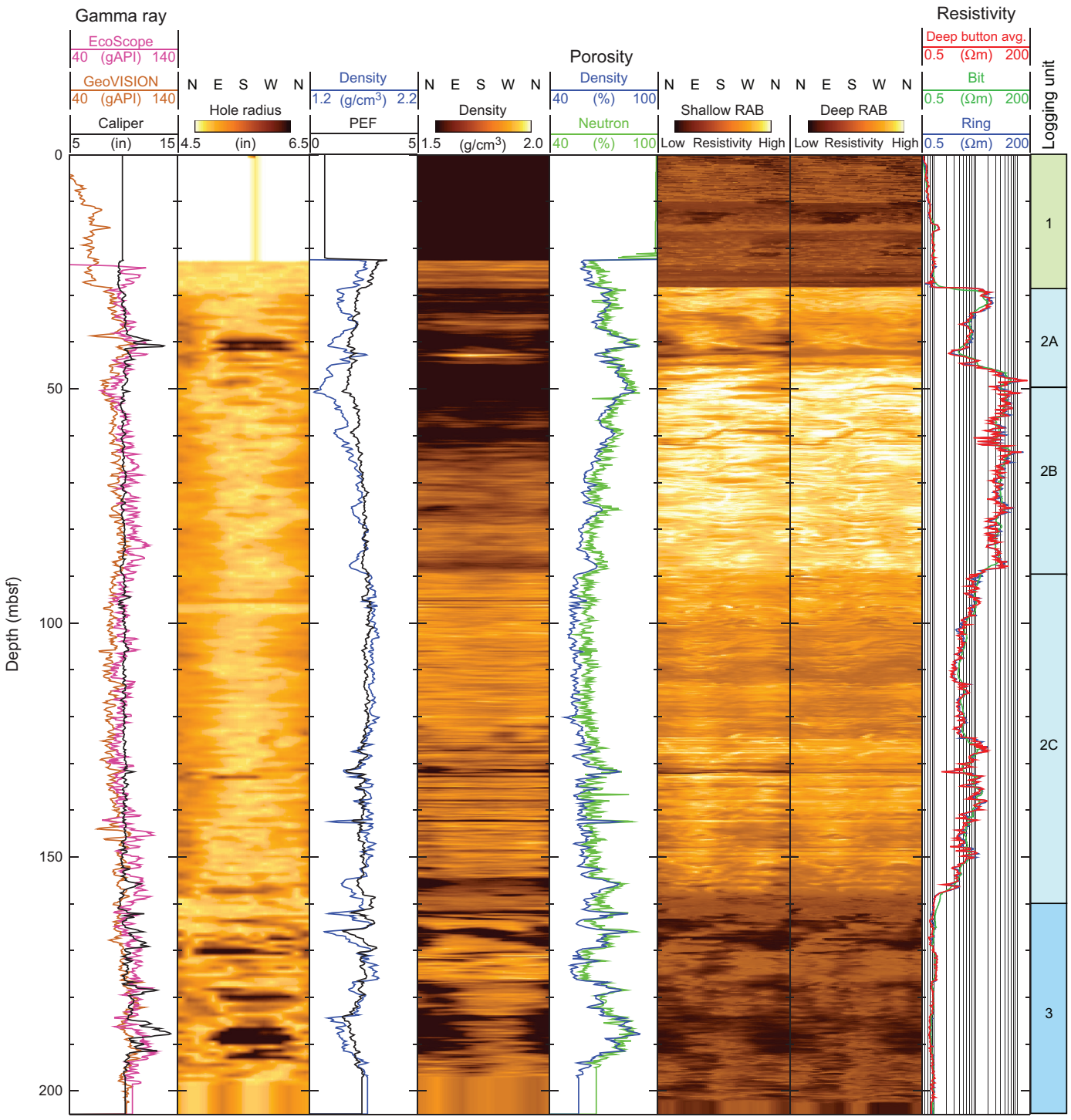
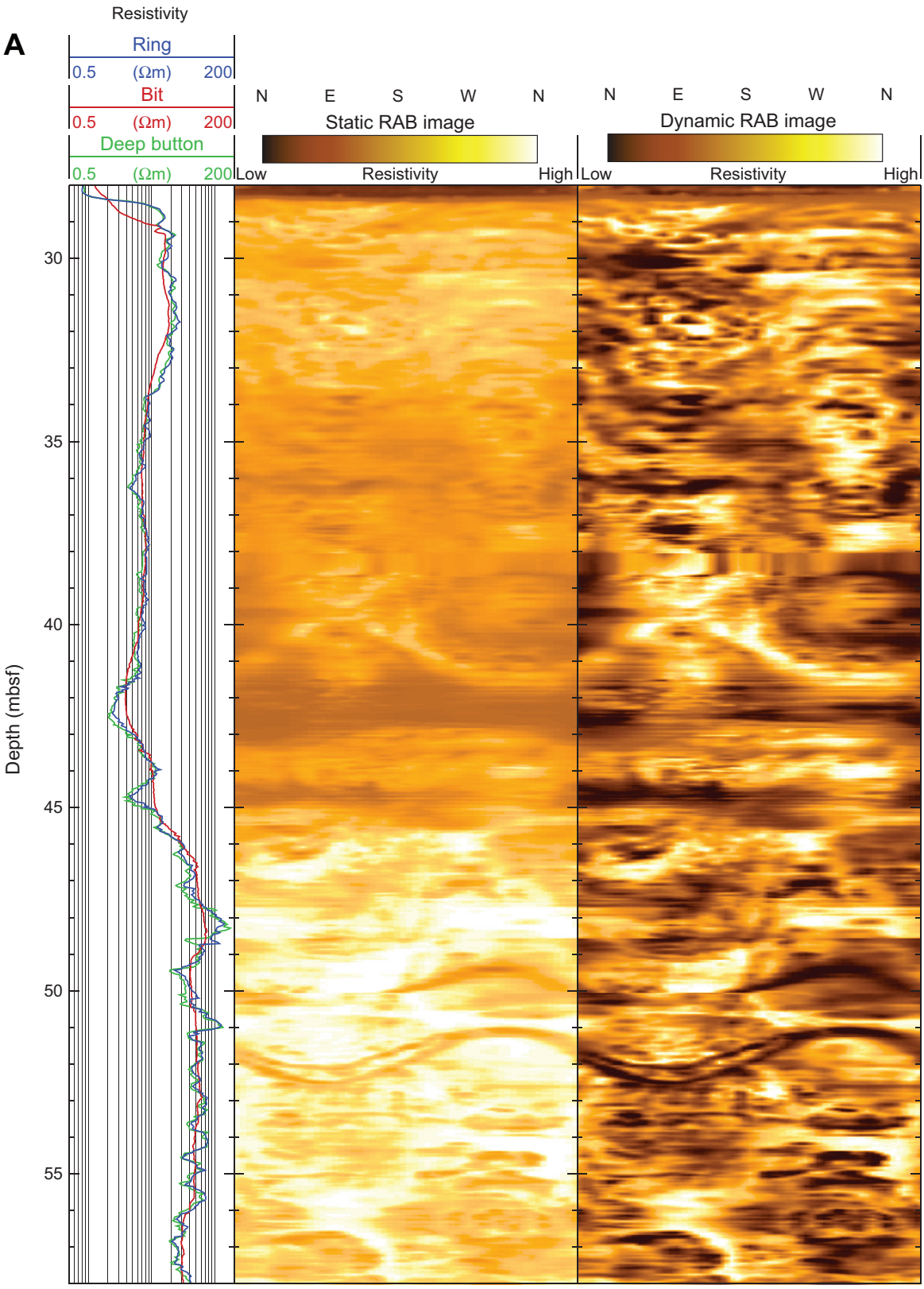
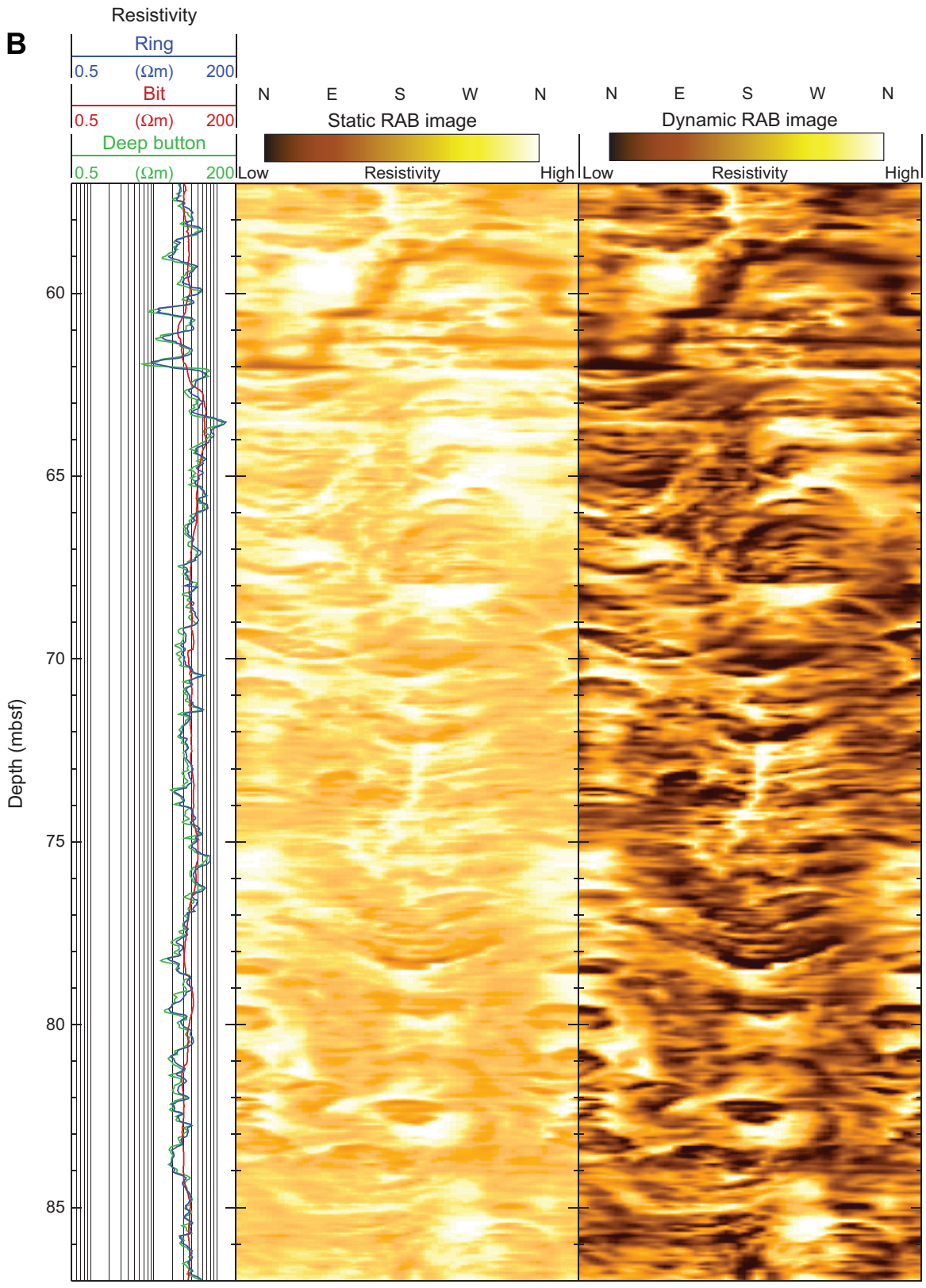


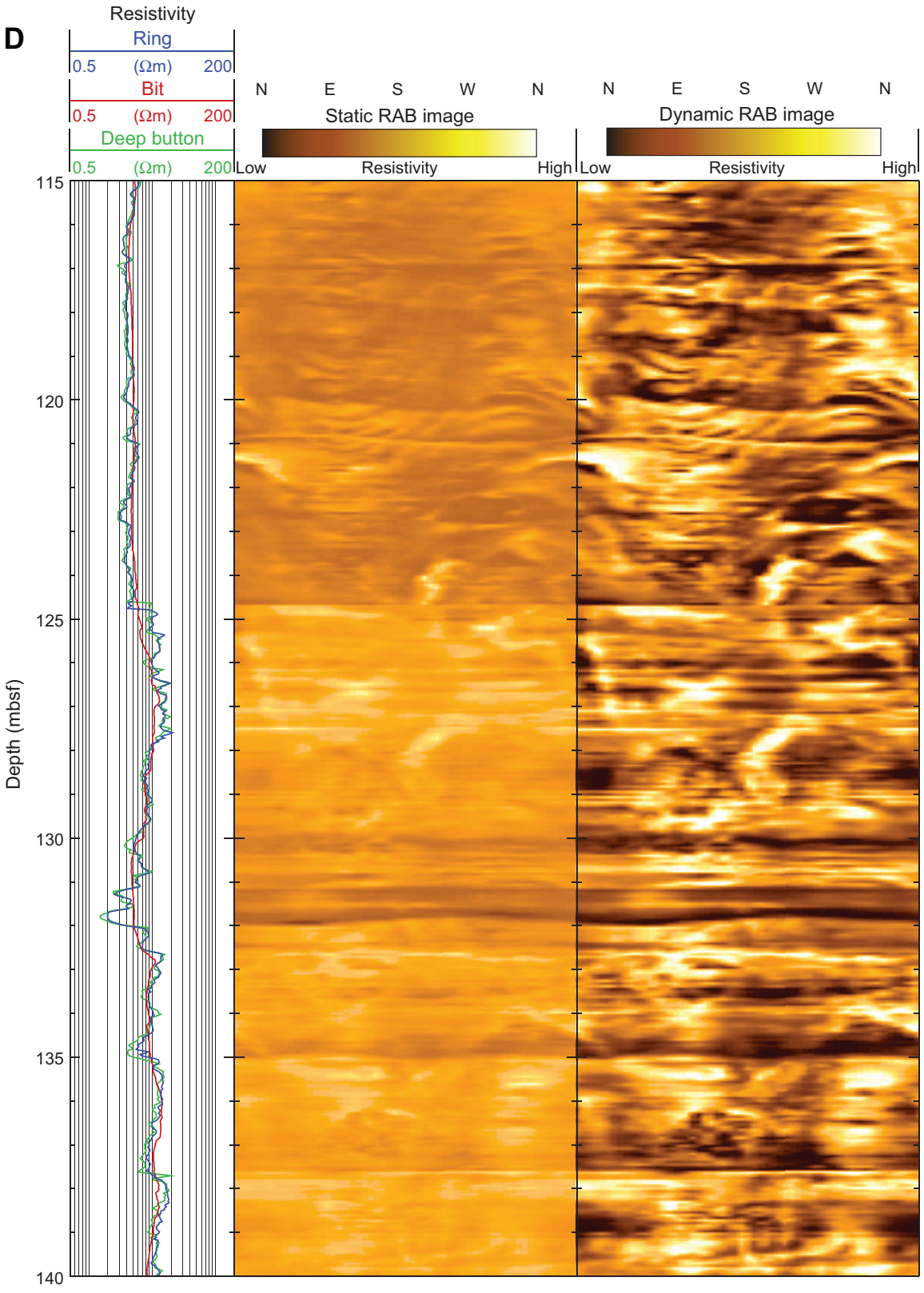
Figure 49. LWD image data from Hole NGHP-01-10A. [LWD, logging-while-drilling; gAPI, American Petroleum Institute gamma ray units; RAB, resistivity-at-bit image obtained by the GeoVISION tool]



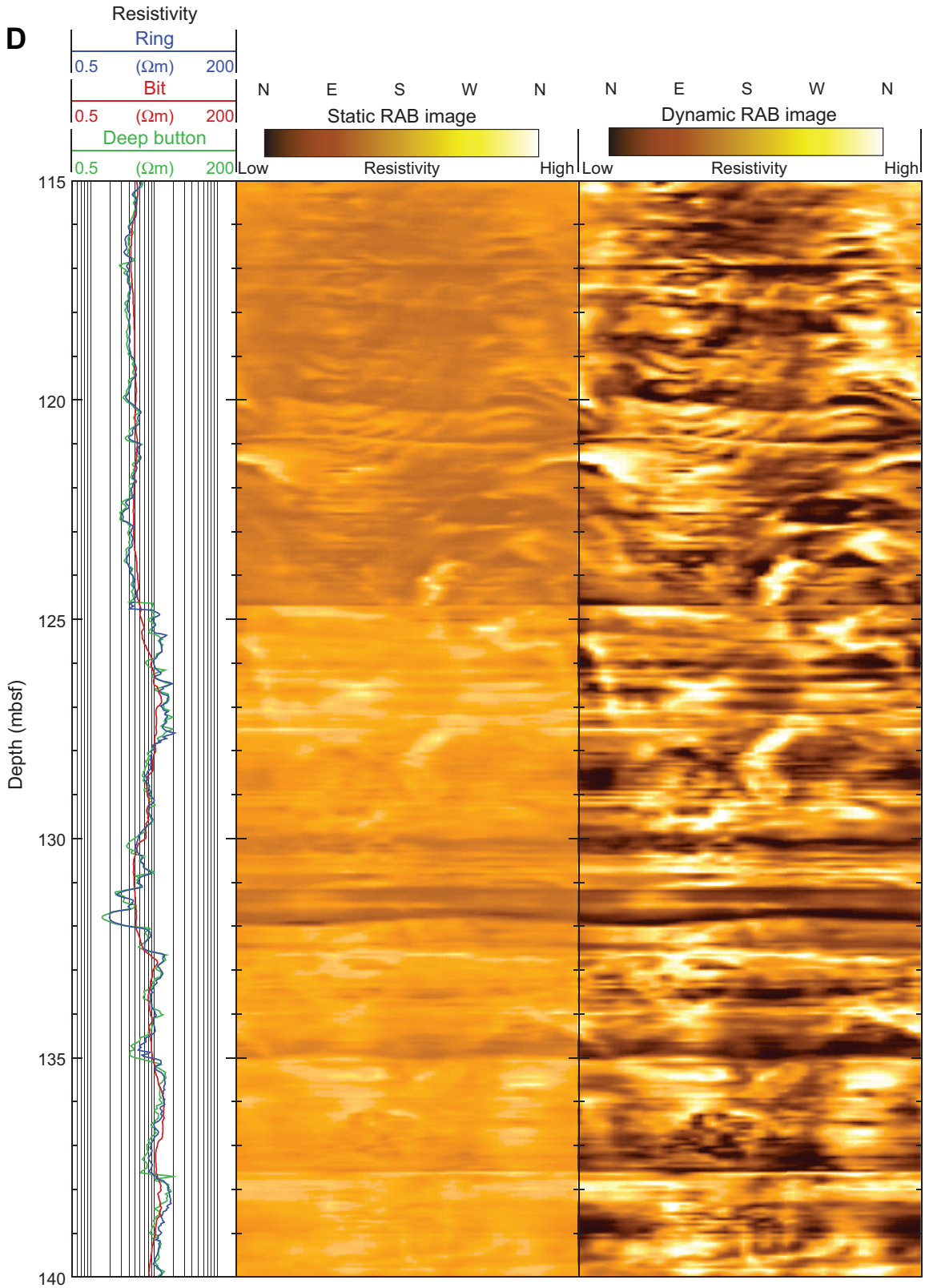
Figures 50. LWD resistivity image (GeoVISION deep button) from Hole NGHP-01-10A. The image on the left ("Static RAB Image") has been equalized throughout the entire logged interval to enhance the contrast between low and high resistivity regions. The image on the right ("Dynamic RAB Image") has been equalized with a 2-m-thick moving window to enhance small-scale features, and it clearly shows a number of sinusoidal features interpreted as steeply-dipping fractures that intersect the borehole. [LWD, logging-while-drilling]



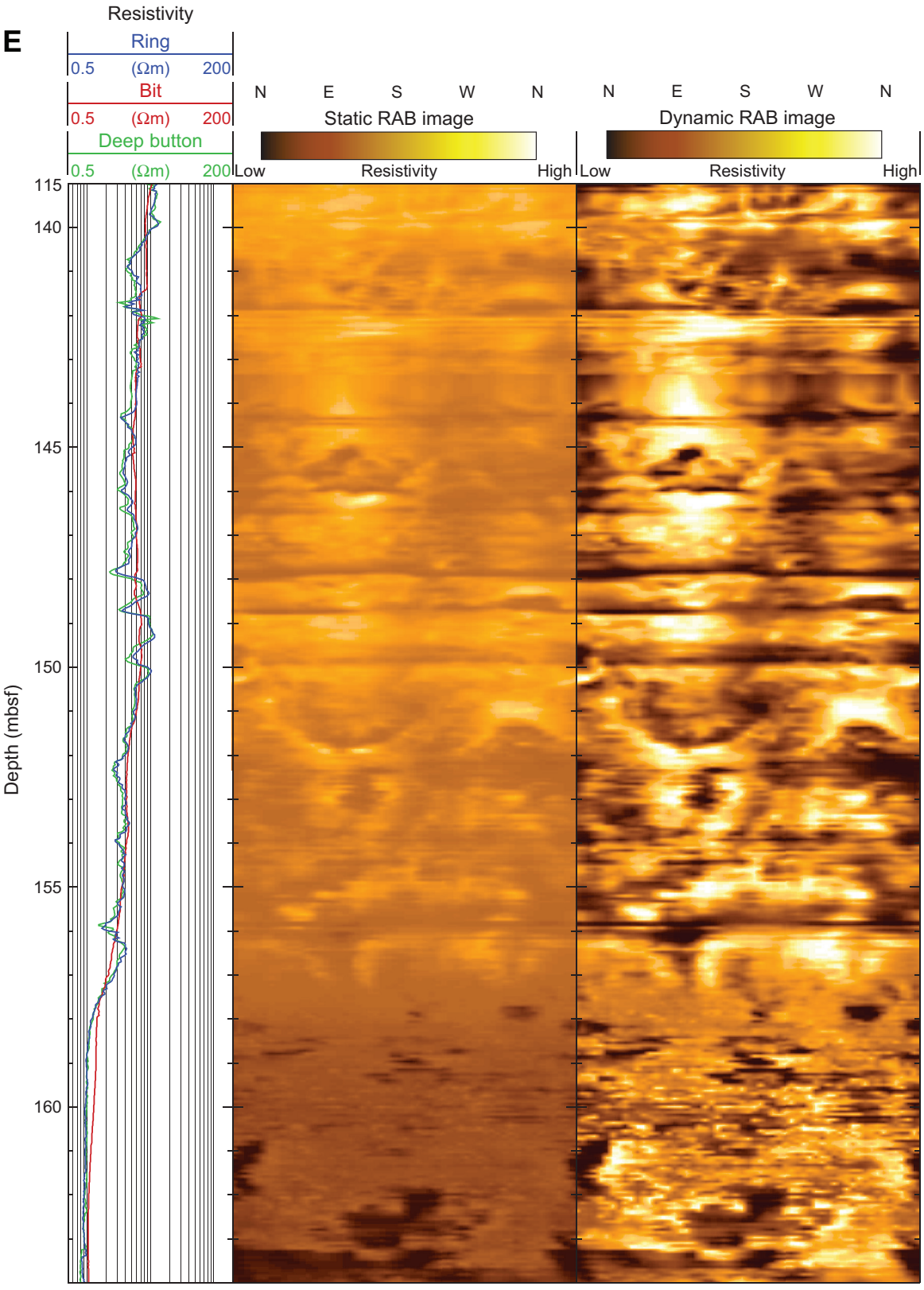
Figures 50. LWD resistivity image (GeoVISION deep button) from Hole NGHP-01-10A. The image on the left ("Static RAB Image") has been equalized throughout the entire logged interval to enhance the contrast between low and high resistivity regions. The image on the right ("Dynamic RAB Image") has been equalized with a 2-m-thick moving window to enhance small-scale features, and it clearly shows a number of sinusoidal features interpreted as steeply-dipping fractures that intersect the borehole. [LWD, logging-while-drilling]—Continued



Figures 50. LWD resistivity image (GeoVISION deep button) from Hole NGHP-01-10A. The image on the left ("Static RAB Image") has been equalized throughout the entire logged interval to enhance the contrast between low and high resistivity regions. The image on the right ("Dynamic RAB Image") has been equalized with a 2-m-thick moving window to enhance small-scale features, and it clearly shows a number of sinusoidal features interpreted as steeply-dipping fractures that intersect the borehole. [LWD, logging-while-drilling]—Continued



Figures 50. LWD resistivity image (GeoVISION deep button) from Hole NGHP-01-10A. The image on the left ("Static RAB Image") has been equalized throughout the entire logged interval to enhance the contrast between low and high resistivity regions. The image on the right ("Dynamic RAB Image") has been equalized with a 2-m-thick moving window to enhance small-scale features, and it clearly shows a number of sinusoidal features interpreted as steeply-dipping fractures that intersect the borehole. [LWD, logging-while-drilling]—Continued



Figures 50. LWD resistivity image (GeoVISION deep button) from Hole NGHP-01-10A. The image on the left ("Static RAB Image") has been equalized throughout the entire logged interval to enhance the contrast between low and high resistivity regions. The image on the right ("Dynamic RAB Image") has been equalized with a 2-m-thick moving window to enhance small-scale features, and it clearly shows a number of sinusoidal features interpreted as steeply-dipping fractures that intersect the borehole. [LWD, logging-while-drilling]—Continued

The third and final run was an attempt to get a vertical seismic profile (VSP) with the Versatile Seismic Imager (VSI, see "Downhole logging" in the "Methods" chapter). Based on our experience at the previous site, the tool was configured with long arms in order to try to improve the quality of the coupling with these unconsolidated sediments. After completion of a survey to detect any marine mammal activity, the tool was lowered at 1130 hr, and reached the maximum depth of 1196 mbrf (145.5 mbsf) at 1240 hr. The first shot was fired at 1245 hr with the tool anchored at 1195 mbrf, and stations were recorded every 5 m from this depth. At this point the heave amplitude was about ~2 m, and despite the heave compensation, its effect was felt in the wire-line tension. It resulted in a generally noisy signal, and multiple additional shots had to be fired at most stations to be able to stack enough reliable waveforms. Out of 17 stations attempts, with a total of 277 shots fired, 12 stations were successful. The air gun was last fired at 1610 hr, and the tool was back at the surface at 1650 hr. Logging rig down was complete at 1710 hr, and the rig floor was cleared for transit to the next site at 1745 hr on 21 June.

Wire-Line Log Quality

Figure 51 shows the main logs recorded in Hole NGHP-01-10D. The hole size, calculated with the two orthogonal calipers of the FMS, indicates that the hole was slightly enlarged and irregular, but that the caliper arms never lost contact with the formation, ensuring that the data are of good quality. The very narrow hole below 140 mbsf shows where hole conditions were starting to deteriorate and illustrates the difficulties encountered while trying to lower the tool below this depth.

The clear sonic waveforms and coherence data in figure 52, and in particular the high coherence in the monopole data, confirm the overall good quality of the data and suggest that the compressional velocity log (V_P) provides a reliable estimate of the velocity profile in the formation. Some additional processing was still necessary to refine this profile and the V_S logs.

Wire-Line Logging in Hole NGHP-01-13A

Operations

Hole NGHP-01-13A was drilled without coring as a hole dedicated for logging to complete the delineation of the gas hydrate formation sampled in Holes NGHP-01-10A, -10B, -10C, -10D and -12A. After failing to reach the target depth of 200 m in Hole NGHP-01-12A, it was decided that acquiring at least a triple combo run in this site located between Sites NGHP-01-10 and NGHP-01-12 would be the most efficient way to use the little time left before the end of Leg 3A.

The target depth of 200 mbsf (1244 mbrf) was reached at 1045 hr on 23 June. The hole was then conditioned with a 50 bbl sepiolite sweep and displaced with 80 bbl of barite. The pipe was then set to the logging depth of 1104.6 mbrf, and after setting back the top drive, the rig floor was prepared for logging, starting at 1330 hr.

Assembling up of the triple combo tools string started at 1425 hr and was complete at 1500 hr. The string was run into the hole (RIH) at 1530 hr, with a go-devil attached at the bottom to open the lockable flapper valve located immediately above the bit. At 1610 hr the bottom of the tool string reached 1101 mbrf, still inside the pipe, but could not go any deeper. After about an hour of unsuccessful efforts, trying in particular to pump heavily to facilitate the way out, we decided to bring the tool to the surface at 1705 hr to see if there would be any indication on the tool of what was the nature of the obstacle. Once the tool was back on the surface at 1740 hr, some fairly deep scars were observed on the go-devil, but did not give any clear indication of what could have caused them. It was decided to send an XCB core barrel with center bit, to check if it would latch properly, and hoping it would clear the way for the logging tool. The triple combo was partially rigged down during this operation. The core barrel was brought back to the surface at 2000 hr, after having successfully latched at the bottom of the pipe, but without giving sign of any anomaly. Additional drilling mud was circulated while the core barrel was at the bottom, in order to help clear any obstruction. Because of the absence of any conclusive indication of anomaly, and considering the time that had been invested in drilling this hole and the importance of delineating the extent of the gas hydrate occurence, it was decided to try one last time to run the triple combo. The tool string was re-built and RIH by 2055 hr, and was at the bit at 2125 hr. The bottom of the string was able to exit the pipe after only a few attempts, but met a new obstruction immediately below. It took additional attempts and pumping to get the tool totally in open hole at 2150 hr. At 2200 hr, the tool reached 1194 mbrf (~150 mbsf) and could not make any progress for the next ten minutes. As this depth was similar to the maximum depth reached by the triple combo in neighboring Hole NGHP-01-10D, it was assumed that the formation was showing the same uncompromising behavior at the bottom of the hydrate stability field, and as time was running out we decided to log from this point. We started recording data at 2210 hr at a logging speed of 900 ft/hr, and at 2225 hr the caliper was closed and the wire-line heave compensator deactivated before reentering the pipe. This proceeded without problem, and the pass was complete at 2255 hr when the gamma ray log indicated the seafloor at 1046 mbrf. The tool string was back at the surface at 2325 hr, rigged down at 0025 hr on 24 June, and the rig floor was clear at 0115 hr for preparations for the transit.

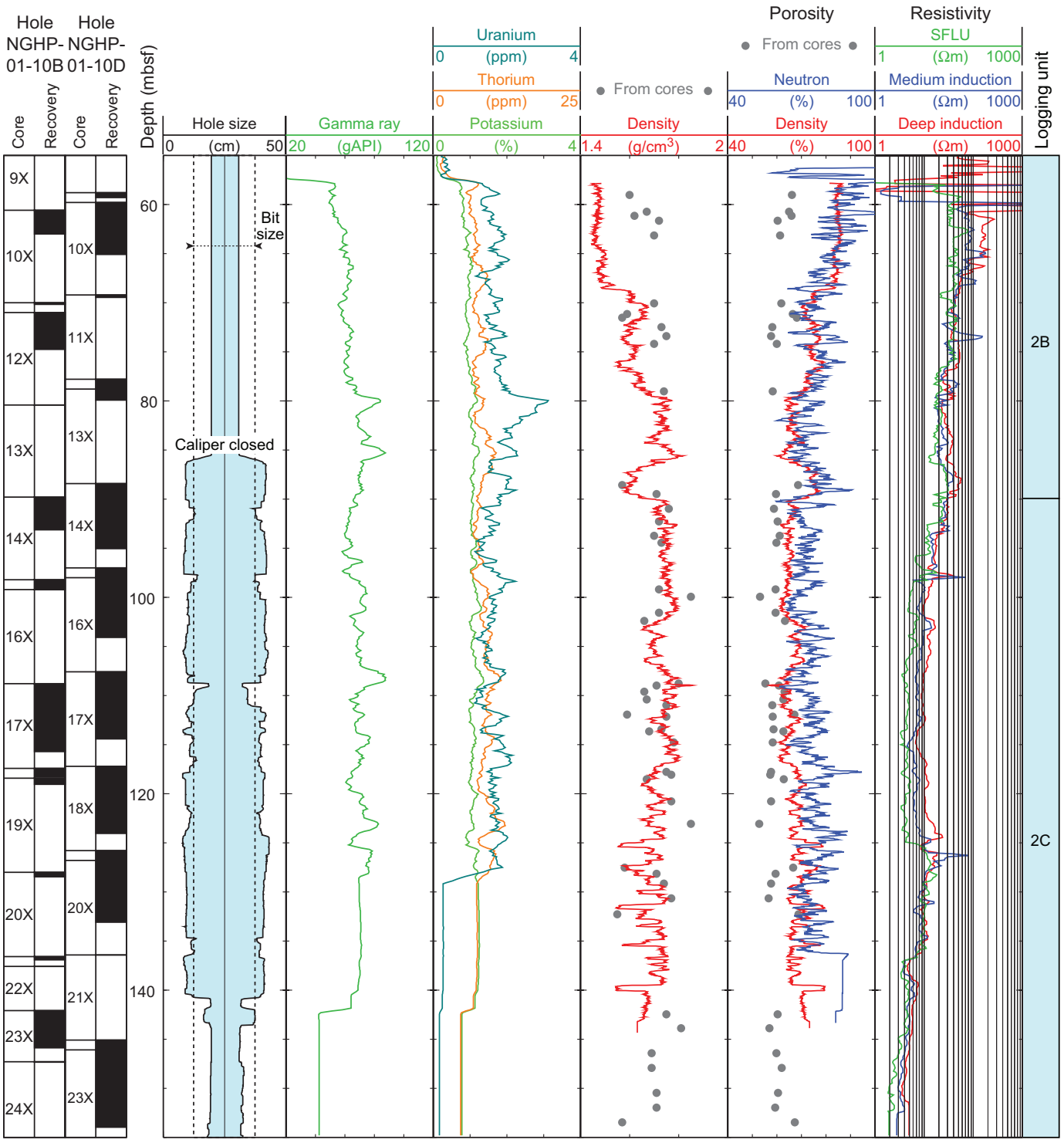


Figure 51. Summary of the wire-line logs recorded in Hole NGHP-01-10D. [SFLU, spherically-focused log]

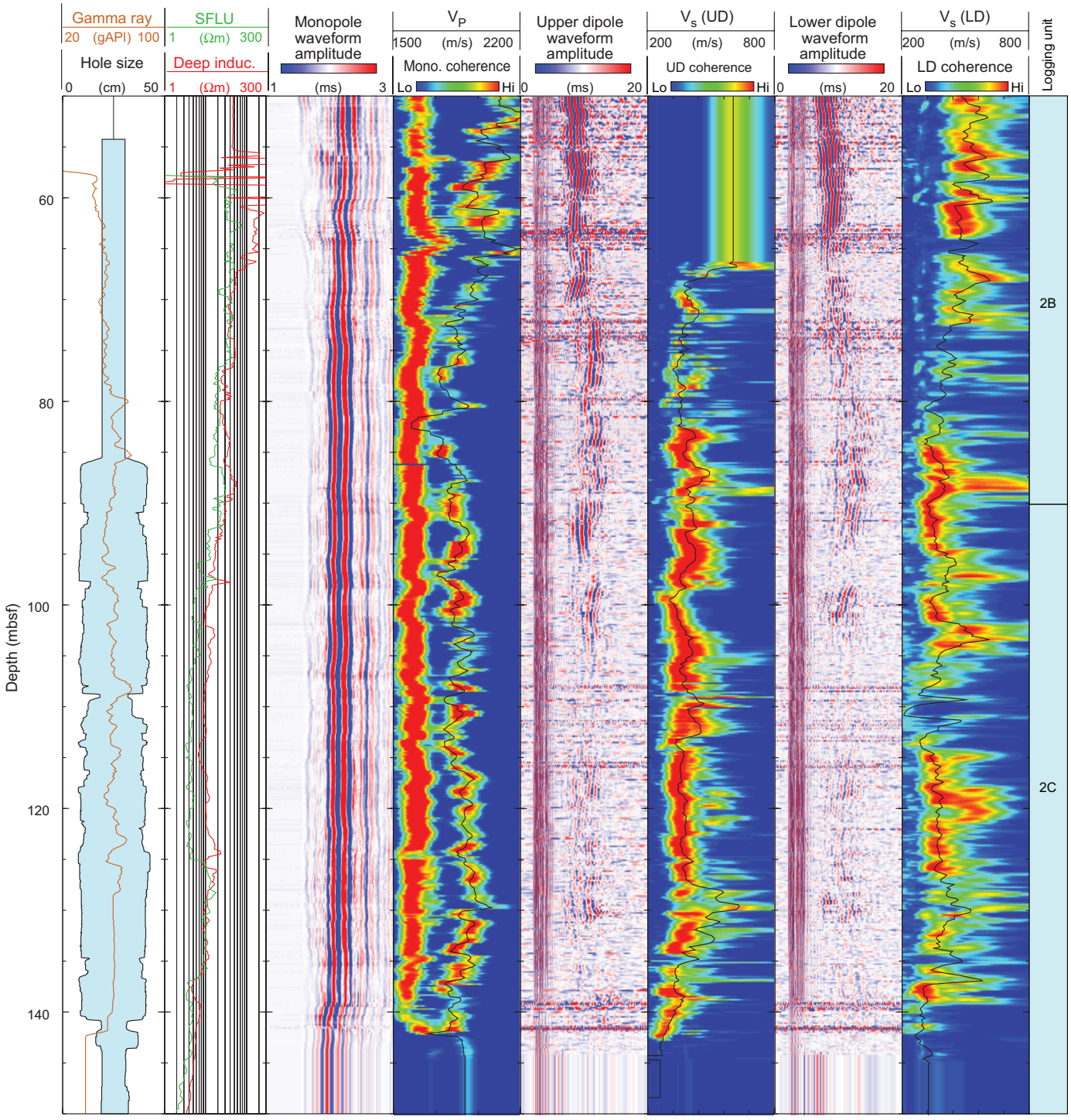


Figure 52. Sonic waveform data, P-wave and S-wave velocities measured by the DSI wire-line log in Hole NGHP-01-10D. The hole size and the gamma ray and resistivity logs are shown for quality control and correlation. [DSI, Dipole Shear Sonic Imager; V_P, P-wave velocity, V_s, S-wave velocity, LD, lower dipole, UD, upper dipole]

Logging Data Quality

The caliper log in Figure 53 shows that the hole was slightly enlarged but very regular over the entire interval logged, and that the tool was able to maintain contact with the borehole wall, assuring the good quality of the density data. However, in the absence of any core data in this hole, the good quality of the data could not be confirmed by comparison with other data sets. The density porosity was derived from the density log by assuming a constant grain density of 2.72 g/cm^3, which was the average value measured on the cores collected in Site NGHP-01-10. The neutron porosity is consistently higher than the density porosity because of the influence of the mineral-bound water in these clay-rich sediments.

Over such a short interval logged, the only noticeable variability in the data is in the resistivity log, with consistently high values over 2 Wm that reach ~30 Wm at ~85 and ~95 mbsf. These values are all significantly higher than the formation resistivity measured in the other neighboring sites and indicate possibly significant gas hydrate concentrations. In particular, the interval between 80 and 95 mbsf displays higher porosity and resistivity values, which is the likely indication of high gas hydrate concentrations.

Logging-While-Drilling and Wire-Line Logging Comparison

Figure 54 shows a comparison between the LWD and wire-line logging data collected at Site NGHP-01-10, using the caliper, gamma ray, porosity, density and resistivity logs from Holes NGHP-01-10A and NGHP-01-10D. The comparison of the two wire-line caliper logs with the bit size and the LWD ultrasonic caliper shows that while the LWD data were recorded in a hole almost on gauge, Hole NGHP-01-10D was significantly enlarged in most places by the time the wire-line logs were acquired. This difference could by itself account for most of the differences between the two data sets, in addition to the fact that the data were not recorded in the same hole. Despite the different hole conditions, all the logs display very similar trends, most notably the density and resistivity logs. The generally larger neutron porosity values measured by the wire-line APS tool are affected by the considerable clay content of the formation, which is corrected for in the LWD log.

Logging Units

The combined analysis of the LWD and wire-line logging data in figures 47, 49, 51, and 52 can identify three logging units where the resistivity, density, gamma ray and/or velocity logs have distinct characters.

Logging unit 1 (0–28 mbsf), only identified by the LWD logs, and only partially due to the low pumping rate at the beginning of the LWD hole, shows an overall increase in gamma ray and low resistivity values, indicating poorly consolidated sediments.

Logging unit 2 (28–160 mbsf) is clearly defined by high resistivity values that could be associated with the presence of significant amounts of gas hydrate. The unit can be divided in three subunits, showing almost stepwise resistivity values. Subunit 2A (~28–50 mbsf) has only moderately elevated resistivities (~10 Wm), slightly decreasing with depth, and shows also a decrease in density with depth, clearly illustrated in the density image in figure 49. Logging subunit 2B (~50–90 mbsf) shows extremely high resistivity values for this type of formation, with most readings in the 10s of Wm and some intervals almost at 1000 Wm, and is most remarkably delineated by the brightest RAB images in figure 49. While density generally increases with depth within this subunit, compressional velocity (V_p) decreases with depth from 2300 m/s at the top to ~1700 m/s. Finally, logging Subunit 2C (90–160 mbsf) is defined by resistivity values of a few Ωm, slightly decreasing with depth, while all other logs are almost constant. The preliminary results of the VSP (see fig. 55) suggest that the BSR, at a two-way travel time of 1.55 s, could be at the bottom of this unit.

Logging unit 3 (160–205 mbsf), also identified only in the LWD logs, is characterized primarily by an enlarged hole, illustrated by the darker caliper images in figure 49, and low density and resistivity values. These characteristics of soft unconsolidated sediments can explain the hole stability problems encountered while trying to lower the wire-line logging tools in Hole NGHP-01-10D.

Gas Hydrate and Free Gas Occurrence

As previously discussed (see "Downhole Logging" in the "Methods" chapter), the presence of gas hydrate is generally characterized by increases in electrical resistivities and acoustic velocities that are not accompanied by a corresponding porosity decrease. Remarkably, in Hole NGHP-01-10A, while porosity surprisingly increases with depth in the interval between 50 and 90 mbsf, resistivity is at its maximum, suggesting extremely high gas hydrate saturations.

To make a quantitative estimate of the amount of gas hydrate around Hole NGHP-01-10A, we followed the procedure described in "Downhole Logging" in the "Methods" chapter, to apply the Archie relationship to the resistivity and porosity logs recorded in this hole. The procedure and the results are shown in figure 56. The pore fluid resistivity (R_w) was estimated from Fofonoff (1985) using a linear temperature profile defined by the *in situ* temperature measurements made in Site NGHP-1-10 (6.5 °C at the seafloor and a gradient of 45 °C/km, see " Physical Properties") and a water salinity of 32.5 ppm, which was an average for the pore water measurements made on samples from this site. The estimated m curve is derived from R_w, the porosity (φ) and resistivity (R_t) logs ($m_{est} = -\log F/\log\varphi$, where $F=R_t / R_w$). The value of m=2.3 is given by the baseline of this curve in the low-resistivity water-saturated formation. Using the porosity log and Archie's equation ($R_0 = (a\, R_w) / \varphi^m$), we derive the predicted resistivity of the water-saturated formation R_o.

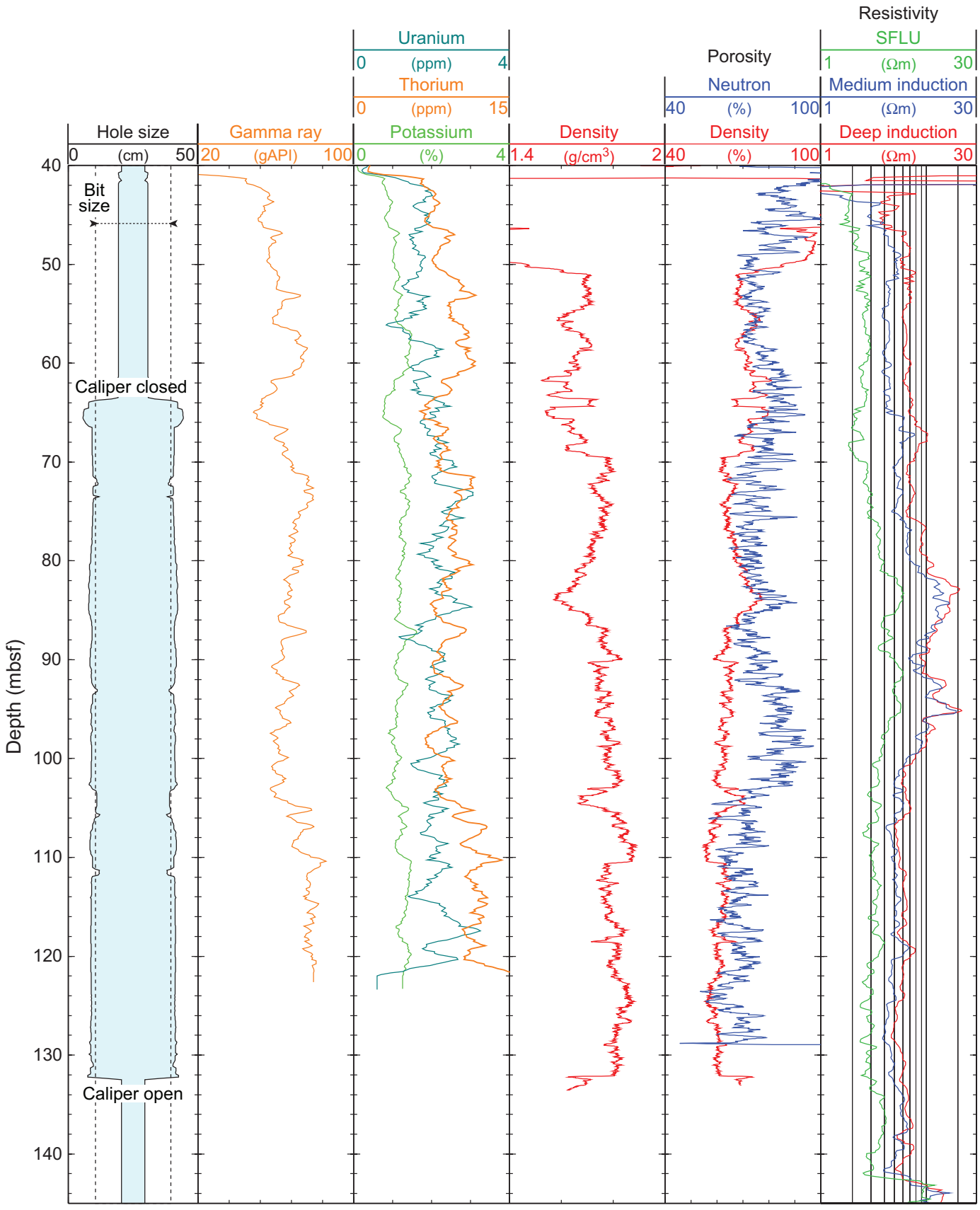


Figure 53. Summary of the wire-line logs recorded in Hole NGHP-01-13A. [SFLU, Spherically focused unaveraged resistivity]

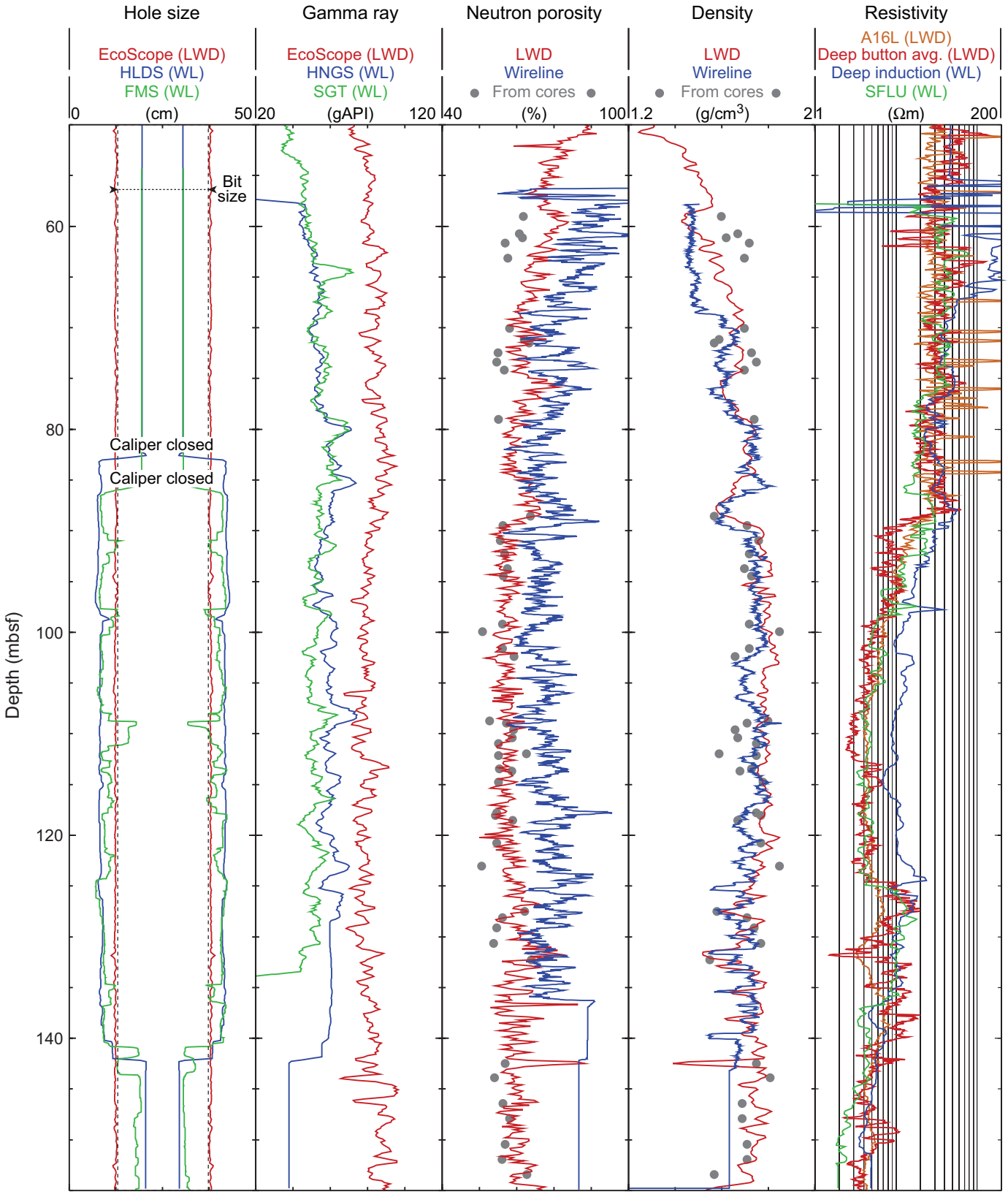


Figure 54. Comparison of LWD (Hole NGHP-01-10A) and wireline log data (Hole NGHP-01-10D). [LWD, logging-while-drilling, WL, Wireline; HLDS, Hostile Environment Litho-Density Sonde; HNGS, Hostile Environment Gamma Ray Sonde; SGT, Scintillation Gamma Ray Tool; SFLU, Spherically focused log]

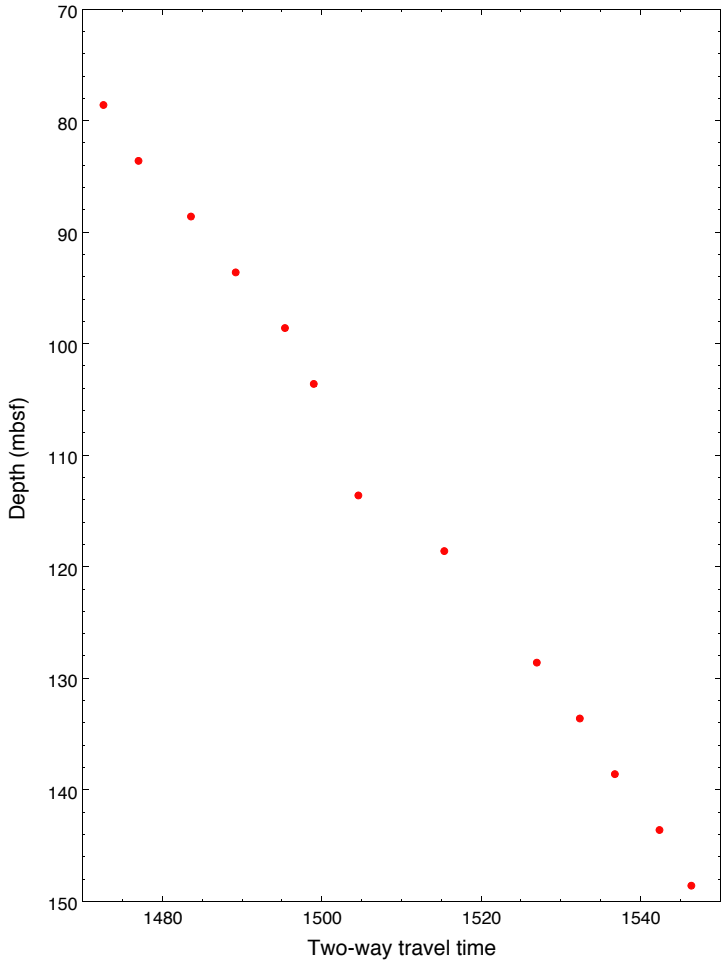


Figure 55. Time-depth plot of first break times in the Hole NGHP-01-10D Vertical Seismic Profile.

A qualitative influence of gas hydrate on the resistivity log is indicated by the difference between the R_0 and the measured resistivity R_t. The actual water saturation, assumed to be the numerical complement of the hydrate saturation, is $S_w = (R_o/R_t)1/n$, where n=2 (Pearson and others, 1983). We used the density porosity computed from the image-derived density (IDRO) and the resistivity from the 16 in, phase-shift, high-frequency propagation resistivity (P16H) measured by the EcoScope tool. We use the P16H curve because it is the resistivity with the highest vertical resolution measured by the EcoScope.

As noted earlier, the high resistivities measured in Hole NGHP-01-10A cannot be explained by a corresponding low porosity, and must correspond to high gas hydrate saturations. The gas hydrate saturations computed from Archie's equation are about 85 percent in the interval 27–90 mbsf, and decrease slightly to 50–75 percent in the interval 90–157 mbsf. These computed gas hydrate saturations will depend on the resistivity curve chosen for R_t. The measured resistivities and porosities, however, are always high in the interval 27–157 mbsf of Hole NGHP-01-10A, and an Archie-based analysis is bound to give a high estimate of gas hydrate saturation.

Gas Hydrate and Free Gas Occurrence in Hole NGHP-01-13A

We used the same method and the same values of temperature and salinity to derive gas hydrate saturations around Hole NGHP-01-13A from the wire-line resistivity and density porosity logs recorded in this hole. We used two resistivity measurements to calculate the estimates shown in figure 57. The Spherically Focused unaveraged resistivity (SFLU) has the highest resolution, but the shallowest penetration, of the resistivity measurements made by the DIT tool and is more sensitive to drilling disturbances; the Deep Induction log (ILD) has the deepest penetration, but a lower vertical resolution. The combination of these two estimates provides a possible range of gas hydrate distribution around Hole NGHP-01-13A.

The results indicate gas hydrate saturations uniformly higher than ~40 percent over the entire interval logged, with the highest values predicted near 80 percent by the deep induction log in the high-resistivity, high-porosity interval around 85 mbsf. These estimates are slightly lower but similar to the saturations derived from the LWD logs in Hole NGHP-01-10A.

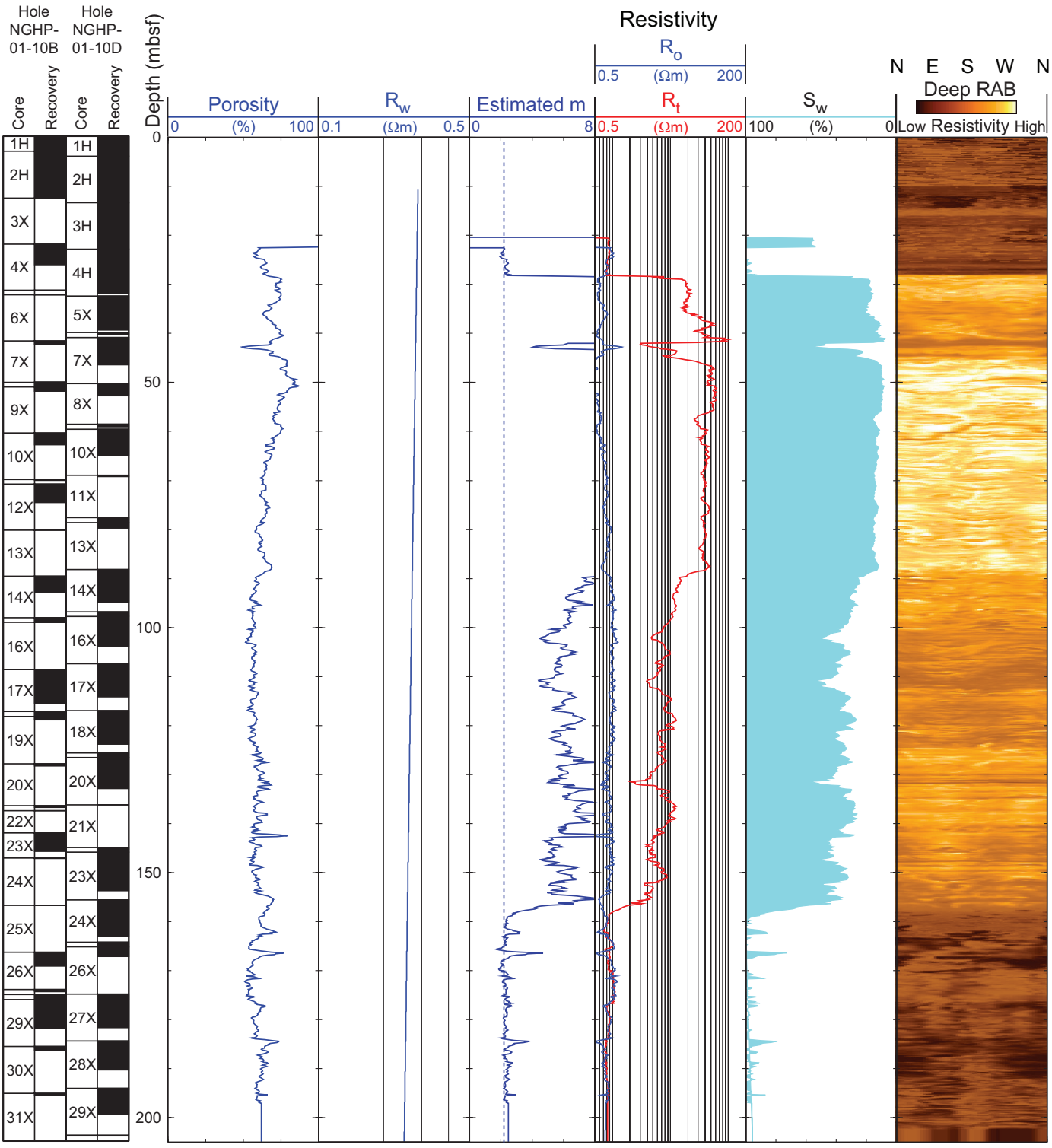


Figure 56. Water saturations from Archie's relationship and LWD porosity and resistivity logs in Hole NGHP- 01-10A. [LWD, logging-while-drilling; R_w, Formation water resistivity; R_0, Computed formation resistivity for 100 percent water saturation; R_t, Measured resistivity; S_w, water saturation]

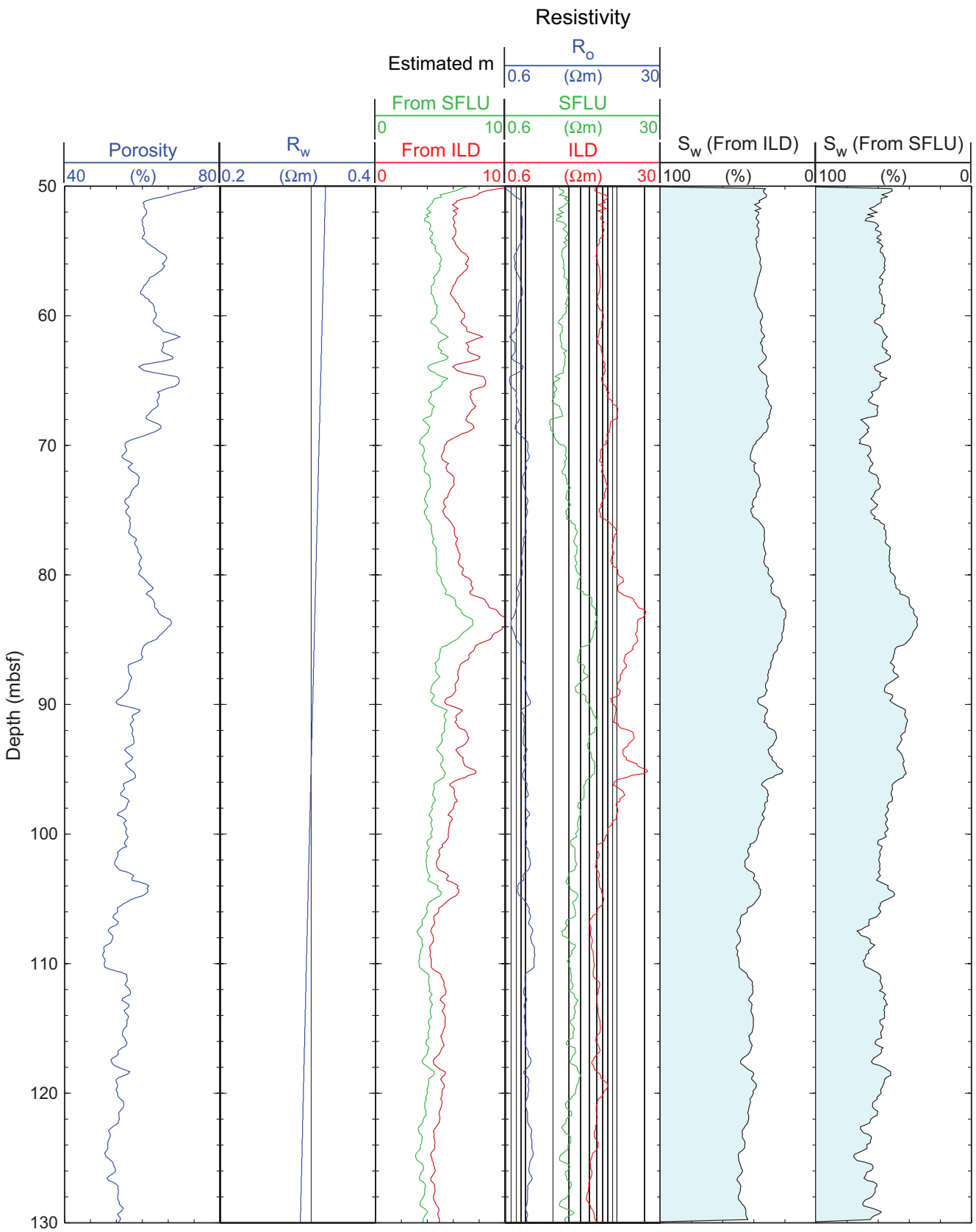


Figure 57. Water saturations from Archie's equation and wireline porosity and resistivity logs in Hole NGHP-01-13A. [R_w, Formation water resistivity; R_0, Computed formation resistivity for 100 percent water saturation; R_t, Measured resistivity; S_w, water saturation; SFLU, Spherically focused unaveraged resistivity; ILD, Deep-induction resistivity log]

References Cited

Adolph, B., Archer, M., Codazzi, D., el-Halawani, T., Perciot, P., Weller, G., Evans, M., Grant, J., Griffiths, R., Hartman, D., Sirkin, G., Ichikawa, M., Scott, G., Tribe, I., and White, D., 2005, No more waiting—Formation evaluation while drilling: Oilfield Review, Autumn 2005, p. 4–21.

Aldred, W., Cook, J., Bern, P., Carpenter, B., Hutchinson, M., Lovell, J., Rezmer-Cooper, I., and Leder, P.C., 1998, Using downhole annular pressure measurements to improve drilling performance: Oilfield Review, Winter 1998, p. 40–55.

Anderson, B., Bryant, I., Luling, M., Spies, B., and Helbig, K., 1994, Oilfield anisotropy—Its origins and electrical characteristics: Oilfield Review, October 1994, p. 48–56.

Bjerrum, L., 1972. Embankments on soft ground. Proceedings of the ASCE Specialty Conference on Performance of Earth and Earth-Supported Structures, Purdue University, v. II, p. 1–54.

Bonner, S.D., Tabanou, J.R., Wu, P.T., Seydoux, J.P., Moriarty, K.A., Seal, B.K., Kwok, E.Y., and Kuchenbecker, M.W., 1995, New 2-MHz multiarray borehole-compensated resistivity tool developed for MWD in slim holes, Paper SPE 30547 *in* Society of Petroleum Engineers Annual Technical Conference and Exhibition, Dallas, October 1995, Proceedings: Richardson, Tex., Society of Petroleum Engineers.

Bonner, S., Fredette, M., Lovell, J., Montaron, B., Rosthal, R., Tabanou, J., Wu, P., Clark, B., Mills, R., and Williams, R., 1996, Resistivity while drilling—Images from the string: Oilfield Review, Spring 1996: 4–19.

Clark, B., Allen, D.F., Best, D.L., Bonner, S.D., Jundt, J., Luling, M.G., and Ross, M.O., 1990, Electromagnetic propagation logging-while-drilling—Theory and experiment: SPE Formation Evaluation, Sept. 1990, p. 263–271.

Collett, T.S., and Ladd, J., 2000, Detection of gas hydrate with downhole logs and assessment of gas hydrate concentrations (saturations) and gas volumes on the Blake Ridge with electrical resistivity log data, *in* Paull, C.K., Matsumoto, R., Wallace, P.J., and Dillon, W.P., eds., Proceedings of the Ocean Drilling Program, Scientific Results, v. 164: College Station, Tex., Ocean Drilling Program, p. 179–191, accessed October 9, 2005 at *http://www.odp.tamu.edu/publications/164_SR/VOLUME/CHAPTERS/SR164_19.PDF*. [CD-ROM; available from: Ocean Drilling Program, Texas A&M University, College Station, Tex. 77845-9547, U.S.A.]

Davis, E.E., Hyndman, R.D., and Villinger, H., 1990, Rates of fluid expulsion across the northern Cascadia accretionary prism—Constraints from new heat flow and multichannel seismic reflection data: Journal of Geophysical Research, v. 95, p. 8869–8889.

Duan, Z., Møller, N., Greenberg, J., and Weare, J.H., 1992, The prediction of methane solubility in natural waters to high ionic strengths from 0° to 250 °C and from 0 to 1600 bar: Geochimica et Cosmochimica Acta, v. 56, p. 1451–1460.

Erickson, S.N., and Jarrard, R.D., 1998, Velocity-porosity relationships for water-saturated siliciclastic sediments: Journal of Geophysical Research, v. 103, p. 30,385–30,406.

Fofonoff, N.P., 1985, Physical properties of seawater: Journal of Geophysical Research, v. 90, no. C2, p. 3332–3342.

Holtz, R.D., and Kovacs, W.D., 1981, An introduction to geotechnical engineering: Englewood Cliffs, N.J., Prentice-Hall, Inc., 733 p.

Hunt, R.E., 1984, Geotechnical engineering investigation manual: New York, McGraw-Hill Book Company, 983 p.

Kvenvolden, K.A., and Lorenson, T.D., 2000, Methane and other hydrocarbon gases in sediment from the southeastern North American continental margin, *in* Paull, C.K., Matsumoto, R., Wallace, P.J., Black, N.R., Borowski, W.S.,Collett, T.S., Damuth, J.E., Dickens, G.R., Egeberg, P.K., Goodman,K., Hesse, R.F., Hiroki, Y., Holbrook, W.S., Hoskins, H., Ladd, J. ,Lodolo, E., Lorenson, T.D.,Musgrave, R.J., Naehr, T.H., Okada, H., Pierre, C., Ruppel, C.D., Satoh, M., Thiery, R., Watanabe, Y., Wehner, H., Winters, W.J.,and Wood, W.T., Gas hydrate sampling on the Blake ridge and Carolina rise—covering leg 164 of the cruises of the drilling vessel JOIDES Resolution, Halifax, Nova Scotia, to Miami, Florida, sites 991–997, 31 October–19 December 1995: Proceedings of the Ocean Drilling Program, Scientific Results, v. 164: College Station, Tex., Ocean Drilling Program, p. 29–36. [CD-ROM; available from: Ocean Drilling Program, Texas A&M University, College Station, Tex. 77845-9547, U.S.A.]

Ladd, C.C., Foote, R., Ishihara, K., Schlosser, F., and Poulos, H.G., 1977, Stress-deformation and strength characteristics, *in* State-of-the-Art Report, International Conference on Soil Mechanics and Foundation Engineering, 9th, Tokyo, Japan, July 1977, Proceedings: London, International Society for Soil Mechanics and Geotechnical Engineering, v. 2, p. 421–494.

Lambe, T. W., Whitman, R.V., 1969, Soil mechanics: New York, John Wiley and Sons, 553 p.

Musgrave, R.J., Bangs, N.L., Larrasoana, J.C., Gracia, E., Hollamby, J., and Vega, M.E., 2006, Rise of the base of the gas hydrate zone since the last glacial recorded by rock magnetism: Geology, v. 34, no. 2, p. 117–120.

Novosel, I., Winters, W.J., Boldina, O.M., Labails, C., and Geli, L., 2007, Thermal conductivity of sediment recovered from the IMAGES VIII/PAGE 127 Gas Hydrate and Paleoclimate Cruise on the R/V Marion Dufresne in the Gulf of Mexico, 2–18 July 2002, chap. 7 *of* Winters, W.J., Lorenson, T.D., and Paull, C.K., eds., Initial report of the IMAGES VIII/PAGE 127 gas hydrate and paleoclimate cruise on the RV Marion Dufresne in the Gulf of Mexico, 2–18 July 2002: U.S. Geological Survey Open-File Report 2004–1358, unpaged. (Also available at *http://woodshole.er.usgs.gov/pubs/of2004-1358/)*

Pearson, C.F., Halleck, P.M., McGuire, P.L., Hermes, R., and Mathews, M., 1983, Natural gas hydrate deposits—A review of *in situ* properties: Journal of Physical Chemistry, v. 87, p. 4180–4185.

Tréhu, A.M., Bohrmann, G., Rack, F.R., Torres, M.E., and others, 2003, Proceedings of the Ocean Drilling Program, Initial Reports 204 [CD-ROM]. Available from: Ocean Drilling Program, Texas A&M University, College Station, Tex. 77845-9547, USA.

Waxman, M.H., and Smits, L. J. M., 1968, Electrical conductivities in oil-bearing shaly sands: SPE Journal, Jun., 107–122.

Xu, W., 2002, Phase balance and dynamic equilibrium during formation and dissociation of methane gas hydrate, *in* International Conference on Gas Hydrates, 4th, Yokohama, Japan, May 2002, Proceedings: Yokohama, Japan, International Conference on Gas Hydrates, p. 195–200.

Xu, W., 2004, Modeling dynamic marine gas hydrate systems: American Mineralogist, v. 89, p. 1271–1279.